# ADVANCED STEEL CONSTRUCTION

*An International Journal*

**Volume 20 Number 3**

**September 2024**

**CONTENTS**

**Technical Papers**




Website: *http://www.hkisc.org*
ISSN 1816-112X
Science Citation Index Expanded, Materials Science Citation Index and ISI Alerting
*Cover: Photo @ Yang Yuhua*
*e-copy of IJASC is free to download at "www.ascjournal.com" in internet and mobile apps.*

ADVANCED STEEL CONSTRUCTION

VOL.20, NO.3 (2024)

ADVANCED STEEL CONSTRUCTION

*an International Journal*

*ISSN 1816-112X*

*Volume 20 Number 3* *September 2024*

ISSN 1816-112X

Science Citation Index Expanded, Materials Science Citation Index and ISI Alerting

# Advanced Steel Construction
*an international journal*



*Cover: Photo @ Yang Yuhua*
*e-copy of IJASC is free to download at "www.ascjournal.com" in internet and mobile apps.*

# General Information
## *Advanced Steel Construction, an international journal*

**Aims and scope**

The International Journal of Advanced Steel Construction provides a platform for the publication and rapid dissemination of original and up-to-date research and technological developments in steel construction, design and analysis. Scope of research papers published in this journal includes but is not limited to theoretical and experimental research on elements, assemblages, systems, material, design philosophy and codification, standards, fabrication, projects of innovative nature and computer techniques. The journal is specifically tailored to channel the exchange of technological know-how between researchers and practitioners. Contributions from all aspects related to the recent developments of advanced steel construction are welcome.



**Subscription inquiries and change of address.** Address all subscription inquiries and correspondence to Member Records, IJASC. Notify an address change as soon as possible. All communications should include both old and new addresses with zip codes and be accompanied by a mailing label from a recent issue. Allow six weeks for all changes to become effective.

**The Hong Kong Institute of Steel Construction**
HKISC
c/o Prof. SL Chan,
Unit 209B, Photonics Centre, No. 2 Science Park East Avenue,
Hong Kong Science Park, Shatin, N.T., Hong Kong, China.
Tel: 852- 3595 6150 Fax: 852- 3619 7238
Email: ceslchan@connect.polyu.hk Website: *http://www.hkisc.org/*
**ISSN 1816-112X**
**Science Citation Index Expanded, Materials Science Citation Index and ISI Alerting**

ISSN 1816-112X

**Science Citation Index Expanded, Materials Science Citation Index and ISI Alerting**



# Advanced Steel Construction
*an international journal*

**VOLUME 20 NUMBER 3 September 2024**

**Technical Papers**

**Advanced Steel Construction** – Vol. 20 No. 3 (2024) 208–221
**DOI:**10.18057/IJASC.2024.20.3.1


# SEISMIC FRAGILITY ANALYSIS OF STEEL FRAMES WITH FULLY-BOLTED CORE TUBE JOINTS

Yun-Peng Chu, Xue-Qin Chen *, Yan Zhong and Hai-Chuan Zhang

*School of Civil Engineering and Architecture, Southwest University of Science and Technology, Mianyang 621010, China*
** (Corresponding author: E-mail: chenxueqinswust@qq.com)*

**ABSTRACT**

In this paper, the joint parameters derived from testing the new fully-bolted core tube beam-column joint were utilized in the finite element analysis of the complete frame structure. The static elastic-plastic time-history analysis of 8, 12, 16, and 20-story steel frames with the braces was carried out. By comparing the maximum inter-layer displacement angles in the X and Y directions when the frame yielded, the rationality of the brace arrangement and the applicability of the new fully-bolted core tube beam-column joints in the multi-story and high-rise steel frames were confirmed. After dividing the range of damage values for the steel frame with the new fully-bolted core tube beam-column joint, the seismic fragility and collapse resistance of the steel frame with the new fully-bolted core tube beam-column joint of different stories were analyzed. The results show that it is important to note that when the number of stories is low, the probability of each stage of the structure being exceeded is high. However, as the number of stories increases, the impact on the probability of the structure being exceeded gradually decreases. Under the action of a large earthquake peak acceleration, the exceedance probability based on a two-parameter damage index is higher than that based on a single-parameter damage index. This indicates that during the large deformation stage of the structure, the influence of cumulative damage on the evaluation of structural performance cannot be ignored. The steel frame of multi-story and high-rise buildings with new joints may be in a serious damage stage under rare earthquakes, and it is possible to collapse under the action of great earthquakes. In addition, the ACMR value of the structure under the action of rare earthquakes meets the evaluation criteria, while the ACMR value under the action of great earthquakes does not meet the requirements. Therefore, in practical engineering, it is necessary to take seismic strengthening measures to ensure that the structure has sufficient safety reserves against collapse during earthquakes.

**ARTICLE HISTORY**

Received: 31 August 2023
Revised: 18 March 2024
Accepted: 3 April 2024

**KEYWORDS**

Fully bolted joint;
Layered assembly steel frame;
Multi-story and high-rise steel frames;
Fragility analysis



## 1. Introduction

The layered assembled steel frame structure has received extensive attention because the individual components of the structure can be extensively prefabricated in the factory, leading to a more conducive environment for achieving efficient and rapid assembly goals. With the development of society and economy, multi-story and high-rise buildings have gradually become an important carrier of urban economic activities. However, the force situation of the multi-story and high-rise steel frame joint during earthquake is quite complex. Therefore, it is necessary to make a reasonable seismic evaluation of the seismic performance of multi-story and high-rise layered assembled steel frame.

Following the Northridge earthquake and the Osaka earthquake, fragility damage was observed in a majority of the conventional steel frame beam-column joints, prompting numerous scholars to initiate research on enhancing welded joints [1–3]. There is still a risk of weld fracture, even though the enhanced joints show excellent seismic performance. As a result, researchers have gradually advanced the concept of fully bolted joints. Using fully bolted joints can significantly increase the ductility, plastic deformation and energy dissipation capacities of the joint, while also reducing seismic damage from bolt slippage.

Based on this, Shahidi et al. [4] studied the influence of the bolt arrangement on the seismic performance of ConXL joints by numerical simulation. The results show that when the bolt is close to the outer edge of the joint plate, the axial stress of the bolt rod is very large. The closer the bolt is to the flange of the beam, the shear of the bolt rod is generated due to the increase of the slip of the end plate of the beam. The seismic performance of the joint with bolts installed in the middle of the gusset plate is good, and the joint with two rows of bolts on each gusset plate has better seismic performance than the joint with one row of bolts. Lee et al. [5] proposed a modular joint with brace, in which the beams and columns are connected by welding and the modules are connected by connecting plates. The test results show that this joint has good seismic performance. Wang et al. [6] conducted low cyclic loading tests on square steel tube column and H-shaped steel beam joints connected with through bolts. The results show that the seismic performance of the joints with such bolt is better, and it is pointed out that for the unfilled steel tube column, the column wall will have symmetrical concave buckling phenomenon. Hosseini et al. [7] proposed a ring-hoop joint. Through finite element analysis of 18 models with this joint, the optimal design parameters of the joint were obtained. Compared with the short connecting plate, using a longer connecting plate at the beam end to connect to the gusset plate can achieve better joint performance. Liu et al. [8-10] developed a a modular beam-column bolt joint. Their tests demonstrated that the joint has excellent seismic performance.

Seismic fragility is essential for evaluating the seismic reliability of structures, improving their seismic design, preventing earthquake disasters, performing follow-up maintenance, and strengthening structures after an earthquake. Lv et al. [11] used the Incremental Dynamic Analysis (IDA) to evaluate the seismic fragility of a non-standard high-rise building. They determine the probability that a structure will surpass its limit state. The results show it can be used to determine the damage and loss of structures in earthquakes. Pushover and IDA were performed on steel frames by Fanaie et al. [12] and Mohebi [13] et al. They classified the limit states based on the damage index as a performance level indicator. The limit state correction coefficients of the structure were finally got. Accounting for random ground motion and structure uncertainty, Pandikkadavath et al [14] analyzed the seismic fragility of the structure. Correction coefficients for the response discounting parameters for the seismic design of enhanced structures were obtained. The collapse probability and anti-collapse reserve coefficient of the structure were quantitatively evaluated by Wang et al. [15] through IDA analysis of a steel frame supported by multi-layer beams with varying joint stiffness. Li et al. [16] used the seismic risk theory to conduct probabilistic seismic demand analysis for structures. The probability of structural earthquake occurrence and the characteristics of structural seismic response are determined.

Currently, the traditional column-through-structure is the main focus of research efforts on the seismic fragility of steel structures. However, there is a lack of extensive research on steel frames with layered assembled connections. Today, the fully bolted joint design concept is more sophisticated [17–20], but there are problems that complex joints are not easy to quickly assemble and simple joints don't have good seismic performance. To address these issues, A novel fully-bolted core tube beam-column joint was proposed and subsequently subjected to quasi-static tests. In order to explore the applicability and feasibility of this kind of joints applied to the middle and high-rise frame, the joint test parameters were introduced into the whole frame structure. Four braced steel frame models with the new joint with total stories of 8, 12, 16, and 20 were established by SAP2000 for static elastic-plastic time history analysis and incremental dynamic analysis. The damage value range of the frame with the new joint was re-divided. The plastic angle distribution and collapse resistance of the frame models with the new joint were obtained. The feasibility and effectiveness of the new joint applied to the multi-story and high-rise steel frame have been systematically evaluated, which serves as a reference for evaluating the seismic performance of similar structures.

## 2. Joint test and simplified mechanical model

### 2.1. Joint test

The seismic performance of the entire structure may be affected by the loading characteristics of the connections between the steel frame beams and columns, as they are the main transmission part of the structure. A new fully bolted core tube joint (XJD) is designed based on the concept of energy dissipation-seismic reduction. The traditional column-through joint (CJD) is used as the control group, and the quasi-static test is carried out on the new and traditional joint [21]. CJD (Fig. 1a) was the commonly used beam-column joint. XJD consists three components: a square steel tube column, an H-shaped beam and a core tube joint.

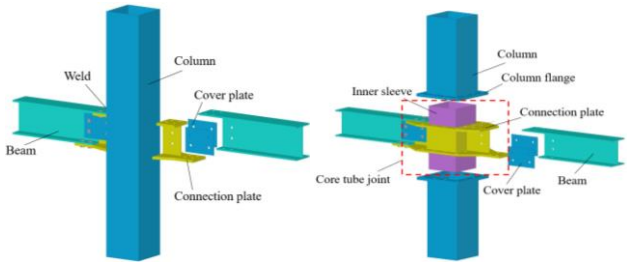


(a) (b)

**Fig. 1** 3D diagram of test joints. (a) CJD. (b) XJD

The CJD and XJD are both constructed as steel frame beam-column joints. The primary difference between two types of joints is XJD by practice. Unlike the CJD, it disconnects the column at the floor connection and establishes connections between the upper and lower columns and beams using a connecting plate located on the column base within the joint domain. This innovative design allows for a layered assembly technique to be implemented. The CJD design features that the column is through, and is connected by setting a connecting plate welded to the column wall at the beam-column connection. This design carries the risk of weld cracking during an earthquake. Through a comparison of the test results from the two kinds of joints, the XJD's enhanced seismic performance can be better demonstrated. Fig. 2 displays the test-loading device and the layout of the site.

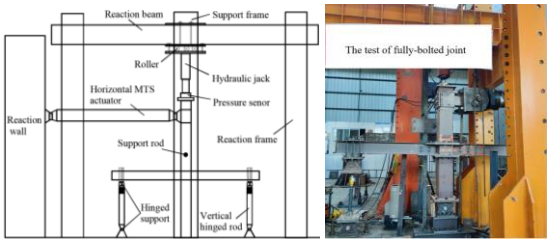


(a) (b)

**Fig. 2** The test-loading device and the layout of the site. (a) Test-loading device. (b) Layout of the site

The test results showed that in comparison to the CJD, the XJD exhibited a 471.39% increase in total energy consumption, a 27.52% increase in ductility coefficient, a 20.35% increase in yield load, and a 38.56% increase in ultimate load. It could be seen that the XJD's seismic performance was obviously better than the CJD.

### 2.2. Simplified mechanical analysis model

Joint differences between steel frame and reinforced concrete frame structures These joints are not fully bonded. A welded joint is called a rigid joint, and a bolted joint is called a flexible joint. The research suggests that because of the still existing some rotational stiffness in welded or bolted joints, they cannot be easily classified as either rigid or flexible joints. In this paper, the Bjorhovde [22] and Eurocode3 [23] procedures are used to determine the XJD's and CJD's properties. The $M_{ratio}$ and $\theta_{ratio}$ are calculated and presented in Fig. 3.

It can be seen from Fig. 3 that the Eurocode3 method has a larger range. The $M_{ratio}$-$\theta_{ratio}$ curves for XJD and CJD are fall within the range of semi-rigid joints based on the Eurocode3 method. Based on the Bjorhovde method, CJD's $M_{ratio}$-$\theta_{ratio}$ curve is classified as semi-rigid. Similarly, the semi-rigid classification also applies to the first half of XJD's $M_{ratio}$-$\theta_{ratio}$ curve. The increase in the angle of rotation of the two joints may be due to bolt slippage or weld cracks, resulting in a gradual increase in the bending moment at the end of the beam. This causes the joints to exhibit a semi-rigid joint performance. The XJD's $M_{ratio}$-$\theta_{ratio}$ curve keeps to increasing, indicating that the bending capacity is excellent. The curve of $M_{ratio}$-$\theta_{ratio}$ in CJD initially increases and then decreases. It can be caused by the reduction in bending capacity during plastic deformation due to weld cracking and column wall buckling. According to Bjorhovde's method, the XJD will remain in the semi-rigid region of the joint during both the plastic and the elastic-plastic deformation stages, although it exhibits rigid joint properties in the later stages of loading due to the continued plastic deformation. According to the two methods for the classification of joint properties, XJD and CJD are considered to be semi-rigid joints.

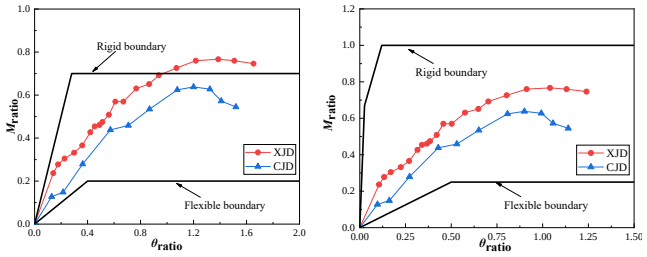


（a）Bjorhovde method （b）Eurocode3 method

**Fig. 3** Connection property calculation results

It has been discovered that both XJD and CJD are types of semi-rigid joints. On the basis of the code GB50017-2017 [24], the rotational angle of the beam-column semi-rigid connection will change when subjected to bending moment, but its rotational stiffness is restrained. To simulate the semi-rigid joint using the nonlinear connector, it is essential to choose a suitable $M$-$\theta$ model. The $M$-$\theta$ curve of the tested joints was subjected to dimensionless processing, taking into account the impact of specimen parameters. It was then fitted using the trilinear model. The equation used for fitting is presented in Table 1. The comparison between the normalized joint test $M$-$\theta$ curve and the fitted $M$-$\theta$ curve is shown in Fig. 4. Based on Fig. 4, it is clear that the $M$-$\theta$ curve closely matches the curve obtained from the test when fitted using the trilinear model. This makes it appropriate for simplifying joint calculations.

**Table 1**
Tri-linear fitting equations for normalized $M$-$\theta$ curves of joints

| Folded line segment | XJD | CJD |
|---|---|---|
| OA | $M/M_{max} = 1.838\,\theta/\theta_{max}$ | $M/M_{max} = 1.363\,\theta/\theta_{max}$ |
| AB | $M/M_{max} = 0.385 + 0.624\,\theta/\theta_{max}$ | $M/M_{max} = 0.292 + 0.689\,\theta/\theta_{max}$ |
| BC | $M/M_{max} = 1.061$ | $M/M_{max} = 1.722 - 0.731\,\theta/\theta_{max}$ |

Note: $M_{max}$ is the bending moment corresponding to the ultimate load, and $\theta_{max}$ is the rotation angle corresponding to the ultimate load.

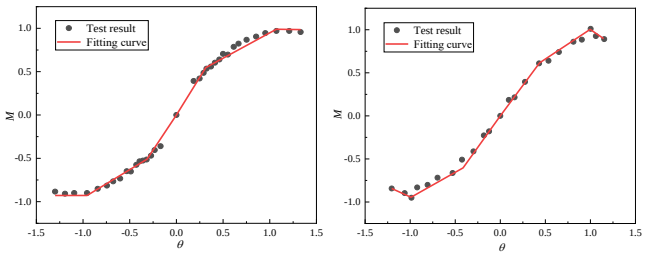


(a) (b)

**Fig. 4** Compare Joint Test and Fitted *M-θ* Curve. (a) XJD. (b) CJD

The semi-rigid connection is simulated using the kinematic restoring force model, and the hysteresis model is shown in Fig. 5. Using the method described above, the FEA models for the new joint and the traditional joint are created in SAP2000. The simplified analysis model is illustrated in Fig. 6.

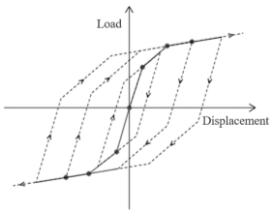


**Fig. 5** Kinematic hysteretic model

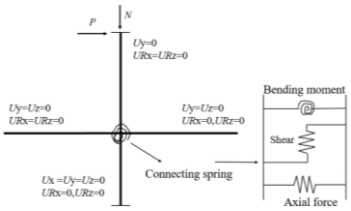


**Fig. 6** Simplified mechanical analysis model

In simplified joint analysis, the beam is represented as a bar element connected to two zero-length rotational springs at the bar ends. The axial and shear deformations of the end torsion springs are not considered, and only their bending deformations are taken into account. Rigid blocks were attached to both ends of the column. These were used to apply loads or set boundary conditions. Both an axial load and a cyclic load have been subjected to the top of the column. The boundary conditions of the numerical model were identical to those of the test joint. At the bottom of the column, three directions of translation were limited, while at the top of the column, translation in the Y direction was limited. The beam ends were restrained to avoid out-of-plane instability in all directions besides the X-direction. The characteristic points in the fitted M-θ curve are defined within the kinematic restoring force model's corner spring unit. The column is subjected to a concentrated load *N* and a reciprocating load *P*. Based on the test conditions, the model constraints are set. The XJD initial torsional rigidity ($K_1$) link spring is $3.4\times10^4$ kN·m/rad. The XJD initial torsional rigidity ($K_2$) link spring is is $3.0\times10^4$ kN·m/rad. Fig.7 compares the results obtained using the simplified model and the joint test.

Based on Fig. 7, it is evident that the *M-θ* curve of the joint between the test and the simplified model exhibits a strong correlation. XJD and CJD had an ultimate bending capacity of 200.59 kN·m and 152.89 kN·m, respectively, according to the test results. Using the simplified model, the ultimate bending capacities of XJD and CJD were calculated as 213.68kN·m and 139.28kN·m, respectively. The errors between the test results and the simplified model calculation results were 6.53% and -8.9% respectively, both percentages were below 15%. This demonstrates that the simplified model is highly accurate for joint simulation and can be used for further analysis of the overall model.

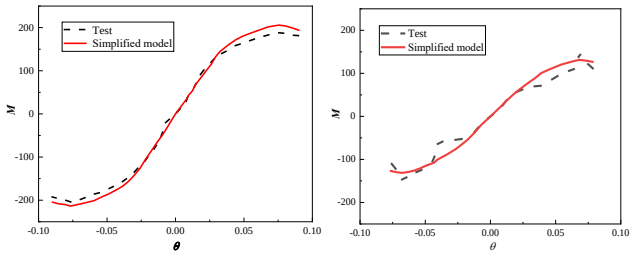


(a) (b)

**Fig. 7** Compare simplified model calculations and test results. (a) XJD. (b) CJD

## 3. Static elastic-plastic time-history analysis

### *3.1. Design basic parameters*

The steel frame structures were situated in an area characterized by a seismic intensity of 8. Design basic ground motion acceleration is 0.2g. Site classification is II, Site characteristic period (Tg) is 0.40s. Site roughness is class C. The design considers a floor dead load of 4.0 kN/m$^2$ and a live load of 2.0 kN/m$^2$. The beam was assigned a line load of 10 kN/m. The snow load on the roof was taken as 0.5 kN/m$^2$. The wind load was taken as 0.3 kN/m$^2$.

### *3.2. Finite element Model*

Four steel frame structures are designed by PKPM as the calculation models, of which the stories are 8, 12, 16, and 20, respectively. In combination with Reference [25], the inverted V-shaped center brace is arranged in the steel frame structures. The size of the structural members is shown in Tables 2 to 5. The actual layout is shown in Fig. 8. Subsequently, the models are established by SAP2000, with the joint parameters referencing the simplified mechanical model mentioned earlier. The foundation is consolidated. The spring element was placed at the fracture of the beam-column joint. The initial stiffness and *M-θ* curve eigenvalues of both the XJD and CJD were defined into the spring element. The load cases were set as gravity load conditions and pushover load conditions. Nonlinear Static Analysis was selected as the type of structural analysis. The geometric nonlinearity is set to *P-Δ* nonlinearity. The initial condition of the pushover load case is relay nonlinear. The loading option is displacement control. The displacement type is selected to monitor the displacement, and the displacement target value is 0.04 times the building height. The coefficients of plastic hinge setting from the end points of the structural components were 0.1 and 0.9, respectively. *PMM* hinge was used for columns, *M* hinge was used for beams and *P* hinge was used for braces.

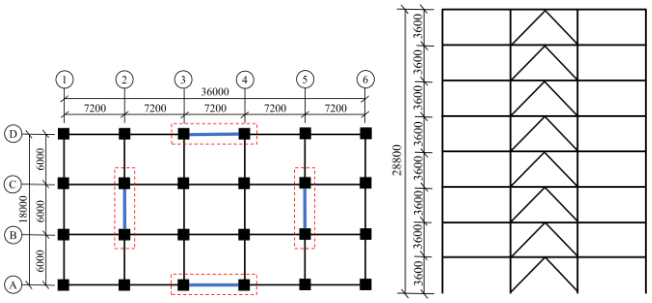


(a) (b)

**Fig. 8** Steel frame layout. (a) Plan layout. (b) Elevation layout

**Table 2**
8-story component size parameters

| Model | Material | Components | Section |
|---|---|---|---|
| 8-story | Q235 | Corner column | 1~8 stories: □500×18 |
| | | Middle column | 1~8 stories: □550×30 |
| | | Beam | 1~8 stories: H400×200×8×13 |
| | | Brace | 1~8 stories: H175×90×5×8 |

**Table 3**
12-story component size parameters.

| Model | Material | Components | Section |
|---|---|---|---|
| 12-story | Q355 | Corner column | 1~6 stories: □500×18; 7~12 stories: □500×16 |
| | | Middle column | 1~3 stories: □700×30; 4~6 stories: □650×30; 7~12 stories: □600×26 |
| | | Beam | 1~6 stories: H600×200×10×15; 7~12 stories: H600×200×10×15 |
| | | Brace | 1~12 stories: H300×150×6.5×9 |

**Table 4**
16-story component size parameters

| Model | Material | Components | Section |
|---|---|---|---|
| 16-story | Q355 | Corner column | 1~8 stories: □500×18； 9~16 stories: □500×16 |
| | | Middle column | 1~3 stories: □650×30； 4~6 stories: □600×28; 7~9 stories: □500×30<br>10~12 stories: □500×28; 13~16 stories: □500×26 |
| | | Beam | 1~8 stories: H500×200×9×14; 9~16 stories: H450×200×9×14 |
| | | Brace | 1~16 stories: H350×175×7×11 |

**Table 5**
20-story component size parameters

| Model | Material | Components | Section |
|---|---|---|---|
| 20-story | Q355 | Corner column | 1~5 stories: □500×30; 6~10 stories: □500×30; 11~20 stories: □500×24 |
| | | Middle column | 1~3 stories: □850×30; 4~6 stories: □750×30; 7~9 stories: □650×30; 10~15 stories: □500×26; 16~18 stories: □500×22; 19~20 stories: □500×18 |
| | | Beam | 1~5 stories: H500×200×9×14; 6~10 stories: H450×200×9×14; 11~15 stories: H500×150×10×16; 16~20 stories: H450×150×9×14 |
| | | Brace | 1~20 stories: H400×200×8×13 |

### *3.3. Distribution of plastic hinges*

The distribution of the interlayer displacement angle and the plastic hinge for the four models at different stages are shown in Figs. 9 to 13. Specifically, (a) indicates the plastic hinge first appears in the brace. (b) indicates the plastic hinge first appears in the beam. (c) indicates the plastic hinge first appears in the column. (d) indicates the plastic hinge distribution of the structure when the maximum inter-layer displacement angle reaches 1/50.

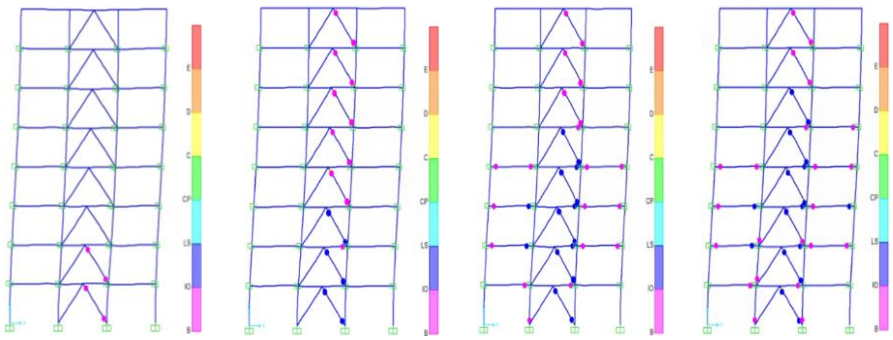


(a) (b) (c) (d)

**Fig. 9** 8-story

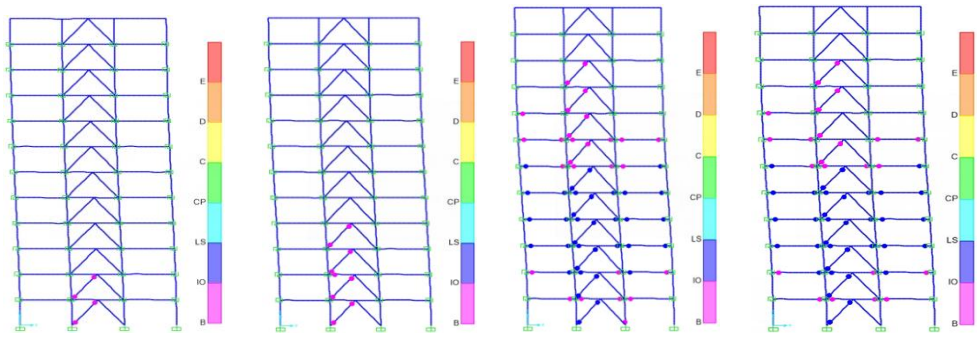


(a) (b) (c) (d)

**Fig. 10** 12-story

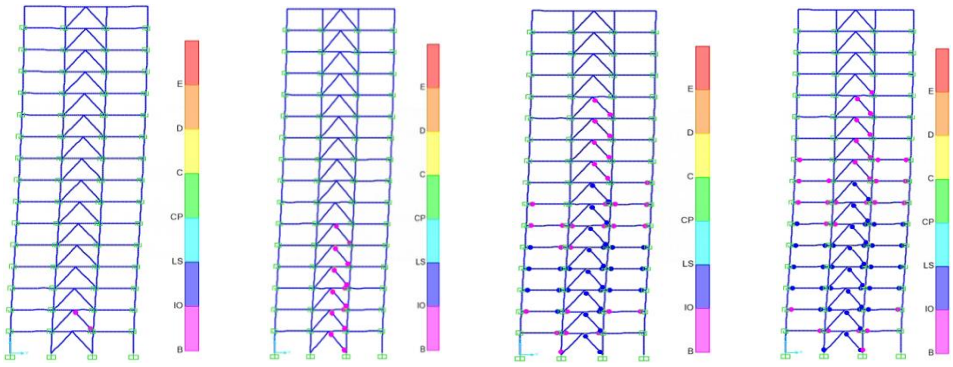


(a) (b) (c) (d)

**Fig. 11** 16-story

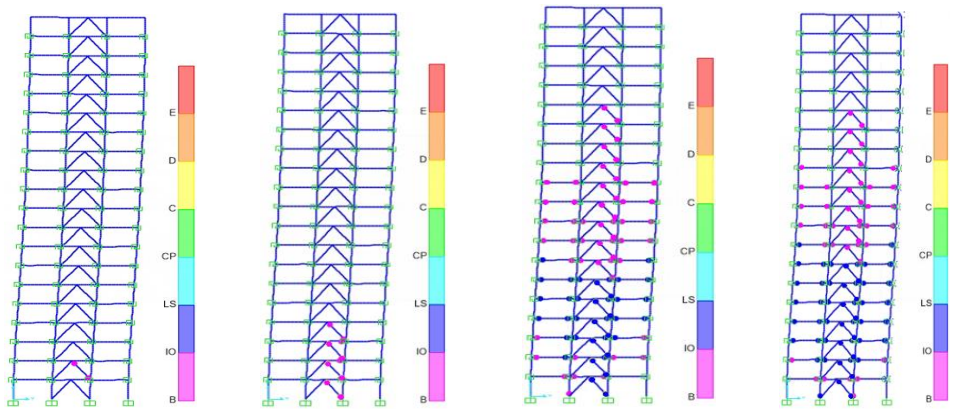


(a) (b) (c) (d)

**Fig. 12** 20-story

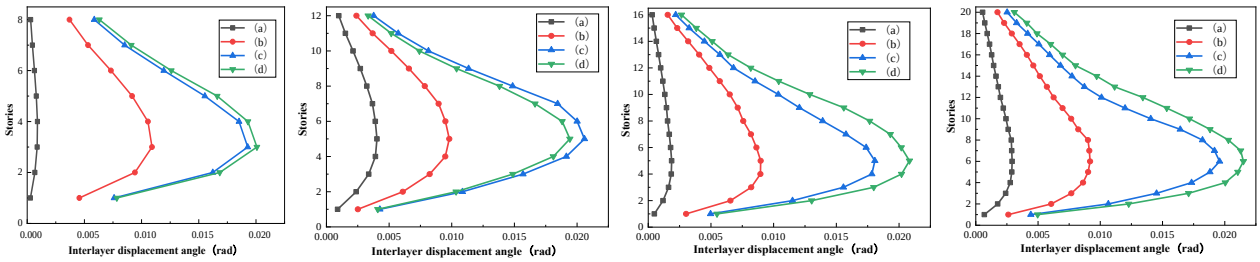


(a) (b) (c) (d)

**Fig. 13** Distribution of interlayer displacement angle. (a) 8-story. (b) 12-story. (c) 16-story. (d) 20-story

The distribution of inter-layer displacement angle is presented in Fig. 13. According to the analysis of the distribution of plastic hinge and inter-layer displacement angle in each stage of the steel frame structure, the plastic hinges first appear in the brace, then in the beam, and finally begins to develop on the column. In addition, before the interlayer displacement angle reaches 0.02 rad, most of the braces and beams have entered the stage of plastic deformation development, and the steel frame presents the fortification requirement of "strong column and weak beam" before the failure of the braces and beams, which conforms to the seismic design concept of the steel frame structure. Moreover, when the inter-layer displacement angle reaches 0.02 rad, only the 1 to 3 story middle columns of the 8-story structure have plastic hinges, while the 16-story and 20-story structures show plastic hinges only in the middle columns of the bottom story and all the columns of the 12-story structure are still in the elastic deformation stage. These mean that four models are in accordance with the idea of “capacity design”. The selection of structural components is appropriate and the arrangement is reasonable. It also means that it is conservative to use the elastic-plastic inter-layer displacement angle of 1/50 as the collapse criterion of the steel frame structure with the new jointed.

### *3.4. Pushover curves*

The response spectrum in SAP2000 is the ATC-40 [26] response spectrum. The parameters $C_A$ and $C_V$ need to be changed to make the structure calculation conform to the Chinese code. $C_A$ and $C_V$ can be calculated by Eq. (1) and Eq. (2), respectively.

$$\eta_2\alpha_{max} = 2.5C_A \quad (1)$$

$$T_g = T_s = C_V / 2.5C_A \quad (2)$$

where, $\eta_2\alpha_{max}$ is the maximum value of the horizontal seismic influence coefficient. The site characteristic period $T_g$ is 0.4 s. For an 8-degree frequent earthquake, $\eta_2\alpha_{max}$ = 0.16, and $C_A$ = 0.064, $C_V$ = 0.064 can be obtained through calculation. For an 8-degree rare earthquake, $\eta_2\alpha_{max}$ = 0.9, and $C_A$ = 0.36, $C_V$ = 0.36 can be obtained through calculation.

In the pushover analysis results, the top displacement, spectral displacement, base shear and spectral acceleration at the performance point can be directly viewed to evaluate the seismic performance of the structure. as shown in Fig. 14. The performance point is located at the intersection of the capability spectrum curve and the demand spectrum curve in the same coordinate system. The performance point can be expressed by spectral displacement and spectral acceleration, and the top displacement and base shear at the performance point can be further obtained by Eq. (3) and Eq. (4).

$$V = \alpha_n G S_a \quad (3)$$

$$D = \gamma_n X_n S_d \quad (4)$$

Where $\alpha_n$ is the mass participation coefficient, $\gamma_n$ is the participation coefficient, and $X_n$ is the vertex amplitude. Because the high-rise steel frame structure is generally dominated by the first vibration mode during the earthquake, only the $\alpha_n$, $\gamma_n$ and $X_n$ under the first vibration mode is taken.

When the displacement demand of the structure under the seismic fortification level is less than the structure's actual seismic displacement response, The point where the capacity spectrum and demand spectrum curves intersect will be visible, indicating that the structure is considered to be safe and reliable. Conversely, if the displacement demand exceeds the actual seismic displacement response of the structure, resulting in no intersection between the two curves, the structural performance point does not exist, suggesting that the structure is not safe and reliable at this time. Its seismic performance does not meet the basic requirements and the seismic fortification goals. In such cases, it becomes necessary to either redesign or reinforce the structure.

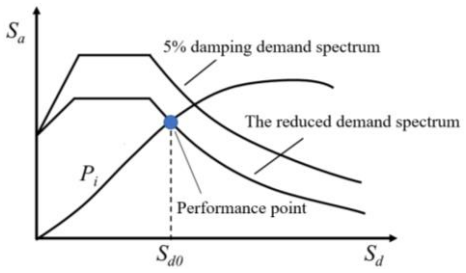


**Fig. 14** Structural performance points

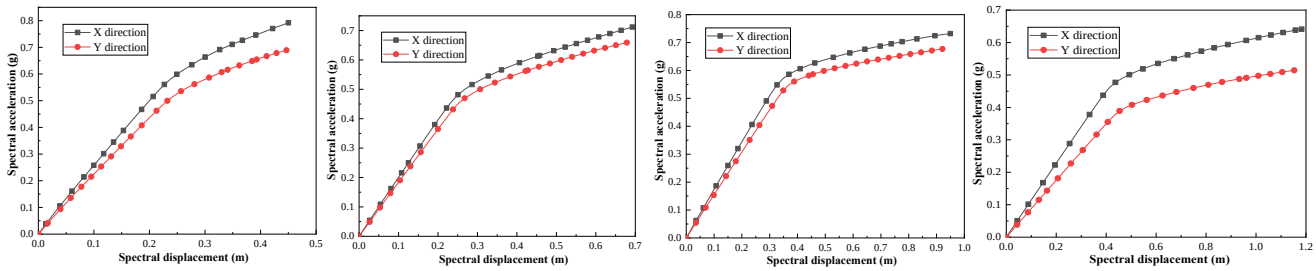


(a) (b) (c) (d)

**Fig. 15** Capacity spectrum curve. (a) 8-story. (b) 12-story. (c) 16-story. (d) 20-story

From Fig. 15, it can be seen that under the action of frequent and rare earthquakes, each model has performance points in the X and Y directions. It means that the structure meets the requirements of seismic fortification and is in the safe state. Additionally, the higher the structural stiffness, the lower the ductility and performance level. Under the action of earthquake, as the number of stories increases, the spectral acceleration at the performance point decreases while the spectral displacement increases.

**Table 6**
Spectral acceleration and spectral displacement (performance points)

| Stories | | X direction | | Y direction | |
|---|---|---|---|---|---|
| | | Spectral acceleration /g | Spectral displacement /mm | Spectral acceleration /g | Spectral displacement /mm |
| Frequent earthquake | 8 | 0.071 | 32.27 | 0.078 | 24.96 |
| | 12 | 0.066 | 33.45 | 0.070 | 25.16 |
| | 16 | 0.062 | 47.00 | 0.063 | 41.01 |
| | 20 | 0.059 | 58.40 | 0.060 | 51.18 |
| Rare earthquake | 8 | 0.461 | 184.03 | 0.463 | 161.56 |
| | 12 | 0.381 | 187.23 | 0.395 | 162.95 |
| | 16 | 0.353 | 283.50 | 0.361 | 229.73 |
| | 20 | 0.332 | 327.42 | 0.352 | 286.73 |

Table 6 shows that under the action of frequent earthquakes, the X-direction spectral displacement of 8-story, 12-story, 16-story, and 20-story models is 29.29%, 32.95%, 14.61%, and 13.91% higher than that of Y-direction, respectively. Similarly, Under the rare earthquakes, the X-direction spectral displacement of 8-story, 12-story, 16-story, and 20-story models is 13.91%, 14.90%, 23.41%, and 14.19% higher than that of Y-direction, respectively. The vibration characteristics of each model in the X direction are larger than those in the Y direction. However, the small difference in the spectral displacement between the two directions, which means that the mass distribution of the structure in the X and Y directions is uniform.

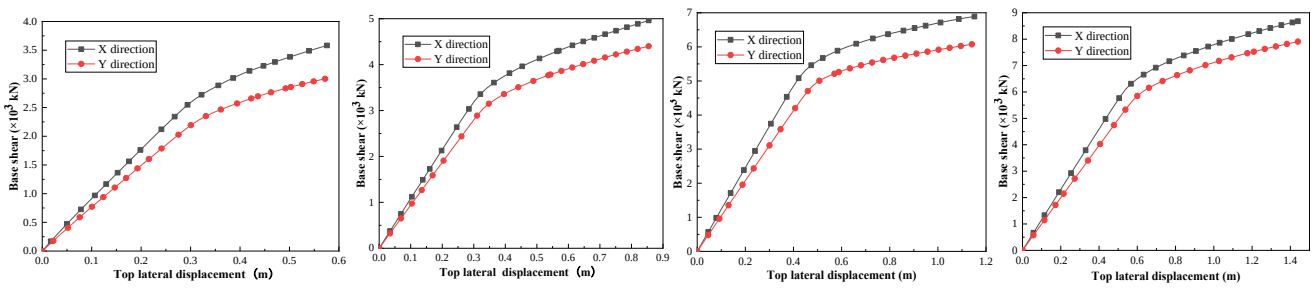


(a) (b) (c) (d)

**Fig. 16** Base shear and top lateral displacement curve. (a) 8-story. (b) 12-story. (c) 16-story. (d) 20-story

Fig.15 shows the base shear-top lateral displacement curve of the model. The corresponding top displacement and base shear of the structural performance points provided in Table 7. Notably, all the curves have obvious inflection points. The X-direction base shear of each model is greater than the Y-direction base shear due to the enhanced X-direction lateral stiffness resulting from the central brace. As the number of structural stories increases, the top lateral displacement and base shear also increase. At the performance point of the structure, the base shear in the Y direction is larger than that in the X direction, while the top lateral displacement in the Y direction is smaller than that in the X direction. This indicates that the vibration characteristics of the structure in the Y-direction are smaller than those in the X-direction during the earthquakes.

**Table 7**
Base shear and top lateral displacement (performance point)

| Stories | | X direction | | Y direction | |
|---|---|---|---|---|---|
| | | Top lateral displacement /mm | Base shear /kN | Top lateral displacement /mm | Base shear /kN |
| Frequent earthquake | 8 | 41.99 | 292.33 | 35.08 | 345.73 |
| | 12 | 43.61 | 341.37 | 37.41 | 486.62 |
| | 16 | 61.83 | 552.07 | 52.98 | 765.24 |
| | 20 | 76.86 | 641.06 | 66.24 | 922.61 |
| Rare earthquake | 8 | 238.54 | 1570.08 | 209.41 | 2085.79 |
| | 12 | 244.26 | 1901.26 | 209.05 | 2694.82 |
| | 16 | 347.02 | 3076.24 | 297.10 | 4242.52 |
| | 20 | 433.13 | 3583.59 | 373.26 | 5141.77 |

According to Table 7, under the action of frequent earthquakes, the top lateral displacement in the X-direction of the 8-story, 12-story, 16-story, and 20-story models is 16.46%, 14.22%, 14.31%, and 13.82% higher than those in the Y-direction, respectively. Under the action of rare earthquakes, the top lateral displacement in the X-direction of the 8-story, 12-story, 16-story, and 20-story models is 12.21%, 14.41%, 14.38%, and 13.82% higher than the top lateral displacement in the Y-direction, respectively. Thus, there is not a significant difference in the lateral displacement between the two directions of the structure under the action of frequent and rare earthquakes.

### *3.5. Yield displacement angle*

The double broken line energy equal area method can be employed to determine the yield point of a structure if the load-displacement curve obtained from pushover analysis does not exhibit a clear yield point. The theoretical model for this method is shown in Fig. 17. The yield point of the structure is defined based on two calculation principles. Firstly, the deformation should be consistent with the energy dissipation, meaning that the area enclosed by the curve is equal to the area enclosed by the double broken line ($S_{OB} = S_{OABE}$). Secondly, the double broken line and the curve are infinitely approximated, and the value that satisfies $m = S_1 + S_2 + S_3$ is minimized. The yield point of the structure is the intersection point $C$ when the above principles are satisfied.

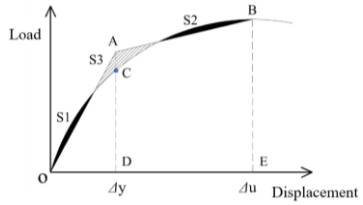


**Fig. 17** Double broken line energy equal area method

Except for the 8-story model, the other models have obvious points of contraflexure, i.e., the 12-story, 16-story, and 20-story models all have structural yield points, according to the structural base shear and top lateral displacement curves in Fig. 16. Thus, the method described above is utilized to identify the yield point of the 8-story model. The top lateral displacement and base shear corresponding to the yield point of the structure are given in Table 8. The inter-layer displacement angle when the structure yields is shown in Fig. 18.

From Table 8 and Fig. 18, it can be observed that the base shear increases with the height of story, but the difference between the base shear in the X and Y directions of the structure is small. Compared with the X-direction, the Y-direction base shear of the 8-story, 12-story, 16-story, and 20-story models increased by 13.97%, 9.82%, 7.98%, and 7.31%, respectively. When each model yields, the top lateral displacement in X direction is greater than that in Y direction. Compared to the Y-direction, the top lateral displacement in the X-direction of the 8-story, 12-story, 16-story, and 20-story models decreased by 2.38%, 1.69%, 1.16%, and 1.91%, respectively. The difference between the X and Y directions of the model is small, and the influence of the second-order effect of gravity on the two directions is not greatly different. When the structure yields, the maximum inter-layer displacement angles of the 8-story model in both X and Y directions are 1/64. For the 12-story model, the maximum inter-layer displacement angles in the X and Y directions are 1/79 and 1/82, respectively. For the 16-story model, the maximum inter-layer displacement angles in the X and Y directions are 1/82 and 1/83, respectively. For the 20-story model, the maximum inter-layer displacement angles in the X and Y directions are 1/73 and 1/74, respectively. When the structure reaches the yield point, the maximum inter-layer displacement angle in both directions is close, indicating that the structural quality distribution is uniform and the brace arrangement is reasonable.

When the structure yields, the top displacement angles of the 8-story model in X and Y directions are 1/160 and 1/196, respectively, and the change rate is 22.50%. The top displacement angles of the 12-story model in X and Y directions are 1/450 and 1/353, respectively, and the change rate is 21.56%. The top displacement angles of the 16-story model in X and Y directions are 1/505 and 1/388, respectively, and the change rate is 23.17%. The top displacement angles of the 20-story model in X and Y directions are 1/438 and 1/350, respectively, and the change rate is 20.01%. The top inter-layer displacement angle of the 8-story model is the largest, while that of the other models is small. The reason is that when the structure yields, all the braces of the 8-story model appear plastic deformation, while the upper braces of the other models are still in the elastic deformation state.

**Table 8**
Base shear and top lateral displacement when the structure yields.

| Stories | X direction | | Y direction | |
|---|---|---|---|---|
| | Top lateral displacement /mm | Base shear /kN | Top lateral displacement /mm | Base shear /kN |
| 8 | 278.17 | 2642.70 | 284.8 | 2273.48 |
| 12 | 341.88 | 3491.32 | 347.67 | 3148.52 |
| 16 | 418.50 | 5304.63 | 423.37 | 4881.23 |
| 20 | 551.64 | 6505.99 | 562.15 | 6030.40 |

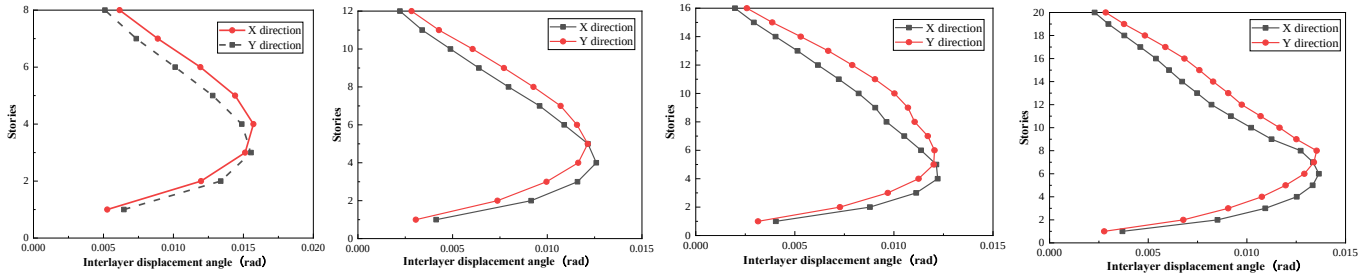


**Fig. 18** Interlayer displacement angle when the structure yields. (a) 8-story. (b) 12-story. (c) 16- story. (d) 20-story

### *3.6. Determination of performance level*

The classification of the performance level of the structure and the determination of its failure state are the key parts of the structural probabilistic seismic capacity analysis. Currently, the main division ideas are based on four performance levels and five failure states. Numerous researchers have conducted quasi-static and shaking table tests on the assembled beam-column joints or frames. Through these tests, the damage development mechanism of the assembled joints is clarified, and the cooperative working ability and damage situation between the joints and other components are understood when applied to the whole frame structure.

In the quasi-static test [27–32], the existing prefabricated beam-column joints did not show the phenomenon of sudden fracture at the joint area or the member, and all of them showed a ductile failure. When the rotation angle of the joint is loaded to 0.02 rad, the specimens are no obviously deformed. When the joint is destroyed, the minimum rotation angle is 0.04 rad and the maximum rotation angle can reach 0.09 rad, showing a good seismic performance. The shaking table test of assembled steel frame structure is less carried out due to its less equipment and limited conditions. Based on the completed shaking table test, the inter-layer displacement angle of assembled steel frame structure [33–35] can reach 1/20 when it is destroyed, which is much higher than the limit of elastic-plastic inter-layer displacement angle of steel frame. Therefore, this paper selects the interlayer displacement angle of 1/25 (when the rotation angle of the joint is 0.04rad) as the collapse critical value of the fabricated steel frame structure for further research.

Referring to the above research content and the Chinese code GB/T 38591-2020 [36], the failure state of the fully bolted assembled steel frame structure is divided into five damage states, and the corresponding four damage limit states are Slight, Moderate, Severe, and Collapse, respectively. The macroscopic description is shown in Table 9.

**Table 9**
Structural performance level division

| Damage states | Beams and columns | Braces | Non-bearing components |
|---|---|---|---|
| No damage | Free from damage | Some slight damage | Some slight damage |
| Slight damage | Slight deformation occurs at some joints. | Some damage | Less slight damage or some obvious damage |
| Moderate Damage | Less plastic deformation occurs at the joints. | Less damage | More obvious damage |
| Severe damage | More beams and columns are severely damaged and there is obvious plastic deformation in the joints. | More damage | Large severe damage |
| Collapse | More beams and columns are severely damaged | Large damage | More than large severe damages |

Note: Some-Less than 10%, Less-10%~30%, more-30%~50%, large-more than 50%.

### *3.7. Determination of structural performance level limit value*

For frame structures with layered properties, the maximum interlayer displacement angle (ISDA) is commonly used to quantify and determine the damage state. The code [37] provides a reference range for the maximum interlayer displacement angle as a quantitative damage index for the damage limit state.

Although the code gives the damage value interval with the maximum inter-layer displacement angle as its index, there are empty intervals and overlaps in each damage value interval. It is not conducive to the subsequent analysis of structural fragility. To address this, the yield displacement angle obtained from the structural pushover curve can be used as the base value and adjusted by multiplying the coefficients of 1, 3, 7, and 10 respectively to obtain the damage values corresponding to different damage states [38]. In this paper, the mean value of the displacement angle in X and Y directions when the structure yields are multiplied by the coefficients to obtain the damage value of the inter-layer displacement angle of each damage state ISDA-1. The ISDA-1 is divided by the structural collapse critical value of 0.04 rad to obtain the structural damage value D1, as shown in Table 10.

**Table 10**
Performance level damage value interval based on yield displacement angle

| Damage states | No damage | Slight damage | Moderate damage | Severe damage | Collapse |
|---|---|---|---|---|---|
| ISDA-1 | ≤ 0.0033 | 0.0033 ~ 0.0066 | 0.0066 ~ 0.0132 | 0.0132 ~ 0.033 | ≥ 0.033 |
| Damage value D1 | ≤ 0.08 | 0.08 ~ 0.25 | 0.25 ~ 0.58 | 0.58 ~ 0.83 | ≥ 0.83 |

Based on the development of the plastic hinge in structural components, the maximum inter-layer displacement angle (ISDA-2) of the brace, beam, and column in the model are obtained when the damage rate reaches 10%, 30%, and 50%. Similarly, the structural damage value D1 is achieved by dividing ISDA-1 by the structural collapse critical value of 0.04 rad, as shown in Fig. 19.

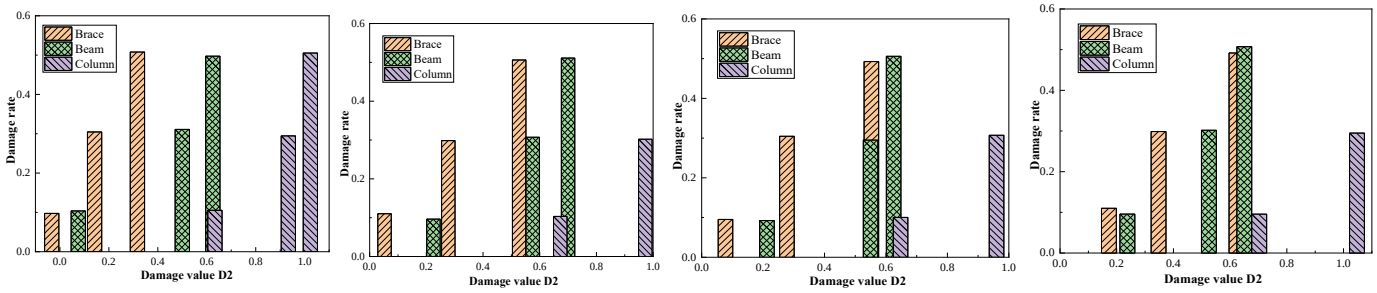


**Fig. 19** Damage value distribution. (a) 8-story. (b) 12-story. (c) 16- story. (d) 20-story

From Fig.19, it can be seen that the development trend of the component damage rate in each model is similar. The brace is first damaged and then rapidly reaches 50% damage rate. The development time of the beam and column from 10% damage rate to 30% damage rate is longer, while the beam and column will soon enter the 50% damage rate stage after reaching the 30% damage rate. When the damage rate of the column is 30%, the beam has reached half of the damage probability. Furthermore, when the damage rate of the column reaches 50%, the maximum inter-layer displacement angle is higher than the collapse limit of 0.04 rad, which further reflects the capability design idea of "strong column and weak beam". Combined with the performance level of structural divided above, the 10% damage rate of the brace, 10% damage rate of the beam, 30% damage rate of the beam and 30% damage rate of the column are proposed as the limits of structural performance level, as shown in Table 11.

**Table 11**
Performance level damage value interval based on component damage rate.

| Damage states | No damage | Slight damage | Moderate damage | Severe damage | Collapse |
|---|---|---|---|---|---|
| ISDA-2 | ≤ 0.004 | 0.004 ~ 0.0085 | 0.0085 ~ 0.023 | 0.023 ~ 0.0330 | ≥ 0.035 |
| Damage value D2 | ≤ 0.10 | 0.10 ~ 0.21 | 0.21~0.58 | 0.58 ~ 0.88 | ≥ 0.88 |

To better improve the damage value of the assembled steel frame for the based-on performance design, referring to the structural damage value interval obtained by the existing researchers on the fragility of steel structures, and taking into account the analysis of the yield displacement angle and the damage rate of the components, The table 9 and Fig.20 presented in this section shows the range of damage values corresponding to each performance level.

**Table 12**
Definition of damage value range of the frame

| Damage states | No damage | Slight damage | Moderate Damage | Severe damage | Collapse |
|---|---|---|---|---|---|
| Damage value | 0 ~ 0.10 | 0.10 ~ 0.25 | 0.25 ~ 0.60 | 0.60 ~ 0.85 | ≥ 0.85 |

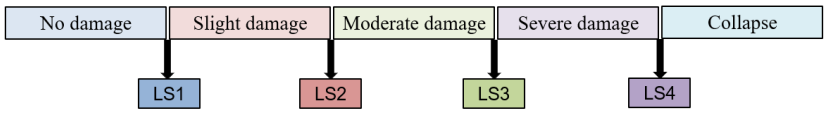


**Fig. 20** Frame structure performance levels and corresponding damage states

## 4. Structural incremental dynamic analysis

### *4.1. Seismic demand parameters*

The peak ground velocity (PGV) is selected as the ground motion intensity parameter (IM). Seismic demand indicators mainly include the strength, stiffness, deformation, and energy consumption etc. Among these indicators, the inter-layer displacement angle (IDSA) is the most widely used. IDSA is used as the overall damage index of the structure, and the single-parameter damage model is established. However, the structure will have cumulative damage under load, and the single-parameter damage model cannot take into account the impact of cumulative energy consumption on the seismic resistance of the structure. Therefore, this paper uses the single-parameter damage model based on the maximum interlayer displacement angle and the two-parameter damage model based on the interlayer displacement angle and energy dissipation to evaluate the seismic performance of the structure.

The single-parameter damage model based on interlayer displacement angle is shown in Eq. (5).

$$D_{\theta} = \frac{\delta_D}{\delta_C} \tag{5}$$

In this equation, $\delta_D$ represents the structure's seismic demand, while $\delta_C$ represents the structure's seismic capacity. For the purposes of this paper, $\delta_C$ is assumed to be 0.04.

The single parameter damage model based on energy dissipation is shown in Eq. (6).

$$D_E = \frac{E_D}{E_C} \tag{6}$$

$$E_C = \frac{2\sum_1^n (W_{ab} f_{yb} \theta_c + W_{uz} f_{yz}) F_D}{M C_y D_y} \tag{7}$$

in which $E_D$ is the structure's energy consumption demand; and $E_C$ is the structure's energy dissipation capacity. $n$ is the number of stories of structure. $n_b$ and $n_z$ is the number of beams and braces in each story, respectively. $F_D$ is the story energy dissipation parameter coefficient. $\theta_c$ is the cumulative plastic rotation angle, which is taken as 0.23. $C_y$ is the earthquake influence coefficient. $D_y$ is the structural yield displacement.

The two-parameter damage model based on the interlayer displacement angle and energy dissipation, as shown in Eq. (8)

$$D_M = \alpha D_{\theta} + \beta D_E \tag{8}$$

In which α and β express the weight combination coefficient, with α=0.3 and

β=0.7, respectively. [39].

### *4.2. Ground motion selection and amplitude modulation*

The ground motion is random, and it is necessary to select a large number of seismic waves when the IDA is carried out. Generally, 10 to 20 seismic waves can be selected to avoid the randomness of ground motion, making the structural seismic demand analysis more accurate. According to the ground motion selection principle of ATC-63 [40], 15 seismic waves that meet the requirements of epicentral distance and wave velocity range are selected in the PEER ground motion database, as shown in Table 13 and Fig. 21.

**Table 13**
Ground motion records

| Number | Name | Gauging point | Seismic level | PGA(g) |
|---|---|---|---|---|
| 1 | San Fernando | LA-Hollywood Stor FF | 5.69 | 0.22 |
| 2 | Friuli, Italy | 8014 Forgaria Cornino | 6.50 | 0.36 |
| 3 | Westmorland | Westmorland Fire | 5.90 | 0.37 |
| 4 | Morgan Hill | Gilroy Array #4 | 6.19 | 0.22 |
| 5 | Superstition Hills | EI CentroImp | 6.54 | 0.36 |
| 6 | Superstition Hills | Poe Road | 6.54 | 0.47 |
| 7 | Loma Prieta | Gilroy Array #3 | 6.93 | 0.56 |
| 8 | Loma Prieta | Gilroy Array #4 | 6.93 | 0.42 |
| 9 | Landers | Yermo Fire Station | 7.28 | 0.25 |
| 10 | Northridge | Beverly Hills－Mulhol | 6.69 | 0.44 |
| 11 | Northridge | Canyon Country-WLC | 6.69 | 0.40 |
| 12 | Northridge | LA-Hollywood Stor FF | 6.69 | 0.24 |
| 13 | Kobe, Japan | Shin-Osaka | 6.90 | 0.23 |
| 14 | Kocali,Turkey | Duzce | 7.51 | 0.32 |
| 15 | Chi-Chi, Taiwan | CHY101 | 7.62 | 0.44 |

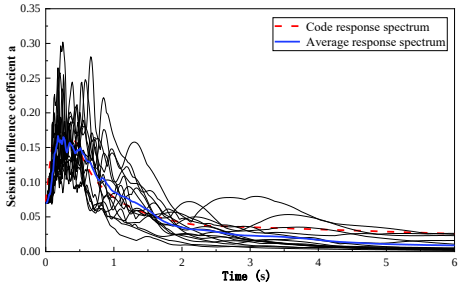


**Fig. 21** Seismic wave response spectrum

The average response spectrum values of 15 seismic waves are in good agreement with the standard response spectrum values, which is suitable for structural analysis. The PGA of the selected seismic waves is adjusted to 0.07g, 0.2g, 0.3g, 0.4g, 0.5g, 0.6g, 0.7g, 0.8g, 0.9g, 1.0g, 1.1g, and 1.2g respectively, and IDA is carried out on the high-rise steel frame model with the new fully-bolted core tube beam-column joint.

### *4.3. IDA results*

When the interlayer displacement angle exceeds 0.04 rad, it is considered that the structure has a large plastic deformation and a tendency to collapse. From Fig. 22, it can be observed that the collapse probability of the model decreases with the increase of stories under the action of 8 degrees rare and great earthquakes. Except for the 8-story model, which has a collapse probability of 2/15, the collapse probability of other models is 0 when subjected to the rare earthquakes. The collapse probabilities of the 8-story, 12-story, 16-story, and 20-story models under the action of great earthquakes are 4/15, 3/15, 2/15, and 1/15, respectively. The intensity of the seismic wave $S_{CP}$ is 0.837 g, 0.991 g, 0.976 g, and 1.054 g for the 8-story, 12-story, 16-story, and 20-story models, respectively, when the collapse probability of the structure is 50%. The higher the intensity of the seismic wave $S_{CP}$, the lower the risk of structural collapse. However, the $S_{CP}$ does not increase with the increase of stories, which is contrary to the fact that the collapse probability decreases with the increase of stories. Therefore, further analysis and judgment are required to determine whether the collapse performance of the structure can be evaluated solely based on the inter-layer displacement angle.

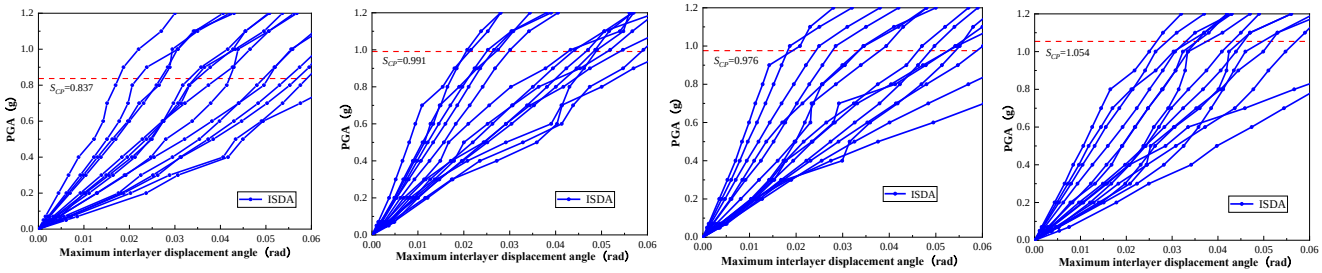


(a) (b) (c) (d)

**Fig. 22** IDA results. (a) 8-story. (b) 12-story. (c) 16-story. (d) 20-story

## 5. Seismic fragility analysis

### *5.1. Seismic fragility expression*

The seismic fragility curve is a plot of the probability of failure as a function of the parameter of the seismic intensity. It can be an objective reflection of the analysis results and is mainly used for the evaluation of the seismic performance of the structures [41]. The structural seismic demand $D_E$ and seismic capacity $C_E$ follow to the normal distribution, and from Eq. (9), the failure probability function $P_f$ is determined:

$$P_f = \Phi\left(\frac{\ln[(e^{a}PGA^{b})/\mu_c]}{\sqrt{\sigma_d^2+\sigma_c^2}}\right) \quad (9)$$

According to the HAZUS specification [42], the $\sqrt{\sigma_s^2+\sigma_c^2}$ value equals to 0.5 when the ground motion parameter is selected as *PGA*; $\mu_c$ is the performance level damage limit.

### 5.2. Seismic demand probability

The relations among the structural seismic demand parameters and the ground motion parameters follow the power exponential function. [43]. To capture this relationship, the logarithm of *PGA* and *D* are determined, respectively, demonstrated in Fig. 23. The IDA results are in regression. Both probabilities for the seismic demand of the structure are given in Table 14.

**Table 14**
Seismic demand parameters for the structure

| Frame | Damage index | Regression equation |
|---|---|---|
| 8-story | $D_\theta$ | $\ln(D_\theta) = 0.8954\ln(PGA) - 0.1799$ |
| | $D_G$ | $\ln(D_c) = 0.8897\ln(PGA) - 0.1481$ |
| 12-story | $D_\theta$ | $\ln(D_\theta) = 0.9707\ln(PGA) - 0.2636$ |
| | $D_G$ | $\ln(D_c) = 0.9572\ln(PGA) - 0.2439$ |
| 16-story | $D_\theta$ | $\ln(D_\theta) = 0.9675\ln(PGA) - 0.2855$ |
| | $D_G$ | $\ln(D_c) = 0.9463\ln(PGA) - 0.2524$ |
| 20-story | $D_\theta$ | $\ln(D_\theta) = 0.9187\ln(PGA) - 0.3091$ |
| | $D_G$ | $\ln(D_c) = 0.8889\ln(PGA) - 0.2875$ |

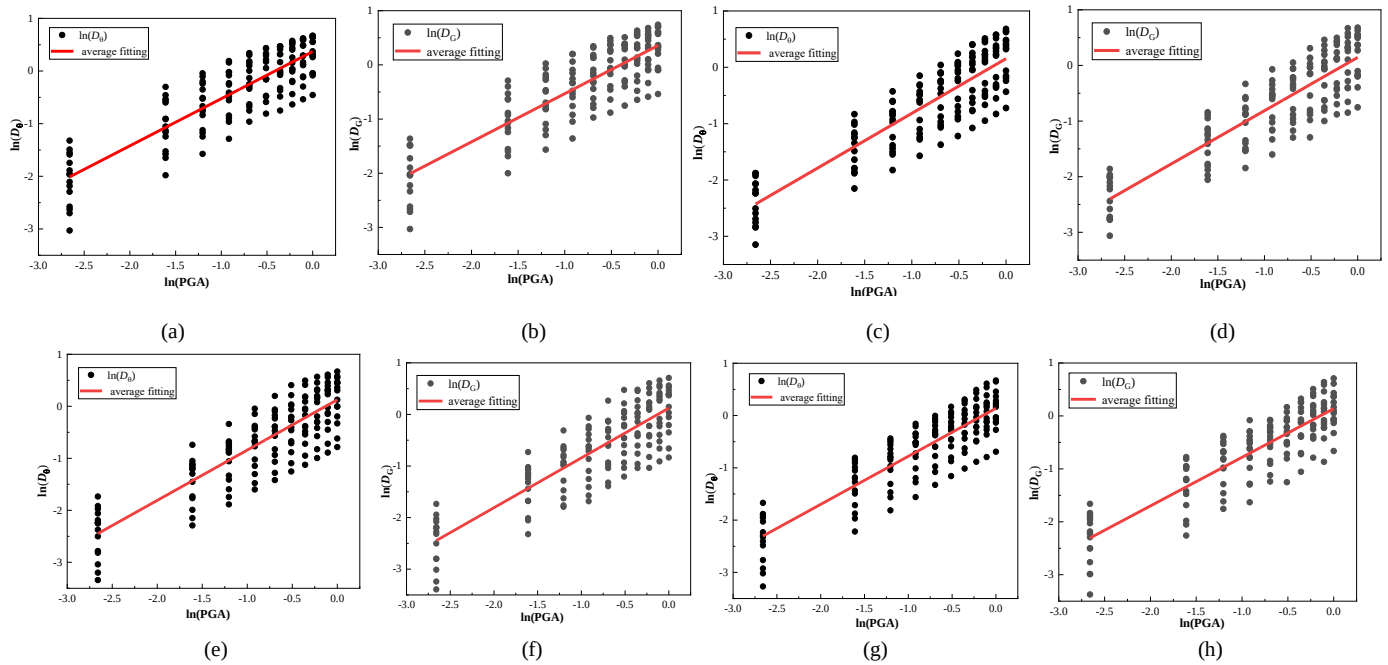


**Fig. 23** Steel frame structures regression analysis. (a) 8-story model $D_\theta$. (b) 8-story model $D_G$. (c) 12-story model $D_\theta$. (d) 12-story model $D_G$. (e) 16-story model $D_\theta$. (f) 16-story model $D_G$. (g) 20-story model $D_\theta$. (h) 20-story model $D_G$

### 5.3. Seismic fragility analysis

By substituting Eq. (5) to (8) into Eq. (9), the fragility expressions of the structure based on $D_\theta$ and $D_G$ can be obtained respectively. The resulting fragility curves are shown in Fig. 24. Considering the unit conversion, the peak acceleration corresponding to the 8-degree rare earthquake and the 8-degree great earthquake is 0.408g and 0.633g, respectively.

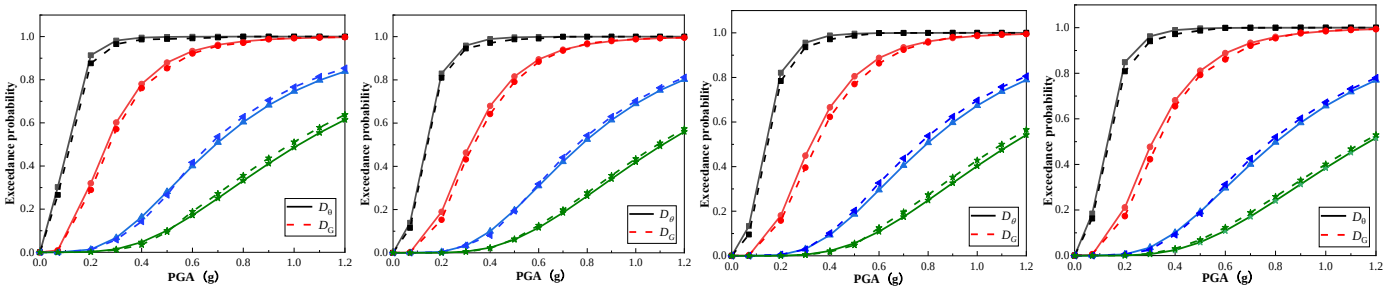


**Fig. 24** Fragility curve comparison. (a) 8-story. (b) 12-story. (c) 16-story. (d) 20-story

From Fig. 24, the change trend of the fragility curve according to the single-and two-parameter damage index is similar. When using $D_\theta$ as the seismic demand index, during 8-degree rare earthquake, the probability of each model exceeding the LS1 and LS2 limit states is greater than 65%, the probability of exceeding the LS3 limit state is between 10% and 20%, and the probability of exceeding the LS4 limit state is less than 5%. Under the action of 8-degree great earthquake, the probability of each model exceeding the LS3 limit state is between 32% and 44%, while the probability of exceeding the LS4 limit state is about 15%, except that the 8-story model reaches 23.63%. This suggests that the structure may be in a moderate damage state under the action of rare earthquakes, and may be in a severe damage state with the possibility of collapse under the action of great earthquakes.

When taking $D_G$ as the seismic demand index, during 8-degree rare earthquake, the probability of each model exceeding the LS1 and LS2 limit states is greater than 60%, the probability of exceeding the LS3 limit state is between 10% and 15%, and the probability of exceeding the LS4 limit state is less than 5%. Under the action of 8-degree great earthquake, the probability of each model exceeding the LS3 limit state is between 34% and 45%, and the probability of exceeding the LS4 limit state is range from 15% to 25. The model will have a moderate damage state under the action of rare earthquakes, and at the most it will be in a severe damage state. Moreover, the possibility of collapse of the structure under the action of a great earthquake increases.

Regardless of whether $D_\theta$ or $D_G$ is used as the seismic demand index. The effect of the number of stories on the probability of structural failure decreases as more stories are added. When the structure is in the limit state of LS3 and LS4, the exceedance probability according to the two-parameter damage index is lower than that according to the single-parameter damage index under the action of the small earthquake peak acceleration. Under the action of the large earthquake peak acceleration, the exceedance probability according to the two-parameter damage index is higher than that according to the single-parameter damage index. It shows that the influence of cumulative damage on the evaluation of structural performance cannot be ignored, especially at the stage of large deformation of the structure. Simply using the maximum inter-layer displacement angle as the damage index will ignore the damage due to plastic deformation of the structure.

## 6. Analysis of seismic collapse resistance of structure

Although the fragility analysis can provide the structure's collapse probability during the earthquake, it is crucial to evaluate the structure's collapse resistance considering the impact of ground motion and structural uncertainty. The evaluation method of structural performance according to the collapse margin ratio (*CMR*) through the nonlinear time history analysis of the structure during the earthquake, after considering the influence of the uncertainty coefficient $\beta_{TOT}$ and the spectral shape factor *SSF* on the *CMR*, the adjusted collapse margin ratio (*ACMR*) is obtained. The *ACMR* is used to judge whether the collapse resistance of the structure meets the demand and evaluate whether the structure meets the collapse performance requirement.

The *CMR* is often used to describe the relationship between the fortification demand of structure and the collapse resistance, also known as the structural collapse reserve coefficient, see Eq. (10).

$$CMR = \frac{S_{CP}}{S_{MT}} \tag{10}$$

where $S_{CT}$ is the spectral acceleration corresponding to median collapse capacity, $S_{MT}$ is the spectral acceleration of the rare earthquake and the great earthquake.

Since many factors affect the structural collapse resistance, including the dimension of structural member, structural ductility, and structural effect coefficients, resulting that the *CMR* cannot adequately reflect the structural collapse resistance. The collapse resistance of the structure is highly sensitive to the spectral characteristics of the ground motion. In order to ensure the rationality and accuracy of the structural collapse performance evaluation, the spectral shape factor *SSF* is introduced to adjust the *CMR*. The expression of the *ACMR* is Eq. (11)

$$ACMR = \alpha \times SSF \times CMR \tag{11}$$

in which, $\alpha$ is the model coefficient, and the planar and spatial models take 1.0 and 1.2, respectively.

$$SSF = \exp[\beta_1(\overline{\varepsilon_0(T)} - \varepsilon(T_1))] \tag{12}$$

where $\beta_1$ is the spectrum characteristic influence coefficient; $\overline{\varepsilon_0(T)}$ is the spectral shape expectation value, taking as 1.45 in this paper; $\varepsilon(T_1)$ is the value of the spectral shape character, when $T_1<0.5$, $\varepsilon(T_1)=0.6$, when $T_1>1.5$ 时, $\varepsilon(T_1)=0$; when $0.5\le T_1\le 1.5$, $\varepsilon(T_1)=0.6\times(1.5-T)$.

The spectrum characteristic influence coefficient can be determined by Eq. (13) and Eq. (14)

$$\mu_c = \frac{\Delta_u}{\Delta_y} \tag{13}$$

$$\beta_1 = 0.17 \times (\mu_0 - 1)^{0.33} \tag{14}$$

where $\Delta_u$ is the structural ultimate displacement; $\Delta_y$ is the structural yield displacement; $\mu_0$ is the structural effective ductility, when $\mu_c < 8$, $\mu_0 = \mu_c$, and when $\mu_c > 8$, $\mu_0 = 8$.

The models in this paper are all spatial models, so the model coefficient $\alpha$ is 1.2. The *ACMR* of each model is shown in Table 15. The *ACMR* of the model increases with the increase of the structural stories under the 8-degree rare and great earthquake. When the structure is subjected to the rare and great earthquakes, the average *ACMR* of the model is 3.67 and 2.37, respectively.

**Table 15**
The average *ACMR* of the structures

| Stories | $\varepsilon(T_1)$ | $\beta_1$ | *SSF* | *ACMR* | |
|---|---|---|---|---|---|
| | | | | Rare earthquake | Great earthquake |
| 8 | 0.24 | 0.1719 | 1.231 | 3.03 | 1.95 |
| 12 | 0 | 0.1898 | 1.317 | 3.81 | 2.45 |
| 16 | 0 | 0.1823 | 1.303 | 3.82 | 2.46 |
| 20 | 0 | 0.1807 | 1.299 | 4.02 | 2.60 |
| | | | Average | 3.67 | 2.37 |

Since there are some differences between the numerical model and the actual structure, the differences are due to the uncertainty of the structure itself. And the *ACMR* of the structure still does not consider this problem. To make the evaluation results more accurate, the FEMA [44] considers various uncertainties and proposes the structural uncertainty coefficient $\beta_{TOT}$ to evaluate the degree of agreement between the numerical model and the actual structure. The numerical model is divided into four categories: excellent, good, general, and very poor. Then, the allowable values of *ACMR* under different collapse probabilities are given according to the structural uncertainty coefficient $\beta_{TOT}$.

The allowable collapse probability of the structure under rare earthquakes is 10% (*ACMR*10%) according to the FEMA evaluation criteria for structural collapse resistance. In general, each group of structures should meet this requirement. However, since the collapse probability of some single structures may exceed this limit, the collapse probability of a single structure should not exceed 20% (*ACMR*20%). Based on this, in view of the uncertainty of the structure, the allowable value of the average *ACMR* for each group of structures is *ACMR*10%, that is, $\overline{ACMR_i} \ge ACMR10\%$. The allowable value of the *ACMR* for a single structure is *ACMR*20%, that is, $ACMR_i \ge ACMR20\%$. If the structure meets the above two evaluation criteria, the steel frame with the new fully-bolted core tube beam-column joint is considered to have good seismic performance and collapse resistance. According to the above analysis,

the analysis results of the simplified mechanical model of the new fully-bolted core tube beam-column joints adopted in this paper are consistent with the experimental data, but there are still some differences. And the actual deformation of the new joints is not fully considered by the simplified mechanical model. The numerical model also does not fully consider the connection structure between the actual floor slabs and brace and the main component, so the quality of the numerical model is defined as general. According to the results of static elastic-plastic analysis, the four models designed in this paper have the ductile failure mode of "strong column and weak beam", which meets the seismic fortification requirements of the specification and reflects the idea of "structural capacity design". Therefore, the structural design quality is at a good level. Considering the influence of the reduced scale effect of the previous test joints, there is a certain gap with the actual structure. Thus, the quality of the structural and component test data is identified as good.

Based on the above analysis, the allowable *ACMR* value of the new fully-bolted core tube joint steel frame after considering the structural uncertainty is shown in Table 16.

**Table 16**
Structure ACMR allowable value

| Structure and component test data quality | Good |
|---|---|
| Structure design quality | Good |
| Numerical model quality | General |
| $\beta_{TOT}$ | 0.75 |
| *ACMR*5% | 3.43 |
| *ACMR*10% | 2.61 |
| *ACMR*15% | 2.18 |
| *ACMR*20% | 1.88 |
| *ACMR*25% | 1.66 |

Note: *ACMR*5% is the structural collapse margin ratio when the collapse probability is 5%, and so on.

Combined with Table 15 and Table 16, the collapse resistance of the new fully bolted steel frame is evaluated. Under the action of rare earthquakes, the average *ACMR* of the model is 3.67, which is greater than the *ACMR*10% allowable value of 2.61, that is, it meets the $\overline{ACMR_i} \geq ACMR10\%$. The *ACMR* values of each model are greater than the *ACMR*20% allowable value of 1.88, which satisfies the $ACMR_i \geq ACMR20\%$. The test results show that the steel frame with the new joint is capable of withstanding rare earthquakes as required by code [45].

Under the action of great earthquakes, the average *ACMR* value of the steel frame model is 2.37, which is between the allowable values of *ACMR*10% and *ACMR*20%, it does not meet the evaluation requirements. However, the *ACMR* values of each model are greater than the *ACMR*20% allowable value, which satisfies the $ACMR_i \geq ACMR20\%$. The *ACMR* value of the 8-story model is the smallest. This may be due to the relatively strict seismic measures for the high-rise structures and relatively loose seismic measures for the low-rise or multi-story structures in the code of China. Therefore, when the new joint is applied to the actual project, some seismic strengthening measures should be taken to ensure that the safety reserve for the collapse resistance of the new fully-bolted assembled joint steel frame structure under the action of great earthquake is sufficient. In conclusion, the new joints are suitable for the multi-story and high-rise steel frame structures, and the steel frame with the new joint in this paper meets the seismic fortification requirements of the code.

## 7. Conclusions

The models for multi-story and high-rise steel frames with new joints have been identified, and the static elastic-plastic time-history analysis was carried out to confirm the rationality of the support arrangement and the applicability of the new joints. After defining the damage value under each damage state, the seismic fragility and collapse resistance of the steel frame models with new joint of different stories were analyzed. The main conclusions can be summarized as follows.

(1) The steel frame structure with new fully-bolted core tube beam-column joint meets the requirements of seismic fortification under the frequent and rare earthquakes. The maximum inter-layer displacement angle in both directions is close, indicating that the mass distribution of the structure is uniform, and the brace arrangement in this paper is reasonable.

(2) The plastic hinge development order of each model is brace-beam-column. When the inter-layer displacement angle of the structure reaches 0.02 rad, most of the braces and beams of each model have plastic hinges, and some of the middle columns in the bottom story enter the plastic deformation stage, indicating that each model conforms to the idea of "capacity design". The new joints are suitable for multi-story and high-rise buildings with the proper component selection and arrangement.

(3) The performance level of the assembled steel frame structure is re-divided. Based on the structural yield displacement angle and the component damage probability, the damage value interval of the new joint steel frame structure is determined to be [0.1, 0.85].

(4) Under the 8-degree rare earthquakes, the steel frame structure with new fully-bolted core tube beam-column joint may be in the severe damage stage at most, while under the 8-degree great earthquakes, the steel frame with new fully-bolted core tube beam-column joint may collapse. This emphasizes the significance of considering cumulative damage during the evaluation of structural performance, particularly in the large deformation stage.

(5) The *ACMR* values of the steel frame structure with new fully-bolted core tube beam-column joint meet the evaluation criteria under the rare earthquakes, However, under the great earthquakes, the *ACMR* values do not meet the evaluation criteria. Therefore, in practical engineering, certain seismic strengthening measures should be taken to make the structure have sufficient safety of collapse resistant under the great earthquakes.

## Acknowledgment

This study was financially supported by the National Natural Science Foundation of China (Grant No.52268029) and the Basic Research Project of Science and Technology Department of Sichuan Province (Grant no. 2023JDZH0035) and Natural Science Foundation of Sichuan Province (Grant No. 2023NSFSC0381).

## References

[1] D. Miller. Lessons learned from the Northridge earthquake. Engineering Structures, 1998, 20 (4): 249-260.
[2] M. Nakashima, K. Inoue, M. Tada. Classification of damage to steel buildings observed in the 1995 Hyogoken-Nanbu earthquake. Engineering Structures, 1998, 20 (4): 271-281.
[3] E.P. Popov, T.S. Yang, S.P. Chang. Design of steel MRF connections before and after 1994 Northridge earthquake. Engineering Structures, 1998, 20 (12): 1030-1038.
[4] Shahidi F, Rezaeian A, Jamal-Omidi M, et al. Investigation of the ConXL moment connection cyclic behavior in box columns without filling concrete with different arrangement of collar bolts[J]. The Structural Design of Tall and Special Buildings, 2015, 24(5): 317-350.
[5] Lee S, Park J, Shon S, et al. Seismic performance evaluation of the ceiling-bracket-type modular joint with various bracket parameters[J]. Journal of Constructional Steel Research, 2018, 150: 298-325.
[6] Y. Wang, Q.Q. Ma, Y.T. Yang, X.L. Liu. Research on mechanical properties of H-shaped steel beam-steel tube column joints of assembled steel structure [J]. Progress of building steel structure, 2019, 21 (03): 13-22.
[7] Hosseini S M, Rahnavard R. Numerical study of steel rigid collar connection affecting cyclic loading[J]. Engineering Structures, 2020, 208: 110314.
[8] X.C. Liu, A.X. Xu, A.L. Zhang, et al. Static and seismic experiment for welded joints in modularized prefabricated steel structure. Journal of Constructional Steel Research, 2015, 112: 183-195.
[9] X.C. Liu, S.H. Pu, A.L. Zhang, et al. Static and seismic experiment for bolted-welded joint in modularized prefabricated steel structure. Journal of Constructional Steel Research, 2015, 115: 417-433.
[10] X.C. Liu, Z.W. Yang, H.X. Wang, et al. Seismic performance of H-section beam to HSS column connection in prefabricated structures. Journal of Constructional Steel Research, 2017, 138: 1-16.
[11] X.L. LU, N.F. SU, Y. ZHOU. IDA-based seis-mic fragility analysis of a complex high-rise structure[J]. Journal of Ertha quake Engineering and Engineering Vibration,2012,32(5):19-25.
[12] Fanaie N, Ezzatshoar S. Studying the seismic behavior of gate braced frames by incremental dynamic analysis (IDA) [J]. Journal of Constructional Steel Research,2014,99:111-120.
[13] Mohebi B, Chegini T A H, Miri T A R. A new damage index for steel MRFs based on incremental dynamic analysis[J]. Journal of Constructional Steel Research,2019,156:137–154.
[14] M.S. Pandikkadavath, K.M. Shaijal, S. Mangalathu, et al. Seismic robustness assessment of steel moment resisting frames employing material uncertainty incorporated incremental dynamic analysis. Journal of Constructional Steel Research, 2022, 191: 107200.
[15] W. Wang, S.L. Hu, C. Zou. Seismic fragility analysis of beam-through braced steel frames based on incremental dynamic analysis [J]. Journal of Building Structures, 2021,42 (04): 42-49.
[16] B. Li, Z. Cai, Z. Duan. Selection of hazard-consistent ground motions for risk-based analyses of structures[J]. Structural Safety, 2023, 104: 102365.
[17] D.A. Kiureghian. Analysis of structural reliability under parameter uncertainties. Probabilistic Engineering Mechanics, 2008, 23(4): 351-358.
[18] X.L. Lv, N.F. Su, Y. Zhou. IDA-based seismic fragility analysis of a complex high-rise structure. Earthquake Engineering and Engineering, 2012, 32(5): 19-25. (in Chinese)
[19] N. Fanaie, S. Ezzatshoar. Studying the seismic behavior of gate braced frames by incremental dynamic analysis (IDA). Journal of Constructional Steel Research, 2014, 99: 111-120.
[20] B. Mohebi. A new damage index for steel MRFs based on incremental dynamic analysis. Journal of Constructional Steel Research, 2019, 156: 137-154.
[21] Y.P. Chu, Y. Zhong, P. Luo, et al. Experimental study on the seismic performance of the

new fully-bolted beam-column joint[J]. Journal of Constructional Steel Research, 2022, 199: 107619.
[22] R. Bjorhovde, A. Colson, J. Brozzetti. Classification system for Beam-to-column Connections. Journal of Structural Engineering, ASCE, 1990,116(11):3059-3076.
[23] Eurocode 3: Design of Steel Structures: Part 1.1 General Rules and Rules for Building, CEN, Bruxelles: Commission of the European Communities, 1993.
[24] GB50017-2017. Standard for design of steel structures. Beijing: China Architecture & Building Press, 2017. (in Chinese)
[25] W.X. Yang. Structural influence coefficient of Y-shaped eccentrically braced steel frames. Shanghai Jiao Tong University, 2011. (in Chinese)
[26] ATC, Seismic Evaluation and Retrofit of Concrete Buildings, ReportNo. ATC-40[S]. Applied Technology Council: Redwood City, California, 1996.
[27] Y.X. Zhang, M.Y. Cheng, A.L. Zhang, et al. Research on the mechanical performance of box column integral core barrel type full bolt connection. Journal of Building Structures, 2020,41 (05): 180-189. (in Chinese)
[28] Y.X. Zhang, X.D. Wang, X. Zhao, et al. Comparative study on performance test of box-type plunger welding and one-way bolt core-cylinder connection joints. 2021, 38 (10): 103-118. (in Chinese)
[29] A.L. Zhang, Z.P. Guo, X.C. Liu, et al. Experimental study on seismic performance of assembled steel frame joints with Z-shaped cantilever beam segment splicing. Engineering Mechanics, 2017,34 (08): 31-41. (in Chinese)
[30] X.C. Liu, M.L. Chen, X.S. Chen. Research on seismic behavior of assembled steel beam-to-column joints with diagonal braces. // Tianjin University, Tianjin Steel Structure Association. (in Chinese)
[31] A.L. Zhang, L. Su, Z.L. Cao, et al. Experimental study on seismic performance and finite element analysis of Z-type fully bolted beam-to-column connections with double-sided connections. Industrial Building, 2021,51 (02): 59-65+89. (in Chinese)
[32] W. Wang, Y.S. Chen, Y.Y. Chen, et al. Experimental study on full-scale shaking table test of layered assembly support steel frame with external PC composite wall panel. Journal of Building Structures, 2019, 40 (02): 88-97. (in Chinese)
[33] Y.S. Chen, W. Wang, Y.Y. Chen. Vibration table test of three-story full-scale layered assembled braced steel frame structure. Journal of Building Structures, 2018,39 (09): 22-29. (in Chinese)
[34] Y.X. Zhang, X.T. Cheng, A.L. Zhang, et al. Shaking table test study on autoclaved aerated concrete wall panels for steel frame steel tube anchor slip joints. Progress in building steel structure, 2021,23 (10): 67-74. (in Chinese)
[35] GB / T 38591-2020 Standard for seismic resilience assessment of buildings [S]. Beijing: China Standard Press, 2021. (in Chinese)
[36] GB50011-2010 Code for seismic design of buildings [S]. Beijing: China Construction Industry Press, 2001. (in Chinese)
[37] G. Li, G.D. Cheng. Performance-based seismic design of structures-theory, method and application [M]. Science Press, 2004.
[38] Q. Xu, S.S. Zhen, Y.Z. Han, et al. Study on seismic fragility of steel frames based on global damage index. Vibration and impact, 2014,33 (11): 78-82. (in Chinese)
[39] ATC-63. Quantification of building seismic performance factors [R].
[40] ATC-63 Project Report (90% Draft), FEMA P695/April 2008.
[41] Y. Pan, Y.L. Bao, Y.X. Liu, Seismic fragility analysis of base-isolation structure connected with large span special-shaped steel corridor. China civil engineering Journal, 2021, 54(2): 20-29. (in Chinese)
[42] HAZUS 99 user's manual: Federal Emergency Management Agency[M]. Washington, D.C., 1999.
[43] C.A. Cornell, F. Jalayer, R.O. Hamburger, et al. Probabilistic basis for 2000 SAC federal emergency management agency steel moment frame guidelines. Journal of structural engineering, 2002, 128(4): 526-533.
[44] Federal Emergency Management Agency. NEHRP provisions for the Seismic Rehabilitation of Buildings[M]. Report FEMA 273 (Guidelines) and 274 (Commentary), Washington, D.C., 1997:144-198.
[45] FEMA, Quantification of building seismic performance factors, FEMA P695, Federal Emergency Management Agency, Washington, DC, June 2009.

**Advanced Steel Construction** – Vol. 20 No. 3 (2024) 222–231
**DOI:**10.18057/IJASC.2024.20.3.2


# UNIFIED FATIGUE LIFE CALCULATION OF Q460C STEEL FILLET WELD CRUCIFORM JOINTS CONSIDERING FATIGUE CRACK INITIATION AND PROPAGATION

Wan-Zhen Wang [1], Zhi-Yu Jie [1, *], Guo-Ji Yu [2], Lin-Feng Xiao [3] and Yu-Zhe Fan [1]

[1] *School of Civil Engineering, Geography and Environment, Ningbo University, Ningbo 315211, China*
[2] *Hongrun Construction Group Co., Ltd, Shanghai 200235, China*
[3] *Ningbo Huacong Architecture Design & Research Institute Co., Ltd, Ningbo 315042, China*
**(Corresponding author: E-mail: jiezhiyu@nbu.edu.cn)*

**ABSTRACT**

The present study experimentally investigates the effects of the relative stress amplitude and the relative nominal maximum stress on the fatigue life of Q460C steel fillet weld cruciform joints. An ellipsoidal fracture model proposed by the first author is used as the criterion of crack tip cracking and fatigue crack instability propagation. Theoretical calculations and numerical simulations were employed to analyze the fatigue crack initiation and propagation in the fillet weld cruciform joint. In addition, the fatigue crack initiation life, stable propagation life and total fatigue life were predicted using a unified fatigue life calculation model proposed by the first author. The calculation results reveal that the proposed unified fatigue life calculation model yield accurate fatigue life estimations, with errors ranging from −12.8% to −0.4%. Conversely, the calculation errors of the fatigue life formulas recommended in GB50017-2017, Eurocode3, and AISC360 range from −64.4% to −8.0%, −72.5% to −29.1%, and −49.4% to +30.7%, respectively.

**ARTICLE HISTORY**

Received: 13 November 2023
Revised: 7 February 2024
Accepted: 16 February 2024

**KEYWORDS**

Fillet weld;
Fatigue test;
Initiation life;
Stable propagation life;
Unified fatigue life calculation model



## 1. Introduction

Recently, high-strength steels have been increasingly used in civil engineering owing to their superior mechanical properties, including strength, ductility, toughness and fatigue. Welding stands out as the primary method of connecting steel structures, valued for its ease of fabrication and reliability in service. However, there are unavoidable defects and inherent residual stresses in the weld metal and heat-affected zone. Consequently, the welded joint may be vulnerable to fatigue damage under fluctuating loads. This has lead many researchers to study the fatigue properties of high-strength steels and their welded joints over the last several decades [1−16].

Many scholars have delved into the fatigue life calculation methodologies. Araujo et al. [1] proposed a new multiaxial fatigue model for fatigue strength estimation of high-strength steels with an average error not exceeding 16 %. Skriko et al. [2, 3] found through experiments that the current fatigue design codes and guidelines were applicable, albeit with somewhat conservatism, in assessing the fatigue strength of longitudinally loaded welded joints and fillet weld joints made of ultra-high-strength steel. The fatigue test results of high strength steel and its welded joint, investigated by Tong et al. [4, 5], indicated that high frequency loading tends to underestimate fatigue life, and fatigue strength of high strength steel surpasses that of ordinary steel. Wang et al. [6] presented a reliable high-cycle fatigue life assessment method for Q460D steel welded cruciform joints based on a unified crack growth approach. Lv et al. [7] found that the unified crack growth approach is able to provide a reliable fatigue life assessment for Q460C steel notched plates through fatigue tests and numerical simulations. Jie et al. [8] conducted experimental and numerical investigations on the fatigue properties of inclined cruciform joints with artificial pits, illustrating that the pitting corrosion damage reduces fatigue strength, but specimens without and those with smaller corrosion pits exhibited similar fatigue strengths at 2 million cycles. The pit depth and radius are the main parameters affecting the relative hot spot stress concentration factor. Guo et al. [9] proposed a fatigue reliability assessment method for the orthotropic steel deck based on a comprehensive vehicle load model and probabilistic multi-scale finite element analysis.

Additionally, the fatigue resistance of structural steel has been studied. Lipiäinen et al. [10] conducted fatigue test on component-sized hot-dip galvanized S960 cut edges and longitudinal welds, revealing that the surface quality has the most significant influence on the fatigue life after microscopic liquid metal embrittlement at the cut edges. Ahola et al. [11] experimentally investigated fatigue strength of non-load-carrying transverse attachment joints fabricated with single-sided fillet weld using of S355 and S1100 steel grades, and evaluated a fatigue life improvement technique for these joints comprising the use of a curved plate edge shape in the attachment. Yue et al. [12] carried out indoor acetic salt spray accelerated corrosion tests and high-cycle fatigue tests on Q690E high-strength steel and Q690qENH high-strength weathering steel. Their findings indicated that, under the same stress range, the fatigue life decreases with the increase of corrosion time. Sui et al. [13] studied the high-cycle S-N characteristics and fatigue cracking behaviors of 42CrMo steel with two different fine/coarse-grain tempered sorbite/bainite microstructures (FGM/CGM), and concluded that fatigue strength is greater for FGM than for CGM. Zhang et al. [14] performed microstructure characterization and fatigue crack propagation tests on the gradient surface-modified layer of high-strength steel. Their study demonstrated that increasing the depth of the surface-modified layer results in a decrease in yield strength and kernel average misorientation value, while the equivalent grain size of the slatted martensite structure and the number of the large-angle boundaries increase. Fang et al. [15] studied the crack-propagation mode and stress characteristics of stop-holes after drilling through fatigue tests and numerical simulations. The results indicated that stop-holes tend to crack in advance of the original crack reaching the edge of hole, with two cracks will propagating in opposite directions at a rapid rate until they meet. Drilling ahead of the crack increases the stress intensity factor at the crack tip by 15%, accelerating crack propagation and weakening the arresting effect. Yamada et al. [16] developed a technique, called impact crack closure retrofit (ICR) treatment, involving the closure of fatigue cracks by inducing plastic yielding at plate surface near fatigue cracks. Fatigue tests on various welded joints demonstrated how applying the ICR treatment improved fatigue life in the cracked welded joints.

The total fatigue life is typically determined by summing the initiation life and stable propagation life of fatigue cracks, excluding consideration the transient instability propagation life. Methods such as the Neuber model [17] and its modified versions, based on the local stress-strain, as well as the fracture mechanics principles such as the Paris-Erdogan law [18] and its modified forms, are commonly utilized. However, inconsistencies arise between the fatigue crack initiation life calculation based on the Neuber model and the fatigue crack propagation life calculation based on the Paris-Erdogan law due to differences in the definition of damage between these approaches.

Owing to the inadequate research on the limit states of fatigue crack initiation, propagation, and fracture in high-strength steels and their welded joints, current standards like China's code GB50017-2017 [19], AISC360 [20], and Eurocode3 [21] employ the allowable stress method and stress amplitude criterion to estimate fatigue life of high-strength steels and their welded joints.

These standards and previous studies fail to distinguish between fatigue crack initiation and propagation, despite variations in crack propagation rates before and after initiation in high-strength steels and their welded joints.

Fillet weld cruciform joints are largely used to connect beam webs and ribs in steel beam bridges. Utilizing high-strength steel in steel bridges allows for the design of smaller and thinner components, leading to steel savings and improved bridge aesthetics. The total fatigue life was divided into fatigue crack initiation life and fatigue crack stable propagation life. The ellipsoidal fracture model proposed by the first author [22] was employed as the criterion for determining crack tip cracking and fatigue crack instability propagation. Theoretical calculations and numerical simulations of fatigue cracking in the fillet weld cruciform joint were performed. Utilizing findings from literature [23, 24], the calculation model for fatigue crack initiation life and fatigue crack propagation life of Q460C steel fillet weld cruciform joints were derived, and the total fatigue life was obtained, leading to more accurate fatigue life calculations. The accuracy of the unified fatigue life calculation model was evaluated in comparison to the fatigue life formulas recommended in GB50017-2017, AISC360, and Eurocode3.

## 2. Fatigue tests of Q460C steel fillet weld cruciform joints

Fig. 1 shows the fillet weld cruciform joints using manual arc welding with Q460C steel and E5516-gas welding rods, according to GB50017-2017. The processed fillet weld cruciform joints are shown in Fig. 2.

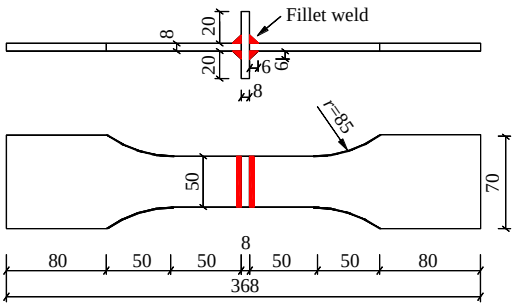


**Fig. 1** Geometrical dimensions of the Q460C steel fillet weld cruciform joints

**Fig. 2** Specimens of Q460C steel fillet weld cruciform joints

The measured length of the fillet weld ($l_w$), leg size ($h_f$), and loading parameters of each specimen are presented in Table 1. The effective bearing area of the fillet weld, denoted as $A_{ew}$, is equal to the fatigue fracture area ($A_f$), thus $A_f$=$A_{ew}$=0.7$h_f$×$l_w$. Additionally, $f_{ys}$ and $f_{uw}$ are the yield strength of the Q460C steel and the ultimate strength of the fillet weld, respectively. The maximum fatigue load ($P_{max}$) is calculated as $A_p$×$\sigma_{max}$=50×8×$\sigma_{max}$, while the minimum fatigue load ($P_{min}$) is expressed as 400×$\sigma_{min}$, where $A_p$ is the cross-sectional area of the steel plate. It should be noted that the fatigue failure of the Q460C steel fillet weld cruciform joint is essentially a fracture problem under cyclic stress loading. In order to make the physical meaning of the parameters ($\sigma_{max}$, $\sigma_{min}$, $\Delta\sigma$) clearer, the loading parameters in this paper are defined as the ratio of the loading stress to the fracture strength of the fillet weld, namely $\sigma_{max}/f_{fw}$, $\sigma_{min}/f_{fw}$, and $\Delta\sigma/f_{fw}$, as opposed to the ratio of the loading stress to the yield strength of the fillet weld, $\sigma_{max}/f_{yw}$, $\sigma_{min}/f_{yw}$, and $\Delta\sigma/f_{yw}$. Tensile testing reveals that the fillet weld undergoes neck contraction upon reaching its ultimate strength $f_{uw}$, while the fracture strength $f_{fw}$ is challenging to measure directly. Given that the mechanical properties of the fillet weld beyond its ultimate strength bear limited engineering significance, this paper conservatively approximates $f_{fw}$≈$f_{uw}$. Consequently, the loading stress parameters are expressed as $\sigma_{max}/f_{uw}$, $\sigma_{min}/f_{uw}$ and $\Delta\sigma/f_{uw}$.

The mechanical properties of the Q460C steel and the fillet weld measured by the material properties test are listed in Table 2, including $f_y$ (yield strength), $f_u$ (ultimate strength), $\varepsilon_y$ (yield strain), $\varepsilon_u$ (ultimate strain), $E$ (Young's modulus), and $\mu$ (Poisson's ratio).

**Table 1**
Geometrical and loading parameters of the Q460C steel fillet weld cruciform joints

| Specimen No. | $l_w$ (mm) | $h_f$ (mm) | $A_{ew}$ (mm²) | $\sigma_{max}/f_{ys}$ | $\sigma_{min}/f_{ys}$ | $\Delta\sigma/f_{ys}$ | $P_{max}$ (kN) | $P_{min}$ (kN) | $\sigma_{max}/f_{uw}$ | $\sigma_{min}/f_{uw}$ | $\Delta\sigma/f_{uw}$ |
|---|---|---|---|---|---|---|---|---|---|---|---|
| FWJ1 | 49.6 | 6.3 | 220.99 | 0.70 | 0.20 | 0.50 | 151.42 | 43.26 | 0.47 | 0.13 | 0.34 |
| FWJ2 | 50.1 | 6.2 | 219.67 | 0.60 | 0.10 | 0.50 | 129.79 | 21.63 | 0.40 | 0.07 | 0.34 |
| FWJ3 | 49.4 | 6.4 | 223.59 | 0.50 | 0.00 | 0.50 | 108.16 | 0.00 | 0.34 | 0.00 | 0.34 |
| FWJ4 | 49.6 | 6.1 | 213.97 | 0.40 | −0.10 | 0.50 | 86.53 | −21.63 | 0.27 | −0.07 | 0.34 |
| FWJ5 | 49.7 | 6.3 | 221.44 | 0.30 | −0.20 | 0.50 | 64.90 | −43.26 | 0.20 | −0.13 | 0.34 |
| FWJ6 | 50.2 | 6.4 | 227.21 | 0.60 | 0.20 | 0.40 | 129.79 | 43.26 | 0.40 | 0.13 | 0.27 |
| FWJ7 | 49.6 | 6.5 | 228.01 | 0.50 | 0.10 | 0.40 | 108.16 | 21.63 | 0.34 | 0.07 | 0.27 |
| FWJ8 | 50.1 | 6.2 | 219.67 | 0.40 | 0.00 | 0.40 | 86.53 | 0.00 | 0.27 | 0.00 | 0.27 |
| FWJ9 | 49.7 | 6.3 | 221.44 | 0.30 | −0.10 | 0.40 | 64.90 | −21.63 | 0.20 | −0.07 | 0.27 |
| FWJ10 | 49.8 | 6.1 | 214.84 | 0.20 | −0.20 | 0.40 | 43.26 | −43.26 | 0.13 | −0.13 | 0.27 |
| FWJ11 | 49.9 | 6.5 | 229.38 | 0.60 | 0.30 | 0.30 | 129.79 | 64.90 | 0.40 | 0.20 | 0.20 |
| FWJ12 | 50.3 | 6.4 | 227.67 | 0.50 | 0.20 | 0.30 | 108.16 | 43.26 | 0.34 | 0.13 | 0.20 |
| FWJ13 | 49.5 | 6.1 | 213.54 | 0.40 | 0.10 | 0.30 | 86.53 | 21.63 | 0.27 | 0.07 | 0.20 |
| FWJ14 | 50.1 | 6.3 | 223.22 | 0.30 | 0.00 | 0.30 | 64.90 | 0.00 | 0.20 | 0.00 | 0.20 |
| FWJ15 | 49.6 | 6.2 | 217.48 | 0.20 | −0.10 | 0.30 | 43.26 | −21.63 | 0.13 | −0.07 | 0.20 |

**Table 2**
Materials properties of the Q460C steel and the fillet weld

| Materials | $f_y$ (MPa) | $f_u$ (MPa) | $\varepsilon_y$ (%) | $\varepsilon_u$ (%) | $E$ (GPa) | $\mu$ |
|---|---|---|---|---|---|---|
| Q460C steel | 540.8 | 629.0 | 0.032 | 14.0 | 202.6 | 0.28 |
| Fillet weld | 719.2 | 802.2 | 0.041 | 15.8 | 206.8 | 0.27 |

The fatigue test of the Q460C steel fillet weld cruciform joint was carried out in compliance with China's code GB/T 3075-2008 [25]. The test setup, the fatigue crack initiation and propagation during the fatigue test, and fractured specimens are shown in Fig. 3. One end of specimen was fixed to the bottom fixture of a fatigue tester named SUNS890-500, while the other end was subjected to cyclic loading. Strain gauges (model: BX120-3AA) are pasted on both ends of the fillet weld, as shown in Fig. 3b, to collect the variation of strain along the loading direction of the weld root of the fillet weld with the number of cyclic loading. When the cracks initiated at the weld root of the fillet weld, the strain data would grow rapidly until the data overflowed. Therefore, loading was suspended before the strain data overflowed in this paper. A 150-fold scale microscope (precision: 0.01mm) was used to observe the fatigue crack initiation length ($a_i$≈0.05mm) at the weld root of the fillet weld, and the number of cyclic loadings at this time $N_i$ was recorded. Subsequently, loading continued until the macro fatigue fracture of the Q460C steel fillet weld cruciform joint occurred.

The fatigue test results reveal that the fatigue crack initiates from the weld root at one end of the fillet weld, traverses the width of the effective bearing section of the fillet weld, and propagates along the length of the fillet weld to the other end within the effective bearing section. The effective bearing section of the fillet weld eventually experiences fatigue fracture.

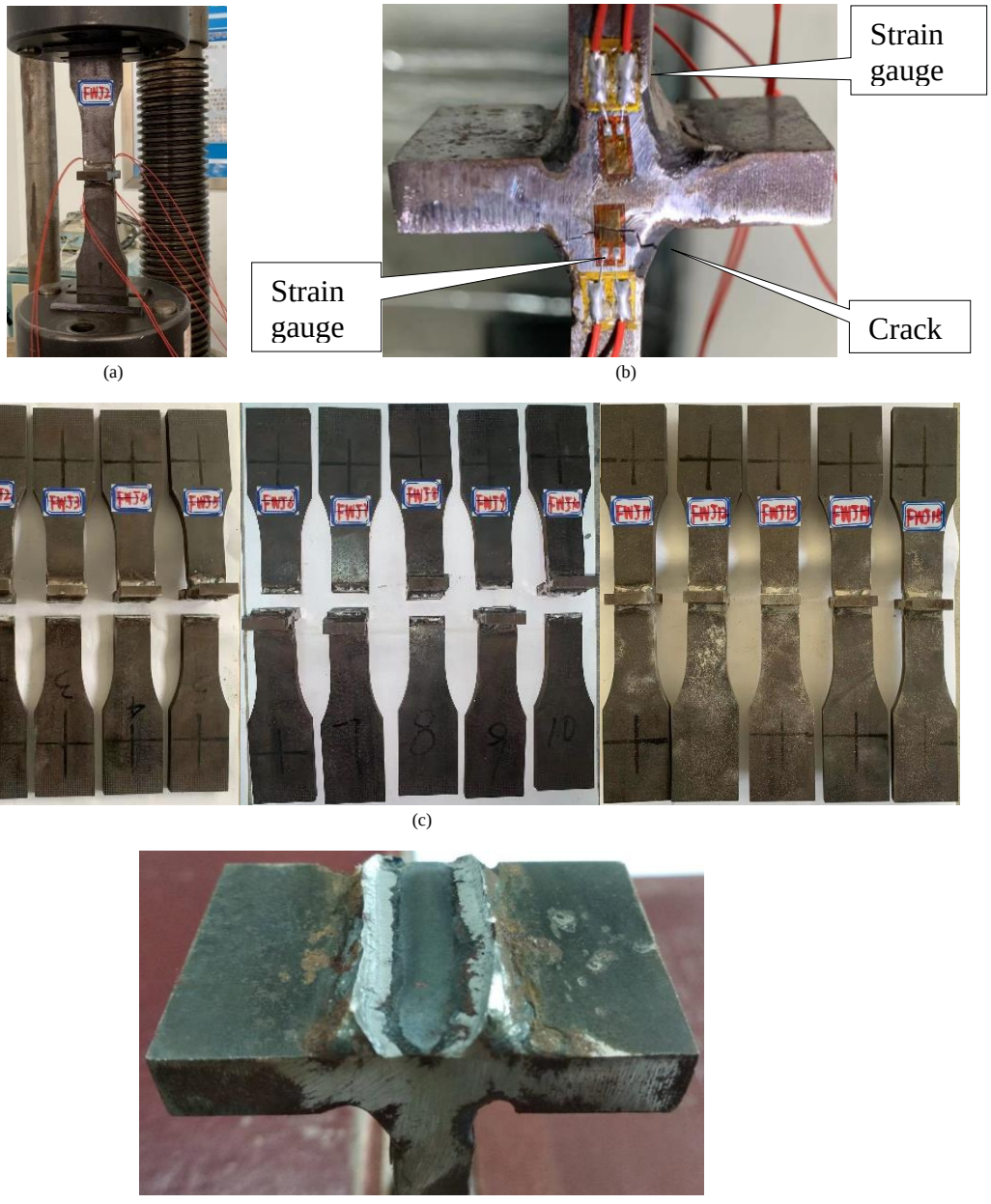


**Fig. 3** Test setup and fatigue fracture of the Q460C steel fillet weld cruciform joints: a) Test setup; b) Crack initiation and propagation; c) Specimens A1−A16; d) Fatigue fracture

The fatigue crack initiation life ($N_{i,t}$), the total fatigue life ($N_{f,t}$), the fatigue crack stable propagation life ($N_{sp,t}$=$N_{f,t}$−$N_{i,t}$) obtained from fatigue testing, and the calculated fatigue life ($N_{f,\,GB}$, $N_{f,\,Eu}$, and $N_{f,\,AISC}$) based on Eqs. (1)~(3) recommended in GB50017-2017 (specimen type Z8: $C_Z$=0.72×10$^{12}$, $\beta_Z$=3), AISC360, and Eurocode3, respectively, for each specimen are presented in Table 3. The errors between the calculated fatigue life ($N_{f,\,GB}$, $N_{f,\,Eu}$, and $N_{f,\,AISC}$) and the tested total fatigue life ($N_{f,t}$), are denoted as $e_{GB\text{-}t}$, $e_{Eu\text{-}t}$, and $e_{AISC\text{-}t}$, respectively. The Eqs. (1)~(3) are presented below:

$$\lg N_{f,GB}=-3.0\lg\Delta\sigma+11.8573 \quad (1)$$

$$\lg N_{f,Eu}=-3.0\lg\Delta\sigma+12.0100 \quad (2)$$

$$\lg N_{f,AISC}=-3.0\lg\Delta\sigma+11.7444 \quad (3)$$

It is noted that the left side of Eqs. (1)~(3) is a dimensionless number, while the dimension of the right side is MPa, resulting in a dimensional discrepancy between both ends of Eqs. (1)~(3).

Table 3 reveals that the fatigue crack initiation life, the stable propagation life, and the total fatigue life of the Q460C steel fillet weld cruciform joint decrease with increasing $\sigma_{max}$ and $\Delta\sigma$. As the nominal maximum stress and the stress amplitude rise, the stress at the weld root of the fillet weld increases, resulting in elevated fatigue crack initiation and propagation rates, leading to reduced fatigue crack initiation life, stable propagation life, and total fatigue life. Therefore, the influence of the stress amplitude and the nominal maximum stress should be considered in the fatigue life calculation of the Q460C steel fillet weld cruciform joint. The ratio of the fatigue crack initiation life to the total fatigue life ranges from 0.43 to 0.54.

The fatigue lives calculated by Eqs. (1) and (2) recommended in GB50017-2017 and AISC360 are too conservative for all specimens, with calculation errors ranging from −64.4% to −8.0% and −72.5% to −29.1%, respectively. Furthermore, the fatigue lives calculated by Eq. (3) recommended in Eurocode3 are conservative for some specimens ($\Delta\sigma/f_{uw}$<0.34 and $\sigma_{max}/f_{uw}$<0.34) and unsafe for others ($\Delta\sigma/f_{uw}\geq$ 0.34 or$\sigma_{max}/f_{uw}\geq$0.34). The overall calculation error exhibits a range of −49.4% to +30.7%.

**Table 3**
Fatigue test results of the Q460C steel fillet weld cruciform joints

| Specimen No. | $N_{i,t}$ (cycles) | $N_{f,t}$ (cycles) | $N_{p,t}$ (cycles) | $N_{i,t}/N_{f,t}$ | $N_{f,GB}$ (cycles) | $e_{GB-t}$ (%) | $N_{f,AISC}$ (cycles) | $e_{AISC-t}$ (%) | $N_{f,Eu}$ (cycles) | $e_{Eu-t}$ (%) |
|---|---|---|---|---|---|---|---|---|---|---|
| FWJ1 | 17000 | 39600 | 22600 | 0.43 | 36415 | −8.0 | 28079 | −29.1 | 51758 | +30.7 |
| FWJ2 | 19500 | 42400 | 22900 | 0.46 | 36415 | −14.1 | 28079 | −33.8 | 51758 | +22.1 |
| FWJ3 | 23300 | 46600 | 23300 | 0.50 | 36415 | −21.9 | 28079 | −39.7 | 51758 | +11.1 |
| FWJ4 | 29300 | 53100 | 23800 | 0.55 | 36415 | −31.4 | 28079 | −47.1 | 51758 | −2.5 |
| FWJ5 | 36900 | 61400 | 24500 | 0.60 | 36415 | −40.7 | 28079 | −54.3 | 51758 | −15.7 |
| FWJ6 | 38500 | 98700 | 60200 | 0.39 | 71123 | −27.9 | 54842 | −44.4 | 101090 | +2.4 |
| FWJ7 | 43600 | 104600 | 61000 | 0.42 | 71123 | −32.0 | 54842 | −47.6 | 101090 | −3.4 |
| FWJ8 | 56400 | 118400 | 62000 | 0.48 | 71123 | −39.9 | 54842 | −53.7 | 101090 | −14.6 |
| FWJ9 | 73500 | 136700 | 63200 | 0.54 | 71123 | −48.0 | 54842 | −59.9 | 101090 | −26.0 |
| FWJ10 | 92200 | 156700 | 64500 | 0.59 | 71123 | −54.6 | 54842 | −65.0 | 101090 | −35.5 |
| FWJ11 | 106200 | 307800 | 201600 | 0.35 | 168588 | −45.2 | 129995 | −57.8 | 239622 | −22.2 |
| FWJ12 | 121100 | 325500 | 204400 | 0.37 | 168588 | −48.2 | 129995 | −60.1 | 239622 | −26.4 |
| FWJ13 | 152100 | 359600 | 207500 | 0.42 | 168588 | −53.1 | 129995 | −63.9 | 239622 | −33.4 |
| FWJ14 | 195200 | 406600 | 211400 | 0.48 | 168588 | −58.5 | 129995 | −68.0 | 239622 | −41.1 |
| FWJ15 | 257100 | 473300 | 216200 | 0.54 | 168588 | −64.4 | 129995 | −72.5 | 239622 | −49.4 |

The fatigue properties of Q460C steel fillet weld cruciform joints surpass those of ordinary steel fillet weld cruciform joints. The fatigue crack initiation rate is lower than the fatigue crack propagation rate in the Q460C steel fillet weld cruciform joint. Achieving accurate fatigue life calculations for these joints entails separately calculating fatigue crack initiation life and stable propagation life. However, Eqs. (1)~(3) recommended in GB50017-2017, AISC360, Eurocode3 are formulated based on fatigue test data of ordinary structural steel fillet weld cruciform joints, lacking differentiate between fatigue crack initiation life and stable propagation life.

## 3. Unified fatigue life calculation model

The fatigue failure of the Q460C steel fillet weld cruciform joint is a process where repeated loading initiates an crack at the weld root of the fillet weld, which then extends and closes until the fatigue fracture due to insufficient net cross-section strength. Therefore, under normal circumstances, the fatigue failure of the Q460C steel fillet weld cruciform joint can be divided into three stages: fatigue crack initiation, stable propagation, and instability propagation.

In this study, the progression of the fatigue crack in the Q460C steel fillet weld cruciform joint, from initiation to stable propagation and then to instability propagation, is considered as a continuous, progressive, complete, and unified failure process in this paper. Therefore, it is reasonable to express the fatigue crack initiation life and stable propagation life as functions of the initiation size and stable propagation length of fatigue crack, respectively.

Wang [23] assumed that the fatigue crack initiation rate increases with the number of load cycles, and proposed a model to calculate the fatigue crack initiation life by integrating the fatigue crack initiation rate.

$$N_i=(a_i/\xi_i)^{1/\eta i} \quad (4)$$

Wang [24] proposed a fatigue crack stable propagation life calculation model based on the assumption that the fatigue crack stable propagation rate increases with the number of load cycles.

$$N_{sp}=(a_{sp}/\xi_{sp})^{1/\eta sp} \quad (5)$$

The unified fatigue life calculation model is derived from Eqs. (4) and (5).

$$N_f=N_i+N_{sp}=(a_i/\xi_i)^{1/\eta i}+(a_{sp}/\xi_{sp})^{1/\eta sp} \quad (6)$$

where $N_i$, $N_{sp}$, and $N_f$ are dimensionless numbers that denotes the fatigue crack initiation life, stable propagation life and the total fatigue life, respectively. The parameters $a_i$ and $a_{sp}$ are the initiation size and stable propagation length of fatigue crack, respectively, measured in millimeters (mm). Additionally, $\xi_i$ and $\xi_{sp}$ are measurements related to the fatigue crack initiation mode and stable propagation mode, respectively, with dimensions in mm. $\eta_i$ and $\eta_{sp}$ are dimensionless numbers.

It is noted that both ends of Eqs. (4)~(6) are expressed as dimensionless numbers.

## 4. Unified fatigue life calculation of the Q460C steel fillet weld cruciform joints

The fatigue failure process of the Q460C steel fillet weld cruciform joints of is divided into three stages: fatigue crack initiation, stable propagation and instability propagation. Correspondingly, the fatigue fracture area, $A_f$, can be divided into fatigue crack initiation area, $A_i$ (where $A_i=a_i\times h_e=0.05\times0.7h_f$, with $a_i$ representing the fatigue crack initiation size and $h_e$ denoting the width of the effective bearing section of the fillet weld), stable propagation area, $A_{sp}$, and instability propagation area, $A_{ip}$. Thus, $A_f$ can be expressed as the sum of $A_i$, $A_{sp}$, and $A_{ip}$, given by the equation $A_f=A_i+A_{sp}+A_{ip}$.

The total fatigue life, $N_f$, can be divided into two distinct components: fatigue crack initiation life, $N_i$, and stable propagation life, $N_{sp}$. Given the brief duration of fatigue crack instability propagation life, it is not incorporated into this division. Therefore, the relationship is expressed as $N_f=N_i+N_{sp}$.

### *4.1. Calculation of fatigue crack stable propagation life*

According to the fatigue crack stable propagation life calculation model suggested by Eq. (5), the parameters $\xi_{sp}$ and $\eta_{sp}$ are determined based on the fatigue crack stable propagation length, $a_{sp}$, and its corresponding fatigue crack stable propagation fatigue life, $N_{sp}$.

*4.1.1. Calculation of fatigue crack stable propagation length*

The fatigue crack instability propagation area can be obtained from the stress field within this area by employing the ellipsoidal fracture model proposed by the first author [22] as the criterion for fatigue crack instability propagation. Experimental findings reveal that the fatigue crack in the Q460C steel fillet weld cruciform joints traverses the width of the effective bearing section of the fillet weld. Consequently, the fatigue crack stable propagation area, $A_{sp}=A_f-A_0-A_i-A_{ip}$, can be used to calculate the fatigue crack stable propagation length, $a_{sp}=A_{sp}/h_e$, where $A_0$ is the area of initial defect. Upon examination of the tested specimens, no initial defects were identified, leading to the conclusion that $A_0=0$.

Wang [22] proposed an ellipsoidal fracture model coupled with an ellipsoidal yield model based on the assumption that fracture strength and yield strength of structural steel are equal when subjected to triaxial equal tensile stresses. This model is represented by Eqs. (7) and (8):

$$(\sigma_{seq}/r)^2+(\sigma_m/q)^2=3\tau_y^2 \tag{7}$$

$$\sigma_{seq}^2+(\sigma_m/q)^2=3\tau_y^2 \tag{8}$$

where $q=\frac{\sqrt{2}(1+\mu)}{3(1-2\mu)}$, $\tau_y=\frac{\sqrt{1+9q^2}}{3\sqrt{3}q}f_y$. $r$ can be derived from $\frac{f_u}{f_y}\approx\frac{f_f}{f_y}=\frac{r\sqrt{1+9q^2}}{\sqrt{r^2+9q^2}}$. $\sigma_{seq}$, $\sigma_m$, $\tau_y$, $f_u$, $f_f$, and $f_y$ are the von Mises equivalent stress, mean stress, shear yield strength, uniaxial ultimate strength, uniaxial fracture strength, and uniaxial yield strength, respectively.

*4.1.1.1. Theoretical calculation of fatigue crack stable propagation length*

Fig. 4 shows the fatigue fracture model of fillet weld in the Q460C steel cruciform joint. The normal stress and shear stress at the effective bearing section of the fillet weld are given as follows:

$$\sigma_z=N/A_{up,tc}=1.414P_{max}/4A_{ip,tc} \tag{9}$$

$$\sigma_x=\mu_w\sigma_x=1.414\mu_wP_{max}/4A_{ip,tc} \tag{10}$$

$$\sigma_y=0 \tag{11}$$

$$\tau_{yz}=V/A_{up,tc}=1.414P_{max}/4A_{ip,tc} \tag{12}$$

$$\sigma_m=(\sigma_x+\sigma_y+\sigma_z)/3=1.414(1+\mu_w)P_{max}/12A_{ip,tc} \tag{13}$$

$$\sigma_{seq}=\sqrt{[(\sigma_x-\sigma_y)^2+(\sigma_y-\sigma_z)^2+(\sigma_z-\sigma_x)^2+6\tau_{yz}^2]/2}$$
$$=\sqrt{2\mu_w^2-2\mu_w+8}\times P_{max}/4A_{ip,tc} \tag{14}$$

where $\mu_w$ is the Poisson's ratio of the fillet weld.

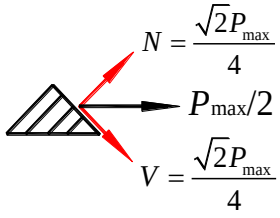


**Fig. 4** Fatigue fracture model of fillet weld

The instability propagation area of the fatigue crack can be determined by substituting Eqs. (13) and (14) into Eq. (8), and the equation is rewritten as follows:

$$A_{up,tc}=\frac{\sqrt{9q_w^2(\mu_w^2-\mu_w+4)+(\mu_w+1)^2r_w^2}\times P_{max}}{6\sqrt{6}q_wr_w\tau_{yw}} \tag{15}$$

The parameters in Eq. (15) are calculated according to the tested material properties of the fillet weld listed in Table 2 as follows: $q_w\approx1.30$, $\tau_{yw}\approx428.65$MPa, and $r_w\approx1.12$.

The instability propagation area, the stable propagation area, and the stable propagation length of the fatigue crack are calculated theoretically as follows:

$$A_{sp,tc}=A_f-A_i-A_{ip,tc} \tag{16}$$

$$a_{sp,ct}=A_{sp,ct}/h_e \tag{17}$$

*4.1.1.2. Numerical calculation of stable propagation length of fatigue crack*

The finite element model of specimen FWJ2 employed to simulate the loading process of fatigue testing, constructed using a three-dimensional solid element Solid95 in ANSYS finite element software, is shown in Fig. 5. The first author [26] has verified the effectiveness of Solid95 for modeling fatigue crack propagation. A total of 60,289 elements and 193,567 nodes were modeled for mesh division. In alignment with the fatigue test methodology, the loading process entailed fixing one end while applying fatigue load to the other end.

The two horizontal steel plates and one vertical steel plate are bonded together by four fillet welds using the "GLUE" command in the ANSYS software to ensure a consistent deformation at the fused section between the fillet weld and the plate. At one edge of fillet weld in the finite element model, a column crack with a vertically penetrating semi-ellipsoidal cross section is implanted. The area of the semi-ellipsoid is denoted as $A_i+A_{sp,tc}$, with a semi-long axis defined as $a_c=a_i+a_{sp,tc}$, and a semi-short axis defined as $b_c=0.05a_c$, to simulate the theoretically calculated initiation and propagation length, $a_i+a_{sp,tc}$, and initiation and propagation area, $A_i+A_{sp,tc}$, of the fatigue crack in the fillet weld cruciform joint.

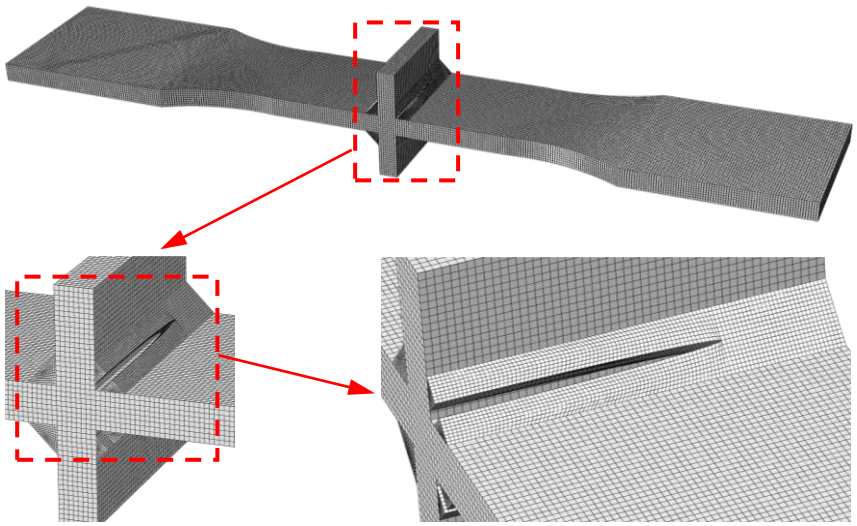

**Fig. 5** Finite element meshes of specimen FWJ2

The ellipsoidal fracture model suggested by Eq. (7) was employed as the cracking criterion of the crack tip, while the "XFEM" module within the ANSYS finite element software was utilized to simulate the propagation and fatigue failure of the fatigue crack.

The fatigue cracking diagram of specimen FWJ2, obtained through numerical calculation, is presented in Fig. 6, accompanied by the corresponding stress field on the instability propagation area of fatigue crack.

The fracture index, $I_f$, and the yield index, $I_y$, are calculated using Eqs. (7) and (8), respectively, as follows:

$$I_f = \sqrt{(\sigma_{seq}/r_w)^2 + (\sigma_m/q_w)^2}/\sqrt{3}\tau_{yw}\ ,\quad I_y = \sqrt{\sigma_{seq}^2 + (\sigma_m/q_w)^2}/\sqrt{3}\tau_{yw}\ .$$

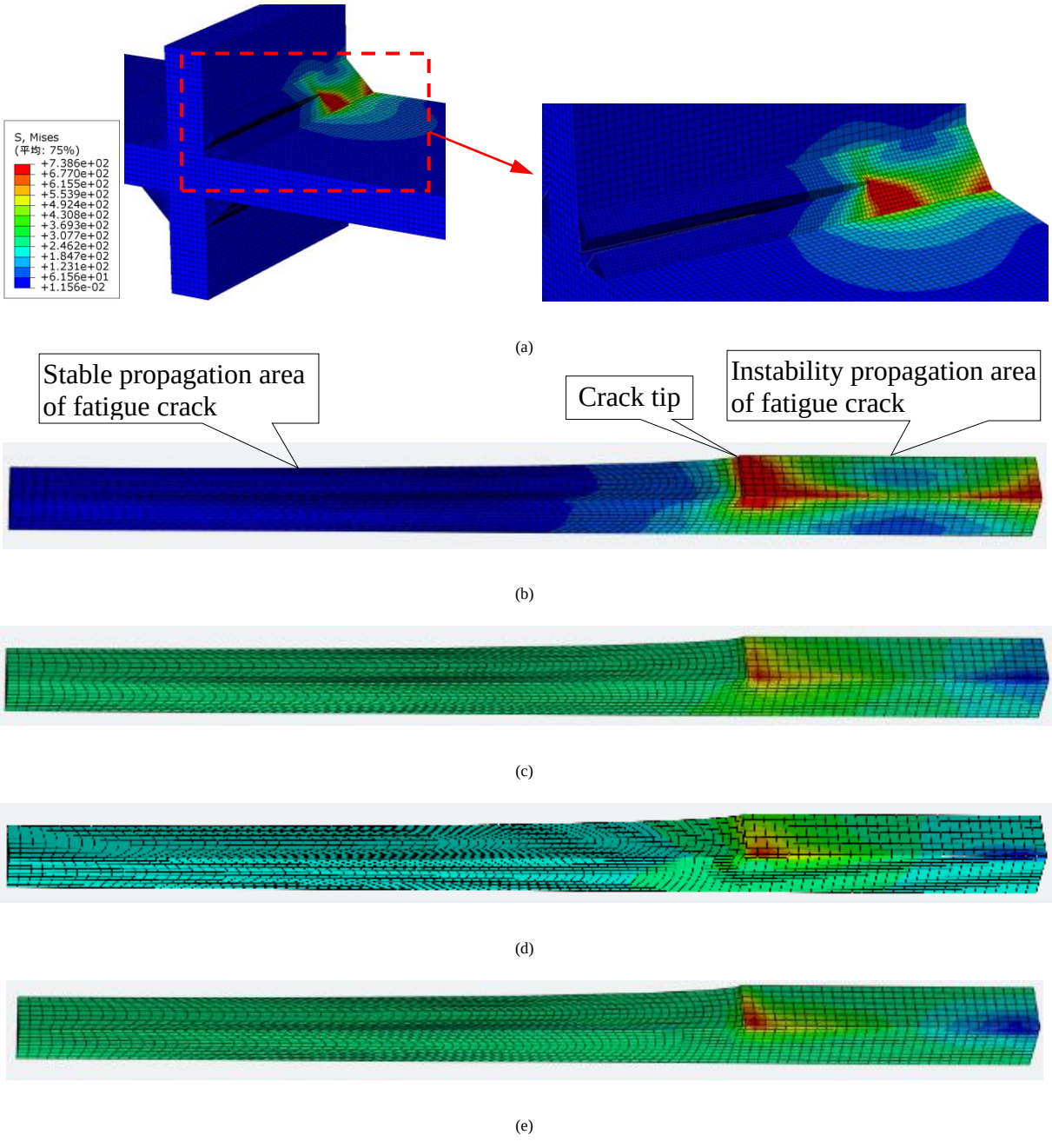


**Fig. 6** Numerical calculated stress on the instability propagation area of fatigue crack in specimen FWJ2: a) Overall Mises equivalent stress; b) Mises equivalent stress; c) The first stress $\sigma_1$; d) The second stress $\sigma_2$; e) The third stress $\sigma_3$; f) The distribution of relative stress; g) The distribution of stress ratio, the fracture index, $I_f$, and the yield index, $I_y$.

Fig. 6a~e visually shows a high stress concentration at the crack tip. The peak values of the relative stresses, $\sigma_1/f_{yw}$, $\sigma_2/f_{yw}$, $\sigma_{seq}/f_{yw}$, and $\sigma_m/f_{yw}$, are all located at the crack tip, as shown in Fig. 6f. As can be seen from Fig. 6g, on the instability propagation area of fatigue crack, the stress triaxility ratio, $\sigma_m/\sigma_{seq}$, ranges from approximately 0.22 to 0.61, while stress constraint coefficient along the length of the butt weld, $\sigma_2/\sigma_1$, varies from about 0.11 to 0.67. Additionally, the stress constraint coefficient along the thickness of the butt weld is very small at this time. This suggests the presence of significant

constraint stresses on the instability propagation area of the fracture crack, particularly at the crack tip and along the length of the fillet weld. The instability propagation area of the fatigue crack has all entered the yield regime ($I_y$>1.0) and is on the verge of experiencing tensile transient fracture ($I_f$≥1.0).

*4.1.2. Calculation of fatigue crack stable propagation life*

The instability propagation area, $A_{ip}$, stable propagation area, $A_{sp}$, and stable propagation length, $a_{sp}$, of fatigue crack in the Q460C steel fillet weld cruciform joints, obtained from the numerical calculation, are listed in Table 4.

**Table 4**
Fitted parameters of fatigue crack propagation life calculation formula

| Specimen No. | $N_{sp,t}$ (cycles) | $A_f$ (mm$^2$) | $A_{up}$ (mm$^2$) | $A_{sp}$ (mm$^2$) | $a_{sp}$ (mm) | $\eta_{sp}$ | $\xi_{sp}$ ($10^{-10}$,mm) | $s_{sp}$ | $\xi_{sp,0.95}$ ($10^{-10}$,mm) | $N_{sp,c}$ (cycles) | $e_{sp,c\text{-}t}$ (%) |
|---|---|---|---|---|---|---|---|---|---|---|---|
| FWJ1 | 22600 | 220.99 | 74.81 | 146.18 | 32.8 | 3.18 | 5067.1 | 0.003 | 5217.5 | 20804 | −7.9 |
| FWJ2 | 22900 | 219.67 | 64.12 | 155.56 | 35.5 | 3.18 | 5067.1 | 0.003 | 5217.5 | 21320 | −6.9 |
| FWJ3 | 23300 | 223.59 | 53.43 | 170.16 | 37.6 | 3.18 | 5067.1 | 0.003 | 5217.5 | 21711 | −6.8 |
| FWJ4 | 23800 | 213.97 | 42.75 | 171.23 | 39.7 | 3.18 | 5067.1 | 0.003 | 5217.5 | 22084 | −7.2 |
| FWJ5 | 24500 | 221.44 | 32.06 | 189.38 | 42.5 | 3.18 | 5067.1 | 0.003 | 5217.5 | 22563 | −7.9 |
| FWJ6 | 60200 | 227.21 | 64.12 | 163.09 | 36.0 | 3.19 | 220.8 | 0.002 | 225.7 | 56608 | −6.0 |
| FWJ7 | 61000 | 228.01 | 53.43 | 174.57 | 38.0 | 3.19 | 220.8 | 0.002 | 225.7 | 57547 | −5.7 |
| FWJ8 | 62000 | 219.76 | 42.75 | 176.93 | 40.4 | 3.19 | 220.8 | 0.002 | 225.7 | 58652 | −5.4 |
| FWJ9 | 63200 | 221.44 | 32.06 | 189.38 | 42.5 | 3.19 | 220.8 | 0.002 | 225.7 | 59616 | −5.7 |
| FWJ10 | 64500 | 214.84 | 21.37 | 193.46 | 44.8 | 3.19 | 220.8 | 0.002 | 225.7 | 60626 | −6.0 |
| FWJ11 | 201600 | 229.38 | 64.12 | 165.27 | 36.0 | 3.20 | 4.1 | 0.002 | 4.2 | 197960 | −1.8 |
| FWJ12 | 204400 | 227.67 | 53.43 | 174.23 | 38.5 | 3.20 | 4.1 | 0.002 | 4.2 | 202247 | −1.1 |
| FWJ13 | 207500 | 213.54 | 42.75 | 170.80 | 39.6 | 3.20 | 4.1 | 0.002 | 4.2 | 204036 | −1.7 |
| FWJ14 | 211400 | 223.22 | 32.06 | 191.16 | 42.9 | 3.20 | 4.1 | 0.002 | 4.2 | 209241 | −1.0 |
| FWJ15 | 216200 | 217.48 | 21.37 | 196.11 | 44.7 | 3.20 | 4.1 | 0.002 | 4.2 | 211986 | −1.9 |

The fatigue crack stable propagation life calculation model, as presented in Eq. (5), is derived by applying a double logarithm transformation to both sides of the equation.

$$\lg N_{sp,t}=(\lg a_{sp}-\lg\xi_{sp})/\eta_{sp} \tag{18}$$

The fatigue crack stable propagation life, $N_{sp,t}$, and stable propagation length, $a_{sp}$, are listed in Table 4. The fitted fatigue crack stable propagation life calculation formulas of specimens FWJ1−FWJ5, FWJ6−WJ10, and FWJ11−FWJ15 are derived accordingly (Fig. 7).

$$\lg N_{sp}=0.3151\lg a_{sp}+3.8736 \tag{19}$$

$$\lg N_{sp}=0.3148\lg a_{sp}+4.2885 \tag{20}$$

$$\lg N_{sp}=0.3133\lg a_{sp}+4.8157 \tag{21}$$

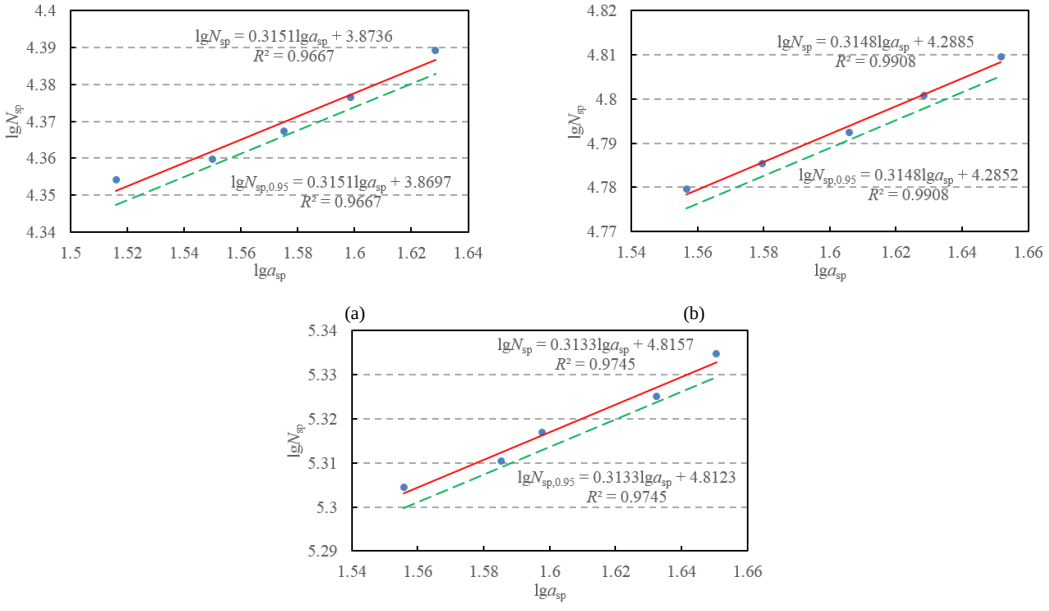


**Fig. 7** Fitted fatigue crack stable propagation life calculation formula: a) Specimens FWJ1−FWJ5; b) Specimens FWJ6−FWJ10; and c) Specimens FWJ11−FWJ15

Table 4 presents the parameters $\xi_{sp}$ and $\eta_{sp}$ of the fatigue crack stable propagation life calculation formulas of specimens FWJ1–FWJ15, fitted from Eqs. (19) to (21).

The 1.645 times standard deviation, $s_{sp}$, corresponding to the fatigue crack stable propagation life of each parameter group was introduced into Eqs. (19) to (21). Subsequently, the fatigue crack stable propagation life, $N_{sp,t}$, and stable propagation critical length, $a_{sp}$, listed in Table 4, were refitted according to Eq. (18) to obtain the green dashed line equations in Fig. 7. The fitting fatigue crack stable propagation life calculation formulas for specimens FWJ1−FWJ5, FWJ6−WJ10, and FWJ11−FWJ15, with a confidence level of 95%, were obtained as follows:

$$\lg N_{sp}=0.3151\lg a_{sp}+3.8697 \tag{22}$$

$$\lg N_{sp}=0.3148\lg a_{sp}+4.2852 \quad (23)$$

$$\lg N_{sp}=0.3133\lg a_{sp}+4.8123 \quad (24)$$

The parameters $\xi_{sp,0.95}$ of the fatigue crack stable propagation life calculation formulas for specimens FWJ1−FWJ15, fitted from Eq. (22)−(24), are listed in Table 4. It can be seen that the parameter $\xi_{sp,0.95}$ increases as $\Delta\sigma/f_{uw}$ increases, and the parameter $\eta_{sp}$ = 3.18−3.20. In this paper, the parameter $\eta_{sp}$ is conservatively taken to be 3.19.

When $\Delta\sigma/f_{uw}$ = 0, it is a static loading condition, and the fatigue crack stable propagation life $N_{sp}$ tends to infinity. According to Eq. (5), when $N_{sp}=\infty$, $\xi_{p,0.95}=0$.

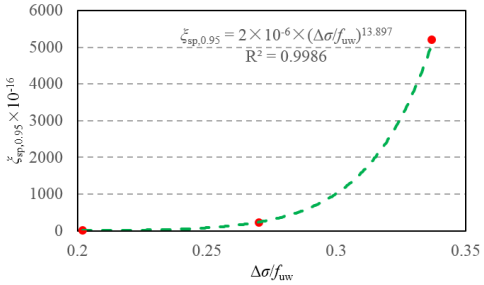


**Fig. 8** Fitting function for the parameters $\xi_{p,0.95}$ and $\Delta\sigma/f_{uw}$

A fitting function for the parameters $\xi_{sp,0.95}$ and $\Delta\sigma/f_{uw}$ with the minimum variance, as shown in Fig. 8, is given by:

$$\xi_{sp,0.95}=2\times10^{-6}\times(\Delta\sigma/f_{uw})^{13.90} \quad (25)$$

Substituting Eq. (25) into Eq. (5) and considering $\eta_{sp}$=3.19, the fatigue crack stable propagation life calculation formula of the Q460C steel fillet weld cruciform joints can be expressed as follows:

$$N_{sp}=\left[\frac{a_{sp}}{2\times10^{-6}\times(\Delta\sigma/f_{uw})^{13.90}}\right]^{\frac{1}{3.19}} \quad (26)$$

The calculated fatigue crack stable propagation lives according to Eq. (26) are presented in Table 4, with a calculation error ranging from −7.9% to −1.0%. The overall calculation results are relatively safe and reliable.

### *4.2. Calculation of fatigue crack initiation life*

The fatigue crack initiation life of the Q460C steel fillet weld cruciform joints, as listed in Table 3, increases as $\sigma_{max}/f_{uw}$ and $\Delta\sigma/f_{uw}$ decrease. According to Eq. (4), the parameter $\eta_i$ is related to the shape of the specimen and is thus independent of $\sigma_{max}/f_{uw}$ and $\Delta\sigma/f_{uw}$. Therefore, the parameter $\xi_i$ is related to $\sigma_{max}/f_{uw}$ and $\Delta\sigma/f_{uw}$.

When $\sigma_{max}/f_{uw}$=1.0, the fillet weld directly fractures, resulting in the fatigue crack initiation life $N_i$=0. According to Eq. (4), when $N_i$=0, $\xi_i=\infty$. Conversely, when $\sigma_{max}$=0, implying no tensile stress in the fillet weld, the fatigue initiation life $N_i=\infty$. According to Eq. (4), when $N_i=\infty$, $\xi_i$=0.

Referring to the fatigue crack stable propagation length, $a_{sp}$, calculated by Eqs. (9) to (17), being a linear function of $\sigma_{max}/f_{uw}$, a function of the parameters $\xi_i$ and $\sigma_{max}/f_{uw}$, satisfying the above conditions, is constructed as follows:

$$\xi_i=k_i\times\left(\frac{\sigma_{max}/f_{uw}}{1-\sigma_{max}/f_{uw}}\right)=k_i\times\left(\frac{\sigma_{max}}{f_{uw}-\sigma_{max}}\right) \quad (27)$$

where $k_i$ is an undetermined coefficient.

Substituting Eq. (27) into Eq. (4) to then taking the logarithm of both sides simplifies the analysis:

$$\log N_i=[-\log(\frac{\sigma_{max}}{f_{uw}-\sigma_{max}})+\log a_i-\log k_i]/\eta_i \quad (28)$$

The experimental data for the fatigue crack initiation life, $N_{i,t}$, and the ratio $\sigma_{max}/(f_{uw}-\sigma_{max})$ are fitted according to Eq. (28), depicted by the red solid line in Fig. 9.

$$\lg N_i=-0.6267\lg[\sigma_{max}/(f_{uw}-\sigma_{max})]+4.1914 \quad (29)$$

$$\lg N_i=-0.6203\lg[\sigma_{max}/(f_{uw}-\sigma_{max})]+4.4764 \quad (30)$$

$$\lg N_i=-0.6177\lg[\sigma_{max}/(f_{uw}-\sigma_{max})]+4.9141 \quad (31)$$

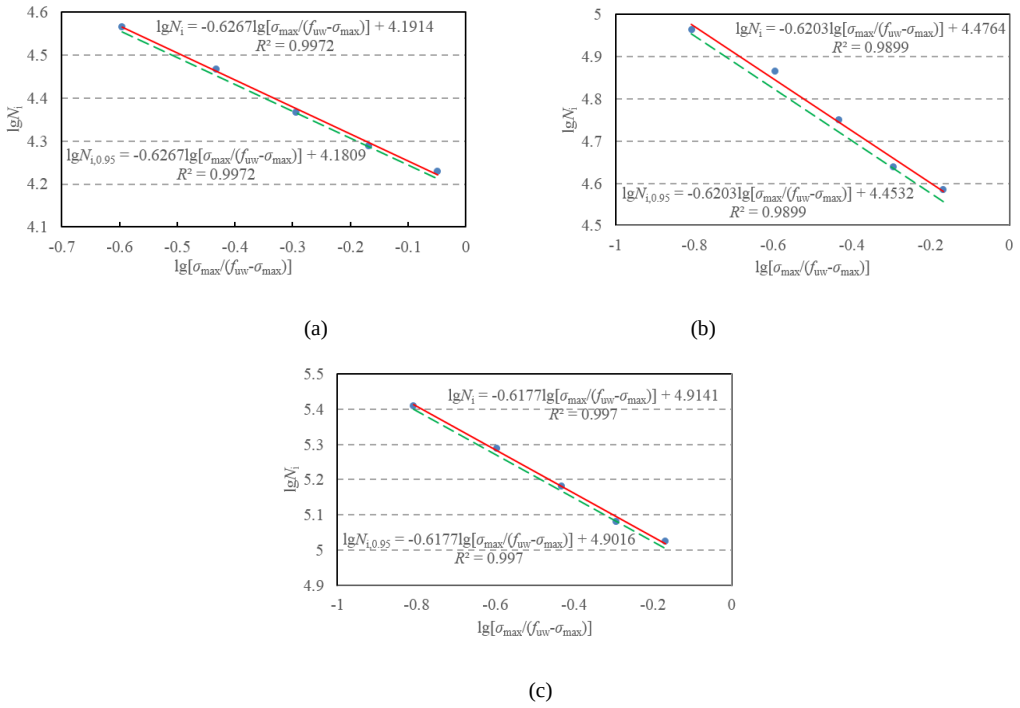


**Fig. 9** Fitted fatigue crack initiation life calculation formula: a) Specimens FWJ1−FWJ5; b) Specimens FWJ6−FWJ10; c) Specimens FWJ11−FWJ15

According to Eqs. (29) to (31), with the fatigue crack initiation length $a_i$=0.05mm, the fitted parameters $k_i$ and $\eta_i$ are listed in Table 5.

Incorporating 1.645 times standard deviation, $s_i$, corresponding to the fatigue crack initiation life, into Eqs. (29) to (31), and the fatigue crack initiation life, $N_{i,t}$, and the ratio $\sigma_{max}/(f_{uw}-\sigma_{max})$, were refitted according to Eq. (27) to obtain the green dotted line equation in Fig. 9. Thus, the fatigue crack initiation life calculation formulas of specimens FWJ1−FWJ5, FWJ6−FWJ10F8, and FWJ11−WJ15, with a 95% confidence level, were obtained as follows:

$$\lg N_i=-0.6267\lg[\sigma_{max}/(f_{uw}-\sigma_{max})]+4.1809 \quad (32)$$

$$\lg N_i=-0.6203\lg[\sigma_{max}/(f_{uw}-\sigma_{max})]+4.4532 \quad (33)$$

$$\lg N_i=-0.6177\lg[\sigma_{max}/(f_{uw}-\sigma_{max})]+4.9016 \quad (34)$$

The parameters $k_{i,0.95}$, derived from Eqs. (32) to (34), are listed in Table 4. It can be seen that $k_{i,0.95}$ decreases as $\Delta\sigma/f_{uw}$ decreases. The parameter $\eta_i$ exhibits minimal variation, ranging from 1.60 to 1.62. In this paper, $\eta_i$ is conservatively taken to be 1.62.

**Table 5**
Fitted parameters of fatigue crack initiation life calculation formula

| Specimen No. | $N_{i,t}$ (cycles) | $\eta_i$ | $k_i$ ($10^{-8}$,mm) | $s_i$ | $k_{i,0.95}$ ($10^{-8}$,mm) | $N_{i,c}$ (cycles) | $e_{i,c\text{-}t}$ (%) | $N_{f,t}$ (cycles) | $N_{f,c}$ (cycles) | $e_{f,c\text{-}t}$ (%) |
|---|---|---|---|---|---|---|---|---|---|---|
| FWJ1 | 17000 | 1.60 | 102.5 | 0.006 | 106.6 | 14237 | −16.3 | 39600 | 35041 | −11.5 |
| FWJ2 | 19500 | 1.60 | 102.5 | 0.006 | 106.6 | 16863 | −13.5 | 42400 | 38183 | −9.9 |
| FWJ3 | 23300 | 1.60 | 102.5 | 0.006 | 106.6 | 20164 | −13.5 | 46600 | 41875 | −10.1 |
| FWJ4 | 29300 | 1.60 | 102.5 | 0.006 | 106.6 | 24567 | −16.2 | 53100 | 46651 | −12.1 |
| FWJ5 | 36900 | 1.60 | 102.5 | 0.006 | 106.6 | 30985 | −16.0 | 61400 | 53547 | −12.8 |
| FWJ6 | 38500 | 1.61 | 30.4 | 0.014 | 33.1 | 37027 | −3.8 | 98700 | 93635 | −5.1 |
| FWJ7 | 43600 | 1.61 | 30.4 | 0.014 | 33.1 | 44274 | +1.5 | 104600 | 101821 | −2.7 |
| FWJ8 | 56400 | 1.61 | 30.4 | 0.014 | 33.1 | 53943 | −4.4 | 118400 | 112595 | −4.9 |
| FWJ9 | 73500 | 1.61 | 30.4 | 0.014 | 33.1 | 68034 | −7.4 | 136700 | 127649 | −6.6 |
| FWJ10 | 92200 | 1.61 | 30.4 | 0.014 | 33.1 | 91869 | −0.4 | 156700 | 152495 | −2.7 |
| FWJ11 | 106200 | 1.62 | 5.5 | 0.008 | 5.8 | 102068 | −3.9 | 307800 | 300028 | −2.5 |
| FWJ12 | 121100 | 1.62 | 5.5 | 0.008 | 5.8 | 122045 | +0.8 | 325500 | 324292 | −0.4 |
| FWJ13 | 152100 | 1.62 | 5.5 | 0.008 | 5.8 | 148697 | −2.2 | 359600 | 352733 | −1.9 |
| FWJ14 | 195200 | 1.62 | 5.5 | 0.008 | 5.8 | 187540 | −3.9 | 406600 | 369782 | −2.4 |
| FWJ15 | 257100 | 1.62 | 5.5 | 0.008 | 5.8 | 253245 | −1.5 | 473300 | 465231 | −1.7 |

When $\Delta\sigma/f_{uw}=0$, representing a static loading condition, and the fatigue crack initiation life $N_i=+\infty$. According to Eqs. (4) and (27), when $N_i=+\infty$, $k_{i,0.95}=0$.

The relationship between $k_{i,0.95}$ and $\Delta\sigma/f_{uw}$ can be fitted using the data in Table 5, and the function should satisfy the boundary condition $k_{i,0.95}|_{\Delta\sigma/fuw=0}=0$. The fitted function is shown in Fig. 10.

$$k_{i,0.95}=5.45\times10^{-6}\times(\Delta\sigma/f_{uw})^{5.7} \quad (35)$$

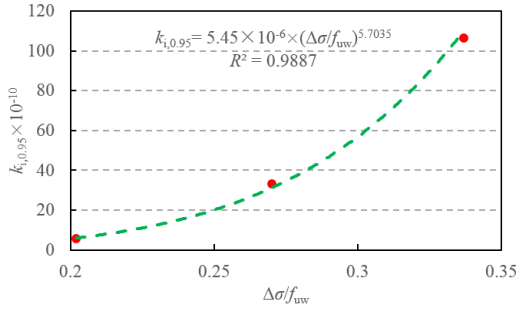


**Fig. 10** Fitting function of the parameters $k_{i,0.95}$ and $\Delta\sigma/f_{uw}$

Substituting Eq. (35) into Eq. (27) and (4), and setting $\eta_i=1.62$, the fatigue crack initiation life calculation formula of the Q460C steel fillet weld cruciform joints is derived as follows:

$$N_i=\left[\frac{a_i}{5.45\times10^{-6}\times(\Delta\sigma/f_{wu})^{5.70}\times\left(\frac{\sigma_{max}}{f_{uw}-\sigma_{max}}\right)}\right]^{\frac{1}{1.62}} \quad (36)$$

The calculated fatigue crack initiation lives according to Eq. (36) are listed in Table 5, with a calculation error ranging from −16.3% to +1.5%.

### *4.3. Unified fatigue life calculation*

Substituting Eqs. (26) and (36) into Eq. (6), the unified fatigue life calculation formula of the Q460C steel fillet weld cruciform joints is obtained as follows:

$$N_f=\left[\frac{a_i}{5.45\times10^{-6}\times(\Delta\sigma/f_{wu})^{5.70}\times\left(\frac{\sigma_{max}}{f_{uw}-\sigma_{max}}\right)}\right]^{\frac{1}{1.62}}+\left[\frac{a_{sp}}{2\times10^{-6}\times(\Delta\sigma/f_{uw})^{13.90}}\right]^{\frac{1}{3.19}} \quad (37)$$

The calculated total fatigue lives according to Eq. (37) and the corresponding calculation errors are listed in Table 5. The calculation error of Eq. (37) is from −12.8% to −0.4%, demonstrating that the calculation accuracy of Eq. (37) is better than that of Eqs. (1) to (3) recommended in GB50017-2017, AISC360, and Eurocode3.

## 5. Discussion

The ellipsoidal fracture model suggested by Eq. (8) serves as the criterion for crack tip cracking and instability propagation of fatigue crack. However, it is important to note that this model is specifically designed for isotropic structural steels characterized by equal tensile and compressive strengths. Therefore, the fatigue life assessment method presented in this paper, along with the fatigue initiation life calculation model, stable propagation life calculation model, and the total fatigue life model suggested by Eqs. (4) to (6), for the Q460C steel fillet weld cruciform joint, are only applicable to isotropic structural steels with uniform tensile and compressive strengths. They may not be applicable to engineered materials with different tensile and compressive strengths.

## 6. Conclusions

Fatigue tests were carried out on the Q460C steel fillet weld cruciform joints. The fatigue crack initiation length was obtained from the experimental analysis. The ellipsoidal fracture model was used as the crack tip cracking criteria and the instability propagation criterion of fatigue crack, and theoretical calculations and numerical simulations on the fatigue crack propagation in the fillet weld cruciform joint were employed. The fatigue life of the fillet weld cruciform joints was evaluated using the unified fatigue life calculation model and the fatigue life formulas recommended in GB50017-2017, Eurocode3, and AISC360. The following conclusions could be drawn:

1. A fatigue crack initiates at the root of the fillet weld due to the presence of a high stress concentration, and then fatigue fractures occur at the effective bearing section of the fillet weld.

2. The fatigue crack initiation life, $N_{i,t}$, stable propagation life, $N_{p,t}$, and total fatigue life, $N_{f,t}$, of the fillet weld cruciform joint decrease as the relative stress amplitude, $\Delta\sigma/f_{uw}$, and the relative nominal maximum stress, $\sigma_{max}/f_{uw}$,

increase. The ratio of the fatigue crack initiation life to the total fatigue life ranges from 0.43 to 0.54.

3. The fatigue life formulas recommended in standards such as GB50017-2017, AISC360, and Eurocode3 are evaluated. The analysis revealed notable discrepancies between the calculated and tested fatigue lives, with calculation errors ranging from −64.4% to +30.7%. Specifically, the recommended formulas tend to be overly conservative, resulting in substantial underestimation of fatigue life.

4. The unified fatigue life calculation model provides more accurate predictions for the fatigue crack initiation life, stable propagation life, and total fatigue life of the fillet weld cruciform joint. The calculation errors associated with this model range from −16.3% to +1.5%, −7.9% to −1.0%, and −12.8% to −0.4%, respectively, indicating its superior performance compared to the recommended formulas.

## Acknowledgement

The financial support provided by the Project of Science and Technology for Public Welfare of Ningbo City (Grant no. 2022S179, 2023S101), Zhejiang Provincial Natural Science Foundation of China (Grant no. LY24E080001), and China Postdoctoral Science Foundation (Grant no. 2023M742607) is gratefully acknowledged. The authors would like to express their sincere thanks for their support.

## References

[1] Araujo LC, Malcher L, Oliveira D, et al. A new multiaxial fatigue endurance model for high strength steels taking into account the presence of small defects. Int J Fatigue 2024;178:107981.
[2] Skriko T, Lipiäinen K, Ahola A, et al. Fatigue strength of longitudinal load-carrying welds in beams made of ultra-high-strength steel. J Constr Steel Res 2021;179:106563.
[3] Skriko T, Ghafouri M, Bjoerk T. Fatigue strength of TIG-dressed ultra-high-strength steel fillet weld joints at high stress ratio. Int J Fatigue 2017; 94: 110–120.
[4] Tong LW, Niu LC, Ren ZZ, et al. Experimental investigation on fatigue behavior of butt-welded high-strength steel plates. Thin Wall Struct 2021;165:107956.
[5] Tong LW, Niu LC, Ren ZZ, et al. Experimental research on fatigue performance of high-strength structural steel series. J Constr Steel Res 2021; 183:106743.
[6] Wang WZ, Shi WZ, Li B, et al. High-cycle fatigue life assessment of welded cruciform joints of Q460D steel. Struct 2023;57(11):105163.
[7] Lv FJ, Wang WZ, Zhao W. Fatigue test and unified fatigue life calculation of Q460C steel notched plates. Build 2023;13(3):697.
[8] Jie ZY, Wang WJ, Zhuge P, et al. Fatigue performance of inclined cruciform welded joints with artificial pits. Adv Steel Constr 2021;17(1):20–27.
[9] Guo T, Liu ZX, Zhu JS. Fatigue reliability assessment of orthotropic steel bridge decks based on probabilistic multi-scale finite element analysis. Adv Steel Constr 2015;11(3):334–346.
[10] Lipiäinen K, Ahola A, Virolainen E, Hirvi A, et al. Fatigue strength of hot-dip galvanized S960 cut edges and longitudinal welds. J. Constr. Steel Res 2022;189:, 107083.
[11] Ahola A, Skriko T, Lipiäinen K, et al. On the weld root fatigue strength and improvement techniques for non-load-carrying transverse attachment joints with single-sided fillet welds and made of mild and ultra-high-strength steels. Eng Struct 2021; 249:113373.
[12] Yue YN, Shuling Gao SL, Li N, et al. High-cycle fatigue performance of corroded Q690E high strength steel and Q690qENH high-strength weathering steel. Constr and Build Mater 2023;401:132835.
[13] Sui GY, Wang ZQ, Li JR, et al. Roles of microstructures in high-cycle fatigue behaviors of 42CrMo high-strength steel under near-yield mean stress. Int J Fatigue 2023;177:107928.
[14] Zhang Y, Sang XG, Xu GT, et al. Fatigue crack propagation of the gradient surface-modified layer of high-strength steel. Int J Fatigue 2023;177:107921.
[15] Fang L, Fu ZQ, Ji, BH, et al. Propagation mode and characteristics of fatigue crack in steel bridge deck after drilling ahead of the crack tip. Adv Steel Constr 2022;18(2):544–551.
[16] Yamada K, Ishikawa T, Kakiichi T. Rehabilitation and improvement of fatigue life of welded joints by ICR treament. Adv Steel Constr 2015;11(3):2944–551.
[17] Neuber H. Theory of stress concentration for shear-strained prismatic bodies with arbitrary nonlinear stress-strain law. J App Mech 1961;28:544–550.
[18] Paris PC, Erdogan F. A critical analysis of crack growth laws. J Bas Eng 1963;85D:528–534.
[19] GB50017-2017, Standard for design of steel structures, Architecture Industrial Press of China, Beijing, China, 2017. (in Chinese)
[20] AISC-360-05, Specification for structural steel buildings, American Institute of Steel Construction, Chicago, 2005.
[21] Eurocode3-2005, EN 1993-1-9, Design of steel structures-fatigue strength of steel structures, British Standards Institution, London, 2005.
[22] Wang WZ. Crack criterion and fracture tests of structural steel. Eng Mech 2008;25:27–31. (in Chinese).
[23] Wang WZ. Calculation model of fatigue crack initiation life and fatigue life calculation of Q460C steel notched plates. Mater Rev 2024;38(4):23010056. (in Chinese).
[24] Wang WZ. Fatigue failure model of Q345 steel round bars. J Harb Inst Technol 2019;51: 58–64. (in Chinese).
[25] GB/T3075-2008, Metallic materials-fatigue testing-axial-force-controlled method, Standards Press of China, Beijing, 2008. (in Chinese)
[26] Wang WZ, Qian XD, Su RQ, et al. Tensile tests and analyses of notched specimens fabricated from high strength steels using a generalized yield model. Fatigue Fract Eng Mat Struct 2010;33:310–319.

**Advanced Steel Construction** – Vol. 20 No. 3 (2024) 232–240
**DOI:**10.18057/IJASC.2024.20.3.3


# STUDY ON THE ULTIMATE SHEAR PERFORMANCE OF CONCRET-FILLED STEEL TUBULAR COMPOSITE COLUMNS

Jian-Gang Wei [1, 2], Jin-Peng Han [1], Zhi-Tao Xie [1], Yan Yang [1] and Wei Zhang [2, 3, *]

[1] *College of Civil Engineering of Fuzhou University, No. 2, Wulongjiang Avenue, Minhou County, Fuzhou, Fujian, China.*
[2] *School of Civil Engineer, Fujian University of Technology, No. 33, Xuefu South Road, Minhou County, Fuzhou, Fujian, China.*
[3] *Institute of Theoretical and Applied Mechanics of the Czech Academy of Sciences Prosecká 809/76, 19000 Prague 9, Czech Republic.*
** (Corresponding author: E-mail: zhangwei621@gmail.com)*

**ABSTRACT**

The shear performance of three concrete-filled steel tubular (CFST) composite columns was investigated via single-point shear tests, considering shear-span ratios of 0.75, 1, and 1.5. The findings indicated that the failure mode of the CFST composite column transitioned from oblique compression shear failure to localized shear failure in the joint areas as shear-span ratio decreased. An extended analysis of the parameters was carried out utilizing the ABAQUS finite element model. The analysis indicates that the ultimate shear resistance capability of steel-concrete composite columns increases with the rise in the strength of the batten concrete, the batten concrete thickness-to-span ratio, and the outer diameter of column limbs. However, it decreases with an increase in shear-span ratio. The accuracy of the calculation methods for existing similar structures was assessed, and based on the force transmission mechanism of CFST composite columns, theoretical and simplified calculation methods were proposed that meet engineering precision requirements. Consequently, this method offers a valuable theoretical reference for engineering applications.

**ARTICLE HISTORY**

Received: 9 July 2023
Revised: 17 February 2024
Accepted: 20 February 2024

**KEYWORDS**

Concrete-filled steel tube;
Composite column;
Shear-span ratio;
Shear capability;
Calculation method



## 1. Introduction

Concrete-Filled Steel Tubular (CFST) composite columns consist of steel tube concrete limbs and concrete strips. In comparison to the steel-filled tubes of lattice columns, the higher stiffness of concrete strips in CFST composite columns leads to superior mechanical performance [1-4].

Currently, scholars have gradually conducted research on CFST composite columns and similar structures. Ou *et al.* [5] performed a comparative investigation into the axial and eccentric compression behavior of CFST composite short columns in contrast to lattice short columns. The findings unveiled the superior compressive strength, flexural rigidity, and load-carrying capability of CFST composite columns when juxtaposed with lattice columns. Furthermore, it was observed that the load-carrying capability of CFST composite columns exhibited constancy irrespective of variations in eccentricity ratio and slenderness ratio.

Xiong *et al.* [6-8] utilized double-layer parallel steel plates as connecting plates, conducting axial compression and lateral loading tests on equal or unequal limbs. The results indicated that compared to CFST columns with single steel plate connections, the double-plate CFST columns exhibited significantly improved load-carrying capability, stability, and lateral stiffness, demonstrating excellent deformation resistance capabilities.

Yong *et al.* [9] conducted pseudo-static tests on Reinforced Concrete (RC) frame-truss composite walls (FTCW). The results revealed that the most effective way to augment the load-bearing capability of RC frame-FTCW is by increasing the number of internal filled FTCW, followed by increasing the reinforcement ratio of the frame columns. The impact of escalating axial compression ratio, concrete strength, or introducing angle steel to the internal diagonal bracing in FTCW on the load-bearing capability is relatively negligible.

Quasi-static and quasi-dynamic tests were conducted on CFST composite columns by Yadav *et al.* [10-12], demonstrating their excellent seismic performance and complete hysteretic curves, which were similar to those observed in lattice columns. Nevertheless, the failure mode of the composite columns underwent a transformation, marked by the occurrence of concrete slab cracking and steel tube tearing.

Zhou et al. [13] undertook a seismic performance investigation involving six composite shear walls. The investigation explored the impact of axial load ratio, load eccentricity on the ductility and stiffness. Building upon these findings, Zhou introduced a shear force calculation methodology aligned with the precision criteria of engineering standards.

Zhang et al. [14] conducted a seismic performance study on five precast concrete-encased carbon fiber reinforced CFST composite walls with twin steel tube connections. The findings indicated that optimizing the wall with C100 steel fiber-reinforced high-strength concrete, as opposed to the reference wall using C80 concrete, led to improvements in structural load-bearing capability, deformation characteristics, and energy dissipation capability. The incorporation of bottom dual-layered steel plates to the high-strength concrete web constrained the web, augmenting deformation capability, while alleviating stiffness degradation and enhancing reparability.

CFST composite columns are frequently employed as bridge piers in various bridges across China [15-18]. However, these bridge piers are susceptible to shear failure induced by seismic events or collisions with vehicles or vessels. Therefore, the investigation of the shear behavior of CFST composite columns is of paramount importance [19]. Currently, scholars both domestically and internationally focus their research on CFST composite columns and similar structures primarily in terms of axial compression, lateral loading, and seismic behavior. The research on the shear performance of CFST composite columns and similar structures is relatively lacking, and the theoretical studies in this area are not comprehensive enough.

Wang *et al.* [20] compares RC filled CPSW with different connectors and axial compression ratios to RC shear walls. The results indicate a significant enhancement in shear capability for CPSW with CFSTs as boundary elements, compared to RC shear walls. Additionally, the study proposes a shear ultimate load-bearing capability calculation method that aligns with engineering precision requirements.

Liao [21] conducted theoretical derivations on the shear capability of CFST lattice columns. Based on the mechanism that the filled tube would not fail before the CFST lattice column, a shear capability calculation method applicable to lattice columns was proposed.

Nevertheless, the established shear capability calculation methods for analogous structures may not be universally applicable to CFST composite columns. Consequently, this paper entailed tests and analyses on three CFST composite columns with varying shear-span ratios. Subsequent to this, experimental data-validated finite element models were employed to conduct parameter expansion analyses. The purpose of these analyses was to examine the impact of various structural parameters, including the shear-span of ratio, thickness span ratio, batten concrete strength, and the outer diameter of the column limb, on the shear performance. Additionally, an evaluation of the accuracy of existing shear capability calculation methods for similar structures was conducted. Based on the force transmission mechanism of CFST composite columns, a study on the shear capability calculation methods for CFST composite columns was also undertaken.

## 2. Experimental program

### *2.1. Specimen design*

The dimensions of the standard test specimen were established Derived from the lower half of the pier of the Ganhaizi bridge in Sichuan Province, specifically, the CFST composite columns. The dimensions were as follows: the column steel pipe measured 114 mm×2 mm, the longitudinal steel batten pipes were 48 mm×2 mm. The specimen's height was 1500 mm. The centroid of the column limb was located 300 mm from the longitudinal axis, while the batten pipes were spaced 150 mm vertically. The transverse batten consisted of a reinforced concrete slab with a width of b and thickness of 50 mm. This slab had embedded steel bars with diameters of 6 mm, spaced 50 mm vertically and 60 mm transversely. The transverse and longitudinal reinforcements of the reinforcement mesh were connected by binding, and the reinforcement mesh was attached to the column limbs via a connecting steel plate. The CFST composite column's shear-span ratio was adjusted by altering the height of the concrete batten b, with heights of 1000 mm, 750 mm, and 500 mm corresponding to shear-span ratios of 0.75, 1, and 1.5, respectively. The detailed diagram and specific parameters can be found in Fig. 1 and Table 1, respectively.

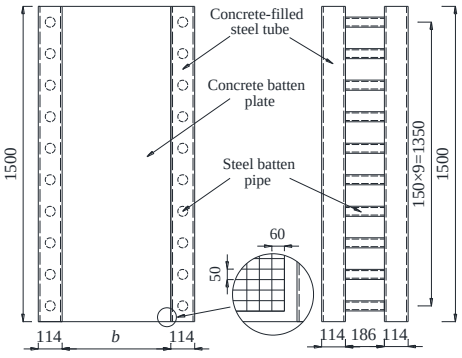


(a) The details of reinforcement

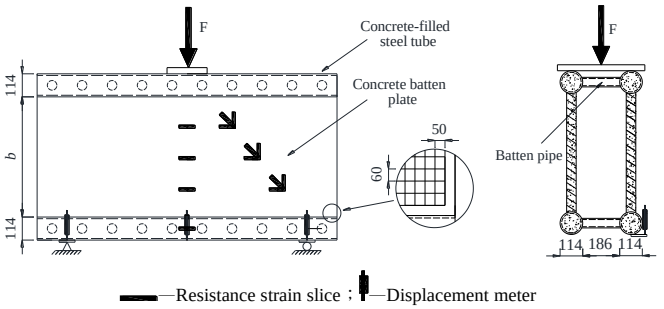


(b) Schematic diagram of test loading

(c) Field diagram of test loading

**Fig. 1** Detail drawing of test loading device and specimen size

**Table 1**
Details of specimens

| Specimen number | Height H/mm | Shear-span a/mm | batten plate width *b*/mm | Shear-span ratio $\lambda$ | $V_{Test}$/kN | $V_{c\text{-}China}$/kN | $V_{c\text{-}simplify}$ /kN |
|---|---|---|---|---|---|---|---|
| S1-$\lambda$-0.75 | 1500 | 750 | 1000 | 0.75 | 621.6 | 1005.0 | 651.6 |
| S2-$\lambda$-1 | | | 750 | 1 | 508.8 | 753.7 | 516.3 |
| S3-$\lambda$-1.5 | | | 500 | 1.5 | 359.1 | 502.5 | 381.0 |

where S stands for the specimen, and the following values indicate the specimen type; $\lambda$=a/b, stands for shear-span ratio a and batten plate width b; Specimens are numbered according to specimen type - physical symbol of shear-span ratio - shear-span ratio value.

### *2.2. Material characteristics*

The concrete and steel properties were tested according to the "Standard for test methods of mechanical properties on ordinary concrete" and "Metallic materials-Tensile testing Part 1: Method of test at room temperature", and the results are illustrated in Table 2.

**Table 2**
Material characteristics

| Material | Elastic modulus *E*/GPa | $f_y$、$f_c$/MPa | $f_t$/MPa | Poisson's ratio $\mu$ |
|---|---|---|---|---|
| Steel pipe (columnar limb and batten pipe) | 206 | 235 | 390 | 0.283 |
| steel bar | 198 | 321 | 519 | 0.3 |
| Concrete (core concrete and batten concrete) | 25.0 | 20.1 | 1.78 | 0.2 |

### *2.3. Loading method and instrumentation*

The experiments were conducted on a 10000 kN hydraulic press at Fuzhou University. The test specimens were positioned on two support devices, with a steel block attached to the upper part of the specimen serving as the loading devices. During the tests, the specimens were subjected to loading through the upper loading device. The loading device and specimen size are illustrated in Fig. 2.

Initially, load control was implemented, employing a loading increment of 25 kN. Each successive load stage endured for a duration of 2-3 minutes to meticulously observe and document the mode and crack condition of the specimen. Subsequently, displacement loading, progressing at a rate of 0.2 mm/min, was employed until reaching the peak of the load curve, equivalent to 0.7 times the anticipated shear capability derived from the finite element method. Upon reaching this juncture, the loading procedure was terminated.

The arrangement of deformation measuring points is illustrated in Fig. 1(b). Displacement gauges were strategically located at both supports and the mid-span to monitor and document specimen deflection. Axial strain gauges were applied to the steel tube and concrete batten at the mid-span's bottom to gauge bending strain. Additionally, strain gauges were installed horizontally, vertically, and obliquely along the line connecting the loading point and supports on the concrete batten to measure shear strain.

## 3. Experimental results

### *3.1. Failure mode*

In the initial loading phase, no noticeable alterations were detected on the specimen surfaces. Nevertheless, with the growing load, a multitude of slender and compact inclined cracks emerged in the concrete batten located between the loading point and the supports. These cracks exhibited an escalation in both width and quantity as the load intensified. Upon reaching its peak, the rate at which cracks widened and multiplied experienced a sudden acceleration, leading to continuous peeling off of the concrete at the loading point in the sectional specimens. As a result, the load could not be further increased, indicating that the composite column had reached its ultimate shear capability.

The ultimate failure mode diagram for each specimen is presented in Fig. 2. The concrete batten exhibited numerous diagonal cracks. In test S1-$\lambda$-0.75, where the shear-span ratio was minimal, the concrete batten near the loading point experienced tearing, while severe crushing and peeling off of concrete occurred at the junctions of reinforcement and upper column limbs. Test S2-$\lambda$-1 and S3-$\lambda$-1.5, which had larger shear-span ratios, exhibited more diagonal cracks than test S1-$\lambda$-0.75, albeit with less pronounced local failure characteristics of concrete spalling at the loading point or supports. The observed phenomenon suggests a shift in the failure mode of the CFST composite column from oblique compression shear failure to localized shear failure in the joint areas, correlating with a decrease in shear-span ratio.

(a) S1- λ -0.75

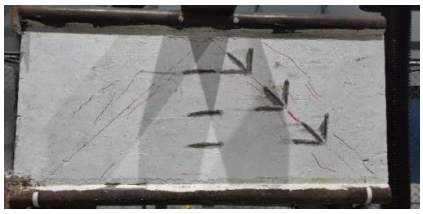

(b) S2- λ -1

(c) S3- λ -1.5

**Fig. 2** Failure diagram of specimen

### *3.2. Load-deflection curve*

The load-deflection (N-*f*) curve depicted in Fig. 3 for tests conducted under various shear-span ratios illustrates that, initially, the deflection of the middle span exhibited an approximately linear relationship with the load. This behavior indicates that the specimens were in the elastic stage during the early loading phase. Subsequently, prior to reaching 0.8 times the peak load, the deflection of the mid-span exhibited a nonlinear increase with the rising load, signaling the transition of the specimens into the elastic-plastic stage. After the load reached the peak value, the load will enter the stage of load-bearing capability decline. In the process of testing, the main failure mode of S2-*λ*-1 and S3-*λ*-1.5 was oblique compression and the shear capability decreased slowly, which showed the high residual load-bearing capability and ductility of these specimen. However, the capability of specimen S1-*λ*-0.75 decreased rapidly because it suffered local shear failure.

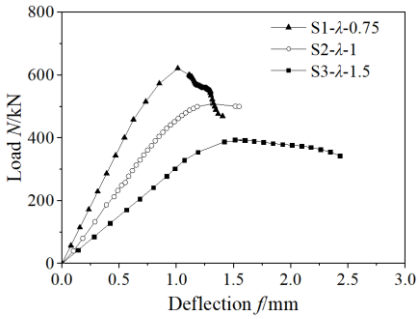


**Fig. 3** Load-deflection curve

The load-deflection curves show that the initial slope and peak load of the curves were larger when shear-span ratio of the composite columns was smaller but the shear stiffness and ultimate shear capability were higher. Taking S3-*λ*-1.5 as the benchmark, the shear stiffness of S2-*λ*-1 and S1-*λ*-0.75 was increased by 237.5% and 462.5%, respectively and the shear capability of these specimens was increased by 28.9% and 57.5%, respectively.

### *3.3. Load-shear strain curve*

The shear deformation at the midspan of the concrete batten was characterized by the most representative abdominal shear strain, and the load-strain curves are depicted in Fig. 4. The shear strain curves of the CFST composite columns exhibited linearity with the load during the initial loading stage, corresponding to the elastic stage of the specimens. In contrast, the shear strain curves of the concrete batten displayed a nonlinear relationship with the load, reaching approximately 0.8 times the peak value, marking the transition of the specimens into the elastic-plastic stage.

The shear strain curves of the specimens increased rapidly while the load approached the peak value, which indicated that the cracks of the concrete batten were in the unstable stage, and the shear deformation increased obviously. The shear force of specimens S2-*λ*-1 and S3-*λ*-1.5 can still be transferred from the column limb to the batten slab, although the force transfer mechanism of specimen S1-*λ*-0.75 changes. Due to the tearing of the joints between the upper concrete batten and the CFST limbs, the shear force of specimen S1-*λ*-0.75 could not be transferred; therefore, the shear strain curve rebounded.

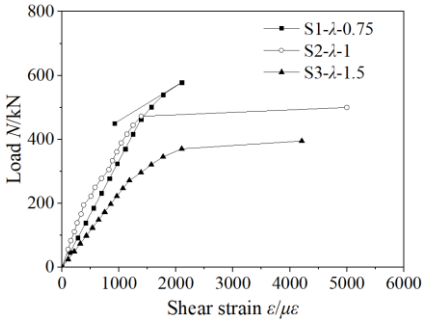


**Fig. 4** Load-shear strain curve

## 4. Numerical simulation analysis

### *4.1. Establishment of the model*

Finite element simulation is a widely adopted method for simulating the stress and deformation behavior of structures under varied conditions, allowing for the convenient analysis of diverse structural parameters. Software applications, including but not limited to ABAQUS, ANSYS, and MARC, have significantly augmented theoretical analysis and engineering practice related to these structures. Owing to the relatively high production difficulty and testing costs associated with the experimental model of steel tube concrete composite columns, further exploration of the structure's failure mechanisms and governing physical laws is warranted. ABAQUS software was employed to carry out simulation and analysis of the composite column. It was observed that the contribution of the transverse reinforcement pipe to the overall shear capability of the composite column was marginal. To enhance computational efficiency, a half-model of the steel tube concrete composite column structure was simulated, as depicted in Fig. 5.

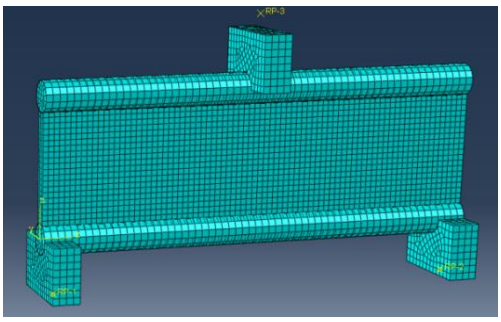

**Fig. 5** Finite element test model

To simulate realistic boundary conditions, a vertical Z-directional load is applied to the composite column from the upper loading device. The displacements in the X and Y directions of the loading device are constrained. Additionally, both bottom supports of the lower two support devices are set as fixed.

The connection between the upper loading device and the lower support devices with the steel tubes employs a surface-to-surface contact approach, designating the loading apparatus or support devices as the primary face and the steel tubes as the secondary face. Normal contact is specified as "hard contact," and tangential contact is modeled using the Coulomb friction model with a friction coefficient set to 0.15 [1].

The interface between the core concrete enclosed by the steel pipe utilizes a surface-to-surface contact approach, designating the steel pipe as the primary face and the core concrete as the secondary face. The normal contact is characterized as "hard contact," and the simulation of tangential contact employs the Coulomb friction model with a friction coefficient established at 0.6 [18]. The linkage between the batten concrete and the steel pipe is classified as "Tie," and the batten steel bars are situated within the "embedded region" of the batten concrete.

To more precisely replicate mechanical responses, including tensile cracking and concrete material crushing within steel tube concrete, researchers both at home and abroad frequently adopt the concrete damage plasticity model.

Following comparative calculations across different constitutive models, the selection ultimately favored the constrained concrete constitutive model proposed by Liu Wei, as delineated in Eq. (1).

$$\begin{cases} \sigma = \sigma_0[2\dfrac{\varepsilon}{\varepsilon_0} - (\dfrac{\varepsilon}{\varepsilon_0})^2] & (0 < \varepsilon \le \varepsilon_0) \\ \sigma = \sigma_0(\dfrac{\varepsilon}{\varepsilon_0})\dfrac{1}{\beta(\dfrac{\varepsilon}{\varepsilon_0}-1)^2 + (\dfrac{\varepsilon}{\varepsilon_0})} & (\varepsilon > \varepsilon_0) \end{cases} \quad (1)$$

$$\sigma_0 = f_c^{'} \qquad \varepsilon_0 = \varepsilon_c + 800\xi^{0.2}$$

$$\varepsilon_c = 1300 + 12.5 f_c^{'}$$

$$\beta = 0.5 \times (2.36 \times 10^{-5})^{[0.25+(\xi-0.5)^7]} (f_c^{'})^{0.5} \ge 0.12$$

The upper loading device and the two lower support devices are both represented as rigid body elements. The batten concrete was simulated using C3D8 solid elements, while the batten reinforcement was represented by T3D2 truss elements. The steel pipe was modeled using S4 shell elements. The damage plastic model was used for the battened concrete and core concrete, and the steel material was characterized using a bilinear elastic-plastic constitutive model [22], as shown in Figs. 6 and 7.

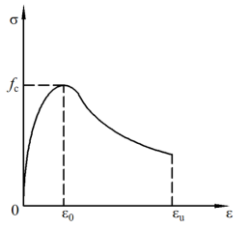


**Fig. 6** Constitutive model of concrete

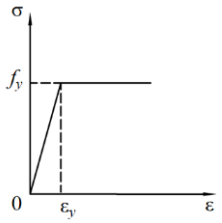


**Fig. 7** Constitutive model of steel

### *4.2. Model validation*

Comparisons between the calculated curves and experimental curves are presented in Fig. 8. The calculation curves closely align with the test curves, demonstrating a substantial overlap. It is noteworthy that only in the case of test S1-$\lambda$-0.75 did the ultimate load-bearing capability precede the simulation; nevertheless, the initial loading phase exhibited good concordance between the test and calculation curves.

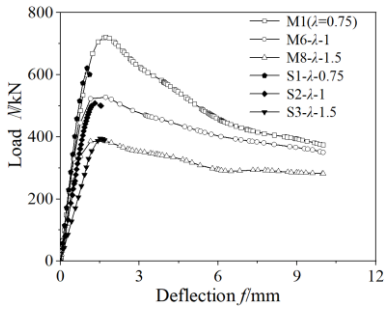


**Fig. 8** Load-deflection comparison diagram of test and simulation

The discrepancy observed in S1-λ-0.75 can be attributed to the higher strength of the connection between the simulated finite element column limbs and the concrete batten, as compared to the actual specimen. Thus, shear failure under oblique compression was the failure mode rather than local shear failure. The results of the deviation analysis indicate the imperative need to enhance the connection between the column limbs and concrete batten, especially in cases with a small shear-span ratio. Furthermore, the results suggest a good correlation between the simulation and experiments, allowing for further parameter analysis based on this FEM.

The deviation analysis results show that it is necessary to strengthen the connection of the column limbs and concrete batten with a small shear-span ratio and indicate that the simulation could provide a reasonable estimation of the shear process of composite columns if the composite columns were inclined to experience compression shear failure.

### *4.3. Stress analysis*

Display the stress maps for the principal tensile and compressive stresses of concrete and steel in Figs. 9 and 10, respectively.

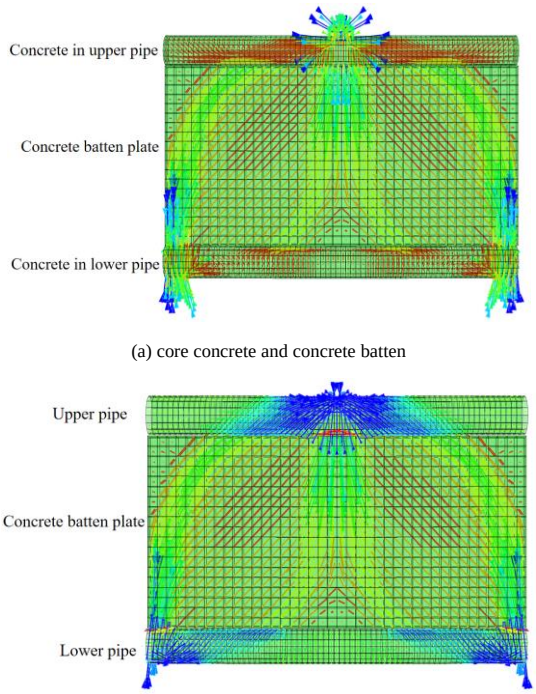


(a) core concrete and concrete batten

(b) steel pipes and concrete batten

**Fig. 9** Direction of principal compressive stress

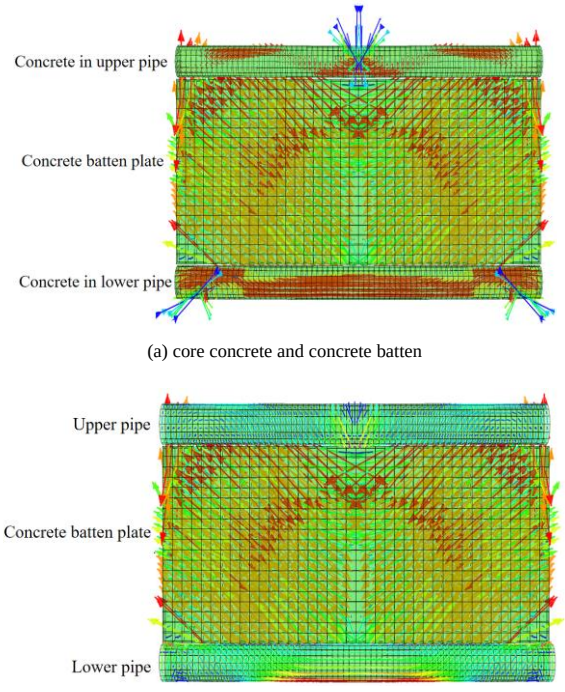


(a) core concrete and concrete batten

(b) steel pipes and concrete batten

**Fig. 10** Direction of principal tensile stress

In addition to the stress flow disorder at the loading point and the supports, the distribution of the principal compressive and tensile stress in the other areas of the upper and lower steel pipes presented good regularity, which could connect with the stress distribution of the concrete batten well, indicating that the shear force could transfer between the steel pipe and the batten plate concrete.

The main pressure and tensile stress flow of the concrete in pipes were relatively disordered due to the circular action of steel pipes. According to the load path method, the main compressive stress area in the same direction was equivalent to the compression bars and the main tensile stress area in the same direction was equivalent to the tension bars. In this way, the strut-and-tie model of composite columns was formed.

In this model, the concrete diagonal strut was equivalent to the pressure bars of the strut-and-tie model and the shear force of the upper and lower steel tubes was transferred to the supports through the concrete diagonal struts. The tension side of the CFST acted as tension bars, ensuring equilibrium with the horizontal force exerted by the diagonal compression bars.

### *4.4. Parameter analysis*

With the verified FEM, the strength of the batten concrete $f_c$ (20 MPa ~ 50 MPa), shear-span ratio of the batten concrete $\lambda$ (0.5~1.75), the thickness span ratio of the concrete batten $t_c$/L (0.033~0.073) and the outer diameter of the column limbs $D$ (90 mm~240 mm) were analyzed. The parameters of each FEM are illustrated in Table 3.

**Table 3**
Basic parameters of finite element analysis

| Specimens number | The strength of batten plate concrete/MPa | The width of barren plate $b$/mm | Shear-span ratio $\lambda$ | The thickness of batten plate $t_c$/mm | Thickness span ratio $t_c/L$ | The outer diameter of column limbs $D$/mm | $V_{FEM}$ | $V_{c\text{-China}}$/kN | $V_{c\text{-Simple}}$/kN |
|---|---|---|---|---|---|---|---|---|---|
| M1 | 30 | 1000 | 0.75 | 50 | 0.033 | 114 | 721.2 | 1005 | 651.6 |
| M2-$f_c$-30 | 20 | 1000 | 0.75 | 50 | 0.033 | 114 | 565.2 | 670 | 547.7 |
| M3-$f_c$-40 | 40 | 1000 | 0.75 | 50 | 0.033 | 114 | 838.8 | 1340 | 739.1 |
| M4-$f_c$-50 | 50 | 1000 | 0.75 | 50 | 0.033 | 114 | 920.8 | 1620 | 816.2 |
| M5-$\lambda$-0.5 | 30 | 1500 | 0.5 | 50 | 0.033 | 114 | 1028 | 1507.5 | 922.1 |
| M6-$\lambda$-1 | 30 | 750 | 1 | 50 | 0.033 | 114 | 527.6 | 753.75 | 516.3 |
| M7-$\lambda$-1.25 | 30 | 600 | 1.25 | 50 | 0.033 | 114 | 457.2 | 603 | 435.1 |
| M8-$\lambda$-1.5 | 30 | 500 | 1.5 | 50 | 0.033 | 114 | 385.6 | 502.5 | 381.0 |
| M9-$\lambda$-1.75 | 30 | 428 | 1.75 | 50 | 0.033 | 114 | 345.2 | 430.14 | 342.0 |
| M10-$\lambda$-2 | 30 | 375 | 2 | 50 | 0.033 | 114 | 316 | 376.87 | 313.3 |
| M11-$t_c$/L-0.040 | 30 | 1000 | 0.75 | 60 | 0.040 | 114 | 788 | 1206 | 764.7 |
| M12-$t_c$/L-0.047 | 30 | 1000 | 0.75 | 70 | 0.047 | 114 | 891.6 | 1407 | 877.9 |
| M13-$t_c$/L-0.053 | 30 | 1000 | 0.75 | 80 | 0.053 | 114 | 994.8 | 1608 | 991.0 |
| M14-$t_c$/L-0.06 | 30 | 1000 | 0.75 | 90 | 0.06 | 114 | 1107.2 | 1809 | 1104.2 |
| M15-$t_c$/L-0.067 | 30 | 1000 | 0.75 | 100 | 0.067 | 114 | 1171.2 | 2010 | 1217.4 |
| M16-$t_c$/L-0.073 | 30 | 1000 | 0.75 | 110 | 0.073 | 114 | 1301.6 | 2211 | 1330.5 |
| M17-$D$-90 | 30 | 1000 | 0.75 | 50 | 0.033 | 90 | 640.4 | - | 610.2 |
| M18-$D$-120 | 30 | 1000 | 0.75 | 50 | 0.033 | 120 | 688.4 | - | 664.7 |
| M19-$D$-150 | 30 | 1000 | 0.75 | 50 | 0.033 | 150 | 784 | - | 749.5 |
| M20-$D$-180 | 30 | 1000 | 0.75 | 50 | 0.033 | 180 | 888 | - | 870.3 |
| M21-$D$-210 | 30 | 1000 | 0.75 | 50 | 0.033 | 210 | 1020 | - | 1032.6 |
| M22-$D$-240 | 30 | 1000 | 0.75 | 50 | 0.033 | 240 | 1245.2 | - | 1241.4 |

In Table 11, specimen Model M1 is designated as the standard model with a concrete strength of 30 MPa, a concrete batten height of 1000 mm, a concrete batten thickness of 50 mm, and an outer diameter of column limbs measuring 114 mm. The corresponding load-deflection curves are depicted in Fig. 11.

Fig. 11(a) shows the load-deflection curves of CFST composite columns with different strengths of the concrete batten $f_c$. With increasing $f_c$, the ultimate shear capability of the composite columns increased obviously while the shear stiffness changed little. The model with $f_c$ of 20 MPa was taken as the benchmark, and with increases in $f_c$ from 20 MPa to 50 MPa in steps of 10 MPa, the ultimate shear capability of each step was increased by 39 kN (27.6%), 29 kN (16.3%) and 21 kN (9.8%). This analysis indicates that the reinforcement effect of increasing concrete strength on the ultimate shear capability of composite columns diminishes as the concrete strength rises. This observation suggests a nonlinear relationship between concrete strength and ultimate shear capability.

Fig. 11(b) illustrates the load-deflection curves of CFST composite columns with different shear-span ratios $\lambda$. With decreasing $\lambda$, the ultimate shear capability of CFST composite columns increased obviously while the shear bearing stiffness changed little. The model of $\lambda$ value was equal to 2 was taken as the benchmark, and with decreases in $\lambda$ from 2 to 0.5 in steps of 0.25, the ultimate shear capability of each step was increased by 7 kN (9.2%), 10 kN (11.7%), 18 kN (18.6%), 18 kN (15.4%), 48 kN (36.7%) and 77 kN (42.5%). The analysis revealed that the impact of the shear-span ratio on the shear capability of CFST composite columns intensifies as shear-span ratio decreases. This observation suggests a nonlinear relationship between shear-span ratio and shear capability.

Fig. 11(c) reveals the load-deflection curves of CFST composite columns with different thickness span ratios of the concrete batten $t_c$/L. With increasing $t_c$/L, the ultimate shear capability and the shear stiffness of the composite columns increased. The model with a $t_c$/L value of 0.033 was taken as the benchmark, and with increases in $t_c$/L from 0.033 to 0.073 in steps of approximately 0.07, the ultimate shear capability of each step was increased by 17 kN (8.5%), 26 kN (11.6%), 26 kN (10.4%), 28 kN (10.2%), 16 kN (5.5%) and 33 kN (10.0%). This analysis indicates that the impact of the thickness span ratio on the shear capability of CFST composite columns remains relatively constant with variations in the thickness span ratio. This suggests an almost linear relationship between the thickness span ratio and shear capability.

Fig. 11(d) shows the load-deflection curves of CFST composite columns with different outer diameters of column limbs $D$. The figure indicates that with increasing $D$, the ultimate shear capability of composite columns increased obviously. The model with a value of $D$ of 90 mm was taken as the benchmark, and with increases in $D$ from 90 mm to 240 mm in steps of 30 mm, the ultimate shear capability of each step was increased by 12 kN (7.0%), 24 kN (12.2%), 26 kN (11.7%), 33 kN (12.9%) and 56 kN (18.1%). This analysis reveals that the impact of the outer diameter of column limbs on the shear capability of composite columns becomes more pronounced with an increase in the outer diameter of the column limbs. This observation suggests a nonlinear relationship between the outer diameter of column limbs and shear capability.

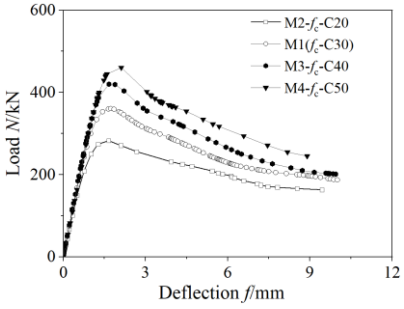


(a)The strength of batten concrete

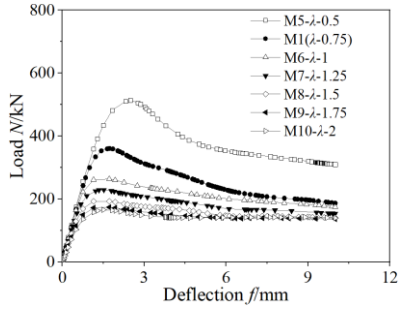


(b)Shear-span ratio

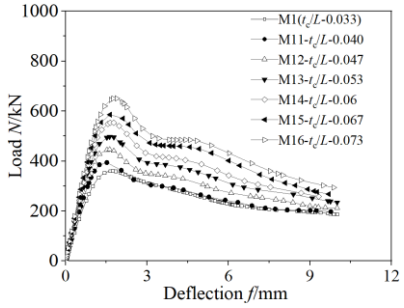


(c)Batten concrete thickness span ratio

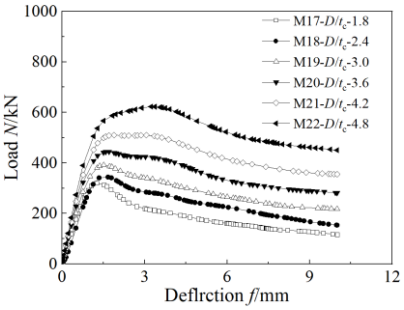


(d)The outer diameter of column limbs

**Fig. 11** Load-deflection curves of CFST composite columns

## 5. Analysis of shear bearing performance

### *5.1. Accuracy evaluation of existing calculation methods*

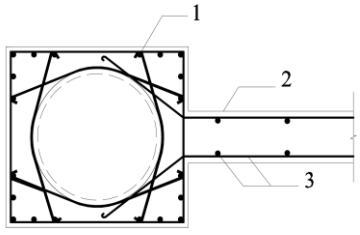


**Fig. 12** CFST shear wall structure

1: End post; 2: Wall; 3 : Distributed reinforcement

Currently, there is a scarcity of research on the calculation methodology for the shear capability of CFST composites, both domestically and internationally. The “Technical specification for steel tube-reinforced concrete column structures” delineates a structure akin to that of a CFST shear wall, comprising a combination of a concrete-filled steel tube and a concrete shear wall, as depicted in Fig. 12.

The shear capability calculation method of this structure is illustrated in Eq. (1). This formula was used to calculate the CFST composite column, and the computed result was juxtaposed against the experimental value (finite element result), as illustrated in Fig. 13.

$$V_c \le 0.25\beta_c f_c b_w h_{w0} \quad (1)$$

$V_c$: the calculation value of the shear capability of the shear wall structure; $f_c$: the compressive strength of the shear wall concrete; $b_w$: the thickness of the shear wall; $h_{w0}$: the height of the shear wall; $\beta_c$: when the concrete strength is below 50 MPa, it is 0.5; when the concrete strength is above 80, it is 0.8.

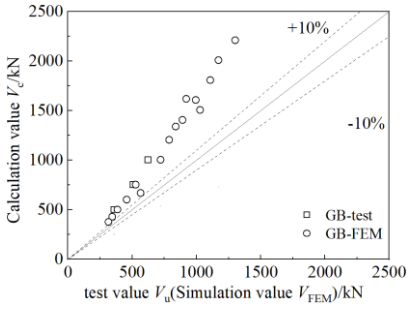


**Fig. 13** Comparison diagram of formula calculation value and test value

Fig. 13 shows that although the CFST shear wall structure is very similar to the CFST composite column, the unique reinforced concrete outer layer of the shear wall structure will provide additional shear capability. Therefore, the calculation value obtained by this method is generally larger than the test value (finite element value), and this method is not suitable for the calculation of composite columns.

Investigation into the calculation methodology for the shear resistance capability of composite columns constitutes a crucial element in the safety assessment and structural design of such composite structures. By understanding the structural carrying capability under shear loads, adjustments to the dimensions, material selection, and construction methods of the structure can be made based on the calculated results. Therefore, it is necessary to design a calculation method that meets engineering precision requirements.

### *5.2. Calculation method*

The test results in Section 1.4 are now analyzed. Firmly connecting the CFST column limbs with the concrete batten split the concrete batten was into several diagonal compression members, and the composite column reached the ultimate shear capability due to the diagonal compression shear failure of the concrete batten.

Due to the limited dataset available for analysis, this study exclusively focused on investigating the shear failure of the concrete batten in CFST composite columns, specifically identifying the failure mode as diagonal compression shear failure. The discussion of localized shear failure in joints has been reserved for subsequent research endeavors.

In alignment with the principal stress direction determined through the stress analysis in Section 2.3, the distribution of the principal stress direction in the concrete batten demonstrated a noteworthy regularity when the CFST composite column exhibited shear failure under oblique compression. Moreover, it was assumed that the diagonal compression bars formed during this failure mode could be considered parallel. Further in-depth exploration and discussion on this topic are anticipated in future studies.

Considering the restraint and load transfer effect of CFST on the concrete batten, the concrete batten and the lower concrete-filled steel pipes can be regarded as the strut-and-tie model of concrete beam shear failure [22], as illustrated in Fig. 14.

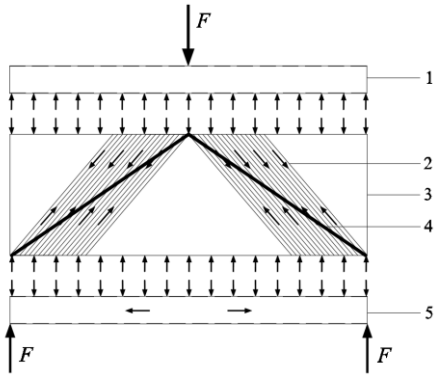


**Fig. 14** Mechanism of shear capability of composite columns

1:Upper concrete-filled steel tubular columnar limb；2:Secondary pressure bars；3:Concrete batten plate；4:Main pressure bar；5:Lower concrete-filled steel tubular column limb

This model is different from the previous strut-and-tie model. The main compression bar connecting the loading center and the reaction center of the bearing can transfer the force. At the same time, due to the constraint of the CFST column at the bottom, the parallel secondary compression bars of the concrete batten can also transfer the force.

The composite column model was slightly different from the previous strut-and-tie model. The main compression bars connecting the loading point and the supports in the concrete infix plate can transmit force. Due to the component force of the top column limb and the restraint of the bottom column limb, the parallel secondary compression bars of the concrete batten can also transmit force [23].

Based on the strut-and-tie theory and the analysis of the influence of different outer diameters of column limbs $D$ on the shear capability of composite columns in Section 2.4, the shear capability of CFST composite columns cannot be ignored.

Consequently, the culmination of the ultimate shear capability in the composite column is attributed to the collaborative effects of the main compression bars and secondary compression bars within the concrete batten, along with the CFST column limbs. The mathematical expression for calculating the shear ultimate load-bearing capability of CFST composite columns is delineated in Eq. (2).

$$V_{\mathrm{RC1}} = \frac{\xi_{\mathrm{b}}}{\xi_{\lambda} \tan \omega} f_{\mathrm{t}} t_{\mathrm{c}} b \tag{2}$$

$V_{\mathrm{RC1}}$: the shear force transferred by the main compression bars;$V_{\mathrm{RC2:}}$ the shear force transferred by the secondary compression bars; $V_{\mathrm{CFST:}}$ the shear force transferred by the CFST column limbs.

### 5.3. Main compression model of the concrete

A full-length diagonal crack manifested along the line extending from the loading point to the supports, signifying the failure of the main compression bars. The main compressive stress diffused in the middle of the concrete batten, and the shape of the main compressive bars was similar to a bottle shape, as illustrated in Fig. 15.

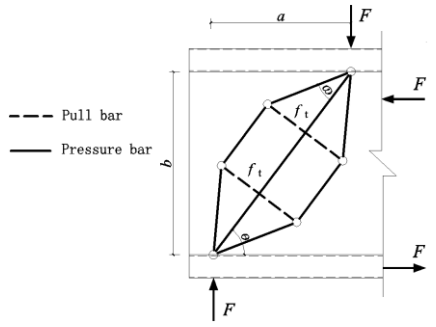


**Fig. 15** Strut and tie model of main strut

In the CFST composite column, the failure of the main compression bars of the concrete batten was caused by the pull rod of the strut-and-tie model reaching the ultimate tensile capability.

The total shear force of the bottle-shaped compression bar model was defined as $V_{\mathrm{RC1}}$. According to the analysis results of the strut-and-tie model in reference, the load-bearing capability of this part can be calculated by Eqs. (3)-(5).

$$V_{\mathrm{RC1}} = \frac{\xi_{\mathrm{b}}}{\xi_{\lambda} \tan \omega} f_{\mathrm{t}} t_{\mathrm{c}} b h \tag{3}$$

$$\xi_{\mathrm{b}} = 1.3 - 0.075 b / t_{\mathrm{c}} \quad (0.6 \le \xi_{\mathrm{b}} \le 1) \tag{4}$$

$$\xi_{\lambda} = \frac{1}{2.5 - \lambda} \quad (0.5 \le \xi_{\lambda} \le 1) \tag{5}$$

$\xi_{\mathrm{b}}$: the impact of height thickness ratio on tensile strength of the concrete batten; $\xi_{\lambda}$: the influence coefficient of shear-span ratio on shear transfer path; $f_{\mathrm{t}}$: the axial tensile strength of the concrete batten and can be calculated by $0.4 f_{\mathrm{c}}^{0.5}$ ;$f_{\mathrm{c}}$: axial compressive strength of the concrete batten;$b$: the width of the concrete batten; $t_{\mathrm{c}}$: the thickness of the concrete batten; $\omega$: the diffusion angle of the main compression bars and compression bars with the shear force transferred indirectly; $\lambda$: shear-span ratio.

### 5.4. Secondary compression model of the concrete batten

The simplified model of the diagonal compression field of the concrete battened secondary compression bars is illustrated in Fig. 16. Through the equilibrium condition, the derivation of the calculation method for the load-bearing capability of the secondary strut is encapsulated in Eq. (6):

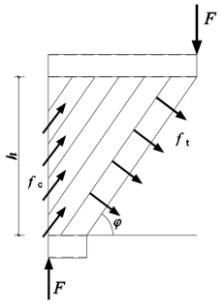


**Fig. 16** Diagrammatic diagram of calculation of diagonal compression field model of secondary compression bar

$$V_{\mathrm{RC2}} = f_{\mathrm{t}} t_{\mathrm{c}} b h \cos \varphi / \sin \varphi \tag{6}$$

$\varphi$: the angle between secondary oblique pressure bars (zones) and horizontal direction in baroclinic field model, and it has a value of 45°; $\sigma_{\mathrm{c}}$ : the compressive stress of the secondary oblique pressure bars (zones) in the baroclinic field model; $\sigma_{\mathrm{t}}$ : the tensile stress between each diagonal compression bars(zones).

### 5.5. Calculation method for the shear capability of CFST column limbs

The shear capability calculation method for CFST column limbs, as detailed in references [24-25] and expressed in Eqs. (7)-(8), was employed. The computed shear capability of the column limbs was then juxtaposed with the shear capability of the concrete batten. The comparison included experimental and finite element values, and the results are depicted in Fig. 17.

$$V_{\mathrm{uCFST}} = 0.71 f_{\mathrm{sc}} A_{\mathrm{sc}} \tag{7}$$

$$f_{\mathrm{sc}} = 1.547 f \frac{\alpha_{\mathrm{sc}}}{\alpha_{\mathrm{sc}} + 1} \tag{8}$$

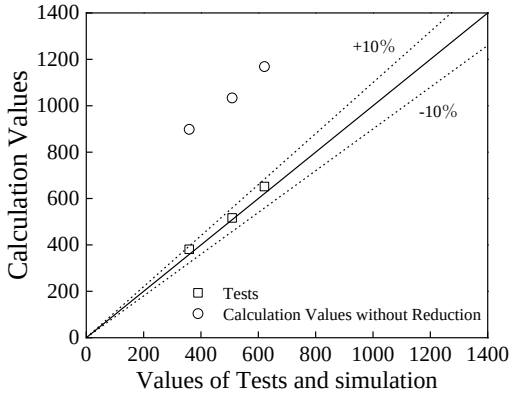


**Fig. 17** Comparison chart of concrete filled steel tubular shear without reduction

Based on the examination of the test failure phenomenon and the findings illustrated in Fig. 17, it was observed that upon reaching the ultimate shear capability, the concrete batten exhibited cracking and crushing, while the CFST column limbs did not reach the shear limit. This observation suggests that the shear capability of the CFST column limbs was not fully utilized. Consequently, a reduction factor is incorporated into the calculation method for the ultimate shear capability of column limbs in composite columns, as delineated in Eqs. (9)-(10).

$$V_{\mathrm{CFST}} = \mu V_{\mathrm{uCFST}} \tag{9}$$

$$\mu = V_{\mathrm{CFST}} / V_{\mathrm{uCFST}} \tag{10}$$

$V_{\mathrm{uCFST}}$: the shear capability of CFST; $f_{\mathrm{sv}}$: the shear strength of CFST; $A_{\mathrm{sc}}$: the sectional area of CFST; $\alpha_{\mathrm{sc}}$: the steel ratio of CFST; $f_{\mathrm{sc}}$: the design value of compressive strength of steel; $\mu$: the reduction factor of the shear capability of CFST column limbs, which can be calculated by Eq. (9); $V_{\mathrm{CFST}}$: obtained by extracting the finite element values of the shear capability of the column limbs.

The shear capability of CFST column limbs has a high correlation with the outer diameter of the limbs *D*. With an increase in *D*, the reduction factor $\mu$ decreases, which indicated that the effect of *D* should be considered in the calculation of $\mu$, as illustrated in Fig. 18.

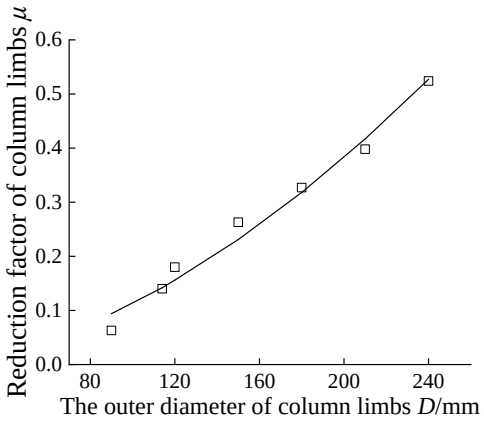


**Fig. 18** Regression analysis of shear capability reduction factor

Through the regression analysis of *D* and $\mu$, the relationship between them was calculated by Eq. (11).

$$\mu = 1.358\times10^{-4.6}\times D^{1.76} \tag{11}$$

*5.6. Simplified calculation method*

According to the American ACI code, if the main compression bars occur at the same time as the secondary compression bars, the minimum angle between the compression bar and the pull rod is 25° and shear-span ratio should be less than 2. If shear-span ratio was more than 2, then no main compression bars occurred in the concrete batten of the CFST composite column. The load was mainly transferred by the secondary compression bars. Therefore, the calculation method introduced in this study is applicable for cases in which shear-span ratio should be less than 2, as illustrated in Eq. (12).

$$V_{\mathrm{c}} = \frac{f_{\mathrm{t}} t_{\mathrm{c}} bh\cos\varphi_1}{\sin\varphi_1} + \frac{\xi_{\mathrm{b}}}{\xi_\lambda \tan\alpha} f_{\mathrm{t}} t_{\mathrm{c}} bh + 0.71\mu f_{\mathrm{sv}} A_{\mathrm{sc}} (\lambda < 2) \tag{12}$$

Eq. (12) is too tedious to apply to engineering applications; therefore, this paper carries out a simplified analysis of this formula. Eq. (9) and Eq. (12) show that parameters $f_{\mathrm{t}}$, $t_{\mathrm{c}}$ and *h* were common between the calculation methods for the shear capability of the shear force $V_{\mathrm{RC1}}$ transmitted by the main compression bars and the shear force $V_{\mathrm{RC2}}$ transmitted by the secondary compression bars. After extracting the common factors, the following Eq. (13) can be obtained.

$$\begin{aligned} V_{\mathrm{c}} &= V_{\mathrm{RC1}} + V_{\mathrm{RC2}} + V_{\mathrm{CFST}} \\ &= \left(\frac{\cos\varphi_1}{\sin\varphi_1} + \frac{\xi_{\mathrm{b}}}{\xi_\lambda \tan\alpha}\right) f_{\mathrm{t}} t_{\mathrm{c}} bh + 0.71\mu f_{\mathrm{sv}} A_{\mathrm{sc}} \\ &= \kappa f_{\mathrm{t}} t_{\mathrm{c}} b + 0.71\mu f_{\mathrm{sv}} A_{\mathrm{sc}} \ (\lambda < 2) \end{aligned} \tag{13}$$

A good linear relationship is observed between $\kappa$ and $\lambda$, as illustrated in Fig. 19. A regression analysis was performed, and the relationship between $\kappa$ and $\lambda$ is illustrated in Eq. (14)

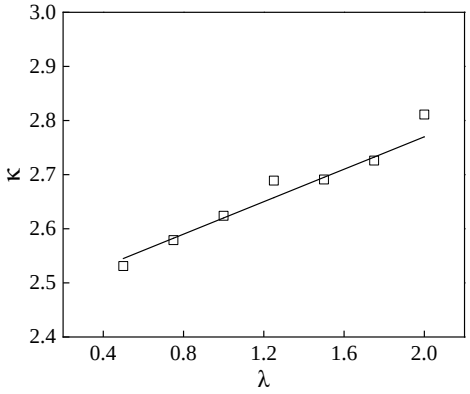


**Fig. 19** Regression analysis of parameters of practical calculation formula

$$\kappa = \left(0.15\lambda + 2.47\right) \tag{14}$$

*5.7. Verification of the calculation method*

The parameters setting and shear capability of the tests and simulation models involved in this paper were illustrated in table1 and table 3. The calculated values obtained according to the calculation method in this paper are compared with the test values or simulation values of similar structures of many scholars, as illustrated in Fig. 20.

Comparisons between the calculated value and the experimental value (Simulation value) are illustrated in Table 2 (Table 3) and Fig. 20. The figure shows that the discrete points composed of the test value (finite element value) and the calculated value obtained by the strut-and-tie theory calculation method and the simplified practical calculation method basically fell near the straight line of $V_{\mathrm{c}}$=$V_{\mathrm{u}}$ ($V_{\mathrm{FEM}}$) and the deviation was generally controlled within 10%.

The data presented in Tables 2 and 3 demonstrate that the average ratios between the test values and the calculated values obtained through the strut-and-tie theory calculation method and the simplified practical calculation method are 1.007 and 1.038, respectively. Their respective standard deviations are 0.023 and 0.020. These results indicate a close agreement between the theoretical and simplified calculation values with the test values, underscoring the high accuracy of the proposed methods in this paper.

This paper introduces theoretical and simplified calculation methods that meet engineering precision requirements. These methods allow designers to

adjust the dimensions, material selection, and construction methods of the structure based on the calculation results, thereby reducing engineering costs. Simultaneously, in the simplified calculation method, the complexity of the calculations is reduced through a fitting process, resulting in models that are easier to understand or analyze. While ensuring the safety of structural design, this significantly enhances the efficiency of load-bearing capability calculations.

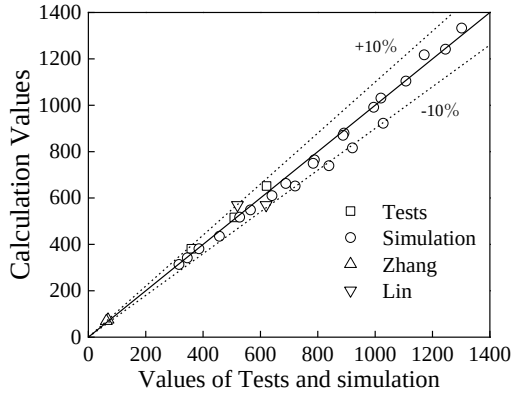


(a) Comparison of theoretical calculation methods

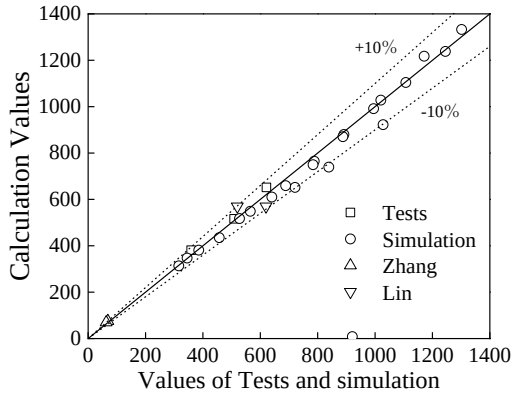


(b) Comparison of simplify calculation methods

**Fig. 20** Comparison diagram of formula calculation value and test value

## 6. Conclusions

This study encompassed shear performance tests of CFST composite columns with varying shear-span ratios, finite element expansion parameter analyses, and an investigation into the load-bearing capability calculation method. The key findings are summarized as follows:

(1) The shear failure mode of CFST composite columns falls into two categories: shear failure under oblique compression and localized failure. The former is typic ally characterized by multiple shear diagonal cracks in concrete battens, more common in composite columns with larger shear-span ratios. The latter is typified by concrete spalling at the junctures of column limbs and concrete battens, often observed in composite columns with smaller shear-span ratios and a less firm connection between column limbs and concrete battens. The load-deflection curves of CFST composite columns are segmented into three stages: elasticity, plasticity, and declining load-bearing capability.

(2) The FEMs constructed in this study accurately simulated the entire shear failure process of CFST composite columns. The findings demonstrated that the shear capability of CFST composite columns escalates with the rise in batten concrete strength and thickness span ratio. Nevertheless, augmenting the outer diameter of the column limbs leads to a more pronounced enhancement in the shear capability of composite columns. Notably, composite columns demonstrate an increased shear capability when the shear-span ratio is minimized, contingent upon a robust connection between the column limb and batten. Therefore, enhancing the thickness span ratio of the batten concrete or the outer diameter of the column limbs can optimize the shear performance of CFST composite columns.

(3) Based on the analysis of CFST composite columns and the strut-and-tie model of the batten concrete, the ultimate shear capability of CFST composite columns is provided by the primary and secondary compression bars of the concrete batten and the CFST column limbs. Additionally, the reduction factor of CFST column limbs was calculated. Ultimately, the theoretical and simplified practical calculation methods, more accurate than the existing calculation methods for similar structures, were established. The deviation in these two calculation methods can be confined to within 10%, rendering the proposed method a reliable reference for the engineering application of CFST composite columns.

## Acknowledgments

The research presented in this paper was supported by the National Natural Science Foundation of China (Grant No. 51578756) and by the Program for Innovative Research Teams in Science and Technology in Fujian Province University. The support is gratefully acknowledged.

## References

[1] Baltay, P. and Gjelsvik, A. Coefficient of friction for steel on concrete at high normal stress. Journal of Materials in Civil Engineering, 1990, 2(1): 46-49.
[2] Chen, B.C. and Wang, T. Overview of concrete filled steel tube arch bridges in China. Practice Periodical on Structural Design and Construction, ASCE, 2009, 14(2):70-80.
[3] Chen, B.C., Yan, Q.L. and Xue, J.Y. Experimental study on compressive property of concrete-filled steel tubular hybrid stub columns. Journal of Building Structures, 2017, 37(5):82-91.
[4] Chen, B.C., Lai, Z. C., Yan, Q. L., Amit, H. Varma. Experimental behavior and design of CFT-RC short columns subjected to concentric axial loading. Journal of Structural Engineering, 2017, 143 (11) :04017148.
[5] Ou, Z.J. and Chen, B.C. Experimental research on influence of eccentrically ratio on concrete filled steel tubular laced columns compressed eccentrically. Journal of Building Structures, 2007, 28(S1):184-190.
[6] Zhang, W., Chen, Z., Xiong, Q. Performance of L-shaped columns comprising concrete-filled steel tubes under axial compression [J]. Journal of Constructional Steel Research, 2018, 145: 573-590.
[7] Xiong Q, Zhihua C, Jingfu K, et al. Experimental and finite element study on seismic performance of the LCFST-D columns [J]. Journal of Constructional Steel Research, 2017, 137(oct.): 119-134.
[8] Xiong Q, Chen Z, Zhang W, et al. Compressive behaviour and design of L-shaped columns fabricated using concrete-filled steel tubes [J]. Engineering Structures, 2017, 152(dec.1): 758-770.
[9] Yong, X., Li, X.L. Experimental study and numerical analysis on seismic behaviors of RC frame- frame truee composite wall. Chinese Journal of Applied Mechanics, 2024, 1-10.
[10] Yadav, R., Chen, B.C., Yuan, H.H., Lian, Z.B. Experimental investigation of CFST-RC bridge piers under cyclic loading. Procedia Engineering.2017, 173: 1723- 1730.
[11] Yadav, R., Chen, B.C., Yuan, H.H., Lian, Z.B. et al. Effect of width of RC-web on seismic performance of CFST–RC pier: experiments. Iranian Journal of Science and Technology, Transactions of Civil Engineering, 2019, 43:685-696.
[12] Yadav, R., Chen, B.C., Yuan, H.H., Lian, Z.B. et al. Analytical behavior of CFST bridge piers under cyclic loading. Procedia Engineering, 2017, 173:1731-1738.
[13] Zhou, J., Li, P., Guo, N.F. Seismic performance assessment of a precast concrete-encased CFST composite wall with twin steel tube connections. Engineering Structures, 2020, 207: 110240.
[14] Zhang, J., Li, X., Yu, C., Cao, W. Cyclic behavior of high-strength concrete shear walls with high-strength reinforcements and boundary CFST columns. Journal of Constructional Steel Research, 2021, 182: 106692.
[15] Fan, J.S., Liu, C., Yang, Y., Bai, Y., Wu, C. Shear capability of 3D composite CFT joints subjected to symmetric loading condition. Journal of Constructional Steel Research, 2015, 112: 242-251.
[16] Wei, J.G., Luo, X., Lai, Z.C., Amit, H. Varma. Experimental behavior and design of high-strength circular concrete-filled steel tube short columns. Journal of Structural Engineering (ASCE), 2020, 146(1): 04019184-1-16.
[17] Yan, Q. L. Research on the Ultimate Load Carrying Capability of Concrete-filled Steel Tubular Composite and Hybrid Columns. Ph.D. Dissertation, Fuzhou University, Fuzhou. 2017.
[18] Olofsson, U. and Holmgren, M. Anvandning av en servo-hydraulisk drag- vridningsmaskin for friktionsmatning mellan stal och betong vid laga glidhastigheter. Swedish National Testing and Research Institute, Boras, Sweden. 1992.
[19] Wu, Q.X., Huang, Y.F., Chen, B.C. Nonlinear aseismic performance of lightweight bridge with CFST composite truss girder and lattice pier. Engineering Mechanics, 2015, 32 (12) :90-98+116.
[20] Wang, J. J., Nie, X., Bu, F. M., Tao, M. X., & Fan, J. S. Experimental study and design method of shear-dominated composite plate shear walls. Engineering Structures, 2020, 215: 110656.
[21] Liao Y.B., Experiment and research on concrete filled steel tubular laced columns under axial compression, Tsinghua University, Beijing. 2009.
[22] Liu, W. Research on Mechanism of Concrete-Filled Steel Tubes Subjected to Local Compression. Ph.D. Dissertation, Fuzhou University, Fuzhou. 2005.
[23] Lin, Y. Experimental investigation and finite element analysis of RC simply supported deep beam. Hunan University, Hunan. 2011.
[24] Zhang, X.J. and Hu, X.S. Analysis for Shear Sterength of Reinfored Concrete Framed Columns. WuHan Urban Consteuction Institute. 1995(12).
[25] Wang, M.P. and Wang, X.T. Shear strength calculation of reinforced concrete beams with small shear-span ratio. Journal of Building Structures, 1996(05):73-78.

**Advanced Steel Construction** – Vol. 20 No. 3 (2024) 241–252
**DOI:**10.18057/IJASC.2024.20.3.4


# RESEARCH ON BENDING PERFORMANCE AND BILINEAR MODEL OF AN IMPROVED BOLT-COLUMN (BC) JOINT

Zhi-Cheng Xiao, Ren Li, Hui-Jun Li *, Guang-Hong Luo and Bao-Hui Li

*College of Water Resources and Architectural Engineering, Northwest A&F University, Yangling 712100, Shaanxi, China*
** (Corresponding author: E-mail: lihuijun2893118@163.com)*

**ABSTRACT**

The semi-rigid bolt-column (BC) joint, which is a component of large-span single-layer reticulated structures, demonstrates a considerable application potential. In this study, the BC joint is innovatively modified using two flanges, one web and two additional high-strength bolts. The comparative analysis between the original and improved joints reveals a notable enhancement in bending performance, including 62.59% increase in initial rotational stiffness, 116.82% increase in initial yield moment, and 87.57% increase in ultimate moment. Subsequently, a total of 66 finite element (FE) models of the improved BC joint, incorporating varying parameters such as bolt diameter, bolts' vertical distance, flange thickness, front plate thickness, and column node thickness, are conducted to systematically evaluate its bending performance. Furthermore, the effect of axial force on the bending performance is discussed. Finally, a bilinear model is developed to predict the moment-rotation relationships of improved BC joint.

**ARTICLE HISTORY**

Received: 13 January 2024
Revised: 18 February 2024
Accepted: 20 February 2024

**KEYWORDS**

Improved BC joint;
Parametric analysis;
Bending performance;
Failure mode;
Bilinear model



## 1. Introduction

The reticulated shell, a common form of large-span structures, is widely applied in large public buildings such as terminals, stadiums and exhibition halls. However, the application of assembled reticulated shells is limited in engineering due to the assumption of ideal hinges for assembled joints despite their advantages including convenient and high-precision construction and reasonable force. In reality, most of the joints exhibit bending performance and semi-rigid features.

As research progresses, an increasing number of scholars have discovered the semi-rigid behavior of assembled joints. Ma *et al* [1-2] and Fan *et al* [3] introduced a new type of semi-rigid connection known as the bolt-column joint, enabling efficient connections with members of H, I, and rectangular section. A series of experimental and numerical tests were conducted by Ma [1-2] to investigate the impact of geometric parameters on the mechanical performance of the joint. Based on Eurocode 3 (EC3) component method, a trilinear mathematical model was developed for predicting its the moment-rotation relationship. Fan [3] utilized optimization analysis in FE models to determine the rotational dimensions of BC joint components, following the principle of 'strong connection and weak plate. However, the BC joint proposed by them, despite its merits, exhibits structural deficiencies in cone head design. The limited bending performance of this joint may constrain its application.

In addition, Han *et al* [4] proposed both theoretical and practical equations to calculate the initial stiffness of welded hollow spherical joints, while also presented a mechanical model that considers the joint's stiffness characteristics. Comparison with experimental results showed an average difference of 8% for the mechanical model's prediction of the load-rotation curve's initial slope, and an average error of 7% for estimating the ultimate bearing capacity. Yan *et al* [5] presented a comprehensive investigation of the welding process involved in connecting hollow spherical joints to pipes, with a specific focus on the welds. This study included an analysis and summary of the distribution pattern and specific mode of residual stress in these joints, while also parametrically investigating how variations in joint configuration dimensions impact the distribution of welding residual stress. Mashrah *et al* [6] proposed two novel types of socket joints: a steel dovetail joint without teeth pattern and a steel dovetail joint with teeth pattern. Experimental and numerical tests were conducted to investigate the bearing capacities and failure modes of these new joint systems under axial tensile loads. According to Fan *et al* [7-8], numerical simulations can provide valuable technical guidance for the design and application of bolt-ball joints and other semi-rigid joints, through comparison between a three-dimensional solid model generated using the ANSYS package and experimental results. Additionally, tests were conducted to examine the mechanical behavior of socket joints and bolt-ball joints. The findings indicated that the initial bending stiffness of these joints is influenced by axial compressive force, while its impact on the bending moment capacity varies across different joint types. Yu *et al* [9] investigated the impact of different parameters related to the bolt-ball joint, such as bolt size, initial tightening force, thickness of cone tail wall and sleeve, on its ability to withstand bending; also the study developed a power function model to establish the relationship between moment and rotation for the bolt-ball joint. Xue *et al* [10] investigated the bending performance of the threaded-sleeve connection through experimental methods and finite element models; additionally, this study proposed a mechanical model based on the Kishi-Chen power model to predict its moment-rotation behavior. Ma *et al* [11] demonstrated the impact of joint stiffness on the seismic behavior of semi-rigid single-layer reticulated shell structures, considering both initial imperfections and progressive material degradation. Shan [12] investigated the failure modes and maximum load-bearing capacities of hub-shaped inlay joints under different loading conditions, confirming that the minimum cross-section could serve as a suitable substitute for determining their load-bearing capacities. Han *et al* [13] have proposed a novel Assembled Hub (AH) joint that incorporates two unique connection types, and also presented theoretical solutions for the elastic stiffness and bearing capacity of this innovative joint system using the component method. Zhang *et al* [14] investigated the impact of size parameters on the bending stiffness and torsional stiffness of hub-shaped inlay joints. The failure mechanisms of the joint were examined under various stiffness conditions, and a moment-rotation relationship model for the joint was derived using regression analysis. Golea *et al* [15] introduced a novel analytical approach utilizing the component method, which was verified by conducting five physical experiments. By incorporating additional analytical equations to characterize fundamental elements of steel joints, this proposed approach expanded the scope of the component method to encompass strain-hardening and ductility considerations in components. The conventional aluminum alloy Temcor joint was enhanced by Ma *et al* [16-18] through the incorporation of a central hollow hexagonal prism and several front bolts. The study utilized FE models to explore the optimal parameters of the joint, taking into account factors such as the number and placement of front bolts, bolt-hole deviation, pretension force in bolts, thickness of the front plate, and heat-affected zone resulting from welding operations. Feng *et al* [19] presented a novel type of bolted connection known as the Ring-sleeve joint, which was specifically developed for single-layer reticulated shells. To investigate the mechanical characteristics of this joint, prototype static experiments and numerical analyses were conducted under various load conditions such as bending moment, shear force, and axial force. The results indicated that the joints exhibited three different failure modes depending on the ratio between bolt bearing capacity and tube bearing capacity. An advanced form of the Aluminum Alloy Temcor joint system, referred to as the Aluminum Alloy Penetrating joint, was introduced by Ma *et al* [20]; and the joint's resistance to rotation was evaluated through an out-of-plane static flexural test. Moreover, the mechanical behavior of T-stub aluminum joints [21-22], MERO ball joints [23-24], aluminum alloy gusset joints [25], and K-joints made from CHS aluminum profiles [26] has been comprehensively investigated in previous studies.

To enhance the bending performance of the BC joint, a novel cone structure is incorporated into the joint design. Firstly, the FE model of BC joint is validated using an existing model. Then the bending performance between the BC joint and the improved one is compared. Secondly, a parametrical study is

conducted to elucidate the general law of the improved BC joint's bending performance. Its moment-rotation curves and failure modes are obtained and discussed. Finally, a bilinear model of the moment-rotation relationship is developed and validated.

## 2. The modeling and verification of BC joints

### 2.1. Modeling

The BC joint is comprised of a hollow column node, a cone component, and two bolts with high strength, in which the cone consists of five components: a front plate, a middle plate, two side plates, and an end plate. The configuration of BC joint is depicted in Fig. 1. In this paper, the BC joint connecting rectangular member is simulated with C3D8R solid element in ABAQUS software package. The analysis of a single bar is conducted based on the structural symmetry and load conditions, as depicted in Fig. 2. In terms of material properties, Q235 steel is used for the cone part and member, while 40Cr steel and 45Mn steel is employed for high-strength bolts and column node respectively, as listed in Table 1. The contact pairs in the setting are defined as follows [1]: binding ties are applied to the surface between bolts and column node, self-contact is considered between bolts and front plate, while surface-to-surface contact is utilized for all other interfaces. As for contact properties, normal direction employs hard contact and tangent direction adopts Coulomb friction with a coefficient of 0.3. The loading surface is selected to be the end face of the member and fixed constraint is used for the cross section of the column node in order to prevent rigid body displacement during the analysis process.

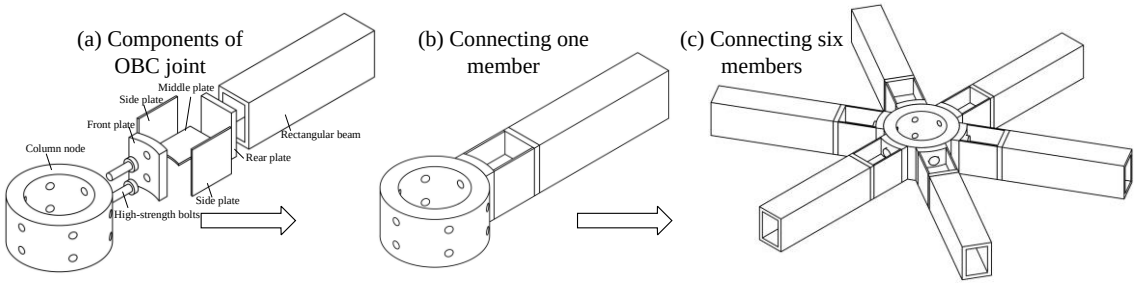


**Fig. 1** The configuration of BC joint

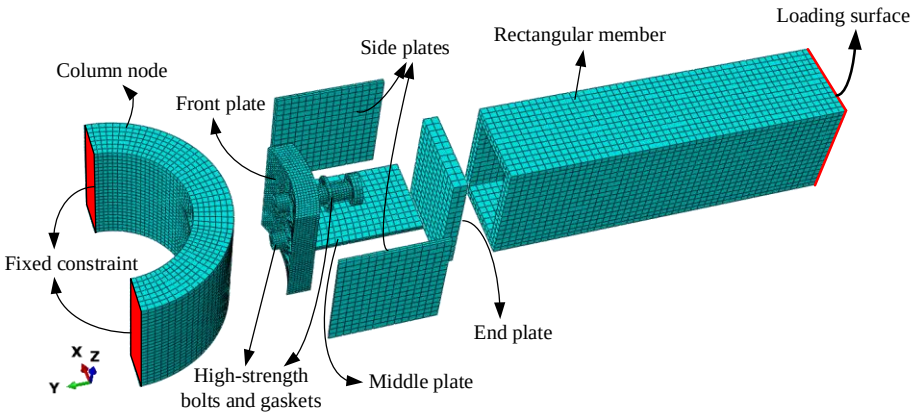


**Fig. 2** The FE model of BC joint

**Table 1**
Material properties of components [1-3]

| Components | Material | Yield strength $f_y\left(\mathrm{N/mm^2}\right)$ | Tensile strength $f_u\left(\mathrm{N/mm^2}\right)$ | Young's modulus $E\left(\mathrm{N/mm^2}\right)$ | Poisson's ratio $\mu$ |
|---|---|---|---|---|---|
| Side and middle plates | Q235 steel | 304 | 456 | 207848 | 0.33 |
| Front and end plates | | 235 | 235 | 210000 | 0.33 |
| beam | | 269 | 407 | 205569 | 0.33 |
| Bolts and gaskets | 40Cr steel | 975 | 1171 | 213302 | 0.33 |
| Column node | 45Mn steel | 355 | 355 | 210000 | 0.29 |

### 2.2. Verification

In order to verify the reliability of numerical tests in this paper, FE model is established based on the specific specimen sizes and loading conditions from previous tests and numerical models from Ma *et al* [1-2] and Fan *et al* [3]. The dimensions of the components are specified as follows: the column node has an outer radius 150mm with a thickness of 50mm; the front plate is 30mm thick and the rear plate is 20mm thick; the side plates and middle plate both have a thickness of 6mm; bolts with a diameter of 24mm are spaced at vertical interval of 78mm and subjected to a pre-tightening force of 225 kN. Additionally, load is applied at the member's end.

The bending moment-rotation curve of the BC joint is depicted in Fig. 3, illustrating its main features such as initial rotational stiffness ( $S_i$ ), initial yield moment ( $M_{inf}$ ) and ultimate moment ( $M_u$ ). Once $M_{inf}$ is reached, the joint transitions into the plastic yield phase; when reaching $M_u$ , failure is deemed to occur. Moreover, the moment and rotation are exerted from the section between rear plate and member.

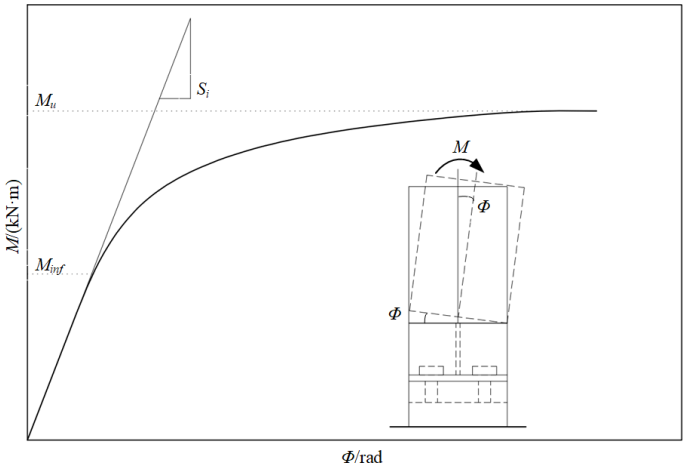


**Fig. 3** Main features of the *M*-$\Phi$ curve

The bending moment-rotation curve from Ref. [1] and numerical result obtained in this study are compared in Fig. 4. The main indexes of these curves are shown in Table 2. It can be observed that the moment-rotation curve from the FE model is in good agreement with the one from Ref. [1] in the inelastic stage, but exhibits a slight deviation in the elastic stage. The initial stiffness, initial moment and ultimate moment deviates by 7.06%, 1.93% and 0.92% respectively, all within an error margin below 10%. It can be seen that the FE model in this paper exhibits effectiveness in representing the real bending behavior of the BC joint.

## 3. Development of improved BC joint and comparison on original BC joint

### *3.1. The improved BC joint*

The Mises stress contour diagram in Fig. 4 reveals that BC joint fails due to the formation of plastic hinge in side plates, which precedes the yield failure of bolts; additionally, a significant yield area is observed in side plates and a small one is seen in bolts, indicating the underutilization of the material properties of bolts. These findings reveal the deficiencies in current dimensions and structural arrangement of BC joint.

To enhance the bending performance of BC joint, modifications are made by the removal of side plates and middle plate and the addition of flanges and web, namely rotating the cone part of BC joint. Furthermore, two additional bolts are included to ensure superior mechanical performance in cases where joint failure occurs due to bolt damage. Based on the material properties and contact pairs in Section 2.1, the finite element model of improved BC joint is established in ABAQUS package, as shown in Fig. 5.

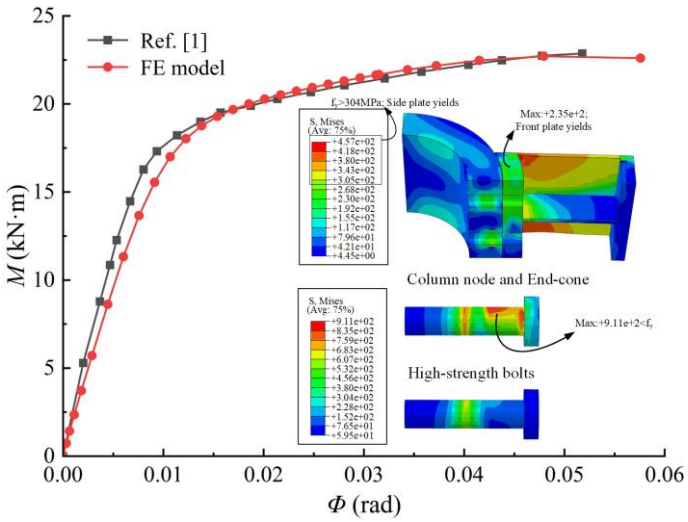


**Fig. 4** Moment-rotation curves comparison between Ref. [1] and FE model in this study

**Table 2**
Main indexes of bending moment-rotation curves of Ref. [1] and FE model

| Model | $S_i$ (kN·m/rad) | $M_{inf}$ (kN·m) | $M_u$ (kN·m) |
|---|---|---|---|
| Ref. [1] | 2062.86 | 8.79 | 22.81 |
| FE model | 1917.19 | 8.62 | 22.60 |

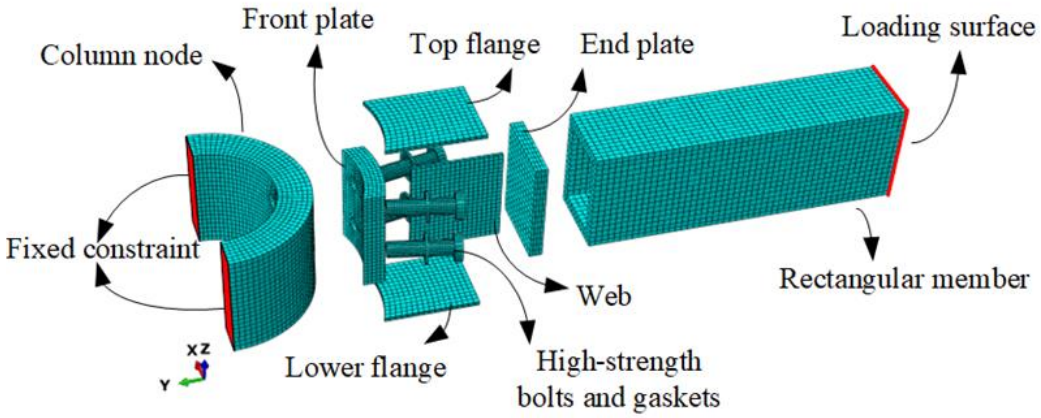


**Fig. 5** Arrangement of the improved BC joint

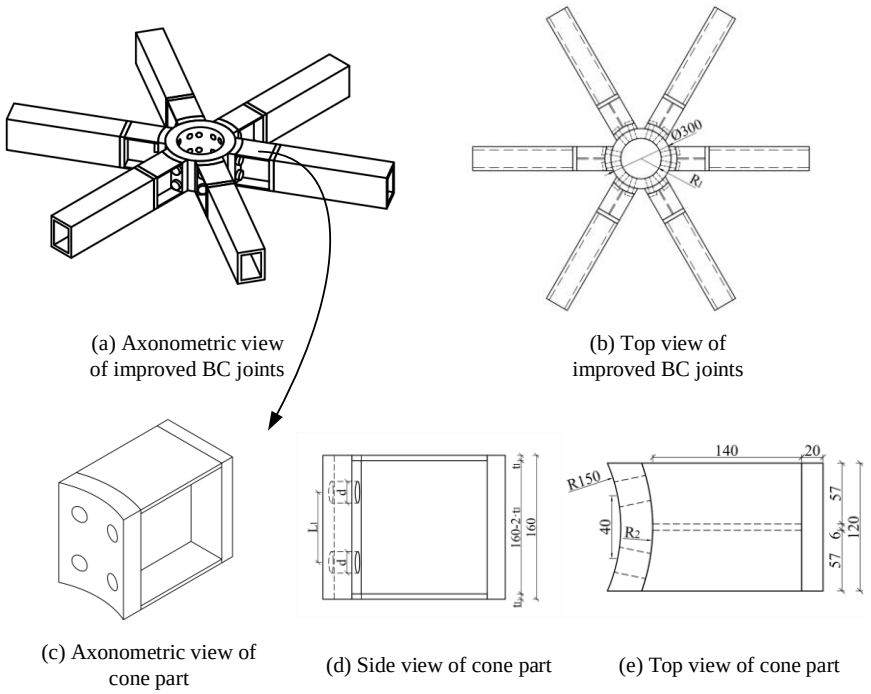


**Fig. 6** Detailed dimensions of improved BC joint

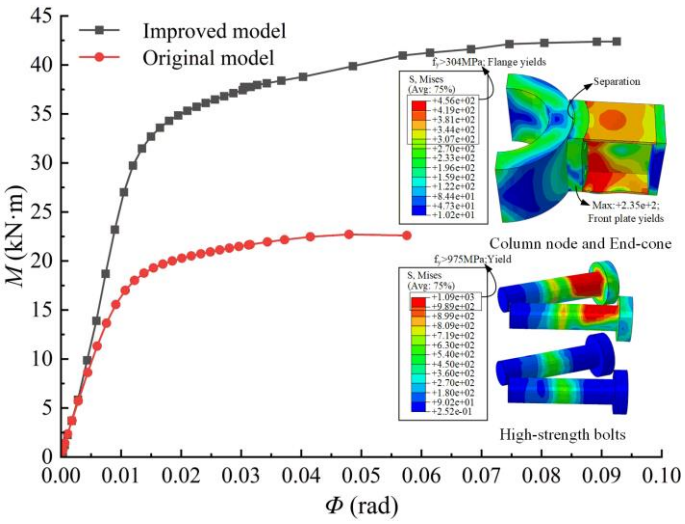


**Fig. 7** Moment-rotation curves of the improved and the original BC joints

### *3.2. Comparative analysis of bending performance between the improved and the original BC joints*

To compare the bending performance of the improved BC joint with the original one, a numerical model of the improved BC joint with dimensions and loading condition of Section 2.2 is established. The specific parameters of the joint are as follows: flange thickness is 6mm; inner diameter of column node is 100mm; outer diameter of front plate is 180mm; bolt diameter is 24mm; vertical distance between bolts is 78mm. The pre-tightening force of bolts is taken as 225kN and other parameters are shown in Fig.6.

The moment-rotation curves of BC joint and improved BC joint, and the stress distribution of the column node, cone part and bolts of the improved BC joint are shown in Fig. 7. It can be observed that the improved model exhibits a substantial enhancement in initial bending stiffness, initial moment and ultimate moment compared to the original model.

Careful examination for stress contour diagram reveals minor separation between the column node and the cone part, remarkable yield and deformation of the flanges and notable increase in stress distribution within the bolts. It indicates that the novel designed structure demonstrates superior utilization in material properties. In addition, Table 3 lists the key joint bending indexes of both the joints, it can be seen that improved BC joint exhibits 62.59% increase in initial rotational stiffness, 116.82% increase in initial yield moment, and 87.57% increase in ultimate moment.

**Table 3**
Main indexes of bending performance of the original and improved models

| Model | $S_i\,(\mathrm{kN\cdot m/rad})$ | $M_{inf}\,(\mathrm{kN\cdot m})$ | $M_u\,(\mathrm{kN\cdot m})$ |
|---|---|---|---|
| Original model | 1917.19 | 8.62 | 22.60 |
| Improved model | 3117.11 | 18.69 | 42.39 |

## 4. Parametric study on bending performance of improved BC joint

In present section, the numerical models of the improved BC joint are used for parametric studies, taking into account bolt diameter, bolts' vertical distance and flange thickness, front plate thickness and column node thickness. The specific geometric dimensions are shown in Table 4. Additionally, the effect of axial force on the bending performance of improved BC joint is discussed in the end of this section.

**Table 4**
Detailed dimensions of the numerical models

| Beam section $(\mathrm{mm})$ | Bolt diameter $d\ (\mathrm{mm})$ | Vertical distance of bolts $L_1(\mathrm{mm})$ | Flange thickness $t_1(\mathrm{mm})$ | Front plate thickness $t_2(\mathrm{mm})$ | Column node thickness $t_3(\mathrm{mm})$ |
|---|---|---|---|---|---|
| □160×120×16×16 | 21,24,27,30 | 78 | 6,8,10,12,14,16 | 30 | 50 |
| □160×120×16×16 | 24 | 72,78,84 | 6,8,10,12,14,16 | 30 | 50 |
| □160×120×16×16 | 24 | 78 | 6,8,10,12,14,16 | 20,25,30,35 | 50 |
| □160×120×16×16 | 24 | 78 | 6,8,10,12,14,16 | 30 | 30,40,50 |

### *4.1. Effect of bolt diameter and flange thickness on the bending performance of the improved BC joint*

The moment-rotation curves and stress distribution of joints with bolt diameter 21, 24, 27 and 30mm, and flange thickness 6, 8, 10, 12, 14 and 16mm are depicted in Figs. 8-9. The influence of bolt diameter and flange thickness on the bending performance of joints is analyzed specifically.

The observation reveals that, with a constant bolt diameter and an increasing flange thickness, the ultimate moment of joints exhibits a significant increase with a gradually diminishing rate, while its initial bending stiffness demonstrates a slight enhancement. Additionally, as the flange thickness increases, there is continuous development in terms of the yield area and deformation of bolts, as well as the separation between the cone part and column node.

Taking the joints with bolt diameter of 21mm as an example, the failure modes of improved BC joint is discussed as follows. When $t_1 \le 8\mathrm{mm}$, severe deformation occurs in both front plate and flanges before separation occurrence between cone part and column node is clear. The plastic hinge formation during first half of cone part results the failure of joints. When $8\mathrm{mm} < t_1 \le 12\mathrm{mm}$, front plate and compression flange still experience significant damage and the separation between front plate and column node is apparent, which means tensile bolt's surface deformation greatly increases. Hence, joints fail due to simultaneous yielding among front plate, flanges and bolts. When $t_1 > 12\mathrm{mm}$, the deformation of flanges is small, and the joints damage attributed to the tensile failure of bolts.

The Mises stress contour diagrams of joints with different bolt diameters show that the yield area of front plate decreases gradually by increasing bolt diameter. It can be attributed to the fact that bolts share more bending moment, and the bending performance of flanges is made better use of. In the case where flange thickness (such as $t_1 = 8\mathrm{mm}$ and $t_1 = 12\mathrm{mm}$) remains constant, as the bolt diameter increases, so does the ultimate moment. However, when $d > 27\mathrm{mm}$, bolt diameter affects the moment-rotation curves slightly.

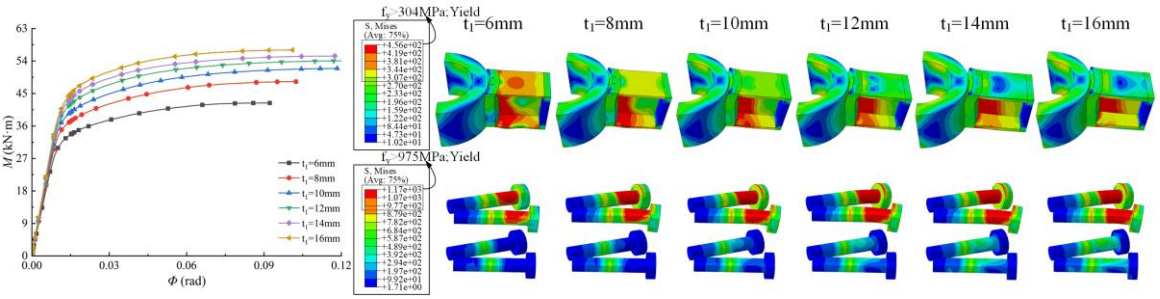


(a) Bolt diameter 21mm

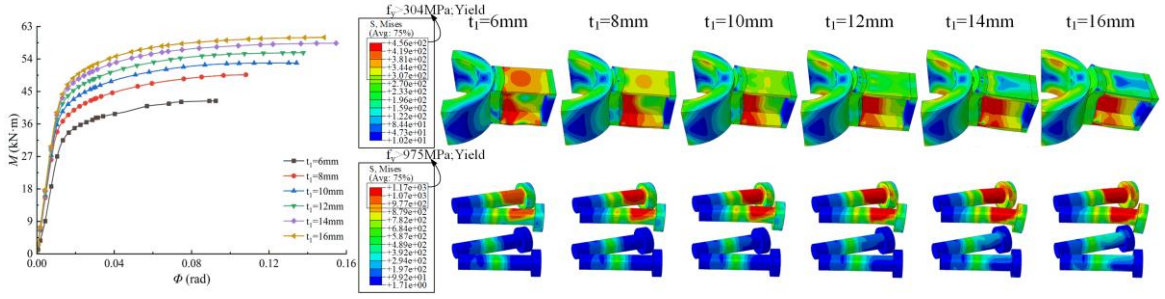


(b) Bolt diameter 24mm

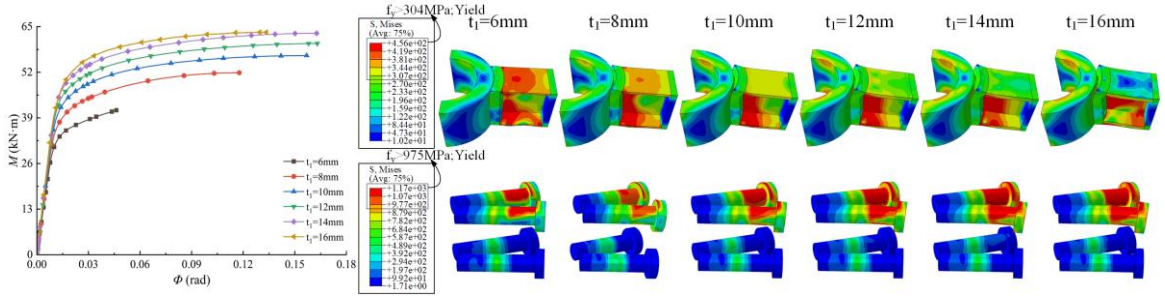


(c) Bolt diameter 27mm

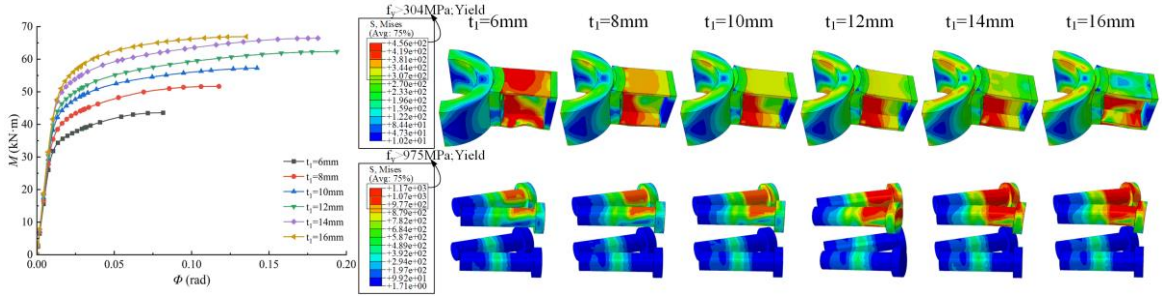


(d) Bolt diameter 30mm

**Fig. 8** Moment-rotation curves and stress distribution of joints with different bolt diameters and flange thicknesses

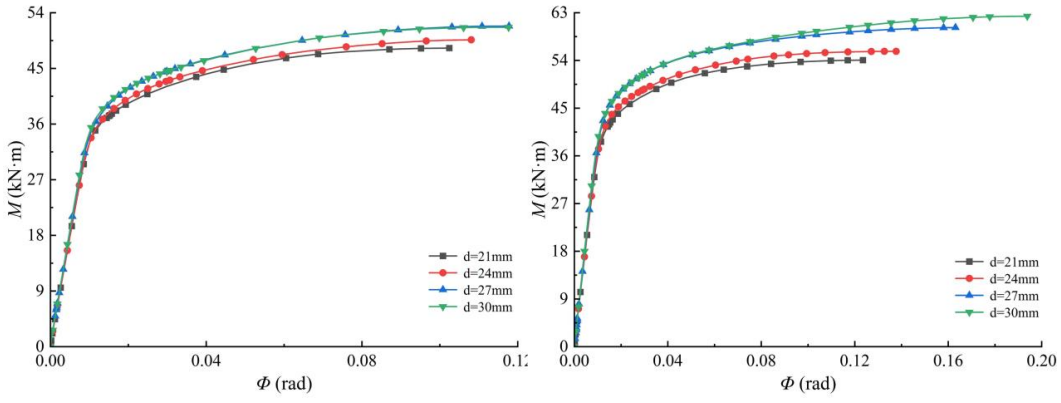


(a) $t_l$=8mm (b) $t_l$=12mm

**Fig. 9** Moment-rotation curves with flange thicknesses of 8mm and 12mm and different bolt diameters

*4.2. Effect of vertical bolt spacing and flange thickness on the bending performance of the improved BC joint*

For the improved BC joint, three bolts' vertical distances, 72, 78 and 84mm, and six flange thicknesses, 6, 8, 10, 12, 14 and 16mm, are considered in the examination. Figs. 10-11 show the moment-rotation response and stress distribution at the column node, cone part and bolts of joints. It can be concluded that the general law of change in the moment-rotation curve and stress distribution of joints is similar to the Section 4.1 by increasing flange thickness.

From the stress distribution of joints, it can be observed that the stress reduction occurs in bolts with increasing vertical distance of bolts; meanwhile the separation between column node and front plate narrows. It indicates that increasing vertical distance of bolts can enhanced the bending performance of joints. Furthermore, as flange thickness (take $t_1 = 8\text{mm}$ and $t_1 = 12\text{mm}$ as examples) stay the same, by increasing bolts' vertical distance, the ultimate moment enhances stably; however, it exhibits little influence on initial bending stiffness.

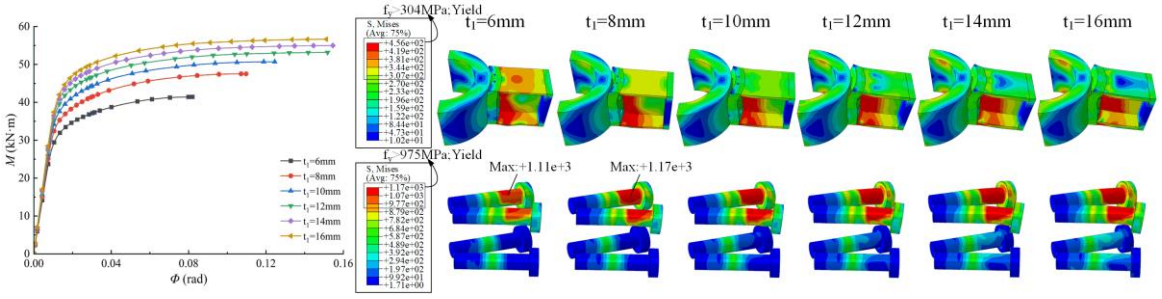


(a) Bolts' vertical distance 72mm

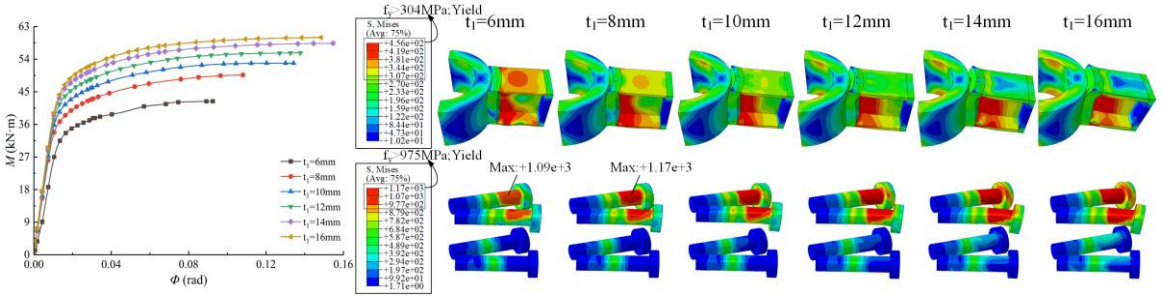


(b) Bolts' vertical distance 78mm

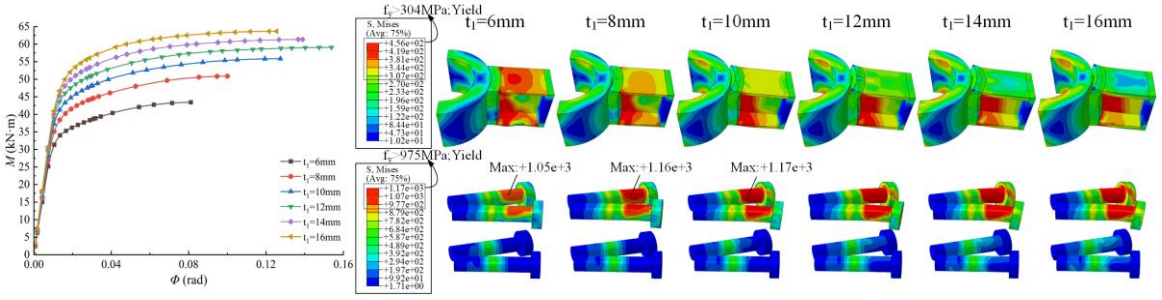


(c) Bolts' vertical distance 84mm

**Fig. 10** Moment-rotation curves and stress distribution of joints with different bolts' vertical distances and flange thicknesses

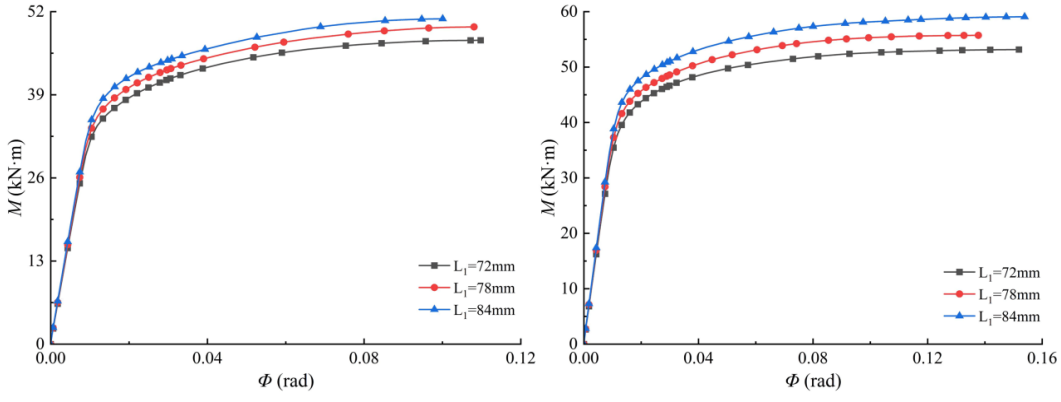


(a) $t_1$=8mm (b) $t_1$=12mm

**Fig. 11** Moment-rotation curves with flange thicknesses of 8mm and 12mm and different vertical distances of bolts

*4.3. Effect of thicknesses of front plate and flange on the bending performance of the improved BC joint*

The front plate thickness of 20, 25, 30 and 35mm and the flange thickness of 6, 8, 10, 12, 14 and 16mm are considered in numerical models. Moment-rotation curves and stress distribution of joints are shown in Figs. 12-13. In the figures, the bending performance increases significantly with increasing flange thickness while keeping a constant thickness of front plate. However, when $t_2 \geq 25\text{mm}$, the flange with thickness over 14mm makes a small influence on the curve. Beyond that, the change rule of stress variation of joints is similar to Section 4.1.

Contrasting the stress distribution of the joints with different thicknesses of front plate, it can be observed that the stress and deformation of flanges increase significantly with an increasing thickness of the front plate, and the separation between column node and cone part decreases noticeably. The stress on bolts increases with a thicker front plate when $t_2 \leq 30\text{mm}$, but it decreases when $t_2 > 30\text{mm}$. Plastic hinge of the flanges is the main failure mode for the joints with front plate thickness of 35mm, except for joints with flange thickness of 16mm. What's more, when flange thickness (for example, $t_1 = 8\text{mm}$ and $t_1 = 12\text{mm}$) is unchanged, the ultimate moment of joint increases apparently and there is a great improvement when $t_2 > 30\text{mm}$.

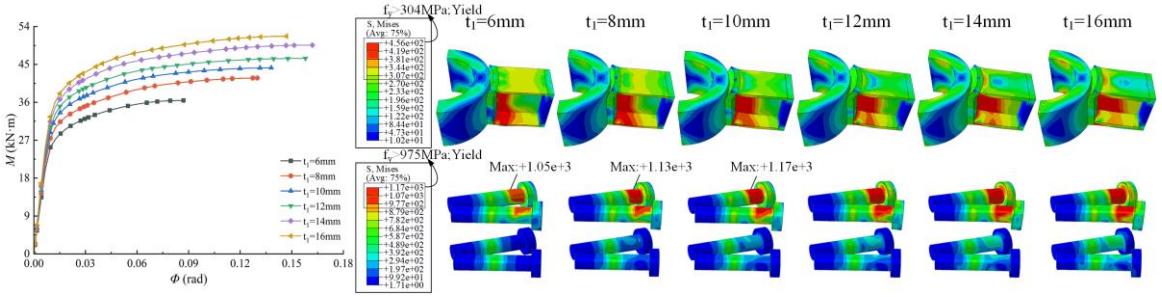


(a) Front plate thickness of 20mm

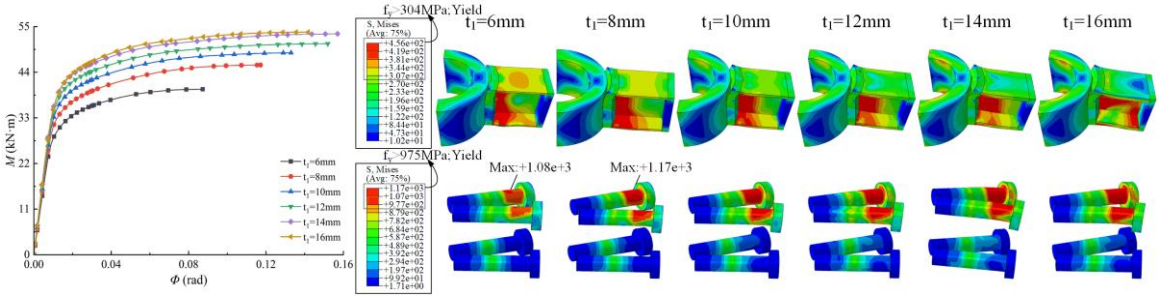


(b) Front plate thickness of 25mm

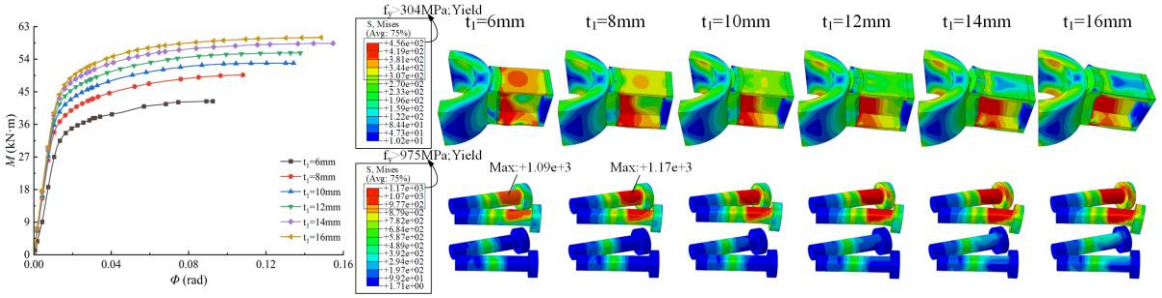


(c) Front plate thickness of 30mm

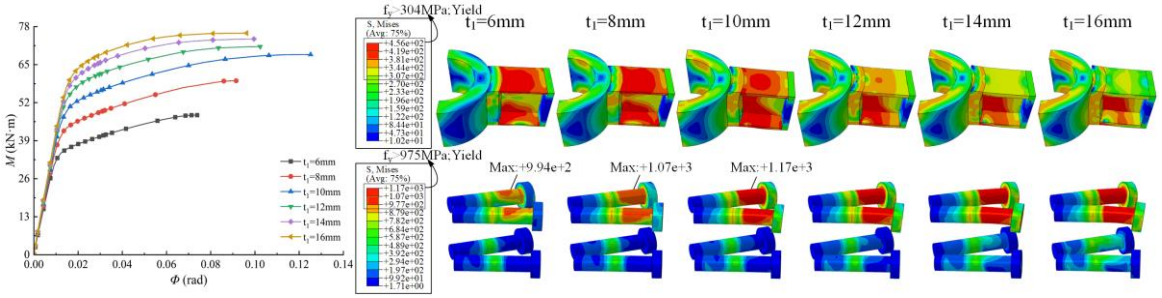


(d) Front plate thickness of 35mm

**Fig. 12** Moment-rotation curves and stress distribution of joints with different front plate's and flange's thicknesses

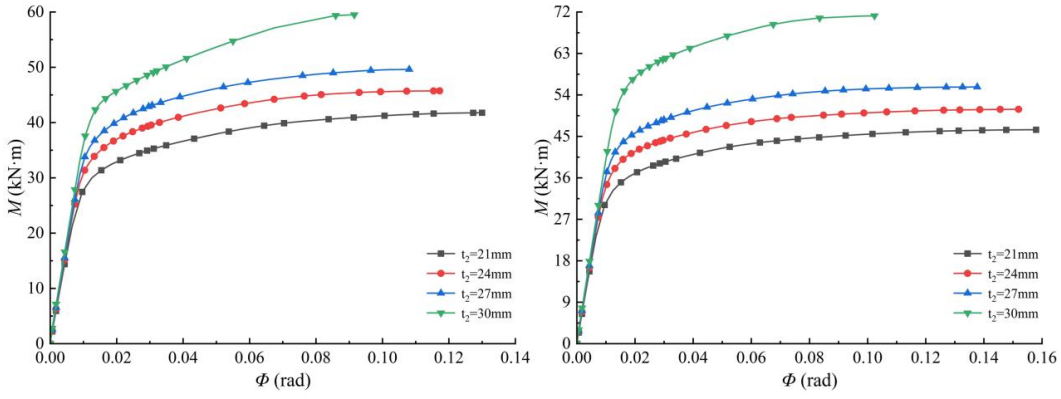


(a) $t_1$=8mm (b) $t_1$=12mm

**Fig. 13** Moment-rotation curves with flange thicknesses of 8mm and 12mm and different thicknesses of front plate

*4.4. Effect of thicknesses of column node and flange on the bending performance of the improved BC joint*

In this section, three column node thicknesses (30, 40 and 50mm) and six flange thicknesses (6, 8, 10, 12, 14 and 16mm) are taken into account. Moment-rotation curves and Mises stress contour diagrams are as shown in Figs. 14-15, it can be seen that when $t_3 \geq 40\text{mm}$, by increasing flange thickness, the change law in moment-rotation curves and stress variation is similar to Section 4.1. However, the law differs when $t_3 < 40\text{mm}$. In this condition, flanges with thickness over 10mm affect the moment-rotation curve slightly; moreover, careful observation for the stress distribution of joints reveals that the failure modes of joints are the same as $t_1 > 8\text{mm}$ : a large area of column node yields, resulting in a plastic hinge and then joint fails. The stress of bolts decreases for the reason that the formation of plastic hinge in column node occurs before full utilization of bolts. Therefore, column node with a thickness less than 40mm should be avoided. Additionally, by increasing the thickness of column node, little change occurs in the moment-rotation curve and stress distribution of joints, except for joints with column node thickness of 30mm, as shown in Fig. 15.

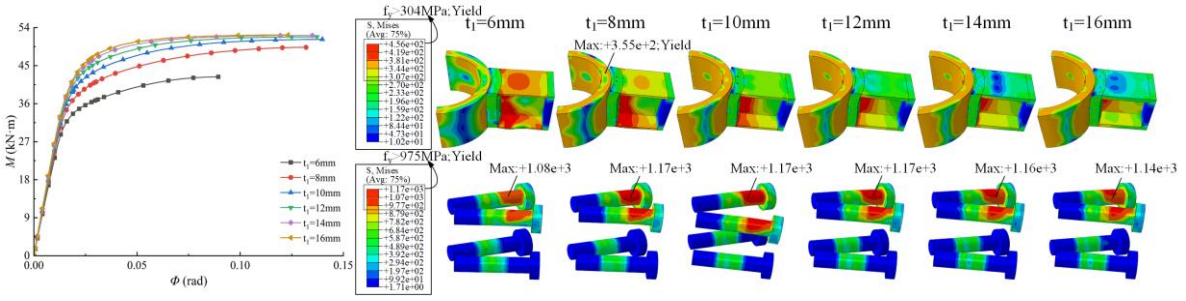


(a) Column node thickness 30mm

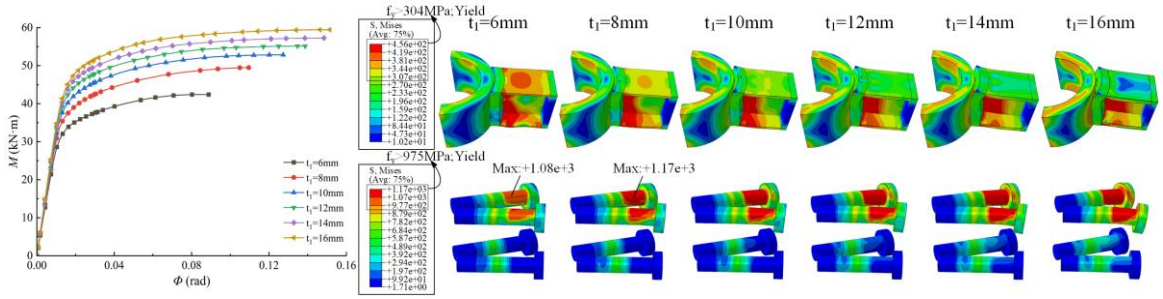


(b) Column node thickness 40mm

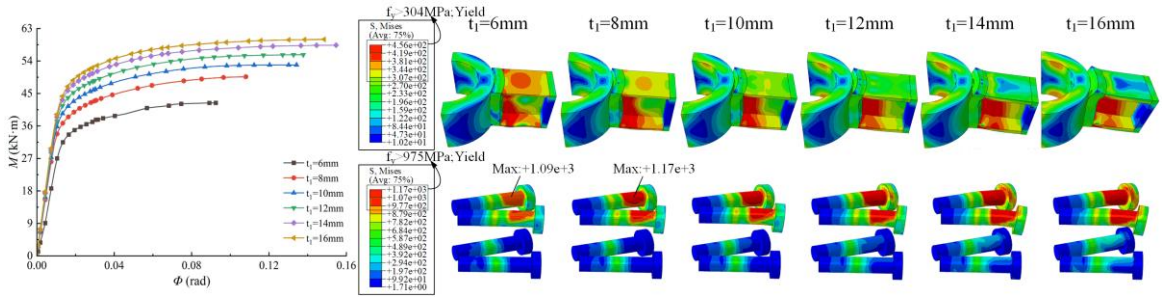


(c) Column node thickness 50mm

**Fig. 14** Moment-rotation curves and stress distribution of joints with different column node's and flange's thicknesses

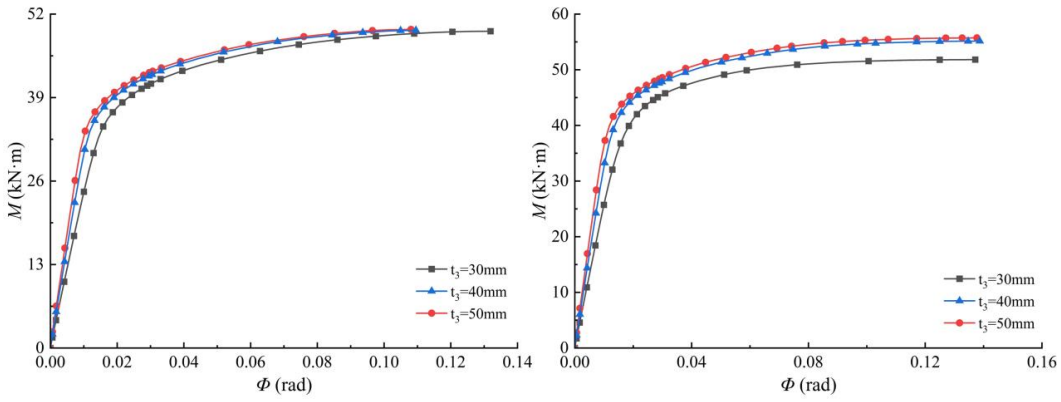


(a) $t_1$=8mm (b) $t_1$=12mm

**Fig. 15** Moment-rotation curves with flange thicknesses of 8mm and 12mm and different thicknesses of column node

*4.5. Effect of axial force on bending performance of the improved BC joint*

Taking improved BC joint with $d$=24mm, $L_1$=78mm, $t_1$=10mm, $t_2$=30mm and $t_3$=50mm as instance, the effect of axial force on its bending performance is discussed in present section. The characteristics for the bending performance of improved BC joint with prescribed axial force is illustrated in Fig. 16. In the figure, $\eta_c$ represents the ratio of the prescribed axial compression to the ultimate axial compression of joint; $\eta_t$ represents the ratio of the prescribed axial tension to the ultimate axial tension of joint. Through numerical axial force

tests on improved BC joint, the values of ultimate axial force are obtained: the ultimate axial compression is 1213.23 kN and the ultimate axial tension is 1277.57 kN. In addition, $K^{\eta_t}_{(j,ini)}/K^{0}_{(j,ini)}$ ( $K^{\eta_c}_{(j,ini)}/K^{0}_{(j,ini)}$ ) represents the ratio of initial stiffness of joints subjected to prescribed tension (compression) to that of joints without prescribed tension (compression); $M^{\eta_t}_u/M^0_u$ ( $M^{\eta_c}_u/M^0_u$ ) represents the ratio of ultimate bending moment of joints subjected to prescribed tension (compression) to that of joints without prescribed tension (compression).

The observation of this figure demonstrates that the axial compression exhibits positive effect on the bending performance when $\eta_c \le 0.3$, while it reveals negative effect when $\eta_c > 0.3$. When $\eta_c \le 0.7$, a significant enhancement occurs in the initial bending stiffness, while the initial elastic stage of the joint exhibits obvious decrease. In addition, with increasing $\eta_c$, the stress of both bolts and tensile flange shows remarkable decline, while the compressive flange exhibits the opposite trend.

For joints with prescribed tension, it demonstrates stable decline in bending performance as $\eta_t$ increasing; in addition, an increasing deformation is observed from the tensile bolts and tensile flange when joint reaches its ultimate moment.

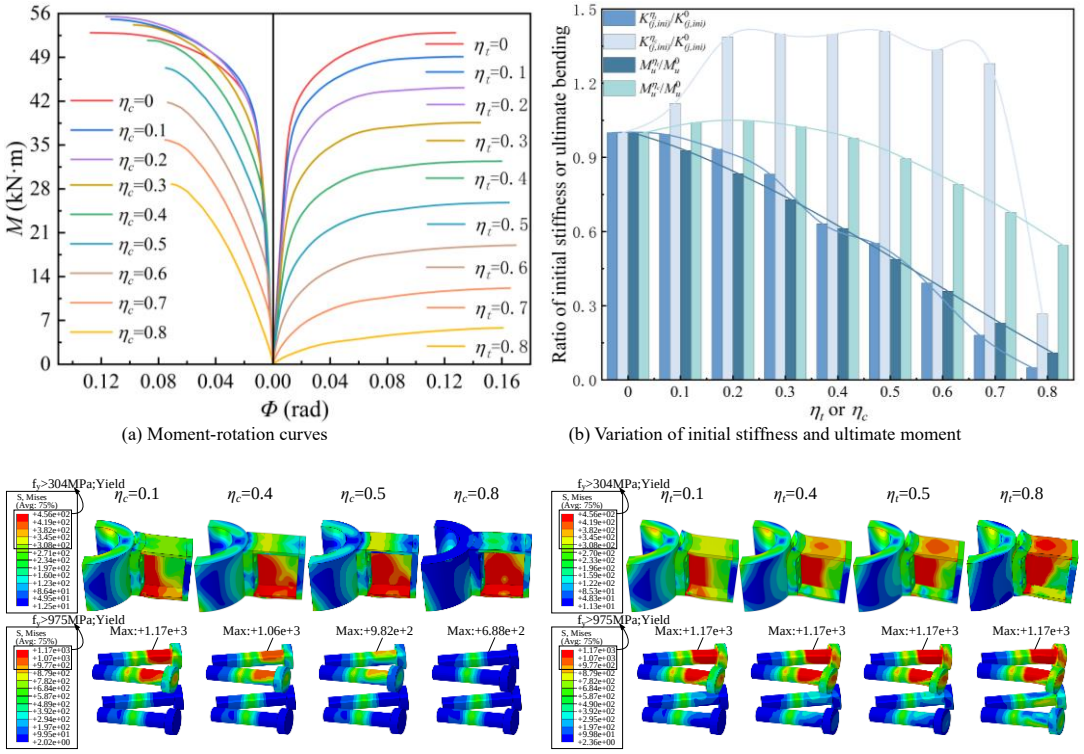


(a) Moment-rotation curves

(b) Variation of initial stiffness and ultimate moment

(c) Mises stress contour diagrams at ultimate moment. (Unit: MPa)

**Fig. 16** Characteristics for bending performance of improved BC joint with a prescribed axial force

## 5. Bilinear model of improved BC joint

### *5.1. Establishment method of bilinear model*

Analyzed as before, the moment-rotation curve of the improved BC joint has obvious feature of bilinear model, which is mainly affected by bolt diameter, vertical distance of bolts, flange thickness and front plate thickness. As shown in Fig. 17 [14], assuming that there is a yield moment $M_s = aM_u$ ( $a$ is yield coefficient and $M_u$ is ultimate moment), $a$ can be calculated through energy equivalence method, namely that the area enclosed by moment-rotation curve is equivalent to the one by bilinear model. In addition, $S_j$ represents initial bending stiffness and $\varphi_u$ represents the rotation corresponding to ultimate moment.

Based on the FE models in Section 4, the bilinear model characteristics ($a$, $\varphi_u$, $S_j$ and $M_u$) of improved BC joint are obtained and listed in Table 5. From the values of $S_j$ and $M_u$ in the table, it can be seen that the improved BC joint is a typical semi-rigid joint.

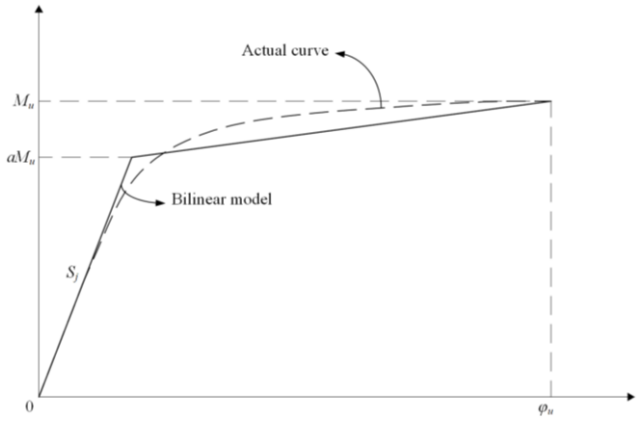


**Fig. 17** Bilinear model

**Table 5**
Bilinear model characteristics of improved BC joint

| $d$(mm) | $L_1$(mm) | $t_1$(mm) | $t_2$(mm) | $a$ | $\varphi_u$(rad) | $S_j$(kN·m/rad) | $M_u$(kN) |
|---|---|---|---|---|---|---|---|
| 21 | 78 | 6 | 30 | 0.859 | 0.092214 | 3545.33 | 42.37 |
| 21 | 78 | 8 | 30 | 0.856 | 0.102434 | 3689.27 | 48.29 |
| 21 | 78 | 10 | 30 | 0.865 | 0.118382 | 3841.79 | 51.94 |
| 21 | 78 | 12 | 30 | 0.883 | 0.123509 | 3997.48 | 54.06 |
| 21 | 78 | 14 | 30 | 0.888 | 0.117440 | 4103.98 | 55.39 |
| 21 | 78 | 16 | 30 | 0.875 | 0.101047 | 4202.85 | 57.06 |

| | | | | | | | |
|---|---|---|---|---|---|---|---|
| 24 | 78 | 6 | 30 | 0.867 | 0.092504 | 2513.08 | 42.39 |
| 24 | 78 | 8 | 30 | 0.856 | 0.108057 | 3510.78 | 49.62 |
| 24 | 78 | 10 | 30 | 0.891 | 0.134250 | 3680.57 | 52.90 |
| 24 | 78 | 12 | 30 | 0.892 | 0.137729 | 3836.38 | 55.72 |
| 24 | 78 | 14 | 30 | 0.899 | 0.154670 | 3961.81 | 58.38 |
| 24 | 78 | 16 | 30 | 0.900 | 0.148507 | 4033.45 | 59.98 |
| 27 | 78 | 6 | 30 | 0.828 | 0.046217 | 3391.20 | 41.17 |
| 27 | 78 | 8 | 30 | 0.860 | 0.117756 | 3644.73 | 51.84 |
| 27 | 78 | 10 | 30 | 0.886 | 0.156922 | 3839.87 | 56.74 |
| 27 | 78 | 12 | 30 | 0.882 | 0.163122 | 3983.61 | 60.20 |
| 27 | 78 | 14 | 30 | 0.883 | 0.162713 | 4109.55 | 63.10 |
| 27 | 78 | 16 | 30 | 0.885 | 0.126968 | 4424.97 | 63.37 |
| 30 | 78 | 6 | 30 | 0.854 | 0.081558 | 3494.01 | 43.56 |
| 30 | 78 | 8 | 30 | 0.866 | 0.117656 | 3707.75 | 51.65 |
| 30 | 78 | 10 | 30 | 0.868 | 0.142283 | 3948.51 | 57.26 |
| 30 | 78 | 12 | 30 | 0.861 | 0.193856 | 4090.67 | 62.34 |
| 30 | 78 | 14 | 30 | 0.864 | 0.181614 | 4238.92 | 66.44 |
| 30 | 78 | 16 | 30 | 0.886 | 0.135286 | 4331.03 | 66.91 |
| 24 | 78 | 6 | 20 | 0.842 | 0.087007 | 3051.73 | 36.45 |
| 24 | 78 | 8 | 20 | 0.846 | 0.129976 | 3273.38 | 41.77 |
| 24 | 78 | 10 | 20 | 0.862 | 0.138057 | 3458.09 | 44.20 |
| 24 | 78 | 12 | 20 | 0.874 | 0.157939 | 3595.02 | 46.44 |
| 24 | 78 | 14 | 20 | 0.861 | 0.161989 | 3744.34 | 49.58 |
| 24 | 78 | 16 | 20 | 0.849 | 0.146848 | 3879.15 | 51.70 |
| 24 | 78 | 6 | 25 | 0.870 | 0.087249 | 3221.83 | 39.91 |
| 24 | 78 | 8 | 25 | 0.862 | 0.117193 | 3456.11 | 45.74 |
| 24 | 78 | 10 | 25 | 0.877 | 0.132965 | 3635.20 | 48.68 |
| 24 | 78 | 12 | 25 | 0.891 | 0.151936 | 3770.84 | 50.87 |
| 24 | 78 | 14 | 25 | 0.887 | 0.156999 | 3850.80 | 53.26 |
| 24 | 78 | 16 | 25 | 0.883 | 0.141736 | 3943.42 | 53.67 |
| 24 | 78 | 6 | 35 | 0.785 | 0.073870 | 3491.49 | 47.73 |
| 24 | 78 | 8 | 35 | 0.793 | 0.091521 | 3651.87 | 59.49 |
| 24 | 78 | 10 | 35 | 0.841 | 0.125197 | 3830.72 | 68.44 |
| 24 | 78 | 12 | 35 | 0.868 | 0.102371 | 4021.64 | 71.17 |
| 24 | 78 | 14 | 35 | 0.894 | 0.099549 | 4137.07 | 73.77 |
| 24 | 78 | 16 | 35 | 0.904 | 0.096214 | 4236.78 | 75.77 |
| 24 | 72 | 6 | 30 | 0.860 | 0.082017 | 3162.17 | 41.43 |
| 24 | 72 | 8 | 30 | 0.868 | 0.109751 | 3387.19 | 47.52 |
| 24 | 72 | 10 | 30 | 0.882 | 0.124530 | 3555.81 | 50.70 |
| 24 | 72 | 12 | 30 | 0.903 | 0.151873 | 3682.95 | 53.16 |
| 24 | 72 | 14 | 30 | 0.905 | 0.154575 | 3786.76 | 54.99 |
| 24 | 72 | 16 | 30 | 0.906 | 0.151191 | 3887.88 | 56.64 |
| 24 | 84 | 6 | 30 | 0.850 | 0.081156 | 3371.43 | 43.45 |
| 24 | 84 | 8 | 30 | 0.863 | 0.100055 | 3478.70 | 50.88 |
| 24 | 84 | 10 | 30 | 0.873 | 0.127490 | 3779.49 | 55.85 |
| 24 | 84 | 12 | 30 | 0.893 | 0.153872 | 3927.23 | 59.07 |
| 24 | 84 | 14 | 30 | 0.893 | 0.138919 | 4071.05 | 61.35 |
| 24 | 84 | 16 | 30 | 0.896 | 0.125525 | 4166.97 | 63.68 |

*5.2. The fitting of key parameters*

Yield coefficient ($a$), initial bending stiffness ($S_j$) and ultimate bending moment ($M_u$) are nonlinearly fitted respectively with Eq. (1), and the ultimate rotation ($\varphi_u$) is nonlinearly fitted with Eq. (2). The independent variables of the fitted formulas are bolt diameter, bolts' vertical distance, flange thickness and front plate thickness. The values of fitted coefficients are obtained and shown in Tables 6 and 7.

The predicted values are obtained by using the fitted formula, and then scatter diagram (Fig. 18) is plotted with true value as x-axis and the predicted value as y-axis. It can be observed that the points basically fall on the ideal fitting line. It indicates that the fitted formula can accurately calculate the main

parameters of the bilinear model, with 1.30% deviation in the yield coefficient, 2.57% deviation in the initial stiffness, 3.82% deviation in the ultimate moment and 8.65% deviation in the ultimate rotation.

$$y = \frac{(c_1 d + c_2 L_1 + c_3 t_1 + c_4 t_2)^{c_5}}{(dL_1 t_1 t_2)^{c_6}} + c_7 \quad (1)$$

$$\varphi_u = \frac{(c_1 d + c_2 L_1 + c_3 t_1 + c_4 t_2)^{6.8}}{(dL_1 t_1 t_2)^{c_5}} + \frac{(c_6 dt_1 + c_7 t_1 t_2 + c_8 t_2 L_1 + c_9 L_1 d)^3}{(dL_1 t_1 t_2)^{c_5}} + c_{10} \quad (2)$$

**Table 6**
Specific values of fitting coefficients of $a$, $S_i$ and $M_u$

| $y$ | $c_1$ | $c_2$ | $c_3$ | $c_4$ | $c_5$ | $c_6$ | $c_7$ |
|---|---|---|---|---|---|---|---|
| a | +1.466e-5 | -1.344e-5 | +2.132e-4 | -9.195e-5 | 5.000 | -2.128e+0 | +8.820e-1 |
| K | +3.145e+2 | +3.327e+2 | +1.202 e+2 | +3.656e+2 | 1.000 | -1.143e-1 | +1.124e+7 |
| $M_u$ | -5.423e-3 | +4.560e-3 | -1.274e-2 | +1.424e-2 | 1.000 | -1.310e+0 | +3.508e+7 |

**Table 7**
Specific values of fitting coefficients of $\varphi_u$

| $c_1$ | $c_2$ | $c_3$ | $c_4$ | $c_5$ | $c_6$ | $c_7$ | $c_8$ | $c_9$ | $c_{10}$ |
|---|---|---|---|---|---|---|---|---|---|
| +9.181e-3 | +1.635e-2 | -2.258e-2 | +2.347e-2 | +5.573e-1 | +4.891e-2 | -2.993e-2 | +8.314e-4 | -5.001e-3 | +1.276e-1 |

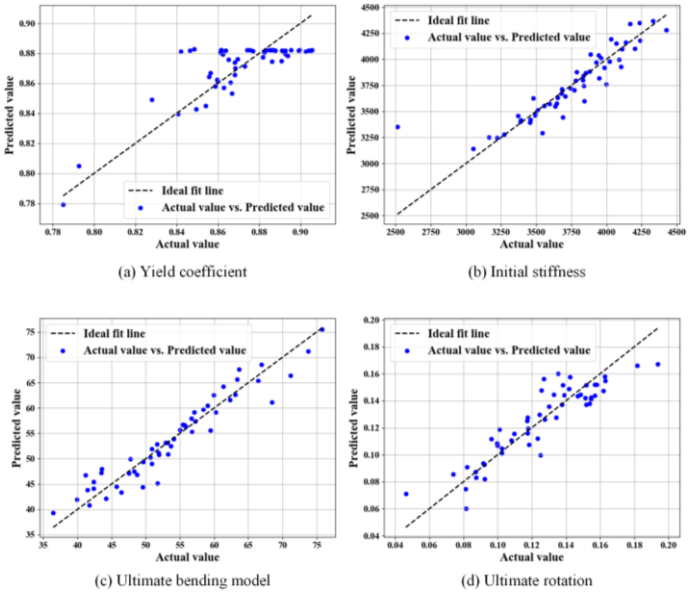


**Fig. 18** Scatter diagram of comparison between actual values and predicted values

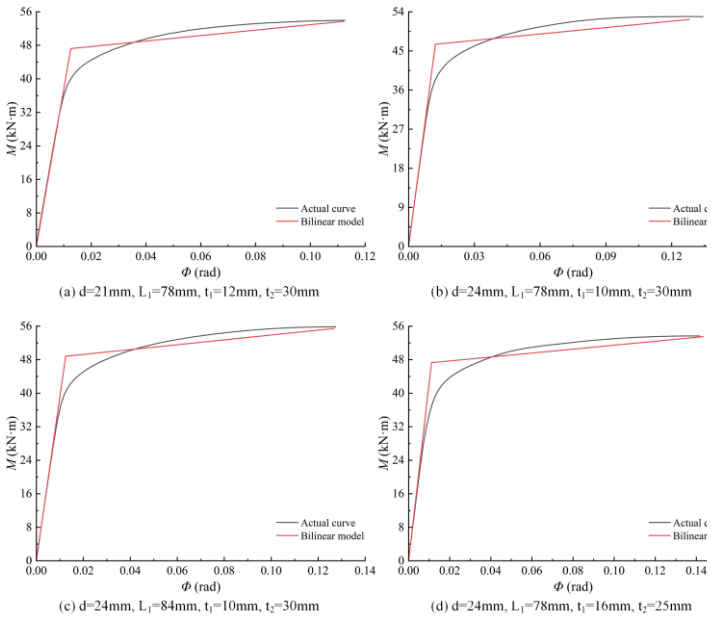


**Fig. 19** Comparison of the moment-rotation relationship between bilinear and actual models

*5.3. Validation of the fitted bilinear model*

In summary, the moment-rotation curve of improved BC joint can be determined according to Eqs. (1)-(2) and Tables 6-7, provided that the bolt diameter, vertical distance between bolts, flange thickness, and front plate thickness of the joint are known. Fig. 19 presents a comparison of moment-rotation curves obtained from the finite element model and the fitted bilinear model. It is evident that the bilinear model accurately represents the stiffness and bending capacity, aligning well with the numerical findings. Hence, it can be inferred that utilizing the bilinear model as a preliminary estimation for predicting the moment-rotation curve of the enhanced BC joint would serve as a reliable reference.

Additionally, it is worth noting that the proposed bilinear model is developed by nonlinear fitting, without any derivation of theory. Thus, its application is constrained by the considered geometrical parameters in Table 5, namely bolt diameter from 21-30mm, bolts' vertical distance from 72-84mm, flange thickness 6-16mm and front plate thickness from 20-35m.

## 6. Conclusions

The present study proposes a novel structure for the traditional BC joint and conducts a comparison on bending performance between the original and the improved joints. Subsequently, parametric investigation of the improved joint including 66 models is conducted in which different parameters, such as bolt diameter, bolts' vertical distance, flange thickness, front plate thickness and column node thickness, are varied. In addition, the effect of axial force on the bending performance of the joint is also discussed. Finally, the bilinear model of the improved BC joint is established and verified based on FE models. The main conclusions in this paper are summarized as follows.

(1) Compared with traditional BC joint, the improved BC joint exhibits a significant improvement in bending performance including 62.59% increase in initial rotational stiffness, 116.82% increase in initial yield moment, and 87.57% increase in ultimate moment.

(2) The general laws that geometric parameters affect the bending performance are obtained from parametric study.

(i) The ultimate moment of joints increases remarkably with a gradually decreasing rate as the flange thickness increases, while the initial bending stiffness experiences a slight increase. Three different failure modes are observed with the progressive increment in flange thickness: (I) the plastic hinge formation in first half of cone part results the failure of joint; (II) joint failure occurs due to simultaneously yielding among front plate, flanges and bolts; (III) joint failure occurs due to the tensile failure of bolts.

(ii) The ultimate moment of the joint increases as the bolt diameter increases, while a slight decrease occurs in the yield area of the front plate and a relatively significant one for bolts. When $d > 27\text{mm}$, the bolt diameter has little effect on the moment-rotation curve.

(iii) The bending performance of joints can be enhanced by increasing the vertical distance between bolts, and a gradual increase in the vertical distance between bolts leads to a stable improvement in the ultimate moment of joints and a reduction in bolt stress.

(iv) As the thickness of the front plate increases, there is a corresponding increase in the ultimate moment of joints, accompanied by an increase in stress and deformation of flanges. Except for joints with a flange thickness of 16mm, the failure mode remains consistent for joints with a front plate thickness of

30mm: both flanges form plastic hinges, resulting in the failure of joint.

(v) The moment-rotation curve remains little change when the thickness of the column node exceeds 40mm. When the thickness is less than 40mm, flanges with thicknesses over 10mm slightly affect the bending performance of the joint, and the failure modes of such joints are that the entire area of the column node yields. Therefore, it is recommended to have a thickness greater than 40mm for the column node.

(3) When axial compression is small, it exhibits positive effect on the bending performance of improved BC joint; however, the axial tension demonstrates negative influence on the bending performance consistently.

(4) A bilinear model is developed by incorporating parameters including bolt diameter, bolts' vertical distance, flange thickness, and front plate thickness. Comparative study demonstrates that the model can accurately predict the bending behavior of the improved BC joint.

## Acknowledgements

This work was supported by National Natural Science Foundation of China (No.51408490), Natural Science Basic Research Program of Shaanxi (2022JM-234, 2023-JC-YB-363), Training Programs of Innovation and Entrepreneurship for Undergraduates (202310712067, 202410712019), are gratefully appreciated.

## References

[1] Huihuan Ma, Shan Ren, Feng Fan. Parametric study and analytical characterization of the bolt-column (BC) joint for single-layer reticulated structures [J]. Engineering Structures, 2016, 123: 108-123. (DOI: 10.1016/j.engstruct.2016.05.037)

[2] Huihuan Ma, Shan Ren, Feng Fan. Experimental and numerical research on a new semi-rigid joint for single-layer reticulated structures [J]. Engineering Structures, 2016, 126: 725-738. (DOI: 10.1016/j. engstruct.2016.08.028.)

[3] Feng Fen, Huihuan Ma, Xin Jiang. Optimization of spatial semi-rigid C-joint and experimental study on its rotational resistance [J]. Journal of Building Structures, 2016, 37(03): 134-140. (DOI: 10.14006/j.jzjgxb.2016.03.016) (in Chinese)

[4] Qinghua Han, Yiming Liu, Ying xu. Stiffness characteristics of joints and influence on the stability of single-layer latticed domes [J]. Thin-Walled Structures, 2016, 107: 514-525. (DOI: 10.1016/j.tws. 2016.07.013)

[5] Ren-Zhang Yan, Chang-Long Zhang, Shuai Wang, *et al*. Distribution of residual stress in the sphere-pipe connection welds of welded hollow spherical joints [J]. Advanced Steel Construction, 2023, 19(03): 262-272. (DOI: 10.18057/IJASC.2023.19.3.7)

[6] Waleed Mashrah, Zhi-Hua Chen, Hong-Bo Liu, *et al*. Experimental, numerical, and theoretical study on static behaviour of novel steel dovetail joint subjected to axial tension load [J]. Advanced Steel Construction, 2022, 18(01): 453-464. (DOI: 10.18057/ IJASC.2022.18.1.4)

[7] Feng Fan, Huihuan Ma, Gengbo Chen et al. Experimental study of semi-rigid joint systems subjected to bending with and without axial force [J]. Journal of Constructional Steel Research, 2012, 68: 126-137. (DOI: 10.1016/j.jcsr.2011.07.020)

[8] Feng Fan, Huihuan Ma, Shizhao Shen. Numerical simulation and experimental study on mechanical characters of bolt-boll joint system [J]. Engineering Mechanics, 2009, 26(12): 92-99. (DOI: 10.1109/CLEOE-EQEC.2009.5194697) (in Chinese)

[9] Xiaochen Yu, Huijun Li, Xu Chen et al. Mechanical properties of bolt-ball joints and establishment of moment-rotation relation formula [J]. Progress in Building Structures, 2022, 24(04): 57-65. (DOI: 10.13849/j.issn.1006-6578.2022.02.056) (in Chinese)

[10] Su-duo Xue, Si-yao Li, Xiong-yan Li, *et al*. Behaviour and mathematical model for semi-rigid threaded-sleeve connection [J]. Advanced Steel Construction, 2019, 15(02): 123-128. (DOI: 10.18057/ IJASC.2019.15.2.1)

[11] Hui-Huan Ma, Yue-Yang Ma, Feng Fan, *et al*. Seismic performance of single-layer spherical reticulated shells considering joint stiffness and bearing capacity [J]. Advanced Steel Construction, 2022, 18(02): 604-616. (DOI: 10.18057/IJASC.2022.18.2.9)

[12] Chen Shan. Analysis of Hub-Shape inlay joint and its influence on the stability of single-layer lattice domes [D]. Tianjin: Tianjing University, 2010. (DOI: 10.7666/d.y1925692) (in Chinese)

[13] Qinghua Han, Yiming Liu, Jinyuan Zhang et al. Mechanical behaviors of the Assembled Hub (AH) joints subjected to bending moment [J]. Journal of Constructional Steel Research, 2017, 138: 806-822. (DOI: 10.1016/j.jcsr.2017.08.026)

[14] Xiaolei Zhang, Huijun Li, Xiaochen Yu et al. Research on stiffness and bilinear model of hub-shape inlay joints [J]. Spatial Structures, 2022, 28(02): 56-86. (DOI: 10.13849/j.issn.1006-6578. 2022. 02. 056) (in Chinese)

[15] Tudor Golea, Jean-Pierre Jaspart, Jean-François Demonceau. Characterisation of the behaviour of beam-to-column steel joints up to failure [J]. Advanced Steel Construction, 2022, 18(03): 679-686. (DOI: 10.18057/IJASC.2022.18.3.5)

[16] Huihuan Ma, Lingwei Yu, Feng Fan et al. Mechanical performance of an improved semi-rigid joint system under bending and axial forces for aluminum single-layer reticulated shells [J]. Thin-Walled Structures, 2019, 142: 322-339. (DOI: 10.1016/j.tws.2019.05.003)

[17] Huihuan Ma, Yuqi Jiang, Chengrui Li et al. Performance analysis and comparison study of two aluminum alloy joint systems under out-of-plane and in-plane loading. An experimental and numerical investigation [J]. Engineering Structures, 2020, 214(2): 110643. (DOI: 10.1016/j.engstruct.2020. 110643)

[18] Huihuan Ma, Lingwei Yu, Wei Wang et al. Static stability of aluminium single-layer elliptical parabolic latticed shell with semi-rigid joints [J]. Engineering Mechanics, 2017, 34(11): 158-166. (DOI: 10.6052/j.issn.1000-4750.2016.07.0535) (in Chinese)

[19] Ruoqing Fan, Fengcheng Liu, Guirong Yan et al. Mechanical behavior of Ring-sleeve joints of single-layer reticulated shells [J]. Journal of Constructional Steel Research, 2017, 128: 601-610. (DOI: 10.1016/j.jcsr.2016.09.023)

[20] Hui-Huan Ma, Chen-Yang Zhao, Yu-Qi Jiang, *et al*. Rotational resistance test of a new aluminum alloy penetrating (aap) joint system [J]. Advanced Steel Construction, 2023, 19(03): 121-129. (DOI: 10.18057/IJASC.2023.19.2.4)

[21] G. De Matteis, A. Mandara, F.M. Mazzolani. T-stub aluminium joints: influence of behavioural parameters [J]. Computers and Structures, 2000, 78(1-3): 311-327. (DOI: 10.1016/S0045-7949 (00)00081-X)

[22] Gianfranco De Matteis, Muhammad Tayyab Naqash, Giuseppe Brando. Effective length of aluminium T-stub connections by parametric analysis [J]. Engineering Structures, 2012, 41: 548-561. (DOI: 10.1016/j.engstruct.2012.03.052)

[23] Chenaghlou M R, Nooshin H. Axial force-bending moment interaction in a jointing system part I: (Experimental study) [J]. Journal of Constructional Steel Research, 2015, 113: 261-276. (DOI: 10.1016/j.jcsr.2015.06.011)

[24] Chenaghlou M R, Nooshin H. Axial force-bending moment interaction in a jointing system part II: Analytical study [J]. Journal of Constructional Steel Research, 2015, 113: 277-285. (DOI: 10.1016/j.jcsr.2015.06.010)

[25] Guo X, Xiong Z, Luo Y, *et al*. Experimental investigation on the semi-rigid behaviour of aluminium alloy gusset joints [J]. Thin-Walled Structures, 2015, 87: 30-40. (DOI: 10.1016/j.tws. 2014.11.001)

[26] Đorđe, Đuričić, Srđa, *et al*. Experimental, theoretical and numerical analysis of K-joint made of CHS aluminium profiles [J]. Thin Walled Structures, 2017, 119: 58-71. (DOI: 10.1016/j.tws.2017. 05.016)

**Advanced Steel Construction** – Vol. 20 No. 3 (2024) 253–265
**DOI:**10.18057/IJASC.2024.20.3.5


# MECHANICAL PROPERTIES OF WEATHER-RESISTANT STEEL BEAM-TO-COLUMN CONNECTIONS

Yue-Dong Wang [1, 2], Ze-Yu Zhang[1, 4, *], Lu-Zhen Jiang [3], Li-Jing Zeng [1, 4] and Jie Liu [1, 4]

[1] *Central Research Institute of Building and Construction Co., Ltd., MCC Group, Beijing, 100088, China*
[2] *Tsinghua University, Beijing, 100084, China*
[3] *School of Civil Engineering, Hebei University of Science and Technology, Shijiazhuang, 050018, China*
[4] *National Engineering Research Centre For Steel Construction, Beijing, 100088, China*
** (Corresponding author: E-mail: 2008.zzy.good@163.com)*

## ABSTRACT

Experimental research and numerical analysis are carried out on weather-resistant steel beam-to-column connections to investigate their mechanical properties in corrosive environment. Experiments of typical beam-to-column connections under normal condition and total corrosion condition are carried out respectively, and mechanical indexes such as failure mode, bearing capacity, deformation performance, and local plastic development of beam-to-column connections are compared and analyzed. Through collection and statistics of the monotonic tensile test data of weather-resistant steel, a calculation method of the constitutive relationship of weather-resistant steel under corrosion conditions is proposed. Accordingly, the numerical analysis of the weather-resistant steel beam-to-column connections is carried out. The results show that deformation and bearing capacities of weather-resistant steel beam-to-column connections decrease with the accumulation of corrosion-induced mass loss. The bearing capacity loss approximately changes in proportion to the corrosion mass loss (1:1), while deformation capacity loss of specimens (specifically referring to the ultimate displacement and ductility factor) is four times as much as the corrosion mass loss. In addition, the local corrosion of upper flange weld of the weather-resistant steel beam-to-column connection has the most significant effect on the deterioration of the mechanical properties of the connection. As the local corrosion zone is far away from the column, the deterioration effect of local corrosion on the beam upper and bottom flange tends to decrease.

## ARTICLE HISTORY

Received: 17 July 2023
Revised: 21 February 2024
Accepted: 23 February 2024

## KEYWORDS

Weather-resistant steel;
Beam-to-column connection;
Experimental research;
Numerical analysis;
Mechanical property



## 1. Introduction

Under the background of advocating green and low-carbon construction, developing high-performance steel structures has become an important part to help the low-carbon transformation of the construction industry and the construction of low-carbon cities. As a typical connection of high-performance steel structures, the investigation of the mechanical properties of weather-resistant steel beam-to-column connections holds significant theoretical and engineering importance.

Weather-resistant steel is based on ordinary steel by adding a small amount of $Cu^0$, $Cr^{00}$, $Ni^{00}$, $Mo^0$, and other alloying elements to form a dense and stable protective layer on the surface of steel matrix, so as to have excellent resistance of atmospheric corrosion. The corrosion resistance of weather-resistant steel can reach 2~8 times$^0$ that of ordinary steel, which can effectively mitigate the corrosion of steel structures. Collecting atmospheric exposure corrosion test data from typical test stations in China, Fig.1 shows the comparison of corrosion resistance performance between weather-resistant steel and ordinary steel. It can be seen that the corrosion resistance of weather-resistant steel is notably superior to that of ordinary steel. Especially with increase of corrosion time, this advantage becomes more and more obvious. In addition, weather-resistant steel not only has the recycling characteristics of ordinary steel but also can realize the application of coating free in actual engineering construction, which avoids the environmental pollution caused by spraying anti-corrosive coating. Based on the advantages mentioned above, weather-resistant steel has been popularized in some construction projects (see Fig.2) and has a very broad application prospect.

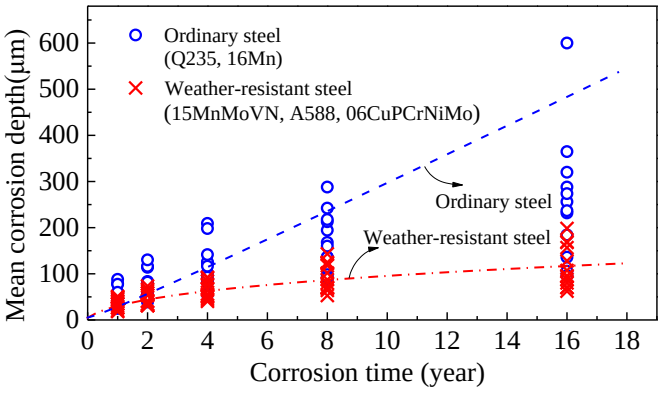


**Fig. 1** Corrosion resistance performance of weather-resistant steel and ordinary steel


(a) Schematic diagram of National Sliding Centre

(b) Application area of weather-resistant steel

(c) Construction of weather-resistant steel frame

**Fig. 2** Application example of weather-resistant steel in China——National Sliding Centre

At present, there have been some related studies on weather-resistant steel. FAN et al.$^0$, Chen W J et al.$^0$, and Gao et al.$^0$ studied the corrosion behavior and morphology of corrosion products of ordinary carbon steel and weather-resistant steel in coastal atmospheric environment through cyclic dry-wet tests. They found that the corrosion rate of weather-resistant steel presents a trend of first fast and then slow, and the corrosion rate is lower than that of ordinary carbon steel. Zong et al.$^0$ and Guo et al.$^0$ studied the degradation law of monotonic tensile properties of weather-resistant steel after

corrosion and quantified the effect of corrosion mass loss on the deterioration of steel strength. Wu et al.[0] studied the mechanical properties of Q355 NHD weather-resistant rolled H-section steel component, and they proposed the partial coefficient of resistance and the design value of the strength for the corresponding component. Su et al.[0] and Zhang et al.[0] carried out high-cycle fatigue tests on weather-resistant steel after corrosion, and found that the corrosion pit could easily cause local stress concentration, which significantly reduced the fatigue resistance of weather-resistant steel. Hu et al.[0] and Albrecht et al.[0] studied the mechanical properties of welded joints of weather-resistant steel, and they found that the strength matching degree of base material and welding material and the pitting corrosion at the welding location would affect the corrosion resistance of welded joints of weather-resistant steel. Tao et al.[0] found that the roughness and treatment method of weather-resistant steel plate surface have a significant influence on the mechanical properties of bolted joints. In general, present researches on weather-resistant steel primarily centers on factors such as alloying element ratio, corrosion resistance of steel, and post-corrosion mechanical properties of steel components, etc. There are few researches on the connection of weather-resistant steel, which needs to be explored.

In this paper, experimental research and numerical analysis are carried out to investigate the mechanical properties such as failure mode, bearing capacity, and deformation capacity of weather-resistant steel beam-to-column connections in corrosive environment. The calculation method of material constitutive model of weather-resistant steel is proposed, and based on this, the influence law of corrosion mass loss and local corrosion location on the mechanical properties of weather-resistant steel beam-to-column connection is explored. The research of this paper is helpful to lay a foundation for improving the seismic design method of high-performance steel structures, which can give full play to the corrosion resistance of weather-resistant steel.

## 2. Experimental study

### 2.1. Specimen design

To explore mechanical properties of weather-resistant steel beam-to-column connections, specimens are designed and made. Fig. 3 shows configuration details of the specimen. The column of the specimen is steel tube with square section, and the sectional dimension $h\times b\times t$ is 200mm×200mm×14mm. The beam of the specimen has H section, and the sectional dimension $h\times b\times t_f\times t_w$ is 300mm×200mm×10mm×10mm. The beam is connected to column by a cantilever beam segment, and the cantilever beam segment is connected to the column by welding. The beam flange is connected with the cantilever beam segment by welding, and the beam web is connected with the cantilever beam segment by connecting plates and high-strength bolts. Stiffeners are arranged at the joint connection position in the column. Both ends of the column are fixed on the reaction frame to prevent sliding and out-of-plane deformation. The steel used in the specimens is weather-resistant steel Q355NH produced by Angang Group, and the bolts are high-strength grade 10.9 bolts (M24) made of weather-resistant steel. According to JGJ 82-2011, the test specimens are assembled and connected.

Two specimens are tested (named LZ-1 and LZ-2), and the difference is corrosion time. The corrosion time of LZ-1 is 0, and the corrosion time of LZ-2 is 360 hours. According to the "Corrosion tests in artificial atmospheres-Salt spray tests"(GB/T 10125-2021), specimen LZ-2 is corroded in Durability Laboratory at Tongji University. Fig. 4 shows the corrosion process of specimen LZ-2. After the specimen of weather-resistant steel beam-to-column connection is assembled, corrosion experiment is conducted in a specific corrosion environment. The corrosion solution used here is 5% NaCl salt solution, characterized by a pH range between 6.5 and 7.2. Fig. 5 shows the appearance of LZ-2 after corrosion. As shown in this figure, the corrosion products are attached to the specimen LZ-2, and the LZ-2 presents reddish brown in the whole body, which is global corrosion. Viewed from the naked eye, the distribution of the corrosion pit is relatively uniform, which shows the typical characteristics of corrosion for the weather-resistant steel.

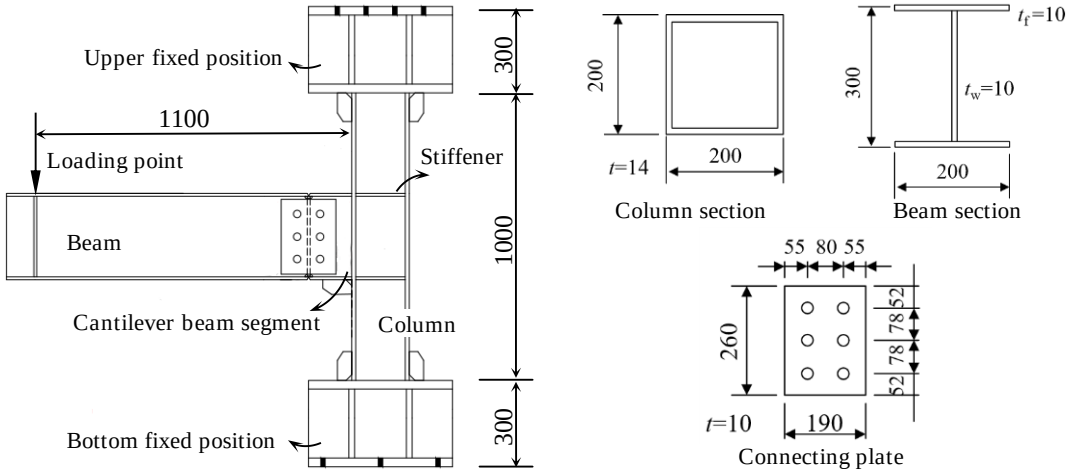


**Fig. 3** Configuration details of the specimen (unit: mm)

(a)Corrosion test chamber (b)Specimen placement (c)Bolt hole protection (d)Corrosion completion

**Fig. 4** Corrosion process of the specimen LZ-2

**Fig. 5** LZ-2 appearance after corrosion

Fig.6 shows the arrangement of measuring points of the specimen. The displacement meters are used to measure the global deformation and the local deformation development is measured by strain gauges. The loading mode of LZ-1 and LZ-2 is the same. Both specimens carry out monotonic loading at the beam end, and the distance from the loading point to the column edge is 1100mm. When the specimen is unable to bear the load due to obvious failure or the beam end load drops to less than 85% of the peak load, the experiment is stopped.

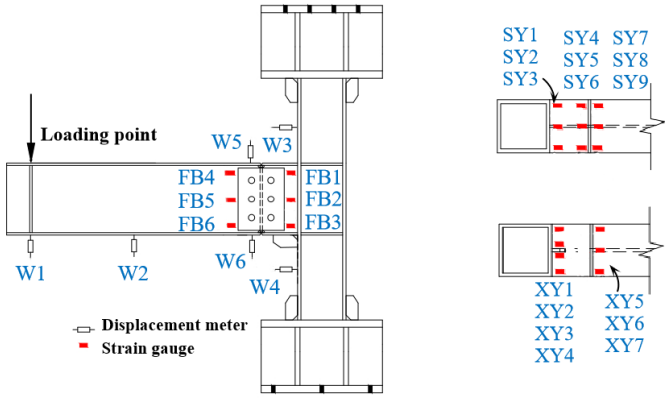


**Fig. 6** Arrangement of measuring points of the specimen

## 2.2. Analysis of experimental results

### 2.2.1. Failure phenomenon

Fig.7 and Fig.8 show the failure phenomenon of LZ-1 and LZ-2, respectively. As shown in these figures, LZ-1 and LZ-2 have the same failure mode. With the increasing load, the beam-to-column connections are affected by the bending moment. The upper flange of beam is under tension, and the bottom flange of beam is under compression. The crack and final failure position of the specimen occurs on the beam's upper flange close to the edge of the column. The crack initiates at the position of flange end. Subsequently, the crack quickly penetrates along the through-thickness direction of the flange and expands towards to the beam web.

(a) Specimen installation

(b) Specimen damage

**Fig. 7** Failure phenomenon of LZ-1

(a)Specimen installation

(b)Specimen damage

(c)Local damage

**Fig. 8** Failure phenomenon of LZ-2

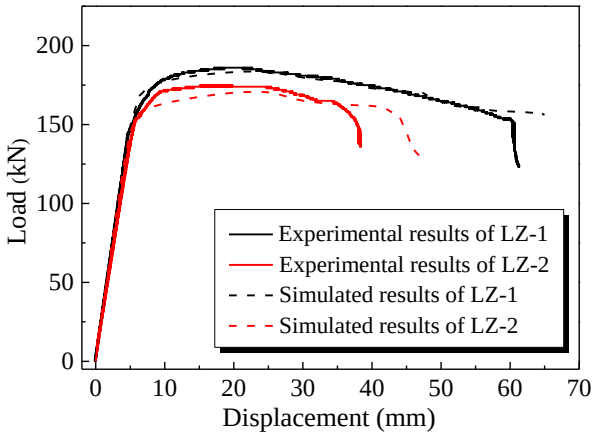


**Fig. 9** Experimental and simulated Load-displacement curves

*2.2.2. Load-displacement curve*

Fig.9 illustrates load-displacement curves for LZ-1 and LZ-2 in the experiment. Firstly, the displacement increases linearly as the load increases. Subsequently, there exists an inflection point on the load-displacement curve, which indicates that the specimen has yielded. As displacement continues to increase, the specimen's load increases to the maximum, and peak load of LZ-1 and LZ-2 are 186kN and 175kN, respectively. Finally, large plastic deformation causes specimen's damage and cracking, leading to degradation of loading capacity. By comparing the two specimens' experimental load-displacement curves, it is evident that their curve forms are consistent. Under the influence of corrosion, compared with LZ-1, LZ-2's bearing capacity decreases by 6% and the deformation capacity decreases by 31.48%. Logically, for the weather-resistant steel beam-to-column connection under total corrosion, the negative effect of corrosion on the deformation is more significant, which should be paid attention to in practical construction.

*2.2.3. Local deformation development*

Fig. 10 shows the relationship between the strain gauge value and the specimen load, which represents the local strain development of the specimen. Throughout the loading process, the specimen's local plasticity mainly develops at beam flange, and the strain at beam web is generally in an elastic state (FB1~FB6). The beam upper flange is continuously under tension, and the strain values are all positive. The plastic development of beam upper flange near column (SY1, SY2, SY3) is the most significant. The beam bottom flange is continuously under compression, and the strain values are all negative. The plastic development of the beam bottom flange near the column (XY1, XY2, XY3, XY4) is significant, especially at the edge position of the flange (XY1 and XY4). The reason for the above result is that the edge position of the beam bottom flange is not constrained by the web and thus is prone to local buckling under compression, which leads to large plastic deformation at that position. In general, the local plastic development degree of LZ-2 is larger than that of LZ-1, due to the influence of corrosion.

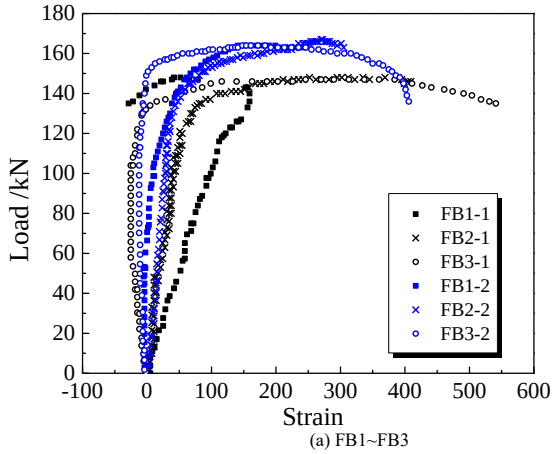


(a) FB1~FB3

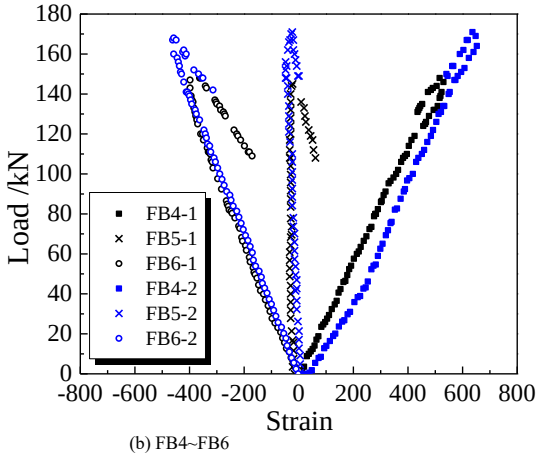


(b) FB4~FB6

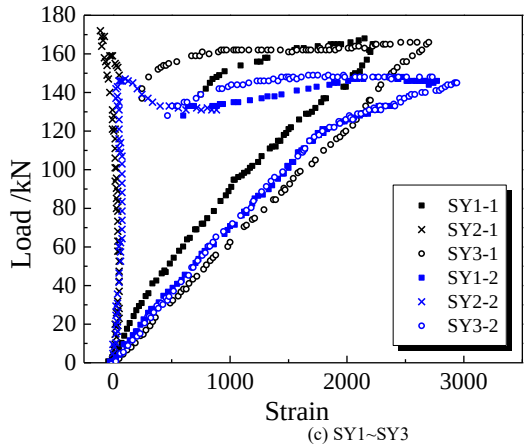


(c) SY1~SY3

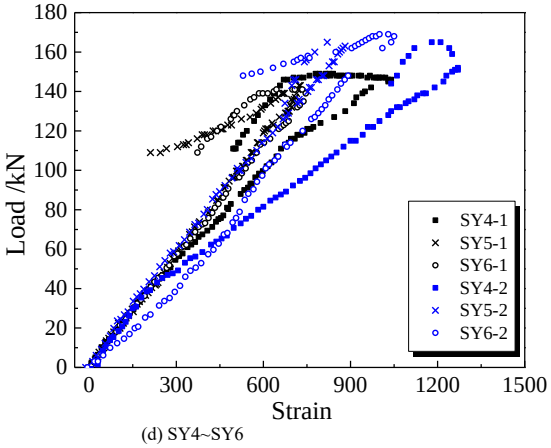


(d) SY4~SY6

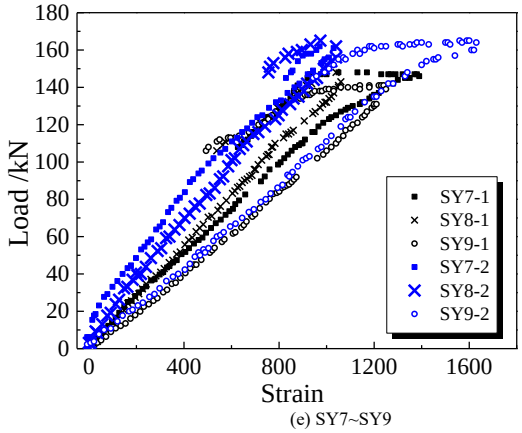


(e) SY7~SY9

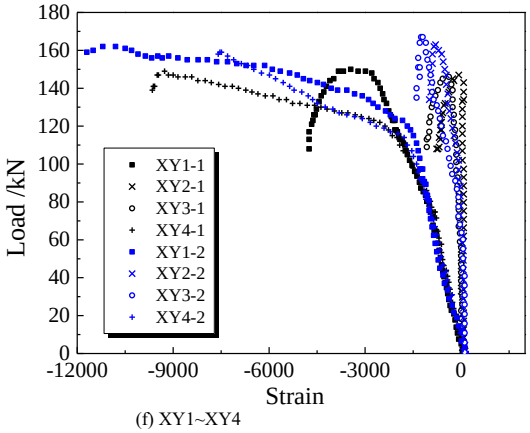


(f) XY1~XY4

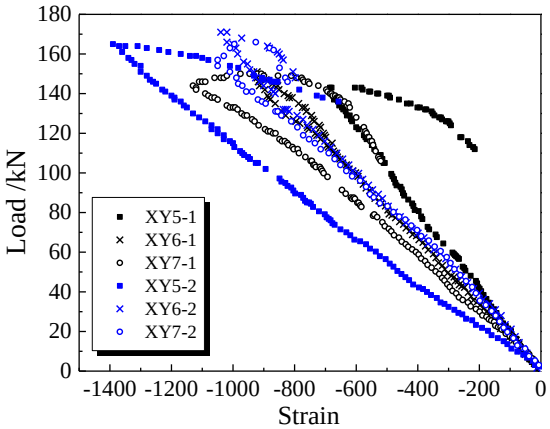


(g) XY5~XY7

**Fig. 10** Local strain development (-1 represents LZ-1, and -2 represents LZ-2)

## 3. Numerical analysis

### *3.1. Finite element model*

Fig.11 shows the specimen's finite element model utilized in ABAQUS platform. The specimen is simulated using solid element C3D8R. Considering calculation accuracy and efficiency, the key area of the specimen conducts mesh refinement. The simulation accurately replicates the practical experiment in terms of the specimen's actual size, boundary conditions, and loading mode. As shown in this figure, the fixed constraint is used as the boundary condition to simulate the constraint condition of column ends. Out-of-plane constraints are added in simulation to avoid the beam torsion. The "dumbbell" model is used to equivalent the actual high-strength bolt, and the preload is applied according to the actual test value. Considering the post-assembly interactions between components, friction coefficient of contact between bolt rod and bolt hole is 0.01, and the friction coefficient of contact between bolt cap and steel plate is 0.05. In addition, the cubic solid element is used to simulate the welding line, which is helpful to describe the mechanical behavior and failure state of beam-to-column connections.

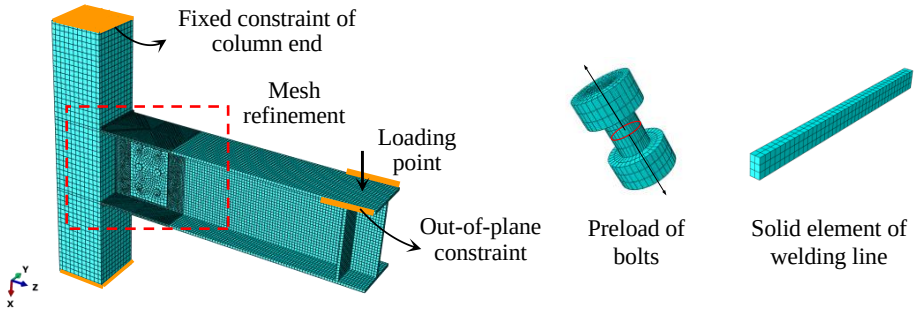


**Fig. 11** Finite element model

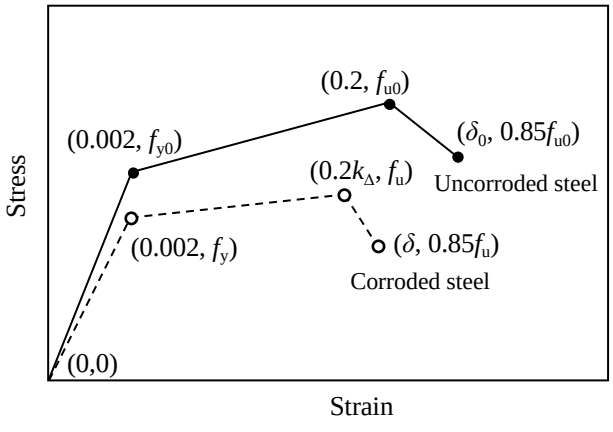


**Fig. 12** Schematic diagram of weather-resistant steel constitutive model

### *3.2. Material model*

To facilitate parametric analysis and mechanical property analysis of weather-resistant steel beam-to-column connections, a calculation method of the constitutive model of weather-resistant steel under different corrosion conditions is proposed. The proposed method transforms the complicated corrosion morphology modeling into a material physical model to approximately consider the corrosion's effect on mechanical properties of steel. In this calculation method, the trilinear model is used to describe the weather-resistant steel's stress-strain relationship under normal condition, and the stress-strain relationship of weather-resistant steel under corroded condition is formed by appropriate adjustment of this model. Fig. 12 shows the schematic diagram of weather-resistant steel constitutive model under normal and corroded conditions. In this figure, solid line represents the constitutive model of the uncorroded weather-resistant steel, which is determined by four coordinate points. Four coordinate points are (0, 0), (0.002, $f_{y0}$), (0.2, $f_{u0}$), and ($\delta_0$, 0.85$f_{u0}$), respectively. Dash line represents the constitutive model of corroded weather-resistant steel, which is also determined by four coordinate points. Four coordinate points are (0, 0), (0.002, $f_y$), (0.2$k_\Delta$, $f_u$), and ($\delta$, 0.85$f_u$), respectively. $f_{y0}$, $f_{u0}$ and $\delta_0$ can be obtained by monotonic tensile test of weather-resistant steel under normal condition. Considering the time-consuming and high cost of corrosion tests, it is necessary to establish a relationship between mechanical properties of corroded steel and those under normal conditions, so as to obtain $f_y$, $f_u$ and $\delta$ more conveniently and quickly.

Table 1 lists mechanical parameters of weather-resistant steel under normal and corrosive conditions. Sources of data include monotonic tensile tests of weather-resistant steel Q355NH[0], Q355NHD[0], Q345CNH[0], and HPS 485W[0]. To further quantify the corrosion's influence on mechanical properties of weather-resistant steel, data are normalized and corrosion reduction factors are introduced. The corrosion reduction factor of weather-resistant steel is determined by the ratio of the post-corrosion value of a mechanical parameter to the corresponding normal value of the mechanical parameter, which is shown as follows:

$$k_y = f_y / f_{y0} \tag{1}$$

$$k_u = f_u / f_{u0} \tag{2}$$

$$k = f_y f_{u0} / f_{y0} f_u \tag{3}$$

$$k_\Delta = \delta / \delta_0 \tag{4}$$

where $k_y$、$k_u$、$k$、$k_\Delta$ are corrosion reduction factors of steel yield strength, tensile strength, yielding-to-tensile ratio, and elongation, respectively. $f_{y0}$ and $f_y$

are yield strength of weather-resistant steel under uncorroded and corroded conditions, respectively. $f_{u0}$ and $f_u$ are tensile strength of weather-resistant steel under uncorroded and corroded conditions, respectively. $\delta_0$ and $\delta$ are elongation of weather-resistant steel under uncorroded and corroded conditions, respectively.

**Table 1**
Mechanical parameters of weather-resistant steel under normal and corrosive conditions

| Steel type | Corrosion mass loss $\eta$(%) | Yield strength (MPa) | Tensile strength (MPa) | Yielding-to-tensile ratio | Elongation (%) |
|---|---|---|---|---|---|
| Q355NH | 0 | 430.50 | 607.00 | 0.709 | 24.45 |
| | 1.501 | 419.33 | 594.00 | 0.706 | 23.68 |
| | 1.553 | 417.00 | 592.67 | 0.704 | 25.15 |
| | 1.867 | 404.33 | 580.33 | 0.697 | 24.62 |
| Q355NHD | 0 | 398.09 | 523.04 | 0.761 | 33.73 |
| | 5.203 | 375.70 | 515.09 | 0.729 | 23.77 |
| | 6.658 | 369.34 | 506.25 | 0.729 | 22.67 |
| Q345CNH | 0 | 588.53 | 859.6 | 0.685 | / |
| | 4.619 | 583.3 | 884.7 | 0.659 | / |
| | 4.500 | 534.8 | 834.3 | 0.641 | / |
| | 5.736 | 548.5 | 838.1 | 0.654 | / |
| | 5.806 | 547.8 | 829.4 | 0.660 | / |
| | 6.732 | 533.9 | 820.1 | 0.651 | / |
| HPS 485W | 0 | 578.9 | 858.4 | 0.674 | / |
| | 4.467 | 524.7 | 820.2 | 0.639 | / |
| | 6.154 | 537.4 | 829.5 | 0.648 | / |
| | 6.196 | 549.3 | 830.4 | 0.661 | / |
| | 6.601 | 526.1 | 827.9 | 0.635 | / |
| | 6.288 | 534.1 | 835.1 | 0.639 | / |

Considering the existing difference of corrosion environment in experiments of different types of weather-resistant steel, corrosion mass loss rather than corrosion time is used to quantify the corrosion degree of weather-resistant steel. According to experimental data, corrosion reduction factors and corrosion mass loss have a linearly negative relationship, which is shown as follows:

$$k_y = -1.094\eta + 1 \tag{5}$$

$$k_u = -0.4728\eta + 1 \tag{6}$$

$$k = -0.7323\eta + 1 \tag{7}$$

$$k_\Delta = -5.659\eta + 1 \tag{8}$$

Fig. 13 shows the expressions of corrosion reduction factors, which can be used to obtain and predict the constitutive model of weather-resistant steel under corrosion conditions. In the corrosion mass loss range of 0~7%, the corrosion-caused deterioration degrees on mechanical properties of steel from high to low are elongation, yield strength, yield-to-tensile ratio, and tensile strength. For example, at a corrosion mass loss of 0.07, the elongation, yield strength, yield-to-tensile ratio, and tensile strength of weather-resistant steel are 0.604, 0.923, 0.949, and 0.967 times of that of non-corroded steel, respectively. Due to the limitation of test data, the rule of performance degradation of other corrosion mass loss is worthy to be further studied.

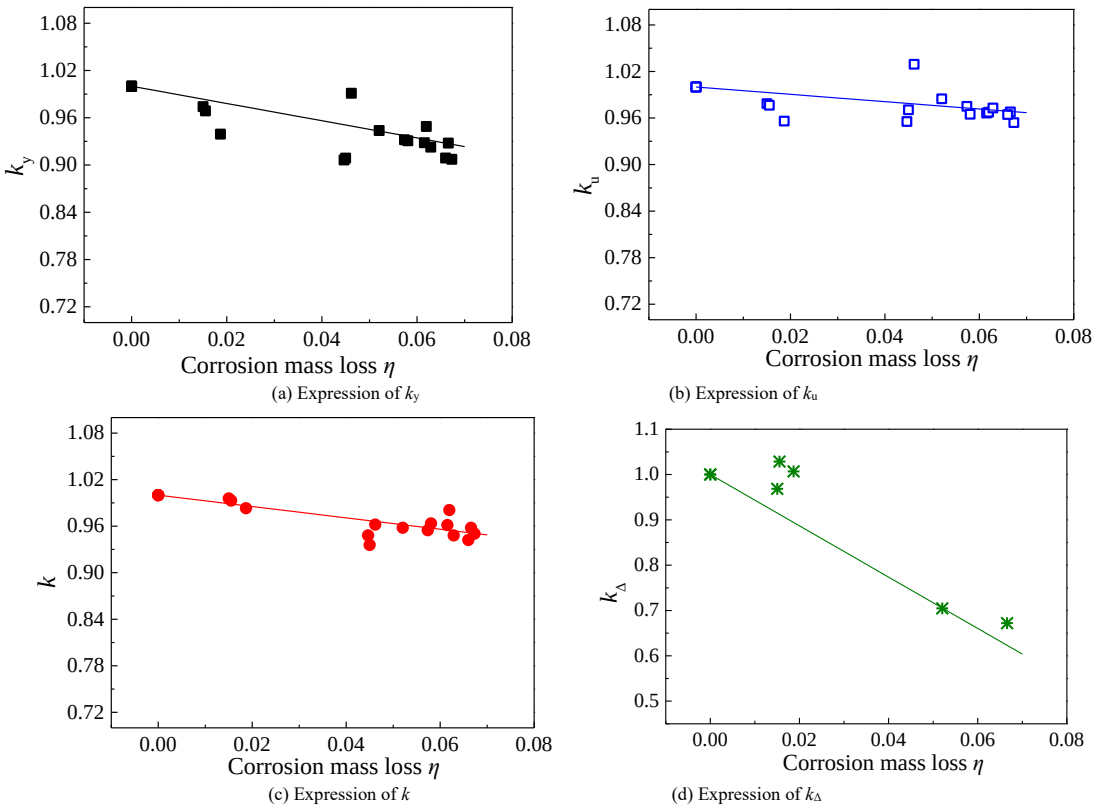


(a) Expression of $k_y$

(b) Expression of $k_u$

(c) Expression of $k$

(d) Expression of $k_\Delta$

**Fig. 13** Expressions of corrosion reduction factors of mechanical parameters

To describe the specimen's damage process, ductile damage model[0] is introduced to the material model in simulation, which is shown as follows:

$$\omega_D = \int_0^{\varepsilon_0^{pl}} \frac{d\varepsilon^{pl}}{\varepsilon_0^{pl}(T)} \tag{9}$$

$$T = \sigma_m / \sigma_e \tag{10}$$

$$\sigma_m = \frac{(\sigma_1 + \sigma_2 + \sigma_3)}{3} \tag{11}$$

$$\sigma_e = \sqrt{\frac{1}{2}\left[(\sigma_1 - \sigma_2)^2 + (\sigma_2 - \sigma_3)^2 + (\sigma_3 - \sigma_1)^2\right]} \tag{12}$$

where $\varepsilon_0^{pl}$ is critical value of equivalent plastic strain. $T$ is stress triaxiality, which can show the element's stress-state. $\omega_D$ is a state variable that monotonically increases with plastic deformation, serving as an indicator for the initiation of damage. $\sigma_1$, $\sigma_2$, and $\sigma_3$ are element's three principal stresses. $\sigma_m$ and $\sigma_e$ are mean stress and Mises equivalent stress, respectively. Damage initiation of the element in the simulated specimen occurs when the state variable accumulates to 1 throughout the loading history.

### *3.3. Simulated results*

Fig.9 shows experimental and simulated load-displacement curves of LZ-1 and LZ-2. The experimental and simulated results exhibit similarity in several aspects, encompassing the curve shape, loading capacity, deformation performance, and capacity degradation. The error of loading capacity between experimental and simulated results is less than 4%. Fig.14 shows the local plasticity development of the specimen. As shown in this figure, the large value of Mises stress and plastic strain of the specimen is located in the beam upper flange close to the column, indicating that the local plasticity is mainly developed in that location. According to the stress triaxiality nephogram, the beam upper flange of the specimen is continuously under tension, while the beam bottom flange is continuously under compression. Some elements of the beam upper flange are under multi-directional tension state ($T$>1/3, and 1/3 represents that the element is under unidirectional tension). Based on damage initiation criterion[0], the critical value of equivalent plastic strain $\varepsilon_0^{pl}$ is relatively small with the increase of the value of $T$ (when $T$>1/3), and thus the damage is more prone to occur at the location where under multi-directional tension state. Fig.15 shows damage development of the specimen. The damage occurs at the beam upper flange end near the column, and the continuous accumulation of damage results in the cracking of the specimen. From these figures, we can see that the load-displacement curves, plasticity development, and the damage mode of experimental and simulated results are highly similar, showing a good accuracy of the finite element model. Therefore, the numerical simulation can effectively capture the mechanical performance of the weather-resistant steel beam-to-column connection, establishing a foundation for subsequent research on parameter analysis.

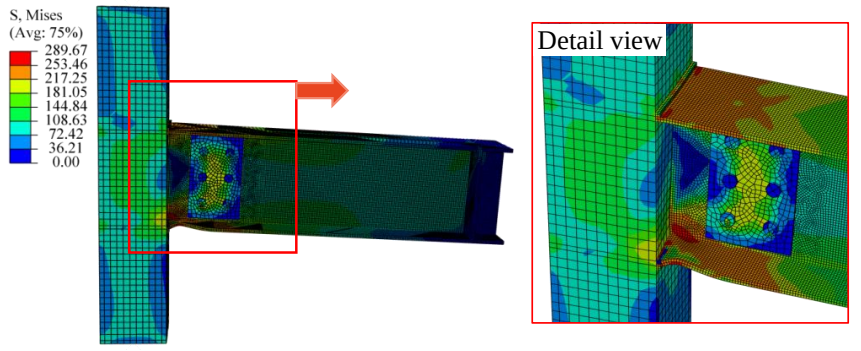


(a) Mises stress nephogram

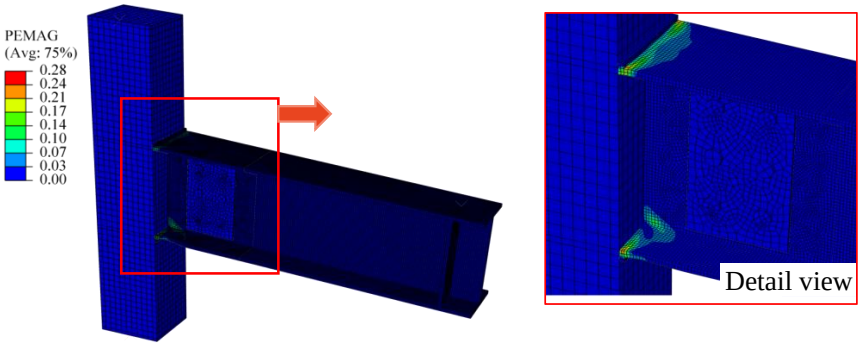


(b) Strain nephogram

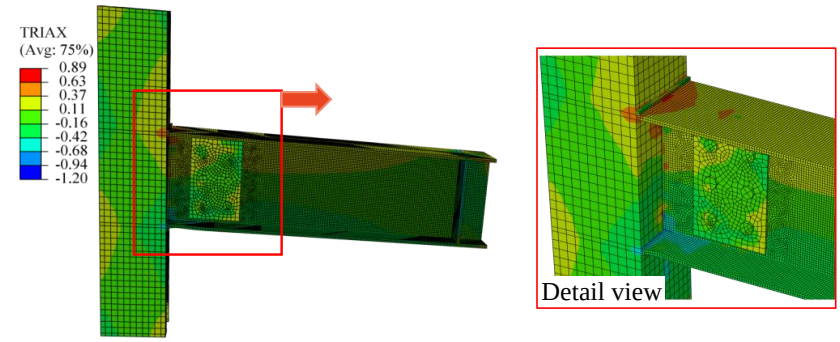


(c) Stress triaxiality nephogram

**Fig. 14** Local plasticity development of the specimen

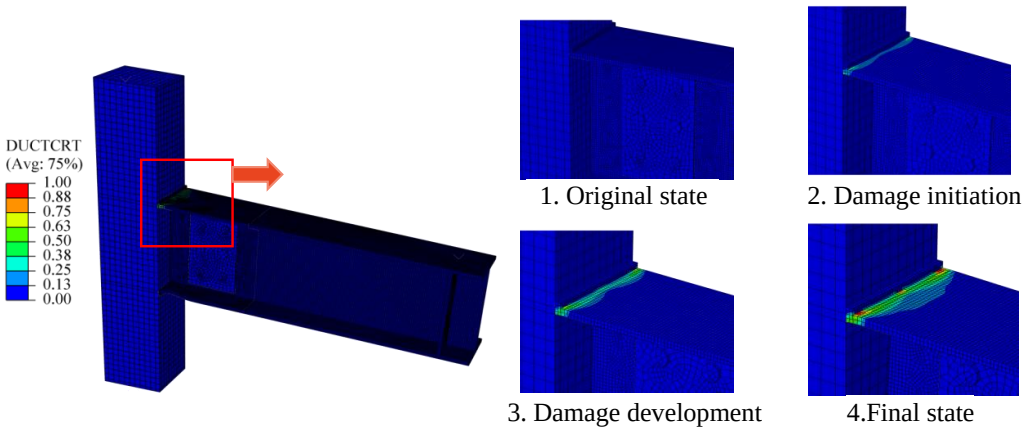


**Fig. 15** Damage development of the specimen

## 4. Parametric analysis

### *4.1. Effect of corrosion degree*

To further understand the influence regularity of corrosion on mechanical properties such as bearing capacity and deformation capacity of weather-resistant steel beam-to-column connections, corrosion mass loss is taken as variables (0, 0.01, 0.02, 0.03, 0.04, 0.05, 0.06, 0.07) to analyze the performance of specimens under total corrosion conditions. Fig. 16 shows specimens' simulated results of load-displacement curves under different corrosion mass losses. The shape of load-displacement curves of specimens is similar, which partly indicates that the failure modes of specimens under different corrosion mass losses are similar. As the corrosion mass loss increases, there is a tendency for the bearing capacity and deformation capacity of the specimen to decrease.

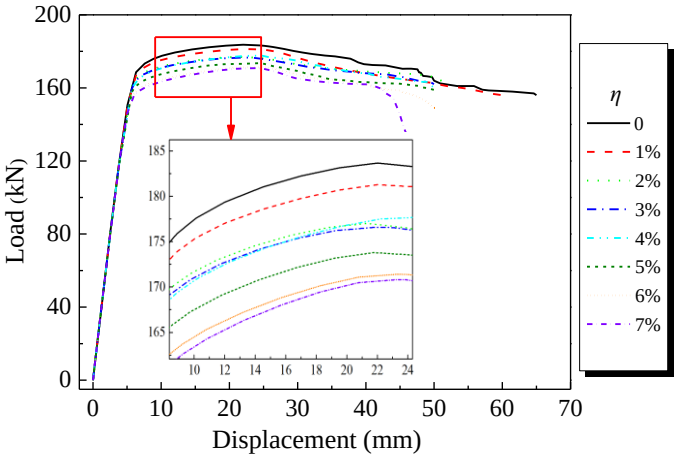


**Fig. 16** Simulated results of load-displacement curves

Based on specimens' load-displacement curves, yield load $F_y$, peak load $F_m$, ultimate load $F_u$ (85% of the peak load), and their corresponding displacements (including yield displacement $\Delta_y$, peak displacement $\Delta_m$, and ultimate displacement $\Delta_u$) are obtained, as shown in Table 2. The ductility factor $\mu$ can be obtained by $\Delta_u/\Delta_y$. Fig. 17 shows the effect of corrosion degree on specimen loading capacity. It can be seen that the value of $F_y$, $F_m$, and $F_u$ decrease with increase of corrosion mass loss which is in the range of 0~7%. Moreover, load loss rate of specimens exhibits a proportional variation with the corrosion mass loss, maintaining a 1:1 relationship. For example, the specimen with a corrosion mass loss of 7% will have a loading capacity loss of about 7% compared to that without corrosion. Fig. 18 shows the effect of corrosion degree on specimen deformation capacity. There is little change in $\Delta_y$ with the increasing corrosion mass loss, while $\Delta_m$, $\Delta_u$, and $\mu$ decrease with the increasing corrosion mass loss in the range of 0~7%. Moreover, the deformation capacity loss rate of specimens (specifically referring to $\Delta_u$ and $\mu$) is four times as much as corrosion mass loss. For example, the specimen with a corrosion mass loss of 7% will have a deformation capacity loss of about 28% compared to that without corrosion.

**Table 2**
Mechanical parameters of weather-resistant steel beam-to-column connections

| Corrosion mass loss $\eta$ | Yield point | | Peak point | | Ultimate point | | Ductility factor $\mu$ |
|---|---|---|---|---|---|---|---|
| | $F_y$/kN | $\Delta_y$/mm | $F_m$/kN | $\Delta_m$/mm | $F_u$/kN | $\Delta_u$/mm | |
| 0 | 168.60 | 6.32 | 183.68 | 22.02 | 155.56 | 64.55 | 10.21 |
| 1% | 167.15 | 6.33 | 181.05 | 24.52 | 158.65 | 60.00 | 9.47 |
| 2% | 160.76 | 5.70 | 177.02 | 21.35 | 162.51 | 52.58 | 9.22 |
| 3% | 161.18 | 5.81 | 176.60 | 22.40 | 161.85 | 51.55 | 8.87 |
| 4% | 159.16 | 5.69 | 177.69 | 24.75 | 160.00 | 50.05 | 8.79 |
| 5% | 158.44 | 5.81 | 173.37 | 24.90 | 158.90 | 50.00 | 8.60 |
| 6% | 157.44 | 6.00 | 171.40 | 23.26 | 148.98 | 48.85 | 8.14 |
| 7% | 156.28 | 6.05 | 170.81 | 23.88 | 145.65 | 44.96 | 7.43 |

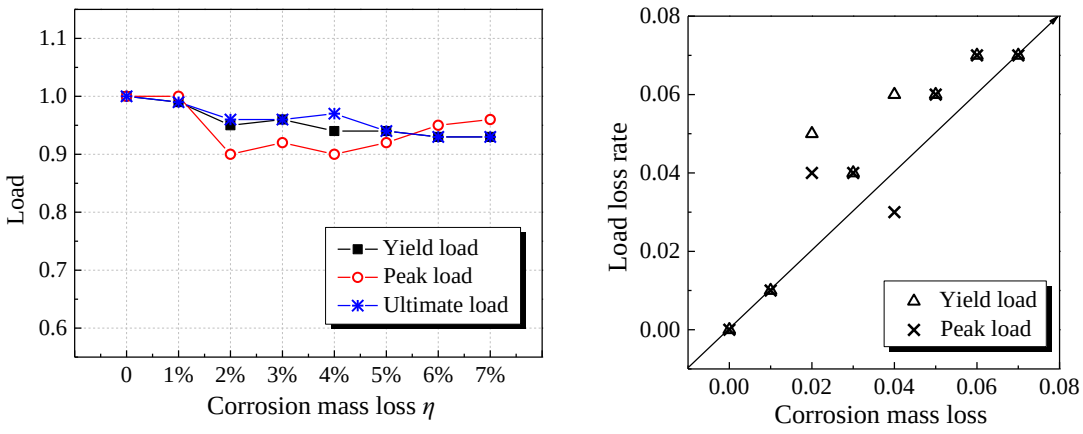


(a) Relationship of load and corrosion mass loss

(b) Relationship of load loss rate and corrosion mass loss

**Fig. 17** Effect of corrosion degree on specimen loading capacity

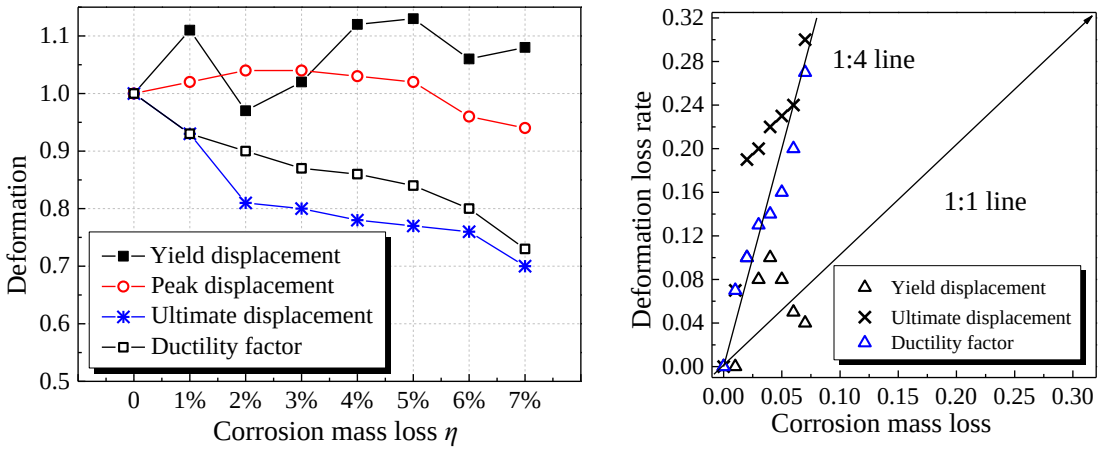


(a) Relationship of deformation and corrosion mass loss

(b) Relationship of deformation loss rate and corrosion mass loss

**Fig. 18** Effect of corrosion degree on specimen deformation capacity

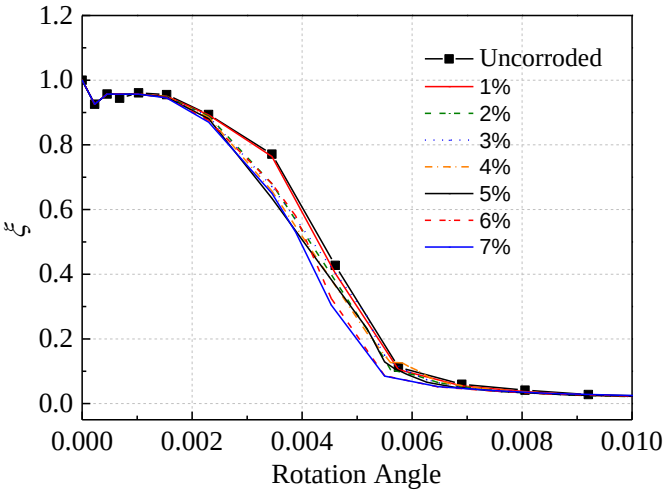


**Fig. 19** Degradation of connection stiffness

To investigate the impact of corrosion degree on the connection stiffness of specimens, Fig. 19 shows the results of degradation of connection stiffness. $\xi$ is the stiffness degradation coefficient, which is used to indicate the degree of stiffness degradation for the specimen. The calculation of this coefficient is Equation (13) and (14). The small value of $\xi$ represents the large degradation.

$$K_i = \frac{\sum_{j=1}^{n} F_i^j}{\sum_{j=1}^{n} d_i^j} \tag{13}$$

$$\xi = \frac{K_i}{K_0} \tag{14}$$

where Ki is secant stiffness at the i-th level of loading, $F_i^j$ is the peak force during the j-th cycle at i-th level of loading, and $d_i^j$ is the horizontal displacement during the j-th cycle at the i-th level of loading. The specimen's secant stiffness decreases as the rotation angle increases. The reduction of ξ shows a slow-fast-slow trend. For beam-to-column connections with different corrosion degrees, their shape of stiffness degradation curves are approximately the same. In general, the large value of corrosion mass loss leads to relatively severe stiffness degradation.

### *4.2. Effect of local corrosion location*

Due to different architectural forms and environmental conditions, apart from total corrosion, local corrosion is also a common type of corrosion in practical structures. Considering the randomness of local corrosion locations, the influence of local corrosion at different locations on mechanical properties of specimens is investigated. Local corrosion locations are W(see Fig.20), FS(see Fig.24), and FX(see Fig.28). W represents the location of welding line of beam and column, which includes W1(welding line of beam upper flange and column), W2(welding line of beam bottom flange and column), and W3(welding line of beam web and column). FS represents the local zone on the beam upper flange. Distance between the center of FS and the column end are 0.25*h*(*h* is the height of beam), 0.5*h*, 0.75*h*, 1.0*h*, 1.25*h*, 1.5*h*, 1.75*h*, and 2.0*h*, respectively, corresponding to FS025, FS050, FS075, FS100, FS125, FS150, FS175, and FS200. FX represents the local zone on the beam bottom flange. Distance between the center of FX and the column end are 0.25*h*(*h* is the height of beam), 0.5*h*, 0.75*h*, 1.0*h*, 1.25*h*, 1.5*h*, 1.75*h*, and 2.0*h*, respectively, corresponding to FX025, FX050, FX075, FX100, FX125, FX150, FX175, and FX200. The area of the local zone is 150mm×*b* (*b* is the width of beam). The constitutive relationship model of weather-resistant steel corresponding to the corrosion mass loss of 7% is taken as material properties of the local corrosion zone, and the numerical simulation analysis of specimens under different local corrosion conditions is carried out.

Fig. 21 shows the specimens' load-displacement curves in the condition of local corrosion of W. Local corrosion of W has a significantly negative effect on the mechanical performance of weather-resistant steel beam-to-column connection. Compared with total corrosion, local corrosion of W has limited influence on the bearing capacity of specimens, but more influence on the deformation of specimens. Fig. 22 shows the loading and deformation capacity of specimens in the condition of local corrosion of W. The local corrosion of W1 has the largest influence on the deterioration of mechanical properties of the specimen. With reference to non-corroded specimens, the local corrosion of W1 can lead to a 5% reduction in loading capacity and a 56% reduction in the deformation capacity of specimens, which should be paid significant attention to in practical engineering. Fig. 23 shows the connection stiffness of specimens in the condition of local corrosion of W. The local corrosion of W1 has the relatively large negative influence on the specimen's rotational stiffness.

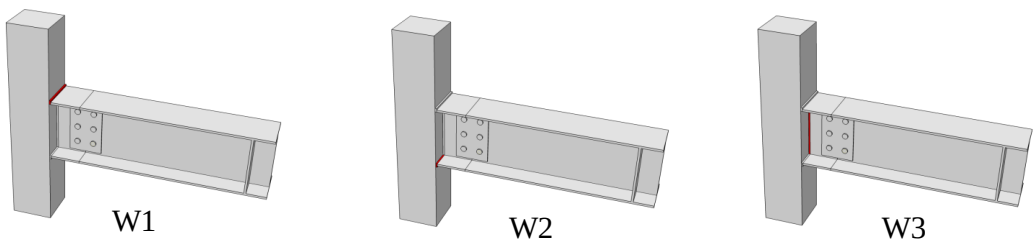


**Fig. 20** Schematic diagram of local corrosion location of W (red represents corrosion)

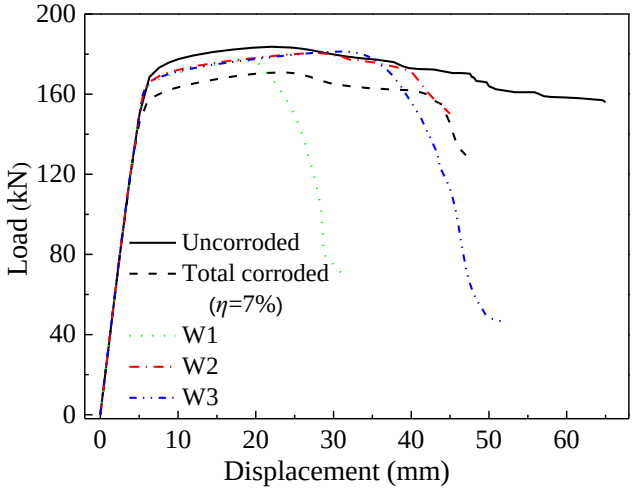


**Fig. 21** Load-displacement curves of local corrosion of W

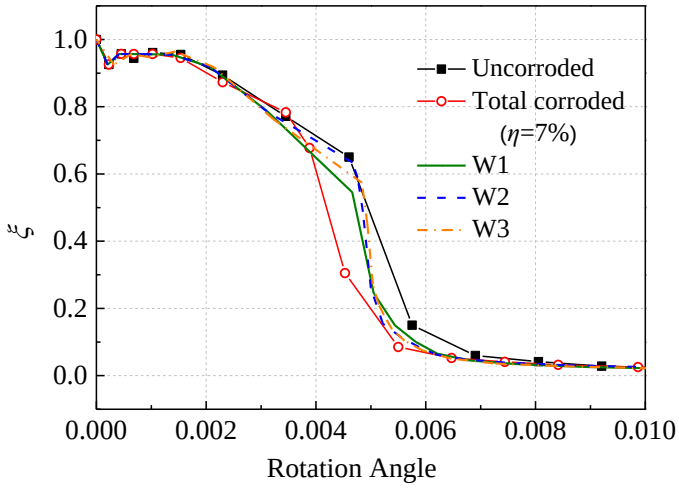


**Fig. 23** Connection stiffness of local corrosion of W

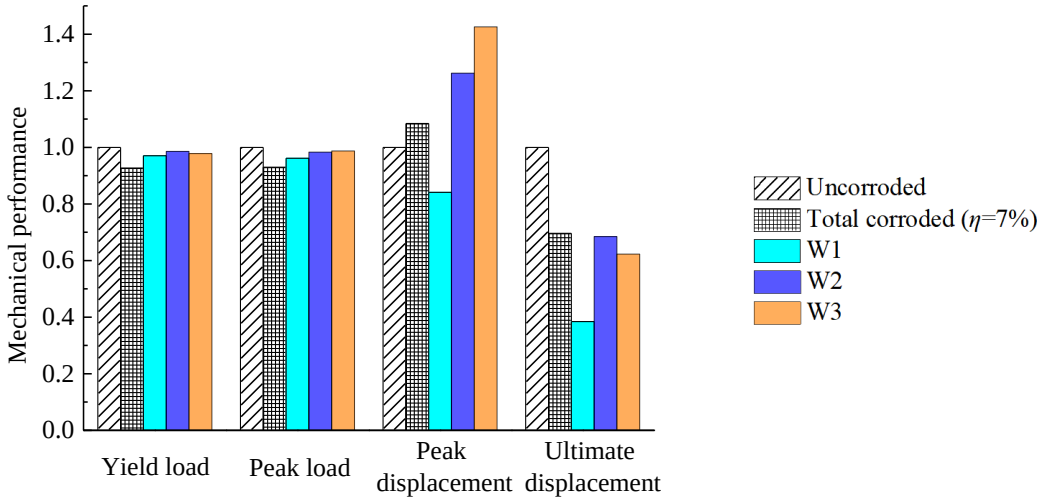


**Fig. 22** Loading and deformation capacity of local corrosion of W

Fig. 25 and Fig. 29 show the specimens' load-displacement curves in the condition of local corrosion of FS and FX, respectively. Fig. 26 and Fig. 30 show the load capacity of specimens in the condition of local corrosion of FS and FX, respectively. In these figures, local corrosion of FS and FX both have a similarly negative effect on the bearing performance of weather-resistant steel beam-to-column connection. Under the condition of local corrosion of FS, the deterioration effect on the bearing capacity comes from tensile damage of steel. Under the condition of local corrosion of FX, the deterioration effect on the bearing capacity comes from the likely local buckling of steel plate. When the distance between the center of local corrosion zone (FS or FX) and the column end is 0.25~0.75 times the beam height, the deterioration effect of local corrosion on the bearing capacity is relatively more significant, which is related to the plastic hinge length at the beam end of the beam-column connection (generally 0.5 times the beam height). Moreover, the closer distance between center of the local corrosion zone and column end, the more significant effect of local corrosion on the deterioration of bearing capacity. For example, for specimens of FS025 and FX025, the bearing capacity decreases by about 4%. When the distance between the center of the local corrosion zone (FS or FX) and column end is larger than 1.25 times the beam height, there will be no effect on the mechanical behavior of the specimen.

Fig. 27 and Fig. 31 show the connection stiffness of specimens in the condition of local corrosion of FS and FX, respectively. In these figures, local corrosion of FS and FX both have a similarly negative effect on the stiffness degradation of weather-resistant steel beam-to-column connection. The deterioration effect of FS corrosion on the rotational stiffness comes from the tensile damage of beam's upper flange, while the the deterioration effect of FX corrosion on the rotational stiffness comes from the likely local buckling of beam's bottom flange. In general, the near distance between the center of local corrosion zone (FS or FX) and the column end results in the relatively severe stiffness degradation.

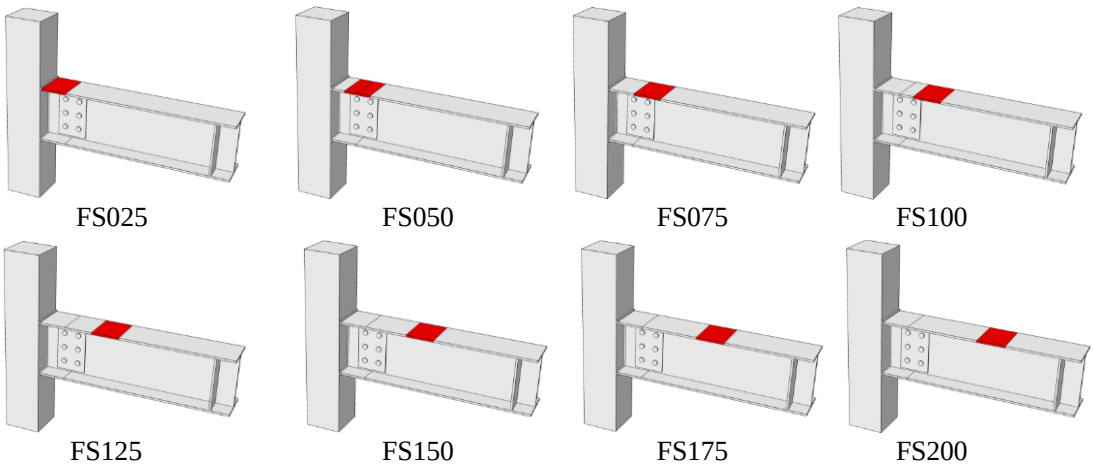


**Fig. 24** Schematic diagram of local corrosion location of FS (red represents corrosion)

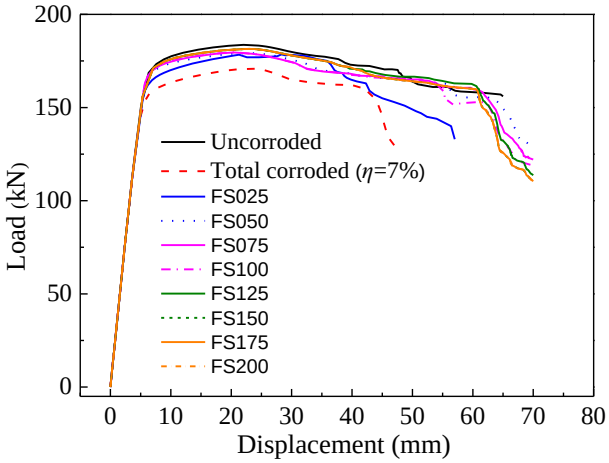


**Fig. 25** Load-displacement curves of local corrosion of FS

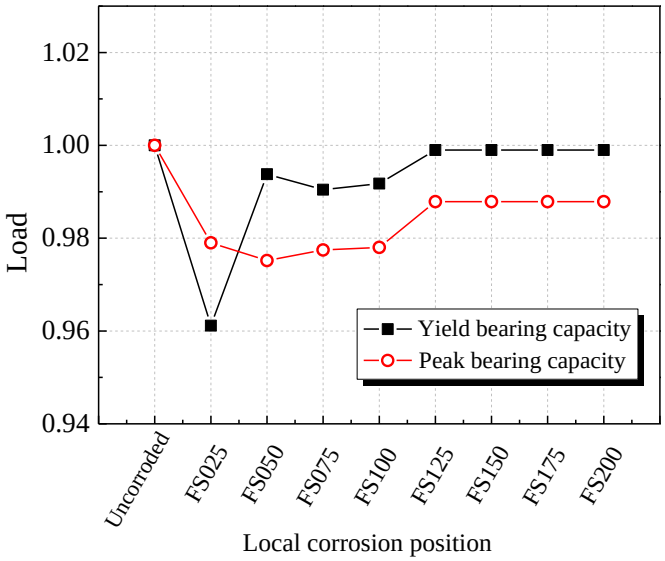


**Fig. 26** Load capacity of local corrosion of FS

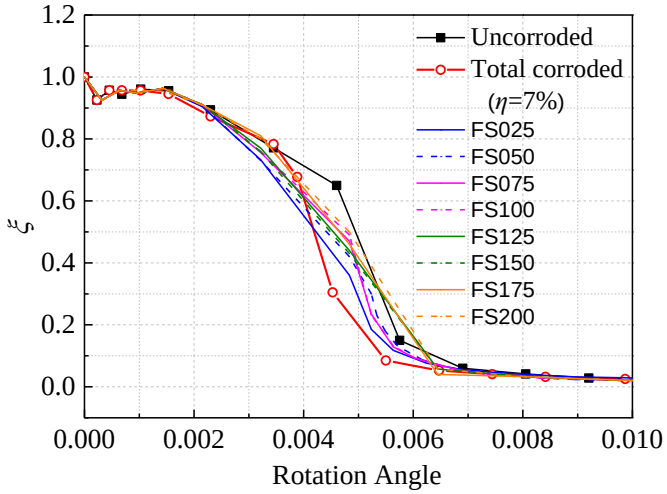


**Fig. 27** Connection stiffness of local corrosion of FS

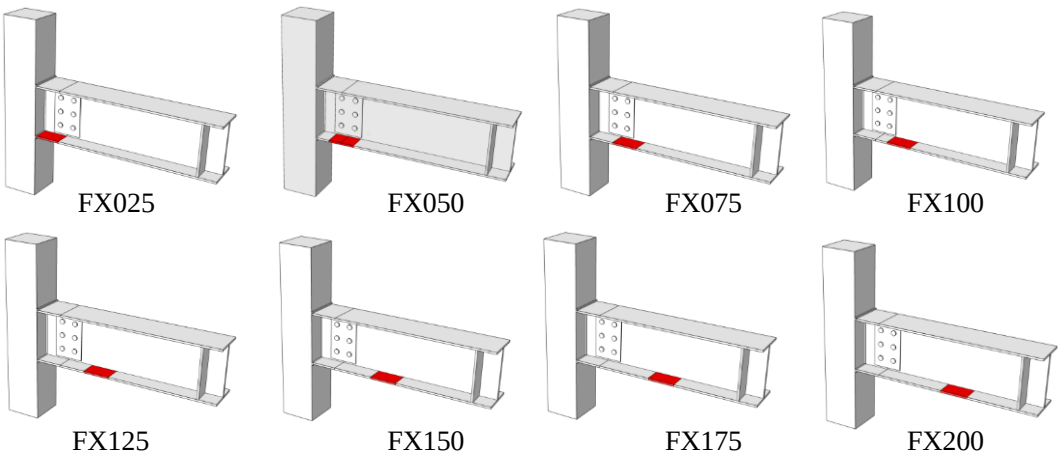


**Fig. 28** Schematic diagram of local corrosion location of FX (red represents corrosion)

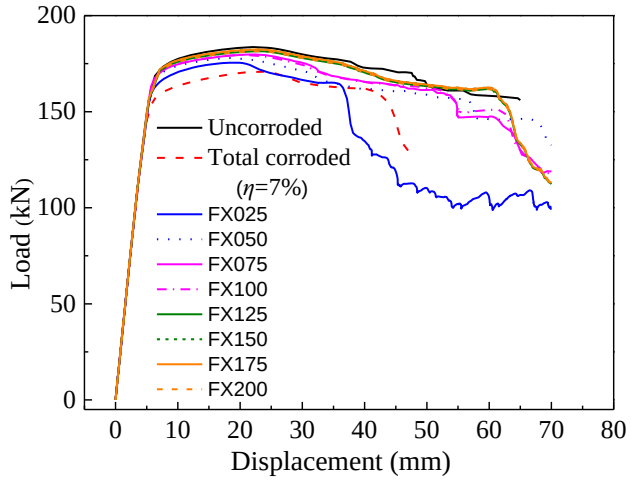


**Fig. 29** Load-displacement curves of local corrosion of FX

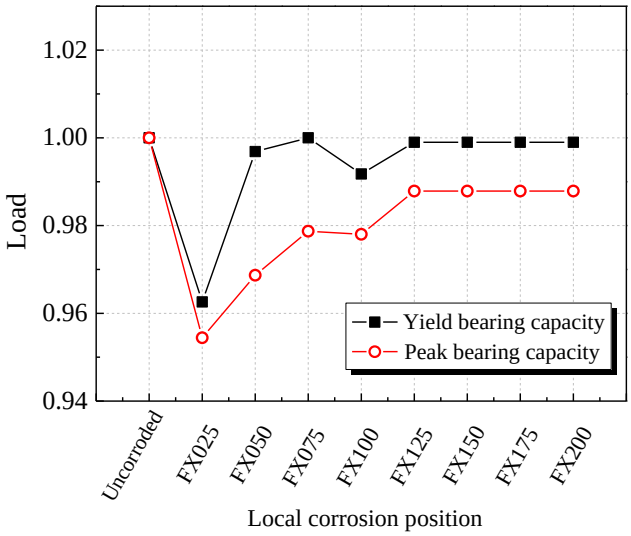


**Fig. 30** Load capacity of local corrosion of FX

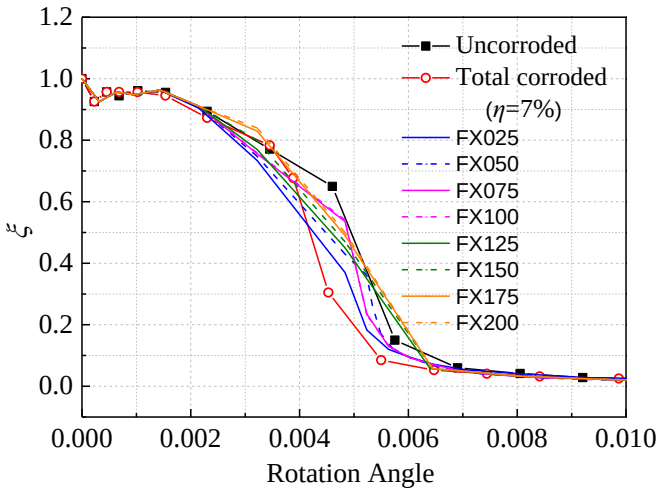


**Fig. 31** Connection stiffness of local corrosion of FX

## 5. Conclusions

Experiments and numerical analysis are carried out on weather-resistant steel beam-to-column connections to investigate the mechanical properties in the corrosive environment. The main findings and conclusions are summarized as follows:

(1) Experimental results show that the weather-resistant steel beam-to-column connection under condition of total corrosion has similar failure mode and plasticity development of the connection under the normal condition. The local plasticity and initial cracking of the specimen mainly develop on beam's upper flange near column end, and the beam web is in an elastic state. Under the same loading condition, the plastic development degree of specimens after total corrosion is higher than that of specimens without corrosion.

(2) Mechanical parameters of weather-resistant steel (including yield strength, tensile strength, yield-to-tensile ratio, and elongation) have a linearly negative relationship with corrosion mass loss. Accordingly, a calculation method of the constitutive model of weather-resistant steel under different corrosion conditions is proposed. Using this method, the mechanical performance and damage development can be truly described.

(3) Under the condition of total corrosion, the bearing capacity, deformation capacity and connection stiffness of weather-resistant steel beam-to-column connections decrease with the increase of corrosion mass loss in the range of 0~7%. The bearing capacity loss of specimens is approximately in the same proportion as the corrosion mass loss (1:1), while the deformation capacity loss of specimens (specifically referring to the ultimate displacement and ductility factor) is four times as much as corrosion mass loss.

(4) The local corrosion of W1 of the weather-resistant steel beam-to-column connection has the most significant effect on the deterioration of the mechanical properties of the connection. With reference to non-corroded specimens, the local corrosion of W1 can lead to 56% reduction in deformation capacity of specimens, which should be paid significant attention to in practical engineering.

(5) When the distance between the center of local corrosion zone (FS or FX) and the column end is 0.25~0.75 times the beam height, the deterioration effect of local corrosion on the bearing capacity is relatively more significant, and closer distance results in more deterioration of bearing capacity. When the distance between the center of the local corrosion zone (FS or FX) and the column end is larger than 1.25 times the beam height, there will be no effect of local corrosion on the mechanical behavior of the specimen.

## Acknowledgments

The authors gratefully acknowledge the financial support from the Jining City Global ranking project (2022JBZP004) and the Science and Technology Planning Project of the Ministry of Housing and Urban-Rural Development of the People's Republic of China (2022-K-145).

## References

[1] Zhang T, Liu W, Chen L, et al. On how the corrosion behavior and the functions of Cu, Ni and Mo of the weathering steel in environments with different NaCl concentrations[J]. Corrosion Science, 2021, 192: 109851.
[2] YANG X, YANG Y,et al. A new understanding of the effect of Cr on the corrosion resistance evolution of weathering steel based on big data technology[J]. Journal of Materials Science and Technology, 2022, 104: 67.
[3] SUN M, DU C, LIU Z, et al. Fundamental understanding on the effect of Cr on corrosion resistance of weathering steel in simulated tropical marine atmosphere[J]. Corrosion Science, 2021, 186: 109427.
[4] Jia J, Liu Z, Cheng X, et al. Development and optimization of Ni-advanced weathering steel: A review[J]. Corrosion Communications, 2021, 2: 82-90.
[5] CHENG X Q, JIN Z, LIU M, et al. Optimizing the nickel content in weathering steels to enhance their corrosion resistance in acidic atmospheres[J]. Corrosion Science, 2017,115:135.
[6] XIAO X M, PENG Y, MA CY, et al. Effects of alloy element and microstructure on corrosion resistant property of deposited metals of weathering steel[J]. International Journal of Iron and Steel Research, 2016, 23(2): 171.
[7] Shi Yongjiu, Yu Xianglin, Ban Huiyong, et al. Research and application on high performance structural steel and its structural system[J]. Building Structure, 2021,51(17):145-151.
[8] FAN Y, LIU W, et al. Evolution of rust layers on carbon steel and weathering steel in high humidity and heat marine atmospheric corrosion[J]. Journal of Materials Science and Technology, 2020, 39: 190.
[9] Chen W J, Hao L, Dong J H, et al. Effect of sulphur dioxide on the corrosion of a low alloy steel in simulated coastal industrial atmosphere[J].Corrosion Science, 2014, 83(7): 155-163.
[10] Gao Xiuhua, Cheng Yujun, Sun Chao, et al. Study on anti-corrosion properties of extra-weathering steel Q350EWR1[J]. Materials Science and Technology, 2019, 27(3):9.
[11] Zong Liang, Zhang Juzheng, Zhao Bo, et al. Study on the mechanical properties of weathering steel Q355NHD after corrosion in an industrial marine atmospheric environment[J]. China Journal of Highway and Transport, 2022, 35(06):168-179.
[12] Guo X Y, Kang J F, Zhu J S, et al. Corrosion behavior and mechanical property degradation of weathering steel in marine atmosphere[J]. Journal of Materials in Civil Engineering, 2019, 31(9): 04019181.
[13] Wu Yaohua, He Wenhui, Wang Houxin. Research on properties and design strength values of weather resistance rolled h-shape steel[J]. Steel Construction, 2019, 34(02):20-30.
[14] Su Han, Zhao Liguo, et al. Study On Fatigue Behavior of Corroded Butt Welded Joints Made of Weathering Steel Q345qDNH[J]. Journal of Building Structures, 2021,42(S2):473-481.
[15] ZHANG Y, ZHENG K, ZHU J, et al. Research on corrosion and fatigue performance of weathering steel and high-performance steel for bridges[J]. Construction and Building Materials, 2021, 289: 123108.
[16] Hu Jie, Huang Cui, He Yaling, et al. Influence of The Match between Weathering Steel Metal and Welding Wire on Stress Corrosion Resistance of Welded Joints[J].Corrosion & Protection, 2018, 39(06):425-430.
[17] Albrecht P, Lenwari A. Fatigue strength of weathered A588 steel beams[J] Journal of Bridge Engineering, 2009, 14(6): 436-443.
[18] Tao Xiaoyan, Shi Zhiqiang, Han Jiyue, et al. Experimental research on high strength bolted

connection of weathering steel bridge[J]. Steel Construction, 2018, 33(01):105-108.
[19] CHEN Y Y, TZEBG H J, WEIB L I, et al. Corrosion resistance and mechanical properties of low-alloy steels under atmospheric conditions[J].Corrosion Science, 2005, 47:1001-1021.
[20] Zhang Lele. Study on corrosion resistance and mechanical properties of weathering steel after corrosion[D]. Hebei University of Science and Technology, 2020.
[21] Zong Liang, Zhang Juzheng, Zhao Bo, Zhang Fujun. Study on the mechanical properties of weathering steel Q355NHD after corrosion in an industrial marine atmospheric environment[J]. China Journal of Highway and Transport, 2022, 35(06):168-179.
[22] Zhang Yu. Research on corrosion fatigue properties of weathering steel and high performance steel[D]. Southwest Jiaotong University, 2020.
[23] Zeng L, Zhang W, Li H. Low-cycle fatigue life prediction of I-shaped steel brace components and braced frames[J]. Thin-Walled Structures, 2021, 163: 107711.

**Advanced Steel Construction** – Vol. 20 No. 3 (2024) 266–279
**DOI:**10.18057/IJASC.2024.20.3.6


# BEHAVIOR AND DESIGN OF COLD-FORMED SQUARE AND RECTANGULAR HOLLOW SECTIONS BASED ON EFFECTIVE PLASTIC WIDTH METHOD

Shuo Ren [1], Xin Cheng [1, *], Xia-Xin Wang [2] and Li-Jun Zhuang [3]

[1] *Department of Civil Engineering, Taiyuan University of Technology, Taiyuan, 030024, China*
[2] *School of Civil Engineering, Southeast University, Nanjing, 210096, China*
[3] *China Shanxi Sijian Group Co., Ltd., Taiyuan, 030006, China*
** (Corresponding author: E-mail: xchengtyut@126.com)*

**ABSTRACT**

Due to the rapid development of cold-forming technology, the application of cold-formed steel members with square hollow sections (SHS) and rectangular hollow sections (RHS) in constructing steel structures is increasingly developing. For practical application, it is of great significance to study the ultimate behavior of cold-formed SHS and RHS steel tubes with different plate thicknesses systematically. In this paper, finite element models considering initial geometric defects, residual stress, and cold-formed effect were established and validated against available test data. Parametric analysis was then conducted considering various width-to-thickness ratios of flange and web and axial force ratios. The influences of the parameters on the ultimate capacity, failure mechanism, and stress development were carefully explored using the results of parametric analysis. The effective plastic width method (EPM) was introduced to calculate the ultimate capacity, taking strain hardening, interactive effect of the plates, and local buckling into account. Finally, the accuracy of EPM was verified through comparison with current specifications and parametric analysis results.

**ARTICLE HISTORY**

Received: 26 July 2023
Revised: 22 February 2024
Accepted: 23 February 2024

**KEYWORDS**

Ultimate capacity;
Cold-formed SHS and RHS;
Effective plastic width method;
Parametric analysis;
Interactive effect of plates



## 1. Introduction

Cold-formed square hollow sections (SHS) and rectangular hollow sections (RHS) are widely utilized due to their excellent rigidity, corrosion resistance, fire protection, and manufacturing efficiency [1]. With improvement in the cold-forming process, the thickness of cold-formed SHS and RHS has been significantly extended, even reaching 25 mm [2-4]. Therefore, the research on the bearing capacity of cold-formed SHS and RHS steel members has recently received extensive attention, especially on those members composed of relatively thick sections [5-9].

Numerous researchers have engaged in studies to validate the accuracy of the ultimate capacities computed for cold-formed SHS and RHS members according to the Chinese design standard GB50018-2002 [10] (abbreviated as GB50018) and the European code EC3-part1-1 [11] (abbreviated as EC3). It is noted that the current GB50018 is applicable to members with a thickness ranging from 2 to 6 mm. Wu et al. [12] and Shen [13] demonstrated that the predictions from GB50018 for the compressive capacity of the members within the specified thickness range were conservative. Li et al. [14], Wen et al. [15], and Hu et al. [16] indicated that the applicability of GB50018 to steel members with a thickness beyond 6 mm was still controversial. Regarding EC3, Wang et al. [17] and Ma et al. [18-20] showed that EC3 was risky for slender sections but prudent for compact ones. Nseir [21] also reported that the section classification limitations in EC3 were not directly applicable to cold-formed steel members. Moreover, the calculation method of EC3 would lead to discontinuity in the bearing capacity of the sections classified as classes 2 and 3 by neglecting the partial plastic development in class 3 sections. Therefore, conducting a thorough study on the ultimate bearing capacity of cold-formed SHS and RHS steel members is necessary.

Many researchers have investigated the bearing capacity of cold-formed SHS and RHS steel tubes experimentally and numerically. For the ultimate compressive capacity, Hou [22] conducted experimental tests and finite element (FE) simulations to obtain the axial compressive capacity of thick-walled columns, and proposed modified formulas for calculating the bearing capacity. Li et al. [14] carried out reliability analysis based on experimental tests and FE analyses, subsequently recommending appropriate partial resistance factors and strength design values for Q235 and Q345 steels. Yao et al. [23] stated that GB50018 could be used to design members with a plate thickness of less than 2 mm. In another work, Wen et al. [15] conducted axial compression tests on thick-walled members, proposed methods for calculating the section yield strength considering the cold bending effect, and demonstrated that GB50018 was conservative. Through experimentation and numerical simulation, Ma et al. [18, 19] proposed an improved direct strength method to calculate the ultimate bearing capacity for high-strength members.

The ultimate capacity of members under combined compression and bending is primarily based on testing or numerical simulation considering eccentric compression. Nseir [21] conducted experiments and FE studies on cold-formed SHS and RHS steel tubes under various loading conditions and proposed an overall interaction method. Yun and Gardner [24] developed a continuous strength method suitable for thick-walled members. Deng [25] also proposed a continuous strength method for thin-walled members. Ma et al. [20, 26] studied the bearing capacity of high-strength members under eccentric compression and revealed that the predictions of the current specifications were 13%–21% lower on average. In addition, Li et al. [27] experimentally examined high-strength, thin-walled members under axial compression and showed that the influence of the interactions of the plates on the compressive capacity should not be ignored. Chen et al. [28, 29] proposed a formula for calculating the constraint coefficient of the plates and critical stress when reaching buckling. Wu et al. [12] determined the stress redistribution of the compressive plate at the ultimate moment and analyzed the plate group effect after the buckling of the rectangular tube. However, these calculations were complex and not easy to use.

Chen et al. [30] introduced the effective plastic width method (EPM) to estimate the ultimate capacity of H-section members subjected to combined compression and bending around the strong axis. This approach was later expanded by Cheng et al. [31] to calculate the bearing capacities of H-section members with combined compression and bending. Shi et al. [32] then utilized EPM to assess the bearing capacity of cold-formed SHS members. EPM operates on the premise that the entire effective section can achieve plasticity, enabling the calculation of the ultimate capacity according to the given stress distribution of the section at the limit state. Compared with other methods, EPM can better consider the influence of interactive effect, local buckling of plates and the strain hardening of section. Furthermore, EPM's applicability is not confined by the classification of sections, leading to more precise and straightforward calculations. Consequently, employing EPM for calculating the ultimate capacity of cold-formed SHS and RHS steel pipes is considered practical and effective.

Considering the research conducted so far, the study of the bearing capacities of cold-formed SHS and RHS steel tubes under compression and combined compression and bending is found to be inadequate. The current computational methods suffer from inadequate consideration of plastic development of section and strain hardening, as well as the interactive effect of plates, resulting in inaccuracies in bearing capacity calculations. Therefore, this paper aims to propose a comprehensive method for calculating the ultimate capacity of members subjected to combined compression and bending based on EPM, taking into account the above aspects.

This paper studies the ultimate capacity of cold-formed SHS and RHS steel members under axial compression and combined compression and

bending, covering different width-to-thickness ratios of the flange and web. The failure mechanisms of members under axial compression and combined compression and bending are summarized, and the stress development law during the loading process is revealed. The EPM for calculating the ultimate capacity taking into account the interactive effects of the plates is also established.

## 2. Establishment and verification of FE models

### *2.1. Establishment of FE models*

The detailed modeling procedure can be referred to Shi et al. [32]. Fig. 1 depicts the FE simulation of the members considering three loading modes, where *w* and Δ respectively represents the axial and lateral displacement of the column top, respectively, and *l* represents the column length. In this paper, the eccentric compression loading mode (Fig. 1b) is used to verify the developed FE model, while the cantilever bending mode (Fig. 1c) is used for parametric analysis. The geometric definition of the section is shown in Fig. 2. The element type of the FE model is S4R shell element, and the mesh size settlement and boundary conditions are illustrated in Fig. 3. In parametric analysis, the first buckling mode (the most unfavorable mode) with an odd number of buckling waves along the length of the column is selected to simulate the initial geometric imperfection, and the amplitude of the defect is taken as min (B/200, H/200) [33]. During the FE model verification, the measured data on material properties and residual stresses are incorporated as inputs. The material model proposed by Gardner and Yun [34] is employed for conducting parametric studies. This model assigns distinct stress-strain characteristics to the corners and flat plates of a structure respectively, deliberately excluding the extension of corner material characteristics. It enhances the Ramberg-Osgood model by integrating findings from extensive material property tests on various cold-formed sections with a range of yield strengths and thicknesses. It is adept at accounting for the diverse strengths, thicknesses, and shapes of cold-formed steels, as well as the cold-formed effect of sections [2,24,32], as illustrated in Fig. 4. For parametric analysis, the longitudinal bending residual stress model proposed by Somodi and Kovesd [38] is applied to assess the impact of residual stress on the component behavior [36,37], as depicted in Fig. 5. This model, validated by tests on both thin-wall and thick-wall cold-formed steel, is noted for its broad applicability and conservative nature due to its assumption of significant longitudinal residual stress amplitudes.

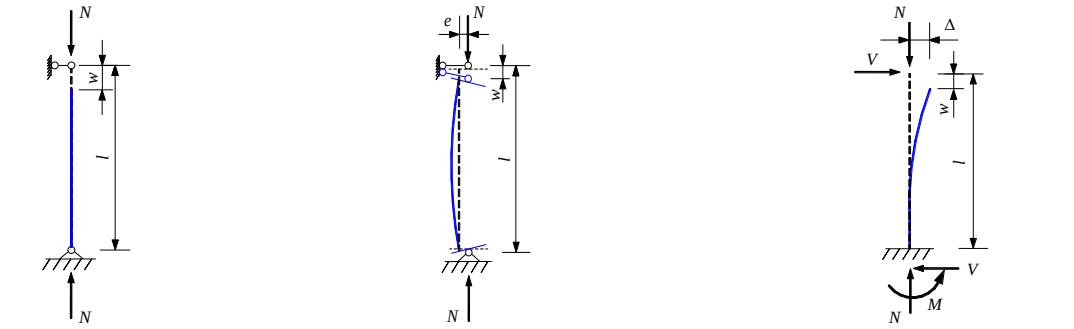


(a) Axial compression (b) Eccentric compression (c) Combined compression and bending

**Fig. 1** The loading modes

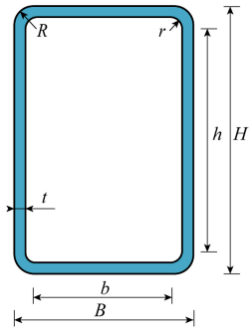


**Fig. 2** The geometric dimensions of the section

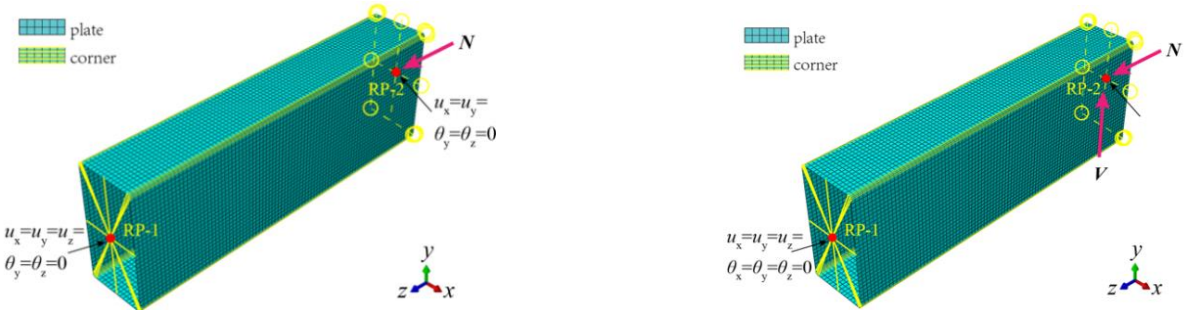


(a) Members subjected to axial compression and eccentric compression (b) Cantilever members subjected to combined compression and bending

**Fig. 3** Mesh generation and boundary conditions

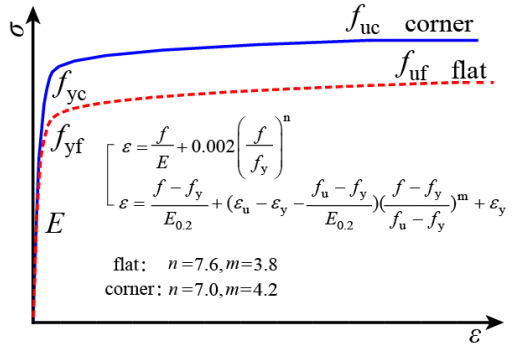


**Fig. 4** The material properties

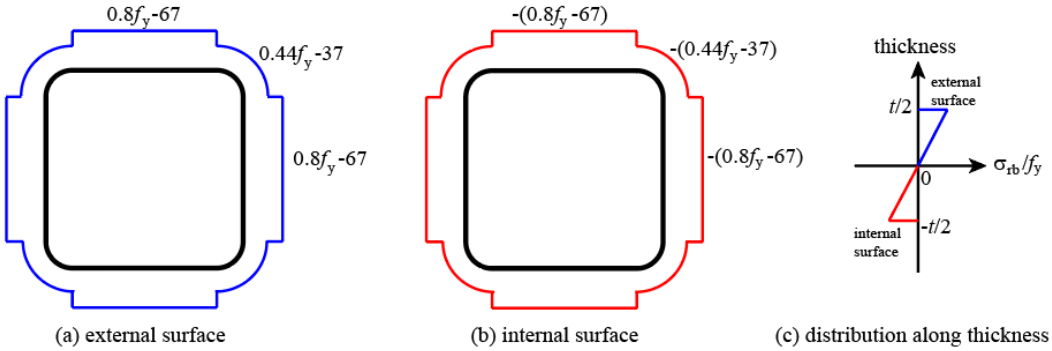


**Fig. 5** The residual stress model

### 2.2. Verification of FE model

In this paper, existing experimental data were summarized to verify the FE model. The basic information of the test specimens is shown in Table 1, where $N_{u,test}$ and $N_{u,FE}$ are the ultimate capacities obtained by test and FE simulation respectively. The failure modes, load-displacement curves ($N$-$w$) and ultimate capacity of the FE model were extracted and compared with the test results, depicted in Figs. 6–8. The comparison results indicate that the FE model can accurately simulate the failure modes, ultimate capacities, and overall trend of the members' behavior throughout the curve. Slight differences in $N$-$w$ curves can result from dimensional errors and alignment errors, among other factors. Thus, the model could accurately simulate the compressive and bending behavior of cold-formed SHS and RHS members.

**Table 1**
Basic information of specimens

| Reference | Specimen number | Steel | $B$ (mm) | $H$ (mm) | $t$ (mm) | $l$ (mm) | $e$ (mm) | $N_{u,test}$ (kN) | $N_{u,FE}$ (kN) | $N_{u,test}$ / $N_{u,FE}$ |
|---|---|---|---|---|---|---|---|---|---|---|
| Nseir [21] | Stub_200 × 100 × 4 | S355 | 100 | 201 | 3.7 | 600 | 0 | 761 | 741 | 0.974 |
| | Stub_220 × 120 × 6 | | 120 | 221 | 5.9 | 600 | 0 | 1648 | 1627 | 0.987 |
| | Stub_200 × 200 × 5 | | 201 | 200 | 4.7 | 600 | 0 | 1296 | 1307 | 1.008 |
| | Stub_200 × 200 × 6 | | 200 | 200 | 5.9 | 600 | 0 | 1957 | 1934 | 0.988 |
| | LC2_200 × 200 × 5 | | 200 | 201 | 4.9 | 700 | 77 | 816 | 816 | 1.004 |
| | LC2_200 × 200 × 6 | | 200 | 200 | 6.1 | 700 | 72 | 1179 | 1150 | 0.976 |
| | LC2_200 × 100 × 4 | | 101 | 200 | 4.0 | 700 | 60 | 597 | 613 | 1.027 |
| | LC2_220 × 120 × 6 | | 121 | 219 | 6.3 | 700 | 67 | 1160 | 1133 | 0.977 |
| | LC4_200 × 100 × 4 | | 200 | 101 | 4.1 | 700 | 35 | 471 | 459 | 0.975 |
| | LC4_220 × 120 × 6 | | 220 | 120 | 6.2 | 700 | 40 | 972 | 963 | 0.991 |
| Hou [22] | SC1 | Q345 | 140 | 140 | 10.0 | 820 | 0 | 2650 | 2631 | 0.993 |
| | SC2 | Q345 | 150 | 150 | 8.0 | 850 | 0 | 2466 | 2547 | 1.033 |
| | SC3 | Q235 | 200 | 200 | 8.0 | 1000 | 0 | 2807 | 2754 | 0.981 |
| | SC4 | Q235 | 200 | 200 | 12.0 | 1000 | 0 | 3606 | 3824 | 1.040 |
| | SC5 | Q345 | 200 | 200 | 16.0 | 1000 | 0 | 5873 | 5876 | 1.000 |
| Gardner et al. [39] | SHS-100-100-4 | Q235 | 101 | 101 | 3.6 | 405 | 0 | 660 | 659 | 0.998 |
| | SHS-60-60-3 | | 60 | 60 | 2.8 | 245 | 0 | 249 | 247 | 0.992 |
| | RHS-60-40-4 | | 60 | 40 | 4.0 | 245 | 0 | 370 | 349 | 0.943 |
| | SHS-40-40-4 | | 40 | 40 | 3.8 | 165 | 0 | 256 | 245 | 0.957 |
| | SHS-40-40-3 | | 40 | 40 | 2.8 | 165 | 0 | 224 | 215 | 0.960 |

| Reference | Specimen number | Steel | $B$ (mm) | $H$ (mm) | $t$ (mm) | $l$ (mm) | $e$ (mm) | $N_{u,test}$ (kN) | $N_{u,FE}$ (kN) | $N_{u,test}$ / $N_{u,FE}$ |
|---|---|---|---|---|---|---|---|---|---|---|
| Hu et al. [40] | | Q345 | 250 | 250 | 9.3 | 910 | 0 | 3600 | 3550 | 0.986 |
| | | | 250 | 250 | 9.2 | 910 | 0 | 3725 | 3905 | 1.048 |
| | | | 250 | 250 | 9.2 | 910 | 0 | 3650 | 3588 | 0.983 |
| | | | 300 | 200 | 9.2 | 909 | 0 | 3490 | 3586 | 1.028 |
| | | | 300 | 200 | 9.3 | 912 | 0 | 3350 | 3257 | 0.972 |
| | | | 300 | 200 | 9.2 | 909 | 0 | 3340 | 3257 | 0.975 |
| Sun et al. [41] | | 690 | 152 | 152 | 8.0 | 498 | 0 | 3734 | 3757 | 1.006 |
| | | 350 | 152 | 152 | 13.0 | 500 | 0 | 3873 | 3817 | 0.985 |
| | | 350 | 152 | 152 | 6.4 | 600 | 0 | 1711 | 1739 | 1.017 |
| Chen [42] | | Q235 | 250 | 250 | 9.0 | 500 | 0 | 2820 | 2874 | 1.019 |
| | | | 300 | 200 | 8.0 | 500 | 0 | 2430 | 2344 | 0.965 |
| Gao [43] | | Q235 | 250 | 100 | 8.0 | 500 | 0 | 1860 | 1886 | 1.014 |
| | | | 200 | 200 | 8.0 | 500 | 0 | 2320 | 2225 | 0.959 |

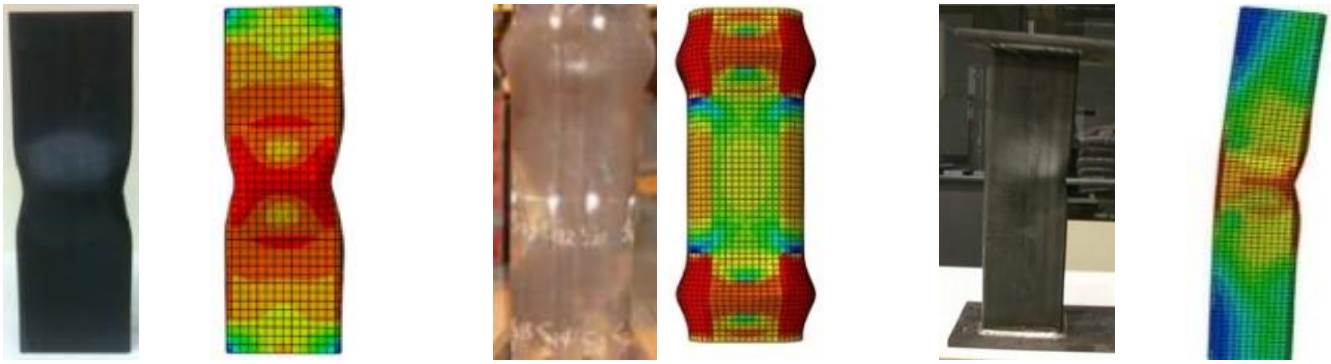

(a) Stub_200 × 200 × 5 (b) SC5 (c) LC2_200 × 200 × 5

**Fig. 6** Comparisons of failure modes of typical members [21,22]

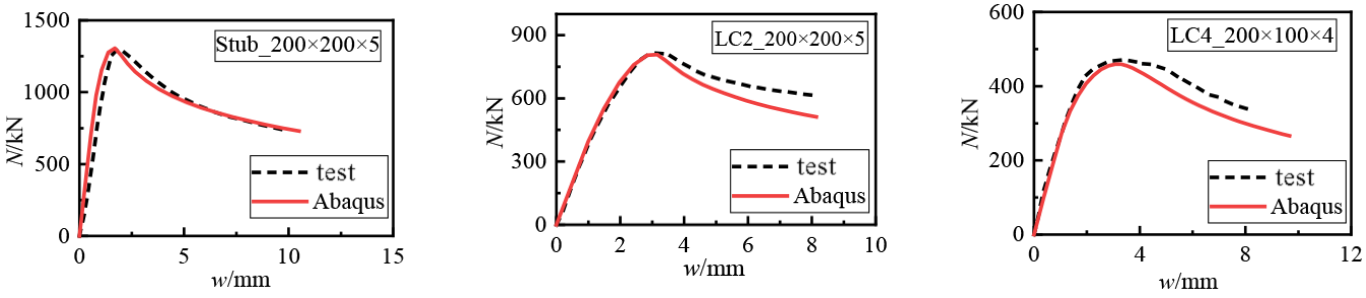


(a) Stub_200 × 200 × 5 [21] (b) LC2_200 × 200 × 5 [21] (c) LC4_200 × 100 × 4 [21]

**Fig. 7** Comparison results of *N*-*w* curves

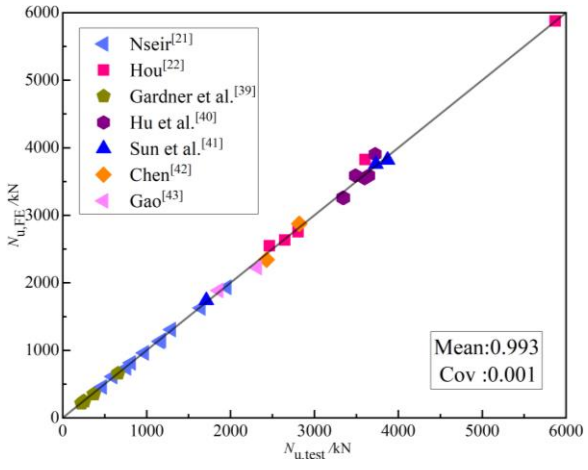


**Fig. 8** Comparison results of ultimate capacities from tests and FE models

### *2.3. Settings of parametric studies*

In order to explore the influences of the axial force ratio ($n$) and the width-to-thickness ratios of the flange ($r_f$) and web ($r_w$) on the ultimate capacity of the cold-formed SHS and RHS members, the parameters of specimens with different combinations of $r_f$, $r_w$, and $n$ were analyzed in this paper. The definitions of the parameters are shown in Table 2.

**Table 2**
Definitions of parameters

| Parameter | $r_f$ | $r_w$ | $\alpha$ | $n$ |
|---|---|---|---|---|
| Definition | $r_f = \frac{b}{t\varepsilon_k}$ | $r_w = \frac{h}{t\varepsilon_k}$ | $\alpha = \frac{h}{b}$ | $n = \frac{N}{N_y}$ |

Note: $\varepsilon_k = \sqrt{f_y/235}$, is the steel grade correction factor. $N_y = Af_{yf}$, indicates the yield axial load.

The settings of parametric studies are tabulated in Table 3. $H$ = 300 mm, $l$ = 3$H$ = 900 mm, and $r$ = 1.5$t$ are consistent for all the parametric models. By

changing the section thickness $t$, flange width $B$ and axial pressure force $N$, the combinations of $r_f$, $r_w$, and $n$ are realized. Finally, 1336 FE models were obtained by parameter grouping, which include most of the cases that may occur in engineering and some cases that are impossible to occur but can be used as a comparison group in this study. In parametric analysis, the yield strength $f_y$ and ultimate tensile strength $f_u$ of the flat are 355 MPa and 442 MPa, respectively. For the corner, $f_y = 444$ MPa and $f_u = 523$ MPa. The axial compression member was named C-$\alpha$-$r_f$ (C indicates axial compression), and the member subjected to combined compression and bending was labeled BC-$\alpha$-$r_f$ (BC denotes combination of compression and bending).

**Table 3**
Parameter settings of sections

| Parameter | Value |
|---|---|
| $r_f$ | 10 15 20 25 30 35 40 45 50 55 60 65 70 75 80 85 90 95 100 105 |
| $\alpha$ | 1 1.25 1.5 1.75 2 2.25 2.5 2.75 3 |
| $n$ | 0 0.1 0.2 0.3 0.4 0.5 0.6 0.7 0.8 0.9 |

## 3. Results of FE modeling

### 3.1. Failure modes

#### 3.1.1. Members under axial compression

Under axial compression, two distinct types of failure modes are commonly observed in the members: (1) the whole section of the member can reach the yield stress at the ultimate state, i.e., fully plastic failure (PF) and (2) local elastic-plastic buckling failure (EF).

Fig. 9 shows the failure process of typical members C-1-20, C-2.5-20, and C-2.5-40, including the Mises-stress nephogram at two critical states, the dimensionless load-displacement curve, and the mean stress development process at critical states, through which the development mechanism of local buckling and bearing capacities of the components with different failure modes are studied. The ultimate state refers to the moment when the member reaches ultimate capacity, and the final state refers to the moment when the bearing capacity drops to 80% of the ultimate capacity. The occurrence of local buckling is determined when mean stress (σ) reaches its maximum value.

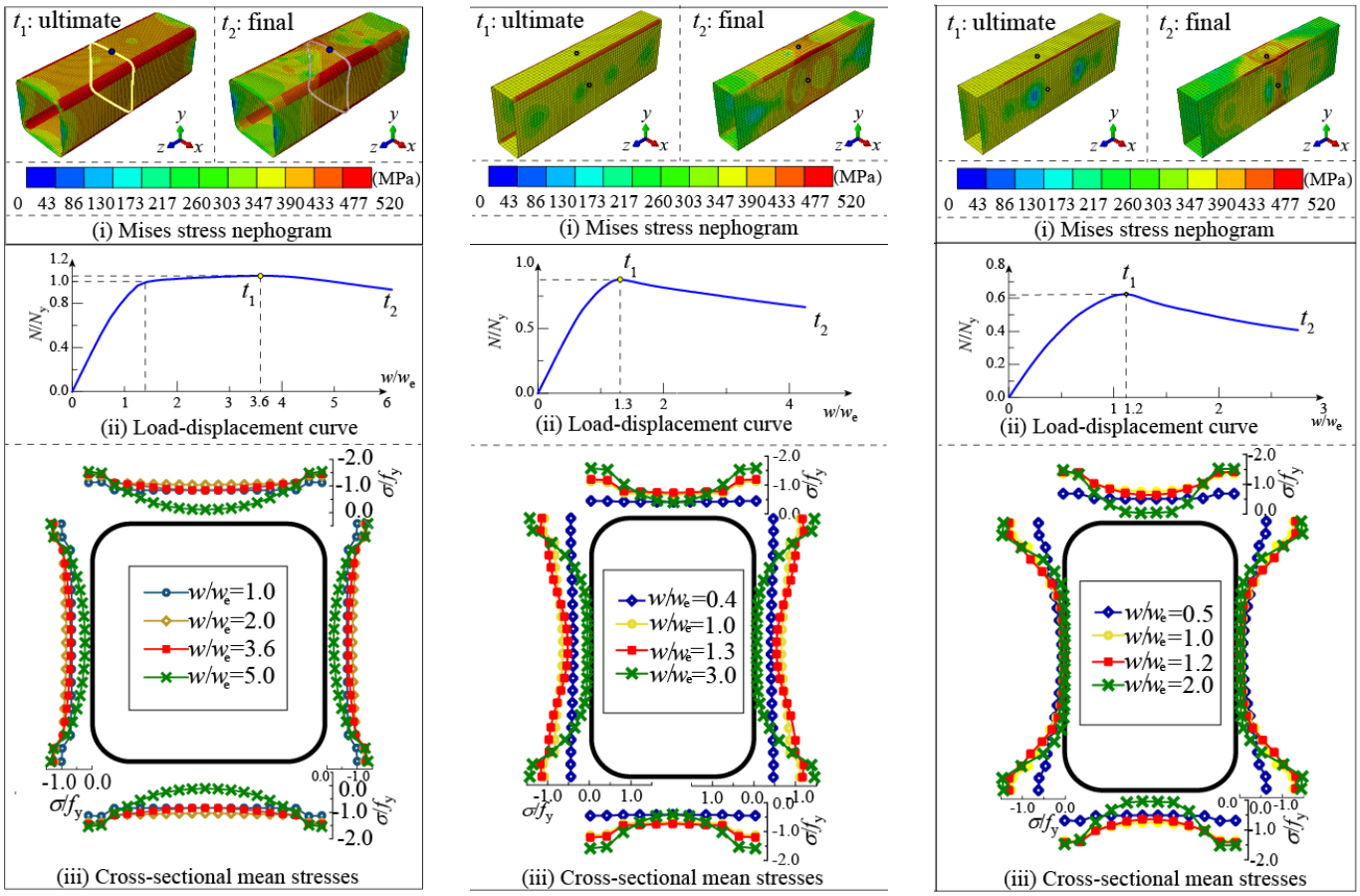


(a) C-1-20 (PF) (b) C-2.5-20 (EF) (c) C-2.5-40 (EF)

**Fig. 9** Failure process of typical axial compression members

According to Fig. 9(a), C-1-20 occurs PF. The mean stress has reached the yield stress when $w/w_e$ = 2.0, and the bearing capacity can further increase due to the cold-formed effect and strain hardening. When $w/w_e$ = 3.6, slight plastic local buckling deformation is developed in the middle of plate, and the total stress of whole section reaches the maximum bearing capacity. At the final state, the section exhibits significant plastic deformation, but the decrease in bearing capacity is minimal, indicating that such sections possess excellent bearing capacity and ductility. According to Figs. 9(b) and 9(c), C-2.5-20 and C-2.5-40 experience EF, and the ultimate capacity of such members cannot reach the yield-bearing capacity. More specifically, at the ultimate state of C-2.5-20 ($w/w_e$ = 1.3), the stress in the middle of the web begins to decrease, demonstrating that elastic buckling occurs on the webs. While for C-2.5-40, at the ultimate state ($w/w_e$ = 1.2), both the flange and the web experience elastic local buckling. Compared with C-2.5-20, the web of C-2.5-40 undergoes severe local buckling at an earlier stage and has a more restricted critical buckling stress.

Therefore, the buckling degrees of plates in members subjected to axial compression is directly related to their width-to-thickness ratios. The higher the width-to-thickness ratio, the earlier local buckling occurs and the smaller critical local buckling stress. With the increase of the width-to-thickness ratios of the flange and web, the failure mode changes from PF to EF, and the bearing capacity and ductility also decrease.

#### 3.1.2. Members under combined compression and bending

Despite the aforementioned failure modes for members under compression (PF and EF), members subjected to combined compression and bending exhibited elastic local buckling under axial pressure yet retained a degree of bending capacity due to post-buckling strength, leading to a compressive buckling failure (CB). Fig. 10 shows the failure mode process of typical components, namely, BC-1.25-40-0, BC-1.25-60-0.2, and BC-2.5-60-0.4, where $M_{ec}$ and $M_{pc}$ are the bending moment of edge yield and full-section plastic considering the axial pressure, respectively, and $\Delta_e$ is theoretical edge yield displacement. The failure mechanism and bearing performance of the members can be thoroughly examined through the analysis of bearing capacities of the components and changes of mean stress.

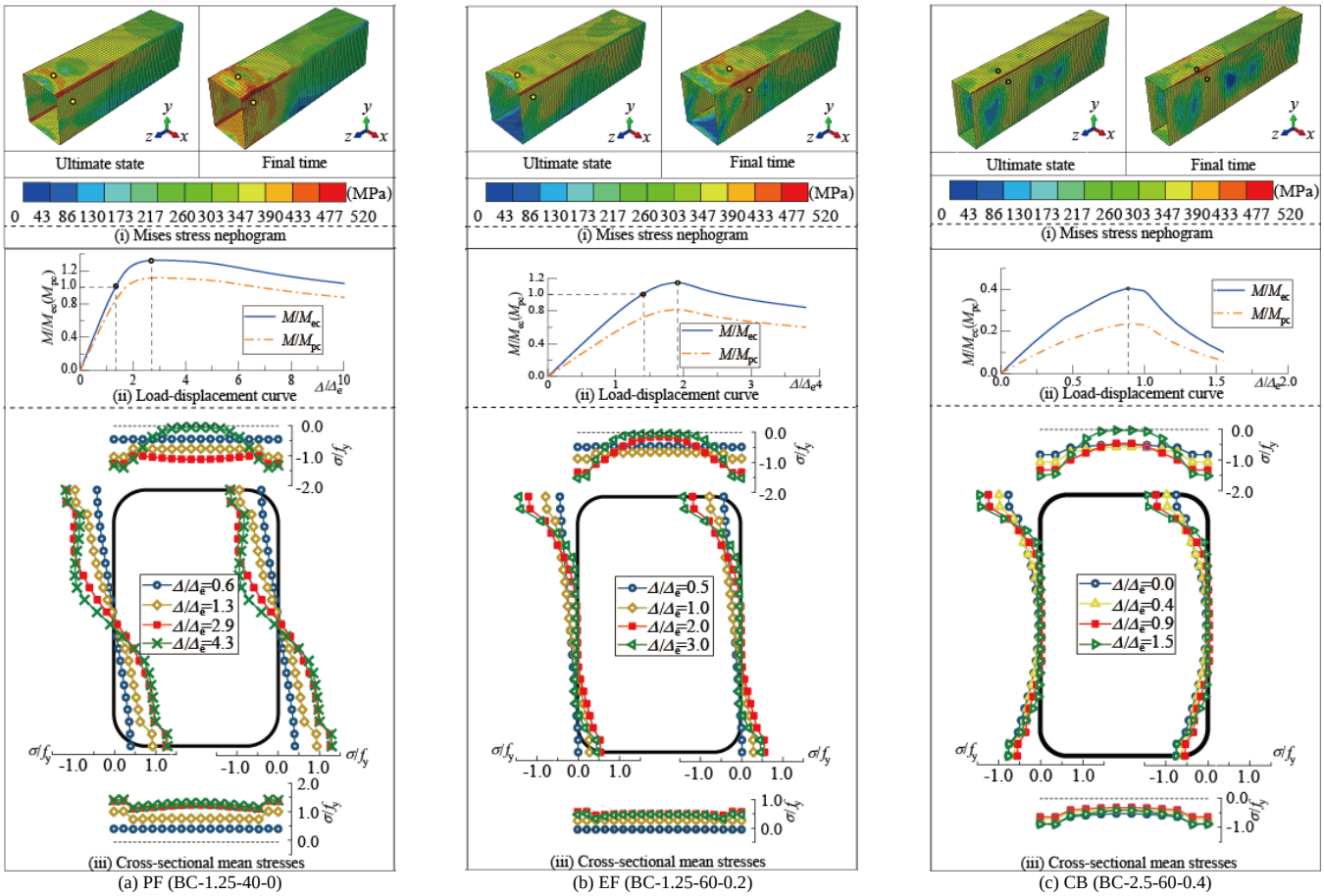


(a) PF (BC-1.25-40-0) (b) EF (BC-1.25-60-0.2) (c) CB (BC-2.5-60-0.4)

**Fig. 10** Failure process of the typical members subjected to combined compression and bending

For BC-1.25-40-0, with relatively small flange width-to-thickness and aspect ratios, the whole section can develop plasticity at the ultimate state, allowing the ultimate capacity to reach $M_{pc}$. BC-1.25-60-0.2, with relatively large flange width-to-thickness and aspect ratios, the elastic local buckling of the compressive flange and web occurs before the ultimate state. Its ultimate capacity reaches $M_{ec}$ but is less than $M_{pc}$. For BC-2.5-60-0.4, with large width-to-thickness ratios and axial force ratio, after the local elastic buckling occurs under axial pressure force, the local buckling of the compressive flange and web is further developed under the bending moment, while the local buckling of tensile flange tends to decrease. The ultimate capacity and ductility of this type of section are substantially limited, resulting in an ultimate capacity that is lower than $M_{ec}$.

Since the stress condition at the ultimate state is a direct reflection of the ultimate capacity of section, the stress at the ultimate state of typical section is extracted and compared to investigate the influence of various parameters on the ultimate capacity, as depicted in Fig. 11 and Fig. 12 according to the axial force ratio and plate width-to-thickness ratio, respectively. It is evident from Fig. 11 that the axial force ratio has little effect on the stress distribution of the compressive flange, but has significant effects on the web. Fig. 12(a) shows the stress distribution of the four members with the same flange width-to-thickness ratio and axial force ratio but different web width-to-thickness ratios, where it is observed that the specimens with larger web width than thickness have less web stress at the ultimate state. The interactive effect of plates, specifically, the smaller the width-to-thickness ratio of web, the greater constraining effect on the compressive flange with a similar $r_f$, leading to an increased stress in the compressive flange, is verified under this loading condition. Similarly, Fig. 12(b) shows that the stress of compressive flange decreases gradually at the ultimate state with an increase of the flange width-to-thickness ratio. It was shown that the smaller the flange width-to-thickness ratio, the more significant constraining effect on web, resulting in higher stress on the web. To sum up, the combination of $n$, $r_f$,and $r_w$ exerts complex interactive effects on the failure modes and ultimate capacities of the members under any of the loading conditions discussed in the paper.

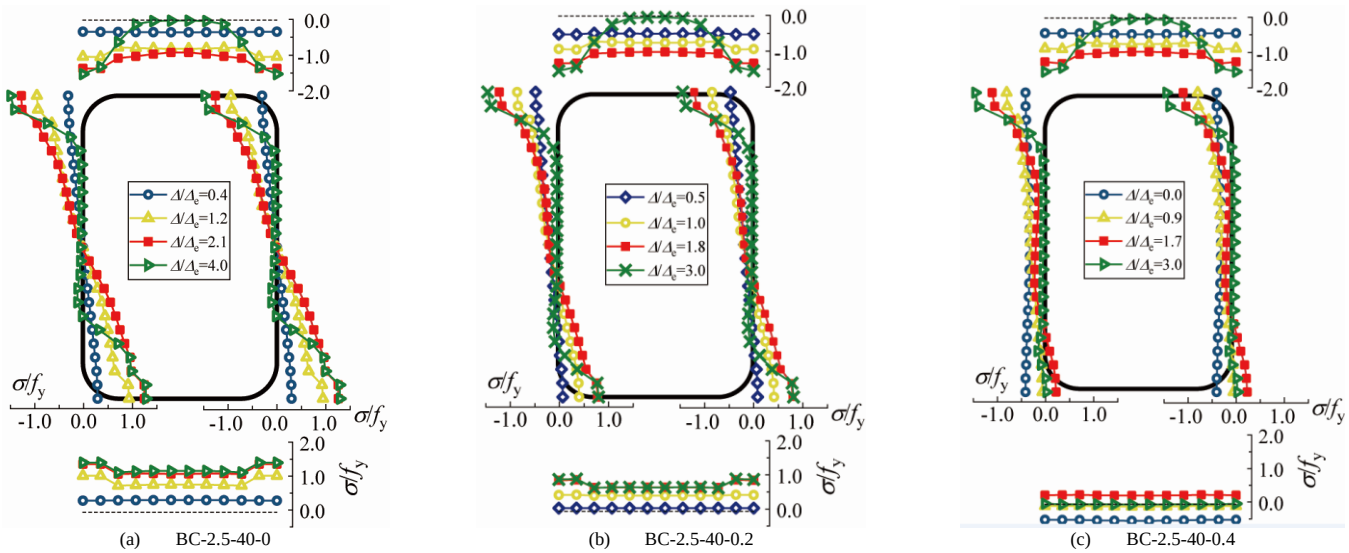


(a) BC-2.5-40-0 (b) BC-2.5-40-0.2 (c) BC-2.5-40-0.4

**Fig. 11** Effects of the axial force ratios on stress distribution

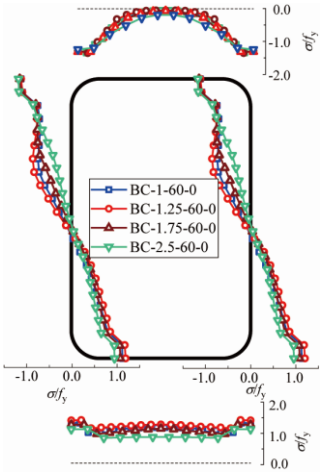


(a) Effects of $r_f$ on stress distribution.

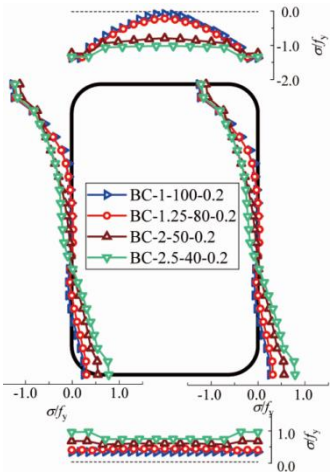


(b) Effects of $r_w$ on stress distribution.

**Fig. 12** Effects of width-to-thickness ratios of webs and flanges

### 3.2. Ultimate capacity

#### 3.2.1. Ultimate compressive capacity

As depicted in Fig. 13(a), the dimensionless ultimate compressive capacity $N_u/N_y$ represents the plastic development degree at the ultimate state. $N_u/N_y$ decreases with an increase of width-to-thickness ratio of the flange as well as aspect ratio. The members with $N_u/N_y \geq 1$, as ranged with the orange area in Fig. 13(b), can achieve the full-section plasticity with certain strengthening. While for the members with $N_u/N_y<1$, as listed in the yellow area in Fig. 13(b), partially plastic effective sections can be reached at the ultimate state, providing a theoretical basis for the model of the axial compressive stress distribution of EPM.

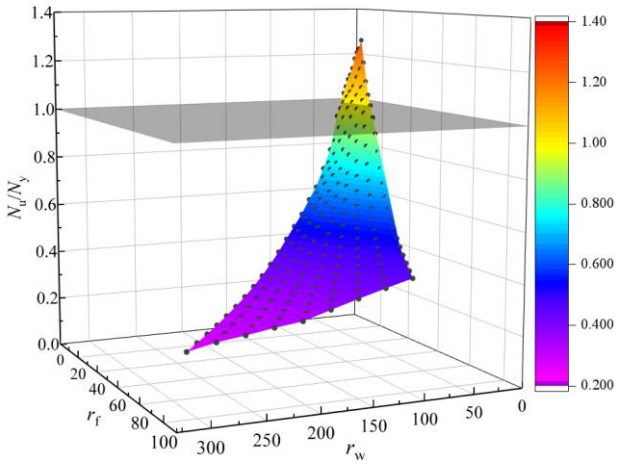


(a) Relationship between $N_u/N_y$, $r_f$,and $r_w$

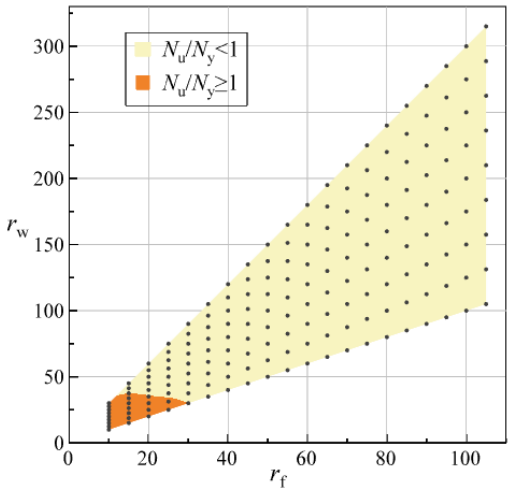


(b) Projection of the three-dimensional diagram

**Fig. 13** The dimensionless ultimate compressive capacity

#### 3.2.2. Ultimate bending capacity

As shown in Fig. 14, $M_u/M_{pc}$ reflects the degree of the plasticity development of different sections at the ultimate state. $M_u/M_{pc}$ decreases with an increase of $r_f$ and $r_w$. When $r_f$ is small, $M_u/M_{pc}$ enlarges with an increase of $n$. When $r_f$ and $r_w$ are large, raising $n$ enhances the local buckling of the plates, so $M_u/M_{pc}$ declines with an increase of $n$.

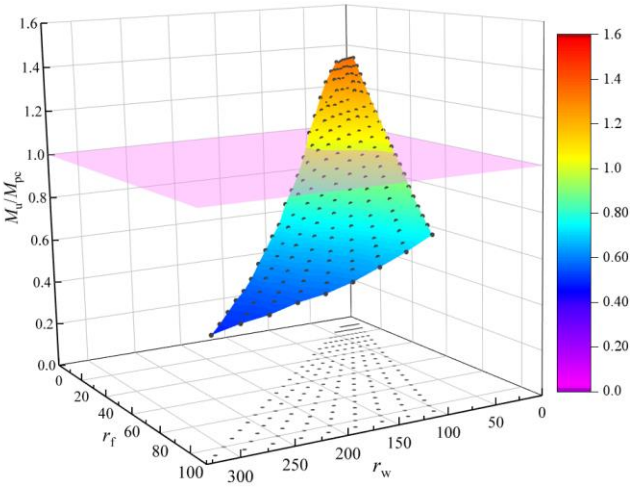


(a) Relationship between $M_u/M_{pc}$, $r_f$,and $r_w$ ($n$ = 0)

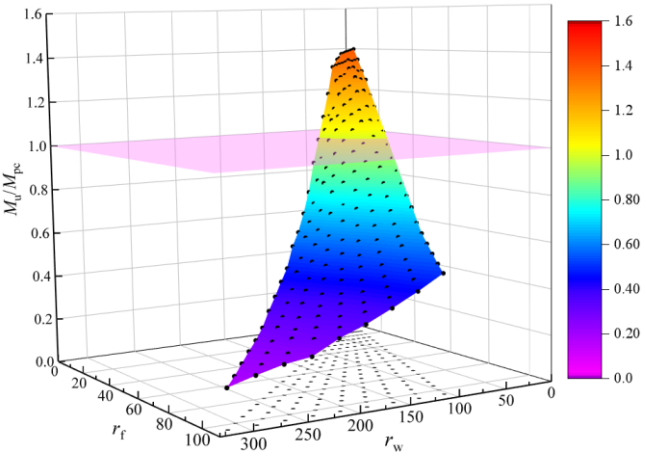


(b) Relationship between $M_u/M_{pc}$, $r_f$,and $r_w$ ($n$ = 0.2)

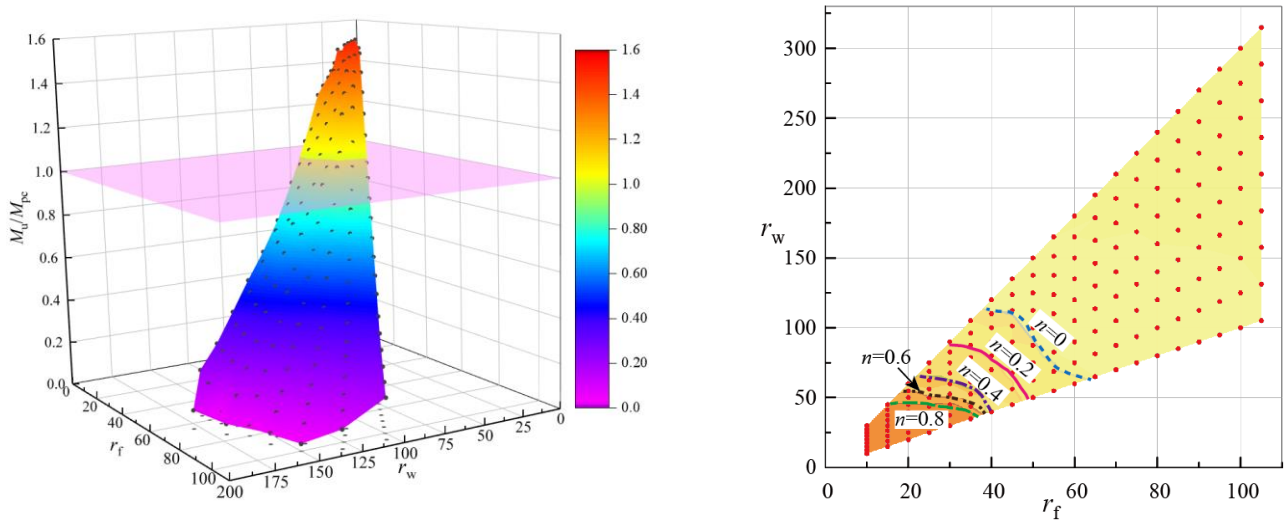


(c) Relationship between $M_u/M_{pc}$, $r_f$,and $r_w$ ($n$ = 0.4)

(d) Critical width-to-thickness ratio assembly curve

**Fig. 14** Dimensionless ultimate bending capacity

Projecting the assembly curve of $M_u/M_{pc} = 1$ in Figs. 14(a)–(c) onto the *x*-*y* plane, as shown in Fig. 14(d), shows that the critical $r_f$ and $r_w$ continuously decrease with raising $n$. Below the critical curve, $M_u/M_{pc} > 1$, implying that the member can develop full-section plasticity and even play the role of strain hardening at the limit state. When the combination point is above the critical curve, $M_u/M_{pc} < 1$, indicating that the section can only develop partial plasticity at the limit state. This provides a theoretical basis for the stress distribution model of EPM under combined compression and bending.

## 4. Effective plastic width method

This section extends the application of EPM to calculate the ultimate capacities of cold-formed SHS and RHS members applicable to members within $r_f \leq 105$, $\alpha = 1-3$, and $n$ = 0–0.9.

### *4.1. Ultimate compressive capacity*

Due to different $r_f$ and $r_w$ values, the buckling degrees of the plates differ at the ultimate state. Thus, different stress distribution models are provided by distinguishing the fully and partially effective sections, and the formulas for calculating the ultimate compressive capacity are proposed using the effective plastic width and stress enhancement coefficient in this section.

#### *4.1.1. Critical width-to-thickness ratio*

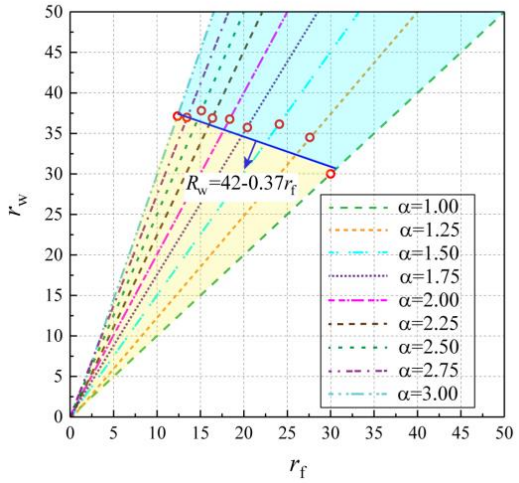


**Fig. 15** The relationship between $r_f$ and $r_w$ when $N_u/N_y = 1$

In order to distinguish the fully effective sections from the partially effective sections, the limit curve in terms of $r_f$ and $r_w$ are extracted when $N_u/N_y = 1$ with different aspect ratios in the red dots, as shown in Fig. 15. and as expressed in Eq. (1):

$$R_w = 42 - 0.37 r_f \tag{1}$$

where $R_w$ is the critical web width-to-thickness ratio of the cold-formed SHS and RHS members under axial load. When $r_w \leq R_w$, as the combination point is located in the yellow area in Fig. 15, the entire section is effective, and when $r_w > R_w$, the section is partially effective.

#### *4.1.2. Stress distribution model of partially effective section*

The stress in the middle area of a buckled plate at the ultimate state is close to zero, which can be regarded as the failure zone. Due to the support effect of adjacent flanges and webs, the mean stresses in and near the corner areas are maintained close to the yield stress, which can be regarded as the effective zones. The assumption is that the effective section and its stress distribution at the ultimate state are depicted in Fig. 16. Based on the stress distribution form, Eqs. (2)–(6) express the formulas for calculating the ultimate compressive capacity $N_u$.

$$N_u = 2N_f + 2N_w + 4N_c = 2b_e \cdot tf_y + 2h_e \cdot tf_y + 4l_c tf_y \tag{2}$$

$$b_e = \rho_{fc} \cdot b \tag{3}$$

$$h_e = \rho_{wc} \cdot h \tag{4}$$

$$\rho_{fc} = 13.5 r_f^{-0.75} \leq 1 \tag{5}$$

$$\rho_{wc} = k_w 13.5 r_w^{-0.75} \leq 1 \tag{6}$$

where $N_f$, $N_w$, and $N_c$ are the bearing capacity of a single flange, web, and corner, respectively; $h_e$ and $b_e$ are the effective width of the plates, respectively; $l_c$ indicates the centerline length of a corner; $\rho_{fc}$ and $\rho_{wc}$ represents the effective width coefficient of flange and web, respectively; $k_w$ denotes the plate correlation interaction coefficient that considering the beneficial restraining effect of flange on the web and is expressed by $k_w = 0.95 + 0.05\alpha$ .

#### *4.1.3. Stress distribution model of fully effective section*

For the fully effective sections, it is assumed that the stress on section $\sigma_c$ is higher than yield strength to consider the favorable effect of strain hardening and the cold-formed effect. The stress distribution of the fully effective section is shown in Fig. 16(c), and its calculation formulas are expressed in Eqs. (7)–(8).

$$N_u = A\sigma_c = A \cdot \eta_c f_y \tag{7}$$

$$\eta_c = 1.35 - 0.003 r_f - 0.008 r_w \geq 1 \tag{8}$$

where $\eta_c$ represents the stress enhancement coefficient under axial compression.

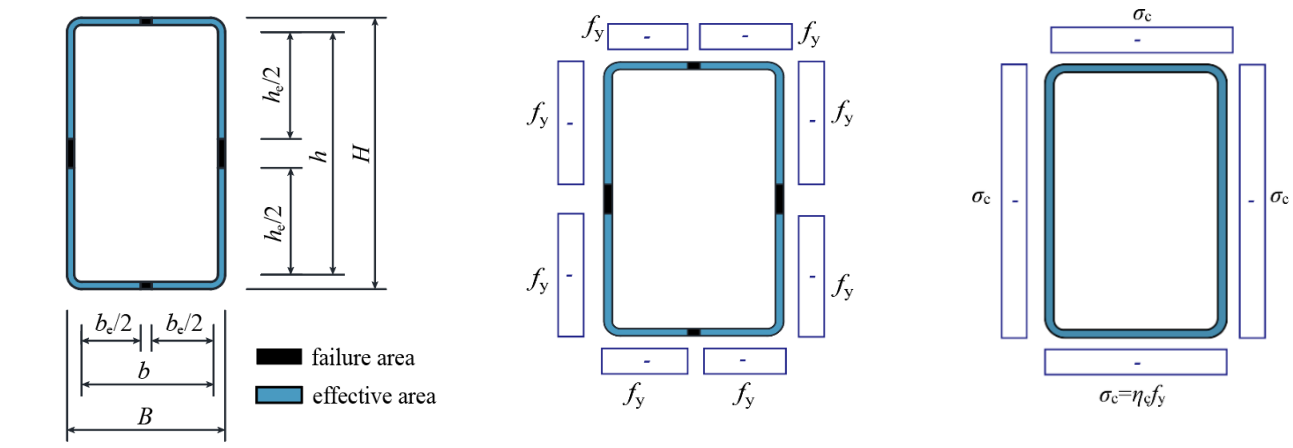


(a) The definition of the effective section (b) The stress distribution of the partially effective section (c) The stress distribution of the fully effective section

**Fig. 16** The stress distribution models of the sections under axial compression

*4.1.4. Evaluation of stress distribution models*

In order to evaluate the calculation model of EMP under axial compression, the actual stress distribution of the typical model at the ultimate state is compared with the stress distribution model of EPM, as shown in Fig. 17, where the dotted red line and the dotted green line represent the stress distribution obtained from FEM and EPM, respectively. The axial compressive stress distribution model of EPM can effectively reflect the trend of the actual stress distribution and can consider the effects of strain hardening and plate buckling.

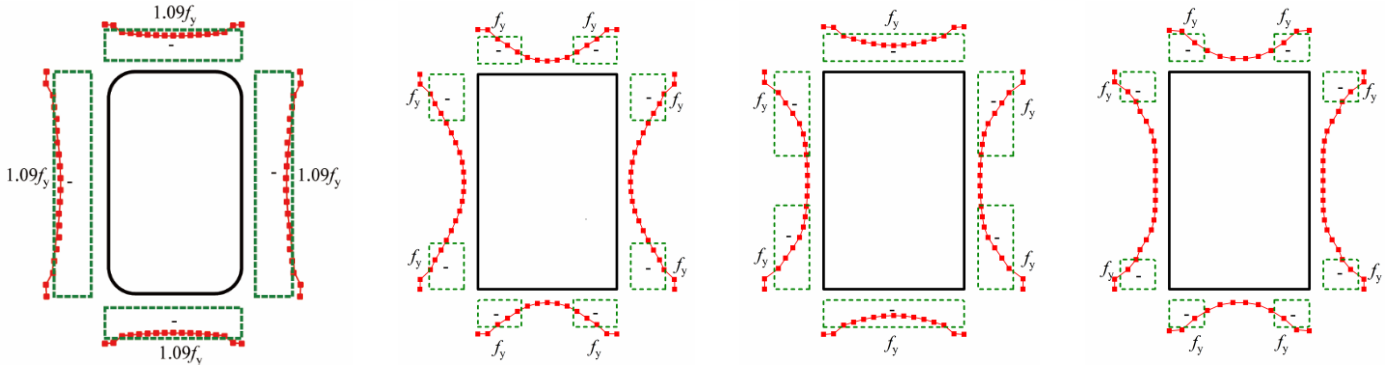


(a) C-1.25-20 (b) C-1.75-60 (c) C-2.5-20 (d) C-2.5-80

**Fig. 17** Comparing the model of EPM with the FE results under axial compression

*4.2. Ultimate bending capacity*

In this section, two stress distribution modes under combined compression and bending are analyzed in detail, and the calculation formulas for calculating the ultimate bending capacity are proposed.

*4.2.1. Stress distribution model of partially effective section*

When the cold-formed SHS and RHS members under combined compression and bending reach ultimate state, different buckling forms and different development degrees will be generated under different combinations of $r_f$, $r_w$, and $n$. It is assumed that the normal stress generated by axial pressure is concentrated at the center of the webs, and with the axial pressure increases, this normal stress gradually extends to the flanges. In order to simplify the calculation, the failure zone of the web is assumed evenly distributed on both sides about the $x$-axis, and the stress $\sigma_{bc}$ is used to consider the favorable effect of strain hardening and cold-formed effect. Based on above assumptions, the stress distribution mode of partially effective section is divided into four cases according to the different effective sections and axial force ratios, as shown in Fig. 18. The four stress distribution models proposed take into account various combination situations of axial compression and bending moment.

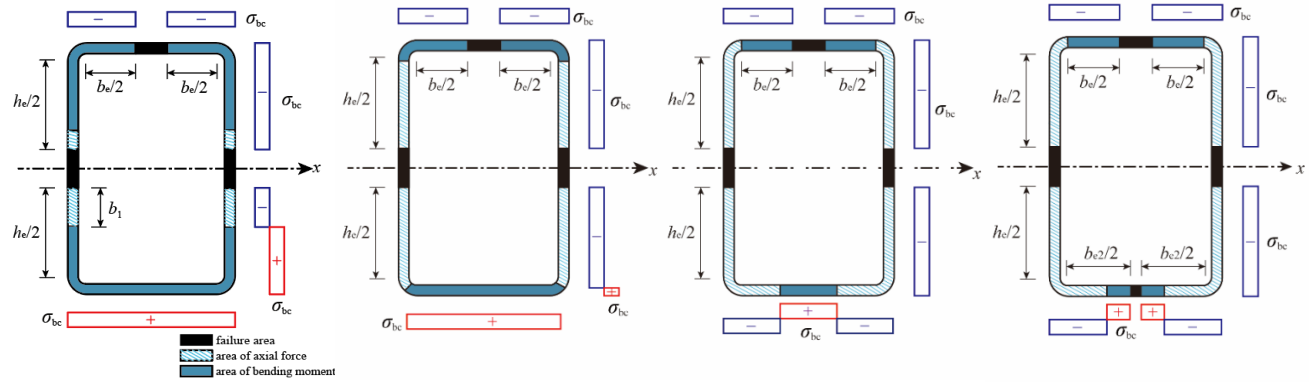


(a) Case 1 (b) Case 2 (c) Case 3 (d) Case 4

**Fig. 18** Stress distribution models of partially effective sections under compression and bending

(1) Case 1

When axial force levels are relatively low, compressive stress is only distributed on the web, i.e., $b_1 < h_e/2$, where $b_1$ is the width of the compressive stress due to the axial pressure distributed on the lower side of the *x*-axis, and can be obtained according to the balance of the axial forces. In this scenario, the compressive plates experience local buckling with the settlement of the failure zone, while the tensile flange remains fully effective, as depicted in Fig. 18(a). The formula for calculating the ultimate bending capacity $M_u$ can be obtained by taking the moment of the stress on the section to the *x*-axis, as expressed in Eqs. (9)–(13).

$$M_u = M_c + M_f + M_w \tag{9}$$

$$M_c = \left(\frac{4(R^3 - r^3)}{3} + \frac{\pi h(R^2 - r^2)}{2}\right)\sigma_{bc} \tag{10}$$

$$M_f = (b_e + b)t\sigma_{bc} \cdot \frac{H}{2} \tag{11}$$

$$M_w = 4\left(\frac{h_e}{2} - b_1\right)t\sigma_{bc} \cdot \left(\frac{h}{2} - \frac{h_e}{4} + \frac{b_1}{2}\right) \tag{12}$$

$$b_1 = \frac{(nl_1 + b - b_e)f_y}{4\sigma_{bc}} \tag{13}$$

where $M_f$, $M_w$, and $M_c$ are the bending moment components of the flange, web, and corner, respectively; $l_1$ is the centerline length of the entire section.

(2) Case 2

As axial pressure increases, compressive stress extends to the corner zone but not reaches the tensile flange, that is, $h_e/2 < b_1 < h_e/2 + l_c$, as presented in Fig. 18(b). The compressive plates experience partially effective due to local buckling, and the tensile flange is fully effective. Compared with Case 1, the web in Case 2 is all compressive, and no bending moment is generated by the webs. Thus, $M_c$ is reduced to $M_c'$ under the influence of extended compressive stress.

$$M_u = M_c' + M_f \tag{14}$$

$$M_c' = M_c - \left(\frac{8(R^3 - r^3)\sin^2(\theta/2)}{3} + \theta h(R^2 - r^2)\right)\sigma_{bc} \tag{15}$$

where $\theta$ is the radian value of the compressive stress penetrating the corner and is expressed in $\theta = \frac{b_1 - h_e/2}{(R+r)/2}$.

(3) Case 3

As the axial pressure increases, compressive stress is distributed across the web, corner, and the tensile flange which is $b_1 > h_e/2 + l_c$, as depicted in Fig. 18(c). Neither the web nor the corner generates the bending moment member, and the bending moment is generated by the stress in the top and bottom flanges. Substituting the formula for calculating $b_1$ into Eq. (17) yields Eq. (18).

$$M_u = M_f' \tag{16}$$

$$M_f' = (b_e + b + 2h_e + 4l_c - 4b_1)t\sigma_{bc} \cdot \frac{H}{2} \tag{17}$$

$$M_u = (2b_e + 2h_e + 4l_c - nl_1)t\sigma_{bc} \cdot \frac{H}{2} \tag{18}$$

(4) Case 4

As axial pressure approaches the ultimate compressive capacity, local buckling would occur at all the plates subjected to axial pressure and bending moment, and the failure zone appears, as depicted in Fig. 18(d), where the effective width of tensile flange is $b_{e2}$. No bending moment member is generated by the webs and the corner zones, thus $M_u = M_f'$. Eqs. (20)–(22) express the calculation process, where $M_{f1}$ and $M_{f2}$ indicate the bending moment components of tensile flange and compressive flange to *x*-axis, respectively. Substituting Eq. (19), the calculation formula for $b_1$, into Eq. (22) yields the final formula for calculating $M_u$. The final formula is the same as Eq. (18), which indicates that the calculation of the ultimate bending capacity in Case 3 and 4 can be considered in the same case.

$$b_1 = \frac{(nl_1 + b_{e2} - b_e)f_y}{4\sigma_{bc}} \tag{19}$$

$$(b_1 - h_e/2 - l_c))t\sigma_{bc} \cdot \frac{H}{2} = (b_{e2} - 2b_1 + h_e + 2l_c)t\sigma_{bc} \cdot \frac{H}{2} \tag{20}$$

$$M_{f2} = (b_e - 2(b_1 - h_e/2 - l_c))t\sigma_{bc} \cdot \frac{H}{2} = (b_e - 2b_1 + h_e + 2l_c)t\sigma_{bc} \cdot \frac{H}{2} \tag{21}$$

$$M_f' = M_{f1} + M_{f2} = (b_e + b_{e2} + 2h_e + 4l_c - 4b_1)t\sigma_{bc} \cdot \frac{H}{2} \tag{22}$$

*4.2.2. Stress distribution model of fully effective section*

When the width-to-thickness ratio of the members is small, the section can develop full plasticity at the ultimate state. According to different axial force levels, the stress distribution mode of the fully effective section can be divided into three cases, as shown in Fig. 19.

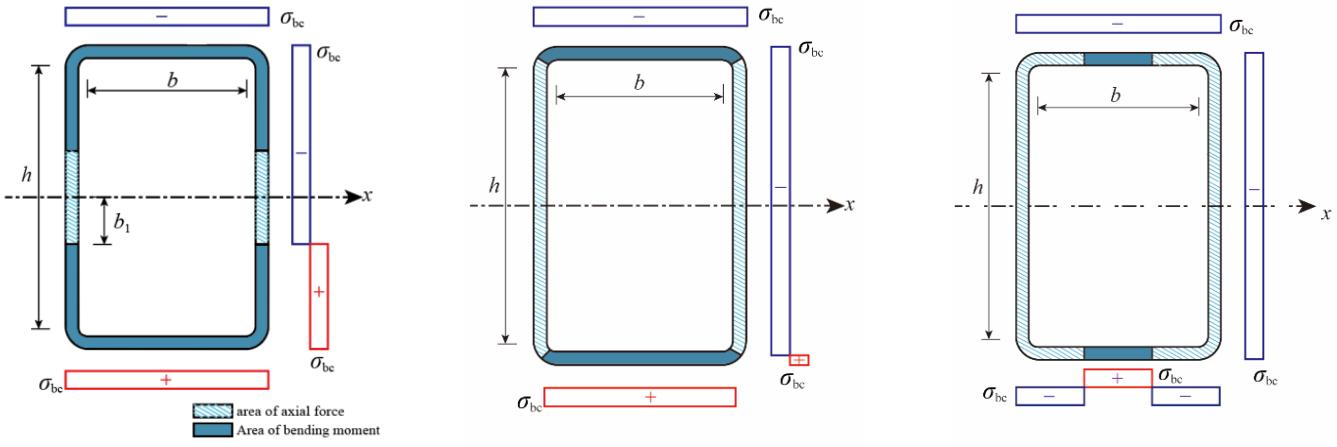


(a) Case 1 (b) Case 2 (c) Case 3

**Fig. 19** The stress distribution models of the fully effective sections under compression and bending

For the three cases, the ultimate bending capacity is still calculated by the formula of situations in Figs. 18(a)–(c), by replacing $b$ and $h$ into $b_e$ and $h_e$ into the corresponding formulas respectively. The stress distribution mode of the fully effective section can consider the strengthening effect of the material and the cold-formed effect of the corner by taking the enhancement of the section stress into account. The stress distribution model of case 3 can regress to the stress distribution of the fully effective section in Fig. 16(c), indicating that EPM stress distribution model of the fully effective section can completely return the situation of combine compression and bending to the axial compression situation.

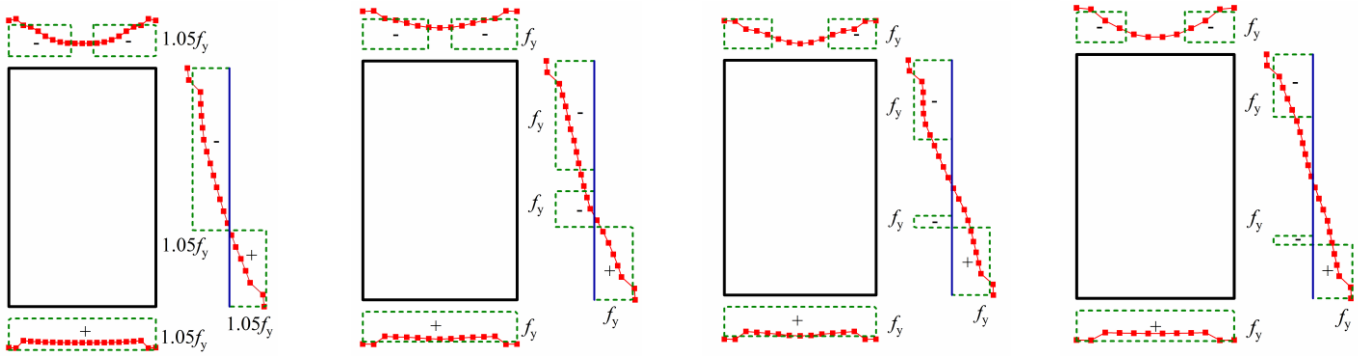


(a) BC-1-40-0.2 (b) BC-1.75-40-0.2 (c) BC-1.75-60-0 (d) BC-2.5-60-0

**Fig. 20** Comparing the model of EPM and the FE results under compression and bending

*4.2.4. Effective plastic width and stress enhancement coefficient*

(1) Effective plastic width

The effective plastic width is a critical parameter of EPM, which not only reflects the reduction of the bearing capacity caused by local buckling and interactive effect of plates, but also represents the balance of the effective section under the simplified plastic stress distribution. It can be obtained by observing parametric analysis results and summarizing the stress development law.

The compressive flange is fully compressive at different axial force ratios. Therefore, it can be assumed that the effective width ($b_e$) of the compressive flange equals that of the plate under axial pressure, as expressed in Eq. (23). The calculation formula for fitting the effective width ($h_e$) of the web is provided in Eq. (24), where $\rho_{wb}$ represents the effective width coefficient of the web under combined compression and bending (Eq. 25). When the axial force ratio reaches its maximum allowable value for the section, the member is infinitely close to the axial compression state, and $n$ can be obtained using Eq. (26). By substituting $n$ into Eq. (25), $\rho_{wb} = \rho_{wc}$ can be obtained, and the stress distribution and effective width of the section are similar to that of the axial compression state.

$$b_e = \rho_{fc} \cdot b \tag{23}$$

$$h_e = \rho_{wb} \cdot h \tag{24}$$

$$\rho_{wb} = \rho_{wc} + [1 - (\frac{n(\alpha+1)}{\rho_{fc}(k_w \alpha^{0.25}+1)})^3] \cdot (\frac{20}{r_w} + \frac{0.1}{\alpha}) \le 1 \tag{25}$$

$$n = \frac{N_u}{Af_y} = \frac{2(\rho_{fc} b + \rho_{wc} h) t f_y + N_c}{Af_y} \approx \frac{\rho_{fc} b + \rho_{wc} h}{b+h} = \frac{\rho_{fc}(k_w \alpha^{0.25}+1)}{\alpha+1} \tag{26}$$

(2) Stress enhancement coefficient

When both the flange and the web are partially effective, the increase of the section stress is not considered, and the section stress equals $f_y$, i.e., $\sigma_{bc} = f_y$. For members with the fully effective section and effective web, the favorable cold-formed effect and strain hardening on the ultimate bending capacity can be considered by the stress enhancement coefficient ($\eta_{bc}$). Eqs. (27) and (28) express the formulas for calculating $\eta_{bc}$ and $\sigma_{bc}$ respectively. When the axial force ratio of the member with the fully effective section reaches the maximum axial force ratio it can bear, that is, $n = \eta_{bc}$ and $\eta_{bc} = \eta_c$, the stress distribution of the section equals that of the fully effective section under axial compression.

$$\eta_{bc} = \eta_c + (1 - \frac{n}{\eta_c}) \cdot \frac{\alpha(100 - 0.5 r_w)}{1200} \ge 1 \tag{27}$$

$$\eta_{bc} = \eta_c + (1 - \frac{n}{\eta_c}) \cdot \frac{\alpha(100 - 0.5 r_w)}{1200} \ge 1 \tag{28}$$

## 5. Evaluation of calculation methods of EPM and specifications

This section summarizes the current design methods for calculating bearing capacities of members in EC3 and GB50018, and the proposed EPM is compared with the specifications to evaluate its feasibility.

*5.1. Evaluation of existing specifications*

*5.1.1. EC3*

The European Code, i.e., EC3, calculates the section bearing capacity based on section classification according to the width-to-thickness ratios of plates, adopting different design criteria. The sections are categorized into classes according to the influence degree of local buckling on bearing capacity. However, EC3 has following shortcomings when calculating the ultimate capacity of different sections:

- The ultimate capacities of classes 1 and 2 sections are partially conservative without considering strain hardening.
- The bearing capacities of sections of classes 2 and 3 are discontinuous because the partial plasticity of the sections is not considered.
- The calculation process of the section of class 4 is complex, which is not conducive to the actual operation.
- EC3 is conservative for compact sections but unsafe for slender ones, and EC3 section classification cannot be directly applied to cold-formed steel members.
- EC3 follows the principle of single plate when classifying sections, assuming that the plate is supported on four sides without considering the interaction between the flanges and webs, and the bearing capacity calculation is not accurate enough.

*5.1.2. GB50018*

Code GB50018 is applicable for cold-formed steel members with a plate thickness ranging from 2 to 6 mm. When calculating the ultimate capacity of cold-formed SHS and RHS members in code GB50018, the plate failure caused by local buckling can be well-considered for thin members. However, the following shortcomings may exist:

- The application scope of the code on thickness is limited. For cold-formed SHS and RHS members beyond the scope, its application is still controversial.

- GB50018 does not consider the development of section plasticity and dramatically underestimates the ultimate capacity of cold-formed SHS and RHS members with small width-to-thickness ratios, so the bearing capacity of cold-formed steel members cannot be fully utilized.
- When calculating the effective width of compression plate, the changes in interactive effects of plates after buckling are ignored, so the calculation of the bearing capacity is conservative.

### *5.2. Comparison of calculation methods*

To assess the accuracy of GB50018, EC3, and EPM, their calculation results of these three methods are compared with parametric analysis results.

#### *5.2.1. Comparison of ultimate compressive capacity*

The ultimate compressive capacities of the members determined by GB50018 ($N_{u,GB50018}$), EC3 ($N_{u,EC3}$), EPM ($N_{u,EPM}$), and the FE model ($N_{u,FEM}$) are compared in dimensionless terms. The results of different aspect ratios are shown in Fig. 21. The results of EPM, EC3, and GB50018 are relatively close to those of the FE model, and GB50018 tends to be the most conservative method. When the aspect ratio is small, the ultimate compressive capacity predicted by EC3 is unsafe, and it is close to the FE model results at aspect ratios higher than 2.25. Both specifications fail to consider the strain hardening at small width-to-thickness ratios, leading to conservative calculation results. Nevertheless, EPM aligns most closely with the results from FE calculations.

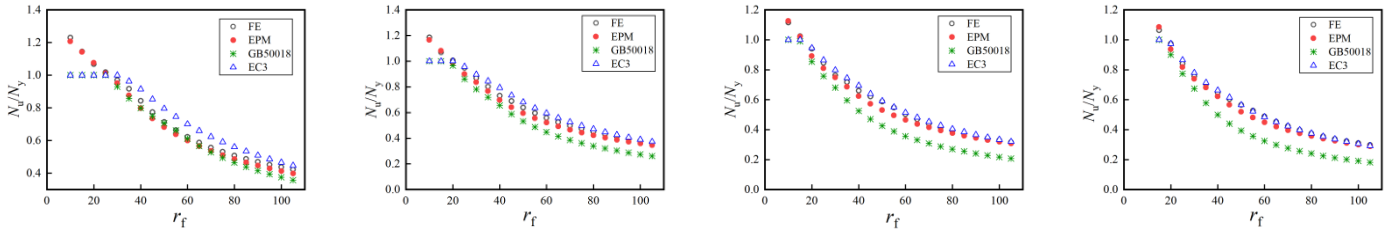


(a) $\alpha$ = 1.25 (b) $\alpha$ = 1.75 (c) $\alpha$ = 2.25 (d) $\alpha$ = 2.75

**Fig. 21** Comparison of the ultimate compressive capacity of the members

The calculations and simulation results are plotted in Fig. 22. Generally, more than half of the results of GB50018 fall outside the -10% range of the diagonal line, indicating that most of the results are conservative. The EC3 calculation method is close to the FE results, and most points fall within the +10% range of the diagonal line. The proposed EPM is very close to the diagonal line, and its calculations are accurate. The above conclusions can also be further confirmed by comparing the results of average value and variance in Table 4.

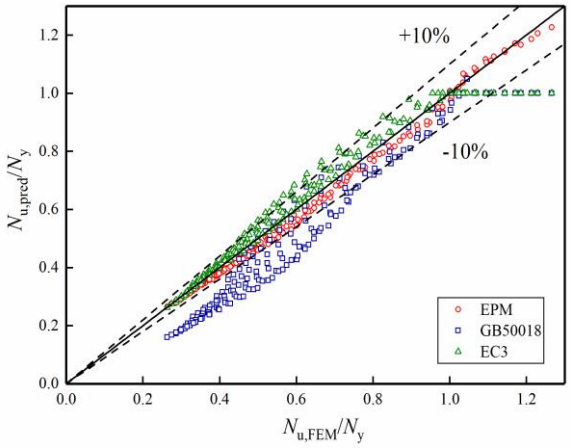


**Fig. 22** Evaluation of the ultimate compressive capacity of the members calculated using three methods

**Table 4**
Comparison of the ultimate compressive capacity calculated using three methods with respect to the FE result

| | $N_{u,EPM}$ / $N_{u,FEM}$ | $N_{u,GB50018}$ / $N_{u,FEM}$ | $N_{u,EC3}$ / $N_{u,FEM}$ |
|---|---|---|---|
| Average value | 0.960 | 0.813 | 1.029 |
| Variance | 0.001 | 0.016 | 0.004 |

#### *5.2.2. Comparison of ultimate bending capacity*

The ultimate bending capacities of the members, as determined by GB50018 ($M_{u,GB50018}$), EC3 ($M_{u,EC3}$), EPM ($M_{u,EPM}$), and the FE model ($M_{u,FEM}$) are presented in a dimensionless form relative to $M_{pc}$ and are illustrated in Fig. 23, categorized according to different axial force ratios. EPM and FE results are relatively close, and most EPM points fall below the FE results, showing that its calculations are slightly conservative.

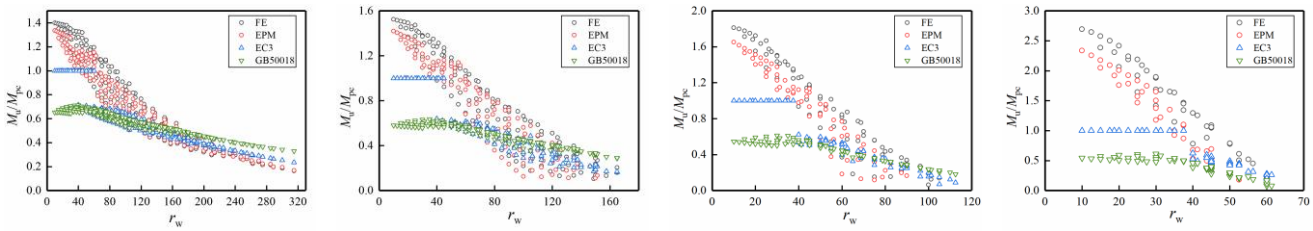


(a) $n$ = 0.2 (b) $n$ = 0.4 (c) $n$ = 0.6 (d) $n$ = 0.8

**Fig. 23** Comparison of the ultimate bending capacity of the members calculated using EPM, GB50018, and EC3

The calculations and simulation results are plotted in Fig. 24 to directly examine the deviation degree of the three calculation methods from the FE model. Table 5 tabulates the average value and variance. According to Fig. 24, the trend of the calculation results of GB50018 deviates from that of the FE. Further, the average value of the ratio is the smallest, and the degree of dispersion is large. EC3 can predict the bearing capacity of members with thin

plates accurately. Additionally, with an increase of *n*, the overall prediction is conservative, and the ratio average is small. The trend of the change in the overall prediction of EPM is consistent with that of the FE results. When *n* is small, it is very close to the FE data, and the prediction is slightly conservative at large *n* values. However, compared with the calculation results of GB50018 and EC3, EPM can provide more accurate results. The average value of the ultimate bending moment of members calculated by EPM with respect to that calculated by the FE model, is close to 1.0 with an essentially small dispersion.

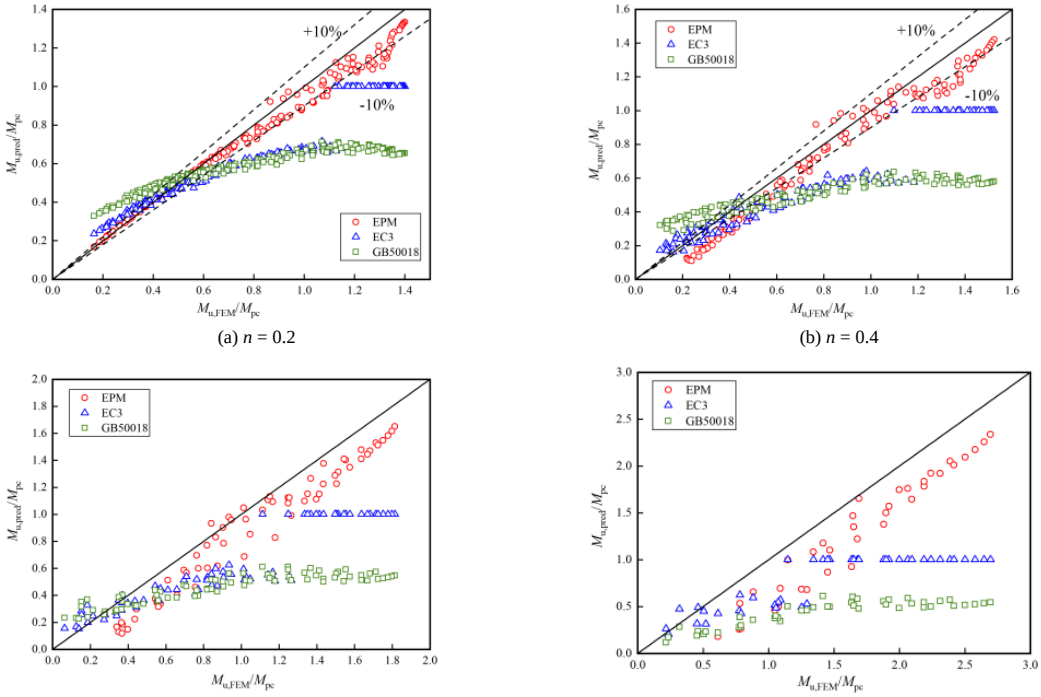


(a) $n$ = 0.2 (b) $n$ = 0.4

(c) $n$ = 0.6 (d) $n$ = 0.8

**Fig. 24** Evaluation of the ultimate bending moments calculated using EPM, GB50018, and EC3

**Table 5**
Comparison of ultimate capacities calculated using three methods with the FE data

| | | $M_{u,EPM}$ / $M_{u,FEM}$ | $M_{u,GB50018}$ / $M_{u,FEM}$ | $M_{u,EC3}$ / $M_{u,FEM}$ |
|---|---|---|---|---|
| $n$ = 0.2 | Average value | 0.966 | 0.879 | 0.878 |
| | Variance | 0.003 | 0.107 | 0.031 |
| $n$ = 0.4 | Average value | 0.860 | 0.756 | 0.768 |
| | Variance | 0.018 | 0.110 | 0.025 |
| $n$ = 0.6 | Average value | 0.801 | 0.527 | 0.663 |
| | Variance | 0.029 | 0.035 | 0.018 |
| $n$ = 0.8 | Average value | 0.719 | 0.311 | 0.540 |
| | Variance | 0.032 | 0.016 | 0.006 |

EPM calculates the ultimate capacity of members based on the actual stress distribution across the section at the limit state, accurately reflecting the real stress conditions of the members. At its core, the method equates the ultimate capacity with the bearing capacity of the effective plastic section. EPM effectively accounts for strain hardening and cold-formed effects of classes 1 and 2 sections, allows for the partial plastic development in class 3 sections, and accommodates the local buckling in class 4 sections by considering the effective plastic width $b_e$ and the stress enhancement coefficient $\eta_{bc}$. This approach overcomes the discontinuities often found in ultimate capacity predictions and transcends the limitations imposed by section classification on ultimate capacity. It also considers the influence of the interactive effect of plates. With its straightforward concept and simple operation, EPM avoids complex iterations, enabling precise calculations of the ultimate capacity for cold-formed SHS and RHS steel members without the need for intricate procedures.

## 6. Conclusions

In this study, a comprehensive parametric study was conducted on cold-formed SHS and RHS steel pipes with various combinations of flange and web width-to-thickness ratios as well as axial force ratios. The research investigated and analyzed the failure modes and bearing capabilities of these cold-formed members under compression and combined compression and bending. Based on the stress distribution of section at the limit state, EPM was introduced for calculating the ultimate capacity of cold-formed SHS and RHS members. The prediction accuracy of EPM was assessed alongside current standards, using FE simulations and experimental data. The key conclusions of this study are as follows:

- Cold-formed SHS and RHS members exhibit varying degrees of local buckling at the limit state, influenced by width-to-thickness ratios and axial force ratios. Buckling severity dictates the failure modes, which for axial compression, range from the fully plastic failure to local elastic-plastic buckling failure. Under combined compression and bending, failure modes include fully plastic failure, local elastic-plastic buckling failure, and compressive buckling failure.
- Stress distribution at the limit state of member can be categorized into fully effective section and partially effective section, with corresponding stress distribution models that more accurately reflect actual stress trends and account for strain hardening and plate buckling effects.
- Depending on the axial force ratios, partially effective stress distribution models are classified into four cases, whereas fully effective section models are split into three. EPM stress distribution model, especially under high axial force ratios, effectively bridges the gap between combined compression and bending to axial compression scenarios, allowing the use of identical calculation formulas, demonstrating significant theoretical value.
- Comparative analysis with FE results and experimental data reveals that the ultimate capacity predictions by the GB50018 standard are conservative. In contrast, the compressive capacity predictions by EC3 are slightly unsafe. The bending resistance predictions by EC3 are relatively precise. However, the ultimate resistance predictions by EPM are notably more accurate.
- EPM, based on the actual stress distribution at the limit state, closely reflects the real stress conditions in members, offering accurate predictions of the ultimate capacities of cold-formed SHS and RHS members. By considering the effective plastic width and the stress enhancement coefficient, the method comprehensively addresses strain hardening, cold-formed effect, and interactive effects of plates, avoiding prediction discontinuities and making more precise calculations.

## Acknowledgments

The research received support from the General Program of the National Natural Science Foundation of China (Grant No. 51978437), the Excellent Youth Cultivation Program of Shanxi Basic Research Plan (Grant No. 202103021222007), and China Postdoctoral Science Foundation Project (Grant No. 2021M692862).

## References

[1] Chen, Y.Y., Wang, W. and Zhou, F. Steel tubular structures: configuration innovation and performance improvement driven by new requirements. Journal of Building Structures, 2019:1-20.

[2] Hou, G., Tong, L.W., Chen, Y.Y. and Li, Z.G. Testing and analysis model for material property of non-thin-walled cold-formed square hollow sections. Engineering Mechanics, 2013. 30(2):372-378,426.

[3] Tong, L.W., Huo, T. and Hou, G. Research on design formula for yield strength of cold-formed rectangular steel tubes with medium-thick wall. Journal of Building Structures, 2018. 39(12):81-90.

[4] Guo, Y.J., Zhu, A.Z., Pi, Y.L. and Tin-Loi, F. Experimental study on compressive strengths of thick-walled cold-formed sections. Journal of Constructional Steel Research, 2007. 63(5): 718-723. https://doi.org/10.1016/j.jcsr.2006.08.008

[5] Wang, W., Fang, C., Qin, X., Chen, Y.Y. and Li, L. Performance of practical beam-to-SHS column connections against progressive collapse. Engineering Structures, 2016. 106(Jan.1): 332-347. https://doi.org/10.1016/j.engstruct.2015.10.040

[6] Wang, W., Fang, C., Chen, Y.Y. and Wang, M.X. Seismic performance of steel H-beam to SHS-column cast modular panel zone joints. Engineering Structures, 2016. 117: 145-160. https://doi.org/10.1016/j.engstruct.2016.03.006

[7] Fang, C., Zhou, F. and Luo, C.H. Cold-formed stainless steel RHSs/SHSs under combined compression and cyclic bending. Journal of Constructional Steel Research, 2018. 141: 9-22. https://doi.org/10.1016/j.jcsr.2017.11.001

[8] Zhou, F., Fang, C. and Chen, Y.S. Experimental and numerical studies on stainless steel tubular members under axial cyclic loading. Engineering Structures, 2018. 171: 72-85. https://doi.org/10.1016/j.engstruct.2018.05.093

[9] Fang, C., Wang, F.C., Wang, C.Y. and Zheng, Y. Cyclic behavior of oval hollow section (OHS) beam-columns. Thin-Walled Structures, 2021. 161: 1-14. https://doi.org/10.1016/j.tws.2020.107430

[10] CSADI. Technical code of cold-formed thin-wall steel structures, in GB50018-2002. 2002, Wuhan.

[11] CEN (European Committee for Standardization). Eurocode 3: Design of steel structures–Part 1-1: General rules and rules for buildings, in EN 1993-1-1:2005. 2005, Brussels, Belgium.

[12] Wu, Y.G. and Zhang, Q.L. Study on post-buckling plate assembly effect of rectangular tube under uniform compression. Chinese Quarterly of Mechanics, 2006. 27(2): 286-294.

[13] Shen, H.X. Buckling coefficients taking into account constraint actions between plate elements of lipped channel struts. Steel Construction, 2006. 21(1): 62-64.

[14] Li, Y.Q., Li, G.W., Shen, Z.Y., Ma, Y.F. and Zhu, S.W. Design reliability analysis of cold-formed thick-walled-steel members under axial compression. Journal of Building Structures, 2015. 36(5): 8-17.

[15] Wen, D.H., Shen, Z.Y., LI, Y.Q. and Zhu, S.W. Experimental research on cold-formed thick-walled steel box stubs and comparison of results with related codes. Journal of Tongji University (Natural Science), 2016. 44(8): 1190-1198.

[16] Hu, S.D., Li, L.X. and Zhou, J.L. Strain hardening of thick-walled cold formed steel rectangular hollow section. Journal of Building Structures, 2011. 32(6): 76-81.

[17] Wang, J., Afshan, S., Schillo, N., Theofanous, M., Feldmann, M. and Gardner, L. Material properties and compressive local buckling response of high strength steel square and rectangular hollow sections. Engineering Structures, 2017. 130(JAN.1): 297-315. https://doi.org/10.1016/j.engstruct.2016.10.023

[18] Ma, J.L., Chan, T.M., and Young, B. Experimental investigation on stub-column behavior of cold-formed high-strength steel tubular sections. Journal of Structural Engineering, 2016. 142(5): 04015174. https://doi.org/10.1061/(ASCE)ST.1943-541X.0001456

[19] Ma, J.L., Chan, T.M., and Young, B. Design of cold-formed high-strength steel tubular stub columns. Journal of Structural Engineering, 2018. 144(6): 04018063. http://dx.doi.org/10.1061/(ASCE)ST.1943-541X.0002046

[20] Ma, J.L., Chan, T.M., and Young, B. Cold-formed high-strength steel rectangular and square hollow sections under combined compression and bending. Journal of Structural Engineering, 2019. 145(12): 04019154. https://doi.org/10.1061/(ASCE)ST.1943-541X.0002446

[21] Nseir, J. Development of a new design method for the cross-section capacity of steel hollow sections. 2015, Belgium: Université de Liège.

[22] Hou, G. Experimental research and numerical analysis on axial compression performance of cold-formed non-thin-walled square hollow sections. 2011, Tongji University: Shanghai.

[23] Yao, X.Y., Guo, Y.L., Liu, Z.Y. and Song, H. Experimental study and load-carrying capacity analysis of cold-formed thin-walled steel axially-compressed rectangular hollow steel columns. Architecture Technology, 2015. 46(09): 853-856.

[24] Yun, X., and Gardner, L. The continuous strength method for the design of cold-formed steel non-slender tubular cross-sections. Engineering Structures, 2018. 175: 549-564. https://doi.org/10.1016/j.engstruct.2018.08.070

[25] Deng, J.M. Research on the local buckling behavior of cold-formed thin-walled SHS and RHS based on CSM. 2018, Chang'an University.

[26] Ma, J.L., Chan, T.M., and Young, B. Cold-formed high strength steel tubular beam-columns. Engineering Structures, 2021. 230(1–3): 111618. https://doi.org/10.1016/j.engstruct.2020.111618

[27] Li, Y.Q., Shen, Z.Y., Wang, L., Wang, Y.M. and Xu, H.L. Analysis method for load-carrying capacity of 550MPa high-strength cold-formed thin-walled steel columns subjected to axial compression. Journal of Building Structures, 2006. 27(3): 18-25.

[28] Chen, S.F. and Hui, Y. Interaction of local buckling in cold-formed members and effective width of edge-stiffened elements. Journal of Xi'an University of Architecture & Technology, 1995. 27(1): 1-7.

[29] Chen, S.F. Plate interactive buckling and ultimate capacity of cold-formed sections. Progress in Steel Building Structures, 2002. 4(01): 3-6.

[30] Chen, Y.Y., Ma, Y., Zhao, J. and Tong, L.W. Tests on high frequency welded H-steel columns with slender elements and its evaluation of seismic resistance. Journal of Tongji University (Natural Science), 2006. 34(11): p. 1421-1426.

[31] Cheng, X. and Chen, Y.Y. Ultimate strength of H-sections under combined compression and uniaxial bending considering plate interaction[J]. Journal of Constructional Steel Research. 2018, 143: 196-207.

[32] Shi, X.P., Cheng, X., Wang, X.X. and Mansour, M. Ultimate behavior and design of cold-formed steel square hollow section members. International Journal of Steel Structures, 2022. 22(3): 767-790. https://doi.org/10.1007/s13296-022-00605-2

[33] CEN (European Committee for Standardization). Eurocode 3: Design of steel structures-Part 1-5:Plated structural elements, in EN 1993-1-5:2006. 2006: Brussels, Belgium.

[34] Gardner, L. and Yun, X. Description of stress-strain curves for cold-formed steels. Construction and Building Materials, 2018. 189: 527-538. https://doi.org/10.1016/j.conbuildmat.2018.08.195

[35] Zhu, A.Z., Zhu, H.P., Zhang, X.W., and Lu, Y. Experimental study and analysis of inner-stiffened cold-formed SHS steel stub columns. Thin-Walled Structures, 2016. 107: 28-38. https://doi.org/10.1016/j.tws.2016.04.026

[36] Key, P.W. and Hancock, G.J. Hancock, A theoretical investigation of the column behaviour of cold-formed square hollow sections. Thin-Walled Structures, 1993. 16(1-4): 31-64. .https://doi.org/10.1016/0263-8231(93)90040-H

[37] Valiente, A. Fracture and fatigue failure in the Spanish codes for design of steel structures. Engineering Failure Analysis, 2009. 16(8): 2658-2667. https://doi.org/10.1016/j.engfailanal.2009.04.025

[38] Somodi, B. and Kovesdi, B. Residual stress measurements on cold-formed HSS hollow section columns. Journal of Constructional Steel Research, 2017. 128: 706-720. https://doi.org/10.1016/j.jcsr.2016.10.008

[39] Gardner, L., Saari, N. and Wang, F. Comparative experimental study of hot-rolled and cold-formed rectangular hollow sections. Thin-Walled Structures, 2010. 48(7): 495-507. https://doi.org/10.1016/j.tws.2010.02.003

[40] Hu, S.D., Ye, B. and Li, L.X. Materials properties of thick-wall cold-rolled welded tube with a rectangular or square hollow section. Construction & Building Materials, 2011. 25(5): 2683-2689. https://doi.org/10.1016/j.conbuildmat.2010.12.019

[41] Sun, M., and Packer, J.A. Direct-formed and continuous-formed rectangular hollow sections-Comparison of static properties. Journal of Constructional Steel Research, 2014. 92: 67-78. .https://doi.org/10.1016/j.jcsr.2013.09.013

[42] Chen, J. Study of ultimate axial compressive capacity of cold-formed medium wall square and rectanglar hollow steel columns with initial imperfections. 2008, Wuhan University of Technology.

[43] Gao, H. Experimental research and FEM simulation of ultimate axial compression of cold-formed medium wall hollow steel columns. 2007, Wuhan University of Technology.

**Advanced Steel Construction** – Vol. 20 No. 3 (2024) 280–291
**DOI:**10.18057/IJASC.2024.20.3.7


# BEHAVIOUR OF LOCALLY DAMAGED Q355 STEEL EQUAL ANGLES SUBJECTED TO COMPRESSION

Song-Yang He [1], Xing Huang [1], Xiang-Yun Liu [1], Zhong Li [1], Tao Gong [1], Hui-Qiang Yan [2, 3] and Shao-Bo Kang [2, 3, *]

[1] *Southwest Electric Power Design Institute Co., LTD., China Power Engineering Consulting Group, 16 Dongfeng Road, Chenghua District, Chengdu 610021, China*

[2] *Key Laboratory of New Technology for Construction of Cities in Mountain Area (Chongqing University), Ministry of Education, Chongqing 400045, China*

[3] *School of Civil Engineering, Chongqing University, Chongqing 400045, China*

** (Corresponding author: E-mail: kang0119@cqu.edu.cn)*

**ABSTRACT**

Steel angles in transmission towers may experience corrosion in the service life due to bad exposure conditions. However, limited experimental results are available about the remaining load capacity of corroded steel angles in compression at present. This paper presents experimental tests, numerical simulations and design method of steel angles with local damages at the mid-height or end induced by corrosion. Five groups of steel angles with different depths of local damages at different locations were tested under axial compression in the experimental programme, and the load capacity and failure mode of steel angles were obtained. Numerical models are developed and validated using test data, and parametric studies are conducted to investigate the influence of depth and slenderness of steel angles on ultimate load. Moreover, design equations are developed for locally damaged steel angles, and comparisons with numerical results show yield reasonably accurate estimations of the ultimate load. Comparisons are also made between the calculated result using the developed equation and existing design curves in the relevant code to demonstrate the effect of local damage on the buckling coefficient of steel angles. It shows that the local damage at the mid-height or the end of steel angles could significantly reduce the buckling coefficient, and therefore, it has to be considered when evaluating the ultimate load of steel angles in transmission towers in service.

**ARTICLE HISTORY**

Received: 7 October 2023
Revised: 27 February 2024
Accepted: 4 March 2024

**KEYWORDS**

Steel equal angles;
Local damage;
Axial compression;
Experimental test;
Numerical simulation;
Design equation



## 1. Introduction

Steel structures may be exposed to local or overall corrosion in the whole service life due to the environmental effects. To evaluate the structural performance after corrosion, experimental tests have been carried out on different types of structural steel and its members. At the material level, studies have been conducted on the residual yield and ultimate strengths of corroded steel plates [1-3]. Design methods have also been proposed in which the effective thickness of steel plates could be used to evaluate the ultimate strength of corroded steel plates [4]. Sarveswaran et al. [5] proposed a computational method to assess the reliability of corroded steel structural components based on interval probability theory.

A wide range of experimental tests and numerical simulations have been conducted to investigate the effect of different types of corrosion on the behaviour of steel beams in bending. Tang et al. [6] and Wang et al. [7] measured the geometric characteristics of corroded high-performance steel beams exposed to different environments using three-dimensional scanning technology and studied the effects of corrosion on the flexural behaviour of the beam. They found that existing design method could predict the flexural capacity of corroded beams conservatively. Peng et al. [8], Zhang et al. [9] and Chai et al. [10], Liu and Zhang [11], and Zhao et al. [12, 13] systematically investigated the influences of location and ratio of corrosion on the moment resistance, buckling and fatigue behaviour of steel beams in bending and concluded that local corrosion had a greater impact on the flexural stiffness of beams compared to overall corrosion. Moreover, design equations were also developed based on experimental results to quantify the moment capacity of corroded steel beams. Sheng et al. [14] also derived design equations to evaluate the yield load and ultimate load of rusted H-beams. Based on monotonic tensile tests on corroded steel beams, Xu et al. [15] obtained the time-dependent failure probability and reliability index of corroded steel beams using the theory of probability density evolution. Under reversed cyclic loading conditions, Wang et al. [16] proposed the skeleton curve and restoring force model, which could be used to describe the seismic performance of corroded steel frames.

With regard to steel columns, existing research mainly focused on the load capacity in compression after corrosion. Toledo et al. [17] established the correlation between residual compressive strength and the severity of corrosion through experiments and numerical modelling. They proposed an evaluation equation for residual compressive strength using corrosion damage volume as a reduction factor. Wang et al. [18] conducted quasi-static tests on seven H-shaped steel columns exposed to atmospheric corrosion. They observed a correlation between the cyclic hardening parameter of corroded steel and the yield-to-tensile strength difference, suggesting the possibility of premature cracking in different loading stages of corroded columns. Hussain et al. [19] proposed a new design method for the plastic failure and stability analysis of single angle members, which simplified the calculation equations for single angle member in design codes. Zhang et al. [20, 21], Zheng et al. [22] and Nie et al. [23] studied the seismic performance of corroded steel columns and proposed a method to predict the ultimate strength of the column under lateral cyclic loading. Xu et al. [1] investigated the failure modes, lateral load-carrying capacity, ductility, and energy dissipation performance of H-shaped steel columns through low-cycle fatigue tests. Even though experimental and numerical investigations have been widely performed on the ultimate load capacity and failure mode of corroded steel columns, there is still a lack of study on the compressive behaviour of steel angles with corrosion, including the buckling resistance and failure mode. Abdelrahman et al. [24] investigated the flexural-torsional buckling behaviour of eccentrically loaded members and established the effective stress-strain relationship for single angle members through finite element and multiple regression analyses.

This paper presents experimental and numerical studies on the compressive behaviour of steel angles with simulated local damages induced by corrosion at the mid-height or end. In the experimental programme, five groups of steel angles with local damages in different regions were tested in compression, and the load capacity and failure mode of the angle were obtained and compared to show the influences of the location and depth of local damage on compression behaviour. Numerical models were also established and validated against test data, and were then used for parametric studies on the influence of the slenderness of steel angles on load resistance. Finally, design equations were developed in accordance with experimental and numerical results which could be used to quantify the ultimate load of steel angles with local damages.

## 2. Experimental programme

### *2.1. Specimen design*

Steel equal angles L125×8 mm with a width of 125 mm and a thickness of 8 mm were used in the experimental programme, as shown in Fig. 1. According to field observations of transmission towers in service, two different locations of local damage were determined, namely, either at the mid-height of steel angles or at the end. A simplified processing method was also adopted to produce the local damage instead of corrosion. In the method, a local damage with a length of 260 mm along the height of steel angles was made by grinding the outer face of the steel angles to a certain depth. Oszvald et al. [25] employed a mechanical milling process method to simulate corrosion by representing it as a reduction in thickness. The study established a correlation between the degree of thickness reduction and the failure modes exhibited by the specimens. Furthermore, based on the prospective behaviour pattern of b/t, the remaining

load-carrying capacity of specimens could be predicted. The author also developed design equations to calculate the remaining load-carrying capacity of compressed steel angles. Note that the two legs of each steel angle were ground to simulate the local damage induced by corrosion, whereas the depth of the local damage varied from 1 mm to 2 mm, as listed in Table 1. Huang et al. [26] investigated towers in different regions with the service life ranging from 25 to 40 years and found that the net thickness of the most severely corroded steel angles was 6.41 mm (with the nominal thickness of 8 mm), while at the tower base, the net thickness of the most severely corroded diagonal angles was only 2.18 mm (with the nominal thickness of 5 mm). Therefore, in this study, a corrosion thickness of 1 to 2 mm was chosen to investigate the corrosion range of commonly used steel angles. Thus, a total of five groups of steel angles were tested in axial compression, including one group of steel angles without damage, two groups with local damage of different depths at the mid-height, and two groups with local damage of different depths at the end. The length of steel angles was kept at 1150 mm, but pin supports were connected to both ends of each steel angle using five bolts on each leg, so that axial compression could be applied to the steel angle. Accordingly, the slenderness of steel angle about the weakest axis was fixed at 50. Table 1 includes the parameters of steel angles. In the designation of steel angles, DCN represents the specimen without local damage, DC-M1 and DC-M2 denote steel angles with 1 mm and 2 mm deep local damages at the mid-height, respectively, and DC-E1 and DC-E2 stand for the specimens with 1 mm and 2 mm deep local damages at the end.

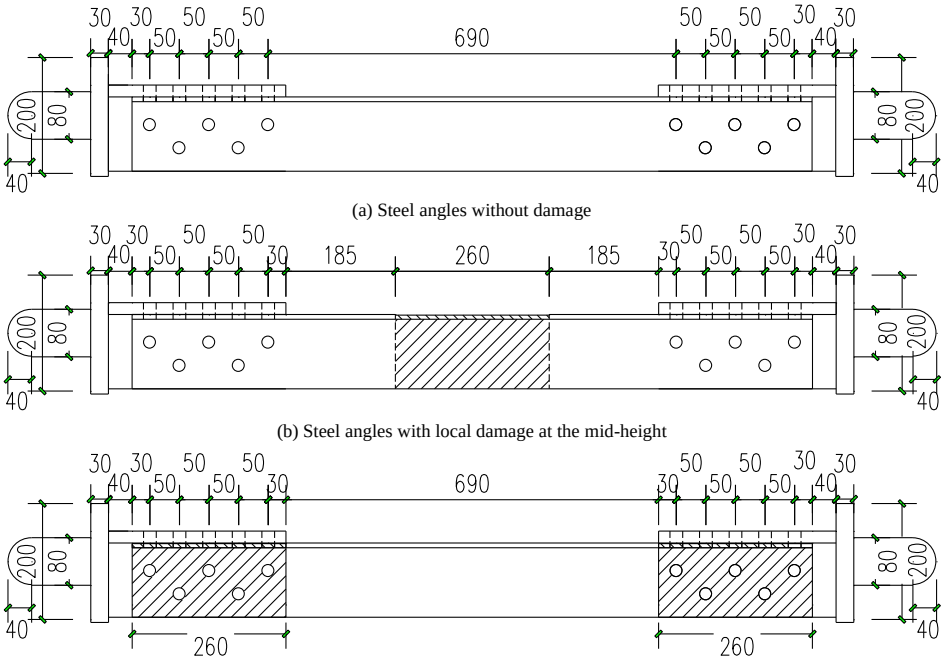


(a) Steel angles without damage

(b) Steel angles with local damage at the mid-height

(c) Steel angles with local damage at the end

**Fig. 1** Details of steel angles in the experimental programme

**Table 1**
Parameters of steel angles in the experimental programme

| Steel angles | Cross-section (mm) | Damage | Location of damage | Geometry of local damage (mm) | Length (mm) |
|---|---|---|---|---|---|
| DCN | L125×8 | No damage | -- | -- | 1150 |
| DC-M1 | L125×8 | Both legs | Mid-height | L=260mm, t=1mm | 1150 |
| DC-M2 | L125×8 | Both legs | Mid-height | L=260mm, t=2mm | 1150 |
| DC-E1 | L125×8 | Both legs | End | L=260mm, t=1mm | 1150 |
| DC-E2 | L125×8 | Both legs | End | L=260mm, t=2mm | 1150 |

*2.2. Tension tests on steel plates*

Fig. 2(a) shows the dimension of steel coupons used in tension tests. The gauge length of steel coupons was 83.8 mm, in which the width of steel was kept at mm. The thickness of steel coupons remained the same as steel angles, namely, 8 mm. Three samples were cut from steel angles along the length and tested in tension. Fig. 2(b) shows the tensile stress-strain curve of coupons. It can be observed from the figure that steel coupons developed elastic stage, yield plateau, hardening stage, and finally necking before fracture. The average yield strength of coupons was 391.4 MPa, and the ultimate tensile strength was 573.7 MPa.

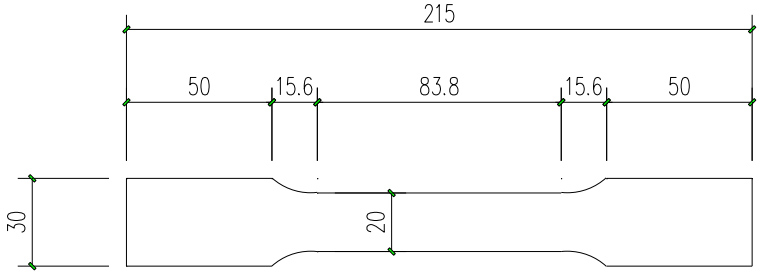


(a) Geometry and dimensions of steel coupons

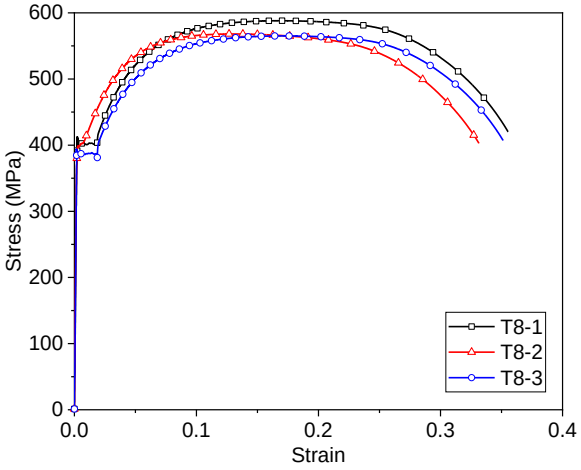


(b) Stress-strain curves of steel plates

**Fig. 2** Typical stress-strain curve of steel angles in tension

*2.3. Test setup and loading procedures*

After the installation of pin supports at both ends of steel angles, an axial compression was applied to the steel angle by using a hydraulic compression machine, as shown in Fig. 3(a). Note that the applied load was in alignment with the centroid of the steel angles and was measured by a load cell. The lateral deflections of steel angles were recorded through linear variable displacement transducers parallel to the legs, as shown in Fig. 3(b). Besides, strain gauges were also attached to the face of steel angles to measure the longitudinal strain (see Figs. 3(b, c and d)). Three sections along the height of steel angles were selected to mount strain gauges, namely, the mid-height and both ends of steel angles.

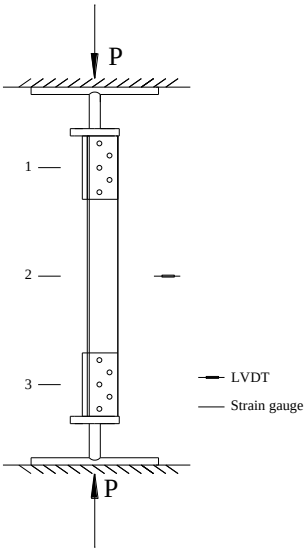


(a) Test setup and instrumentation

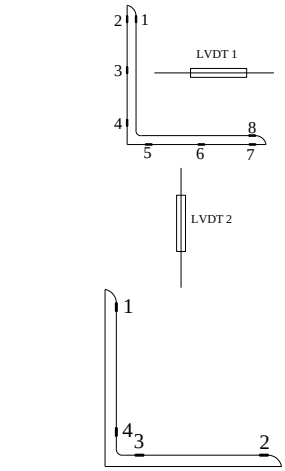


(b) Layout of strain gauges for angles with local damage at the mid-height

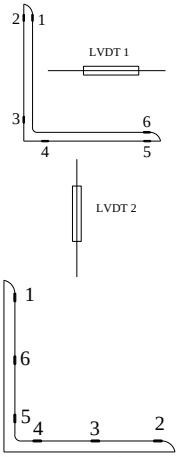


(c) Layout of strain gauges for angles with local damage at the end

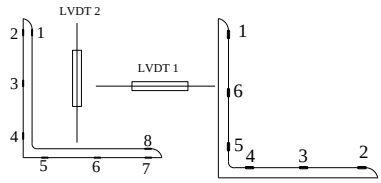


(d) Layout of strain gauges for angles without damage

**Fig. 3** Schematic view of test setup and instrumentation

## 3. Experimental tests and discussions

*3.1. Load-deflection curves*

Fig. 4 shows the load-deflection curve of steel angle DCN without local damage. Note that deflections perpendicular to the two legs were measured using LVDTs. It can be observed from the figure that steel angles started to deflect with increasing axial compression, but the deflections measured in the two directions differed greatly from each other due to the presence of initial imperfections. The lateral deflection increased gradually until the ultimate load was reached. Following the attainment of the peak load, the lateral deflection increased rapidly with decreasing load, indicating the failure of steel angles. The final failure of the steel angles was induced by global buckling in which bending and twisting were combined. The ultimate load of the steel angle was 441.0 kN, corresponding to a mid-height deflection of 6.7 mm. It should be pointed out that the deflection of DCN-1 in direction 2 decreased before the attainment of the ultimate load, possibly as a result of the twisting of the steel angle during global buckling.

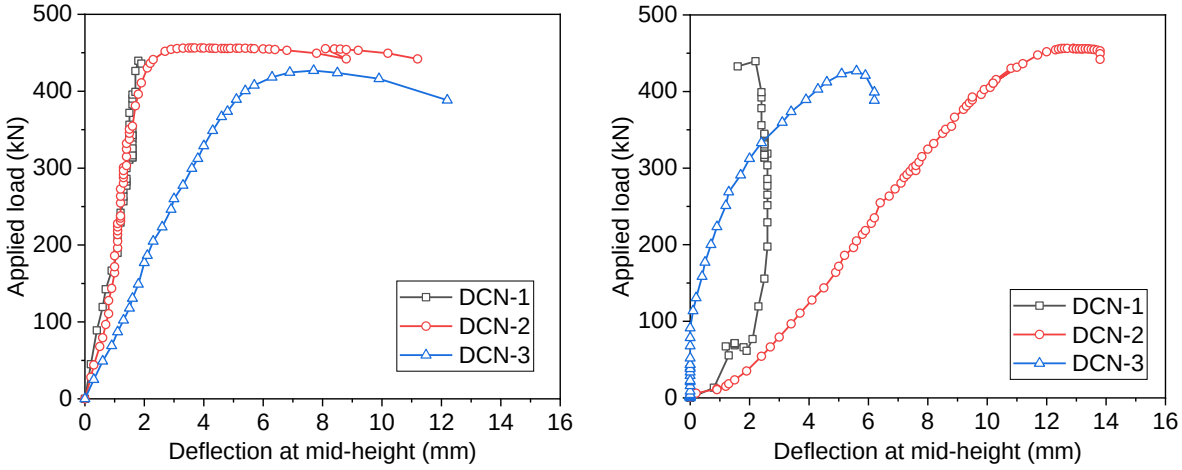


(a) Deflection 1 (b) Deflection 2

**Fig. 4** Load-deflection curves of steel angles without local damage

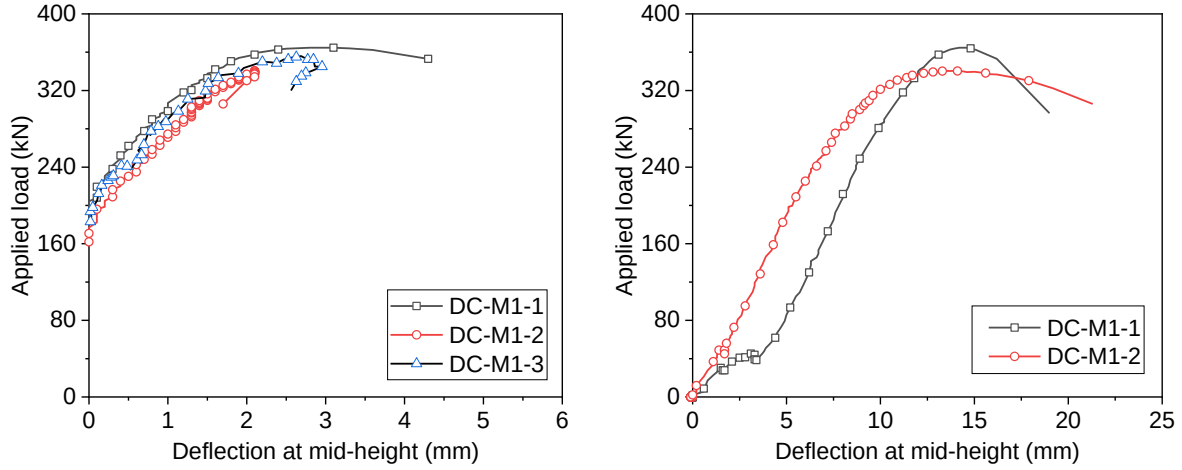


(a) Deflection 1 of DC-M1 (b) Deflection 2 of DC-M1

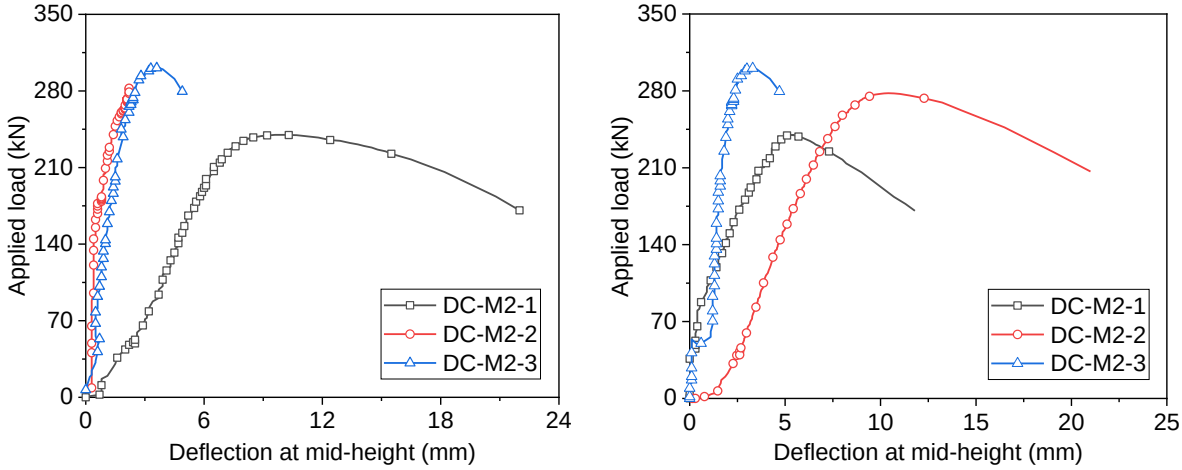


(c) Deflection 1 of DC-M2 (d) Deflection 2 of DC-M2

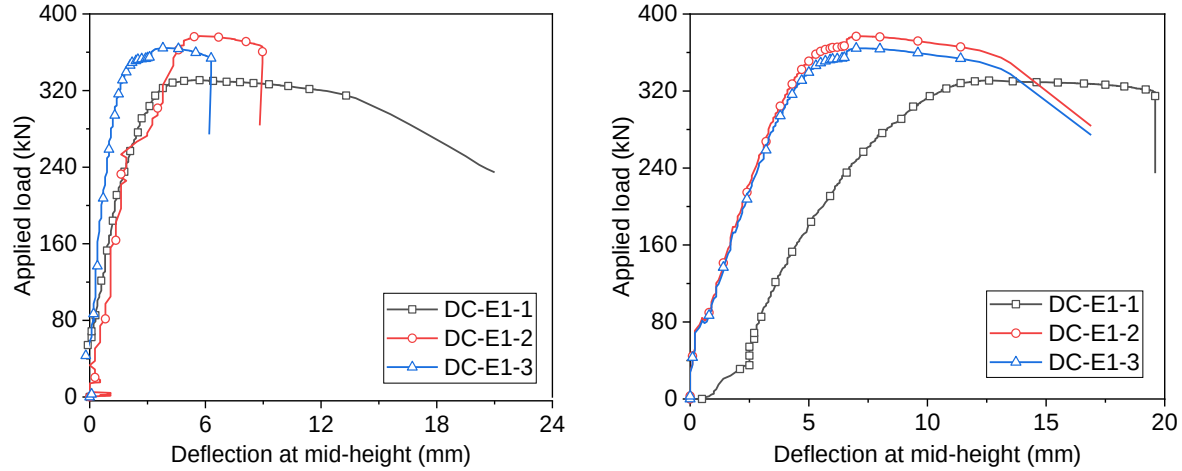


(e) Deflection 1 of DC-E1 (f) Deflection 2 of DC-E1

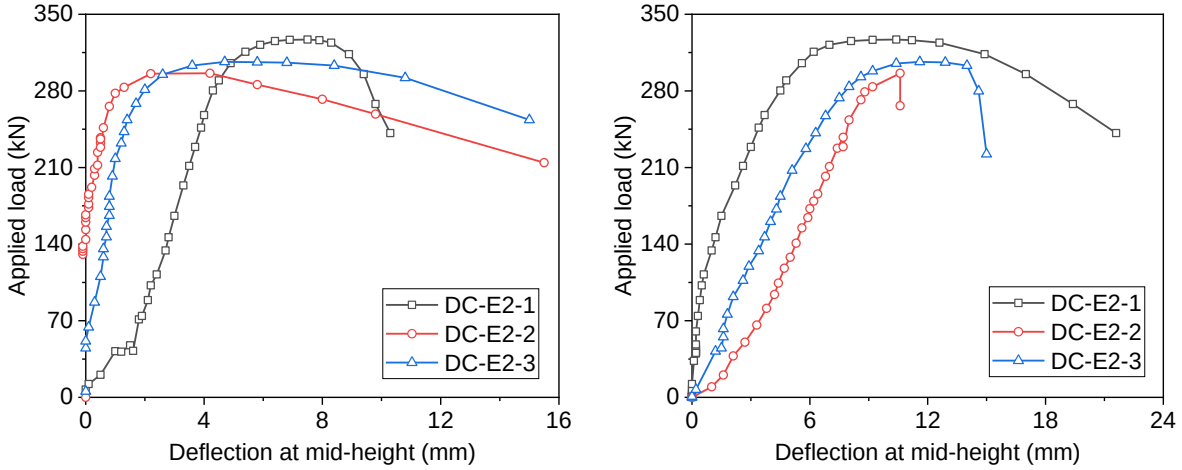


(g) Deflection 1 of DC-E2 (h) Deflection 2 of DC-E2

**Fig. 5** Load-deflection curves of steel angles with local damage

Fig. 5 shows the load-deflection curves of steel angles with different depths of damage at different regions. It can be observed that locally damaged steel angles began to deflect with the increase in the applied load, and the lateral deflection at the mid-height increased slowly until the ultimate load of steel angles was reached. However, apparent differences existed in the overall trend of load-deflection curves in the two directions, as shown in Figs. 5(a and b), which might be related to the different angles of bending and twisting when local buckling occurred in the locally damaged region. Comparisons among load-deflection curves of steel angles suggested that the ultimate load of steel angles with different depths of local damage differed greatly from each other. The ultimate load of DC-M1 with a 1 mm deep local damage was 353.7 kN, whereas that of DC-M2 was reduced by 18.8% to only 287.1 kN with the depth of local damage was increased to 2 mm (see Figs. 5(c and d)). Therefore, the ultimate load of steel angles decreased significantly with the increase of the depth of local damage at the mid-height.

When the local damage was located at the end of steel angles, similar load-deflection curves were obtained for DC-E1, as shown in Figs. 5(e and f). The ultimate load of DC-E1 was 347.7 kN, close to that of DC-M1, indicating that the location of damage did not have a significant effect on the ultimate load of steel angles when the depth of the local damage was only 1 mm. If the depth of local damage at the end was increased to 2 mm, the ultimate load of steel angle DC-E2 was reduced to 310.4 kN, around 11.7% lower than that of DC-E1. However, when compared with DC-M2, the ultimate load of DC-E2 was roughly 8.1% higher, indicating that a deeper local damage near the end of steel angles did not decrease the ultimate load of steel angles as much as that at the mid-height did.

### *3.2. Failure modes of steel angles*

Fig. 6 shows the typical failure modes of steel angles under axial compression. It can be observed that overall buckling occurred in the steel angle without local damage (see Fig. 6(a)). The steel angle mainly developed significant lateral deflections at the initial stage of loading. Once the applied load reached the peak value, the lateral deflection increased rapidly, and the steel angle exhibited twisting. However, in addition to overall deflections, local buckling in the locally damaged region was also observed with regard to steel angles with local damage, as shown in Figs. 6(b-e). For instance, steel angles DC-M1 and DC-M2 with local damage at the mid-height showed local buckling in the proximity of the mid-height. Similar failure modes were also observed near the end of steel angles DC-E1 and DC-E2. It is observed that the undamaged steel angle experienced overall buckling. However, in the case of locally damaged steel angles, the local damage significantly reduced the resistance at that specific location. During the compression process, the affected location could develop localised buckling failure due to the increased width-to-thickness ratio.

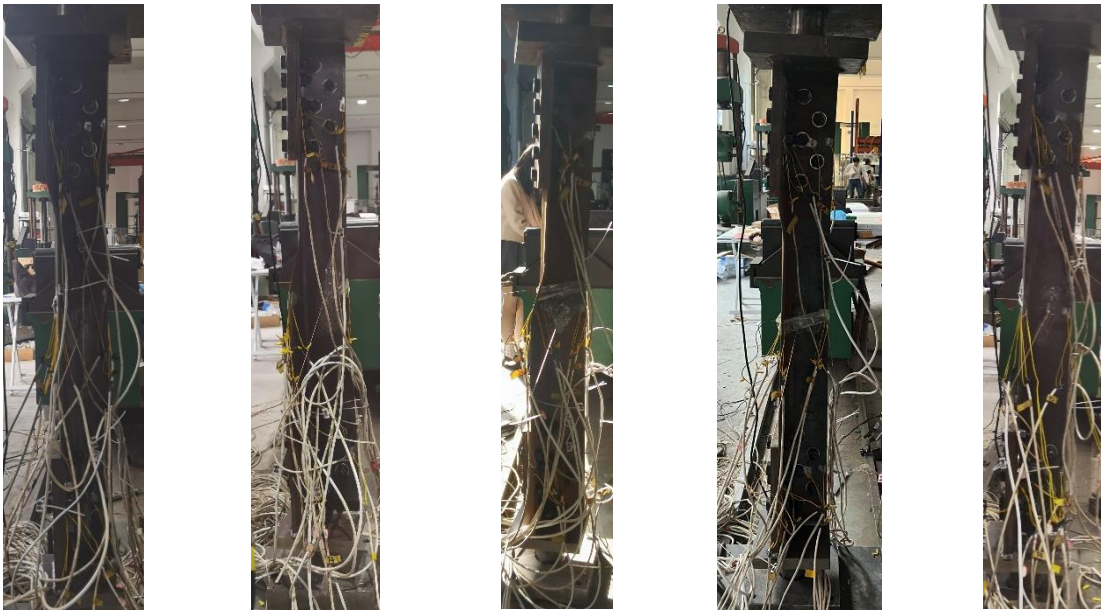

(a) DCN (b) DC-M1 (c) DC-M2 (d) DC-E1 (e) DC-E2

**Fig. 6** Typical failure modes of steel angles in compression

### *3.3. Discussions on test results*

Fig. 10 shows the effect of local damage depth on the ultimate load of steel angles under axial compression. Test results showed that the ultimate load of the undamaged steel angle DCN was 441.7 kN. When a local damage of 1 mm depth was produced at the mid-height, the ultimate load was reduced to by 20.0% to 353.7 kN, and the value was further decreased to 287.1 kN if the local damage depth was increased to 2 mm. When the local damage was located at the end of steel angles, similar conclusions could be obtained when comparisons were made between the undamaged and damaged steel angles, as shown in Fig. 10.

It is noteworthy that when the local damage depth was 1 mm, the ultimate loads of steel angles with local damages at the mid-height and end remained rather close to each other. Nevertheless, if the depth of local damage was increased to 2 mm, the ultimate load of steel angles with damaged end was 310.4 kN, considerably greater than that with the local damage at the mid-height. Hence, when the depth of local damage was 2 mm, it was more detrimental to the ultimate load of steel angles when it is located at the mid-height compared with that at the end.

### *3.4. Load-strain curves*

Fig. 7 shows the load-strain relationship of steel angles under axial compression. It can be observed that steel angle DCN without local damage developed different longitudinal strain at the mid-height and the end. The measured strain at the mid-height increased with the increasing axial compression, as shown in Fig. 7(a). Nonetheless, the compressive strain of M4 and M5 was significantly smaller than that of M8 and M9 due to the bending of the steel angles about the minor axis. When the axial load approached the ultimate load, the strain of M4 and M5 gradually changed from compressive strain to tensile strain, but that of M8 and M9 increased rapidly with the increasing axial compression. Note that the maximum strain associated with the load capacity had exceeded the yield strain of steel angles, indicating that the steel angle failed at the inelastic stage. Different variations of steel strains were measured at the end of steel angles, as shown in Fig. 7(b). Strains E1 and E2 at one toe of the angles were compressive and increased rapidly with the increasing load. However, strains E5 and E6 at the other toe were rather close to zero in the whole loading process. Moreover, the peak compressive strain corresponding to the load capacity was much smaller than the yield strain.

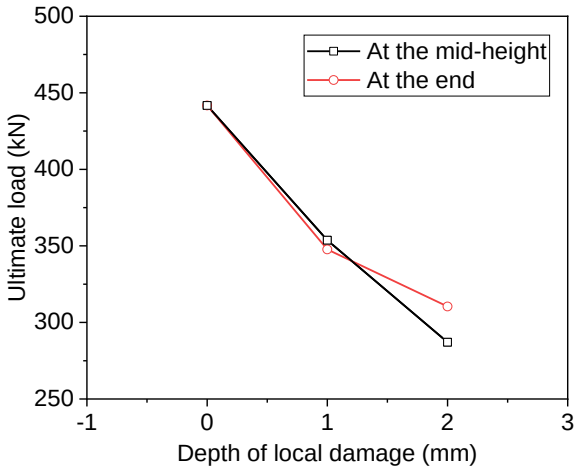


**Fig. 10** Effect of local damage on load capacity of steel angles

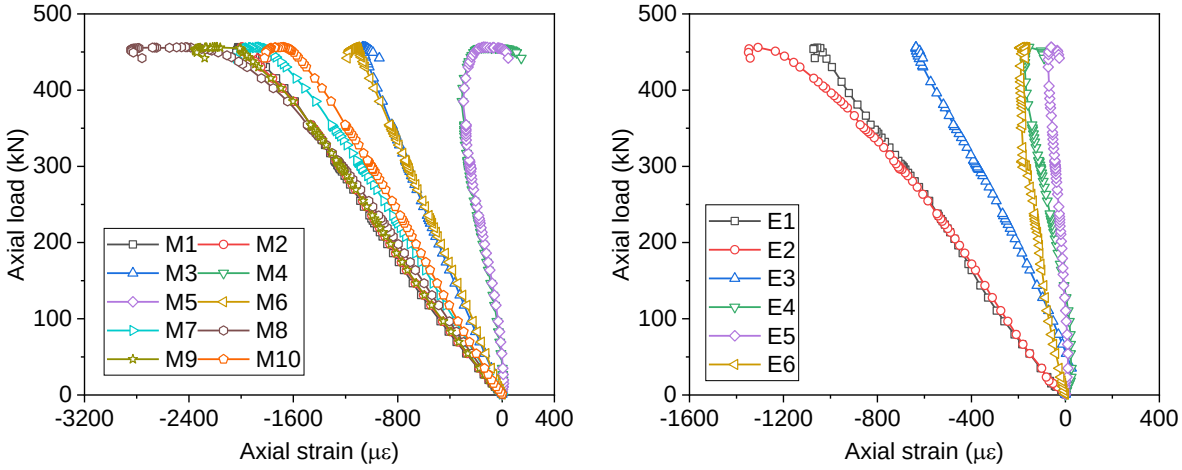


(a) Strain at the mid-height (b) Strain at the end

**Fig. 7** Longitudinal strains measured at different sections of steel angle DCN

When the steel angle was produced with a 2 mm deep local damage at the mid-height, most of the measured strains varied similarly to those of DCN, as shown in Fig. 8(a). Special attention should be paid to strains M6 and M7 at the mid-height. During failure of the steel angle, the measured strains M6 and M7 changed their signs from compression to tension, indicating the local buckling of the angle at the mid-height accompanying the overall buckling. As for the strain measured at the end of the steel angle, it was in general similar to that of DCN, as shown in Fig. 8(b).

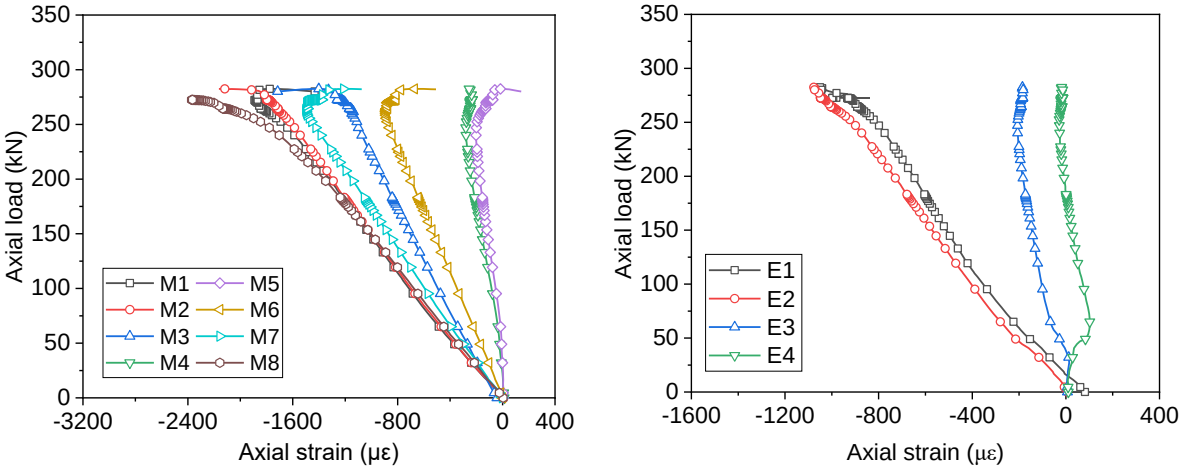


(a) Strain at the mid-height (b) Strain at the end

**Fig. 8** Longitudinal strains measured at different sections of steel angle DC-M2

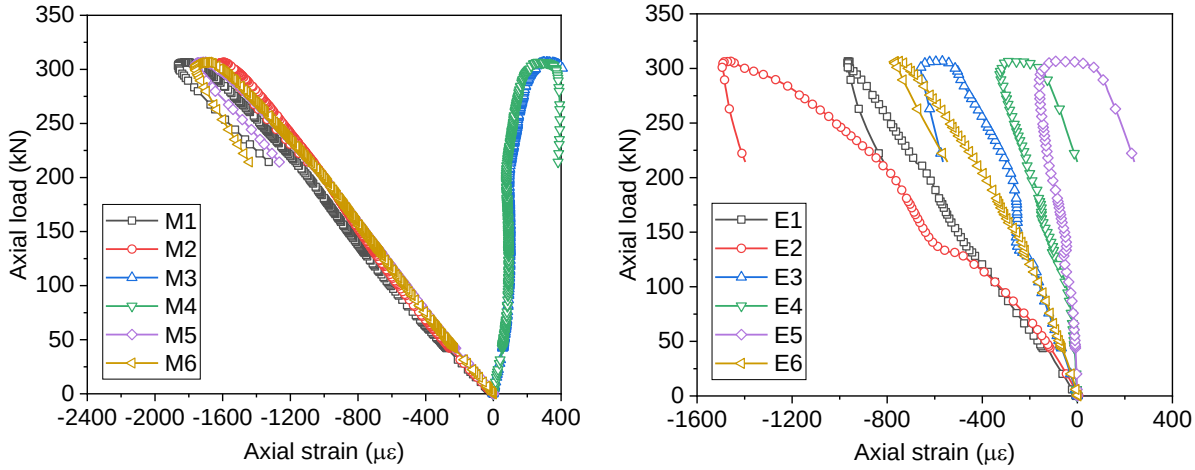


(a) Strain at the mid-height (b) Strain at the end

**Fig. 9** Longitudinal strains measured at different sections of steel angle DC-E2

When a 2 mm deep local damage was produced at the end, the load-strain curve of steel angle DC-E2 differed greatly from that of undamaged steel angles, as shown in Fig. 9. The strain of M3 and M4 was tensile immediately after loading (see Fig. 9(a)). This phenomenon was induced by the local deformation near the locally damaged region which eventually developed local buckling. The measured tensile strain by M3 and M4 decreased during loading, and then increased rapidly when the ultimate load was reached. Note that strain gauges M1 through M4 measured compressive strains in the whole loading process, and the maximum compressive strain measured at the ultimate load was still considerably smaller than the yield strain. Thus, the locally damage region was at the elastic stage when the steel angle failed. The measured strain at the end of steel angles was in general similar to that at the mid-height, as shown in Fig. 9(b), but the strain of E4 and E5 was compressive rather than tensile at the end.

## 4. Numerical modelling of steel angles

### *4.1. Establishment of numerical models*

Besides experimental tests, numerical modelling is also performed using ABAQUS [27] to investigate the behaviour of locally damaged steel angles under axial compression. Fig. 11 shows the numerical model for steel angles. In the numerical model, solid element C3D8R is used to model the steel angle and the end plate. The local damage at the mid-height and the end is modelled by reducing the thickness of the steel angle. To simplify the model, steel bolts connecting the steel angle and the end plate are neglected, and the two parts are tied together. Two reference points are defined at both ends of each steel angle to simulate the pin support. Before simulations, the mesh size is properly selected so that it will not affect the accuracy of the numerical model. The mesh size is determined to be 2 mm in the thickness direction and 10 mm along the height of steel angles.

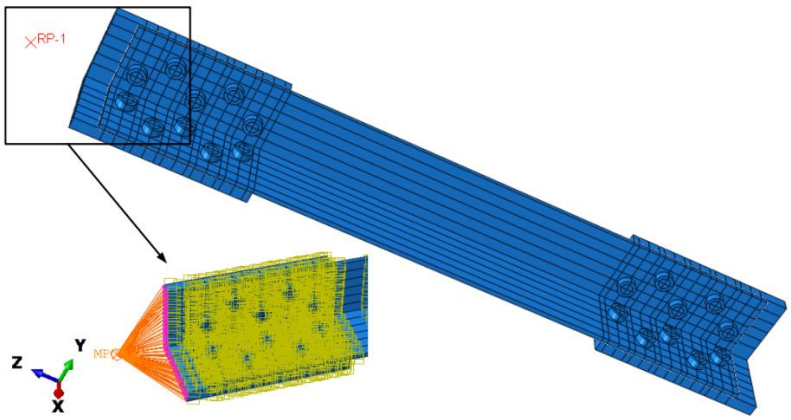


**Fig. 11** Numerical models for steel angles under axial compression

**Table 2**
Comparison between numerical and experimental ultimate loads

| Steel angles | Experimental value of ultimate load (kN) | Numerical value of ultimate load (kN) | Numerical value/experimental value |
|---|---|---|---|
| DCN | 441.0 | 427.5 | 0.97 |
| DC-M1 | 353.7 | 340.5 | 0.96 |
| DC-M2 | 287.1 | 289.6 | 1.00 |
| DC-E1 | 357.4 | 362.8 | 1.02 |
| DC-E2 | 310.4 | 331.1 | 1.07 |
| Average value | | | 1.00 |
| Coefficient of variation | | | 4.3% |

### *4.2. Material properties and initial imperfections*

The average mechanical properties of steel plates measured through tension tests are adopted in the numerical model. To simplify the stress-strain curve, a bilinear stress-strain curve is employed, of which the elastic modulus remains the same as that measured in the tension tests, and the hardening modulus is calculated as the slope of the stress-strain curve between the yield and ultimate stresses. In addition to the mechanical properties, residual stresses in steel angles are also defined in the numerical model, and the distribution of residual stress across the section is taken from GB 50017-2017 [28]. Initial geometric imperfections are also considered. In most design codes, the initial bending of steel members is assumed to be 1/1000 of the height. This value is also used in the present study.

### *4.3. Model validation*

Table 2 summarises the comparisons between numerical and experimental ultimate loads of locally damaged steel angles under axial compression. It can

be observed from the table that the numerical results are in good agreement with the experimental results. The average ratio of numerical to experimental results is 1.00, with a coefficient of variation of 4.3%. Therefore, the numerical model is capable of predicting the ultimate load of steel angles with good accuracy. In addition to the ultimate load, the load-deflection curve of steel angles can also be predicted with reasonably good accuracy using the numerical model. Fig. 12 shows the comparison between numerical and experimental load-deflection curve of steel angles. Differences exist at the initial stage of loading. The numerical load-deflection curve in general overestimate the initial stiffness of steel angles, as the gap between steel angles and bolts at the top and bottom ends is not considered in the numerical model. In addition, the steel angles might have certain initial deformations or geometric defects, resulting in uncertainty in the location of the largest deflection. However, the presence of gaps between bolts and holes does not significantly affect the ultimate load. When the ultimate load is reached, the numerical deflection increases rapidly with decreasing load.

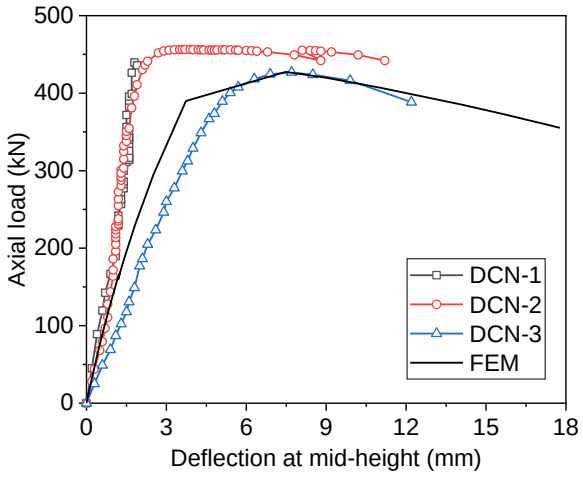


(a) DCN

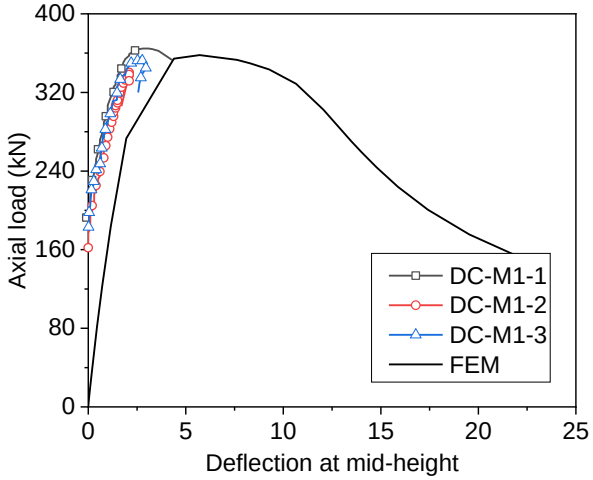


(b) DC-M1 ( (mm) should be added to the x axis)

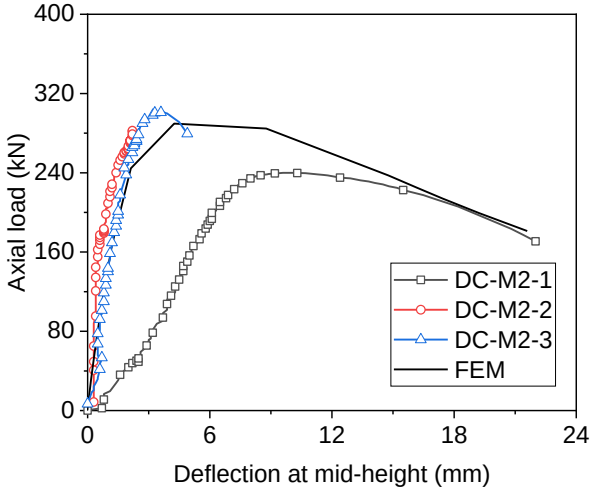


(c) DC-M2

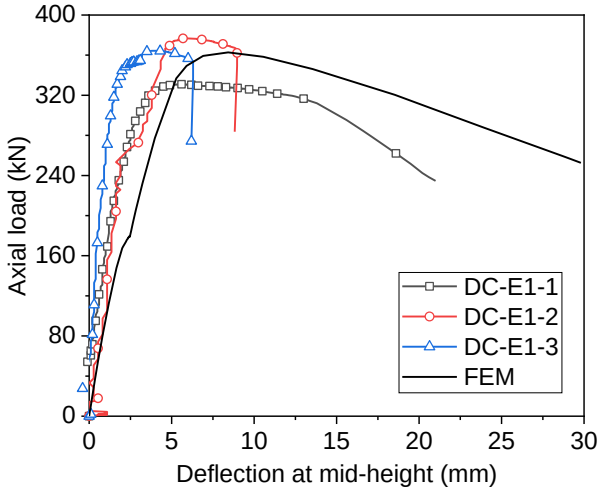


(d) DC-E1

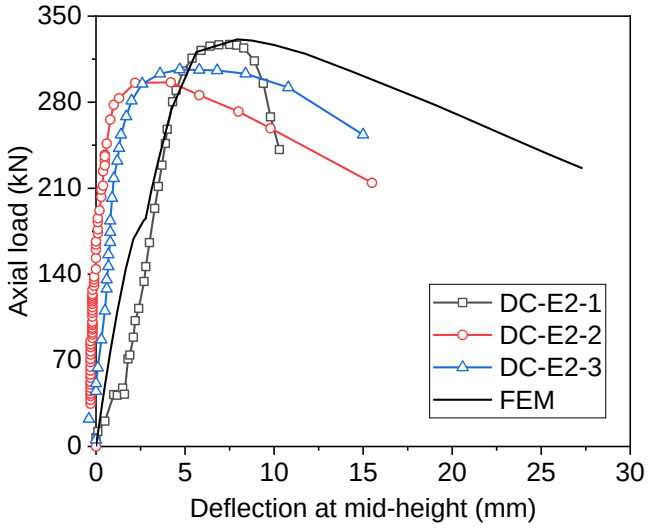


(e) DC-E2

**Fig. 12** Comparisons between experimental and numerical load-deflection curves of steel angles

Fig. 13 shows the failure mode of steel angles using numerical simulations. Global buckling of the undamaged steel angle DCN can be observed in Fig. 13(a). The maximum deflection of the steel angle occurs at the mid-height due to the local deformation near the mid-height. The maximum stress appears at

the angle toe and has exceeded the yield strength of steel angles. When local damage is produced at the mid-height, stress concentration in the damaged region can be observed, as shown in Figs. 13(b and c). Eventually, local buckling of steel angles also takes place in the damaged region, leading to the significantly greater Mises stresses. It can be seen that the maximum stress of DC-M1 in the mid-span is 471.0 MPa, whereas that of DC-M2 is 467.7 MPa, indicating that the maximum stress is not significantly affected by the depth of local damage. However, the Mises stress in steel angles with local damage at the mid-height is also increased as compared with that in the undamaged steel angle. By contrast, when the end of steel angles is damaged, the region with the maximum Mises stress gradually moves towards the end, as shown in Figs. 13(d and e). The maximum local deformation of DC-E1 still occurs at the mid-height, whereas that of DC-E2 appears at the end of the steel angle. Note that the numerical deformation profile of DC-E1 is different from the experimental observation, as in the numerical model the steel angles and the end plate are tied together which prevents the development of local deformation near the end.

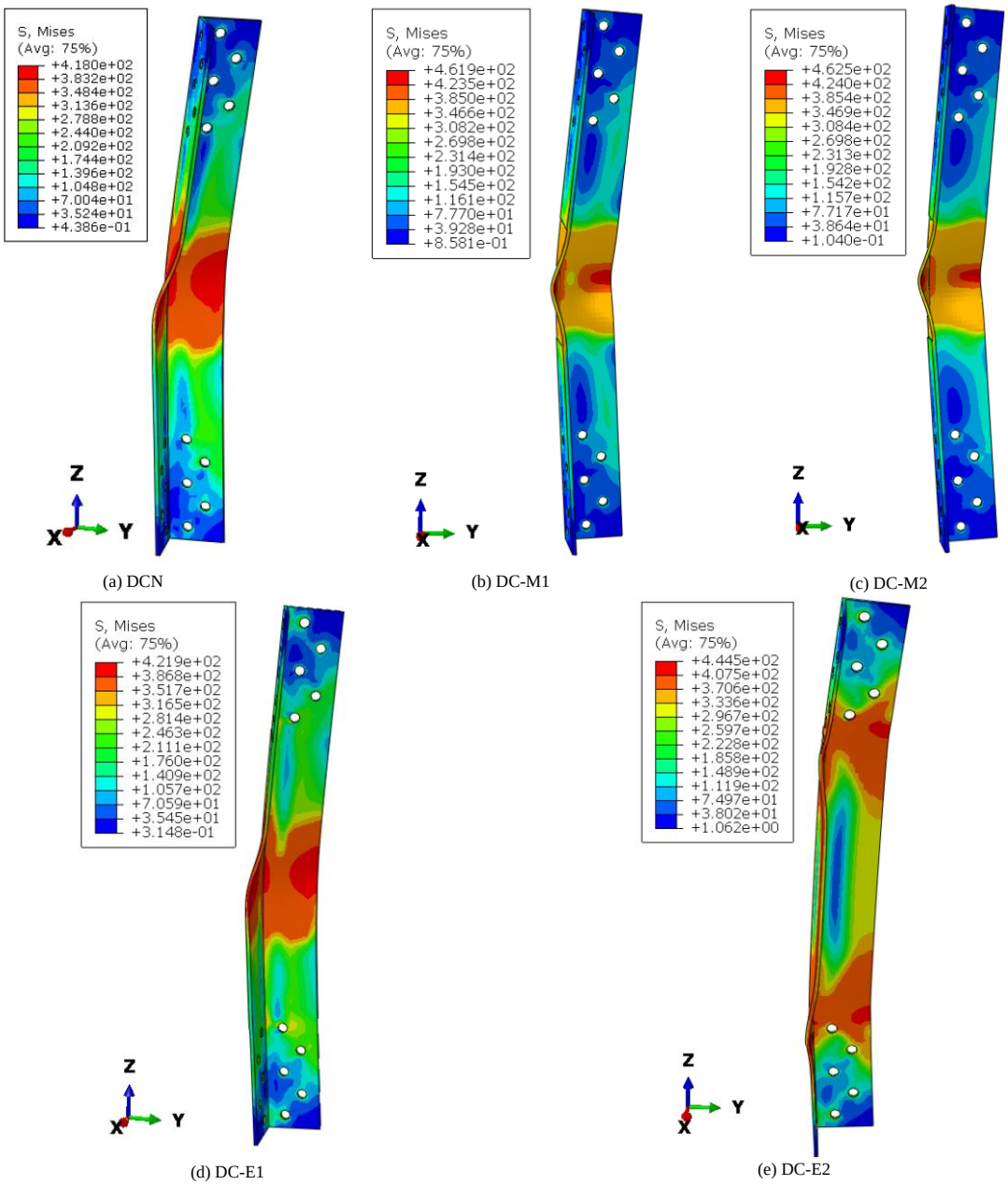


**Fig. 13** Numerical failure modes of steel angles with damages

## 5. Parametric study

With the verified numerical model, a series of parametric study was conducted to investigate the effects of slenderness and local damage depth on the ultimate load of damaged steel angles, as shown in Figs. 14 and 15. The three aspect ratios are intended to compare the effects of local damage depth and slenderness on the ultimate load-carrying capacity of specimens. The selection of these three aspect ratios is found to reveal underlying patterns during the analysis. Detailed analyses and discussions can be found in the following section.

### *5.1. Effect of slenderness*

Fig. 14 shows the effect of slenderness on the ultimate load of damaged steel angles subjected to axial compression. It can be observed that when the local damage is located at the mid-height of steel angles, the ultimate load decreases almost linearly with increasing slenderness from 50 to 100 (see Fig. 14(a)). For instance, for a damage depth of 1 mm, the ultimate load of steel angles with a slenderness of 50 is 340.5 kN, whereas that of steel angles is reduced to 209.1 kN when the slenderness is increased from 50 to 100. When the damage depth is increased to 2 mm, a similar load-slenderness relationship is obtained for damaged steel angles. However, the slope of the curve is significantly reduced in comparison with the curve of steel angles with 1 mm deep local damage. It indicates that when the damage depth is increased from 1 mm to 2 mm, the effect of slenderness becomes less significant. Fig. 14(b) shows the ultimate load-slenderness relationship when the local damage is located at the end of steel angles. The overall relationship remains similar to those with the local damage at the mid-height. However, it should be pointed out that when the slenderness of steel angles exceeds 50, the ultimate load of steel angles with 1 mm deep local damage is rather close to that with 2 mm deep local damage. It is attributed to the fact that with increasing slenderness, buckling of steel angles dominates in which the local damage at the end plays a limited part.

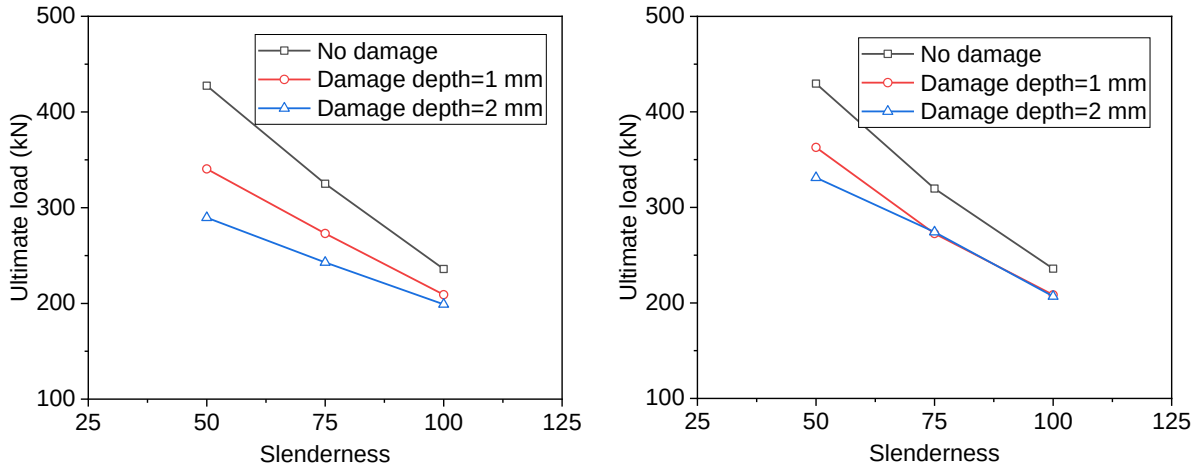


(a) Steel angles with local damage at mid-height (b) Steel angles with local damage at the end

**Fig. 14** Effect of slenderness on load capacity of steel angles

*5.2. Effect of local damage depth*

Fig. 15 shows the effect of local damage depth on the ultimate load of steel angles. It can be observed that for a given slenderness of steel angles, the ultimate load of steel angles decreases significantly with increasing depth of local damage at the mid-height (see Fig. 15(a)). For steel angles with a slenderness of 50, the ultimate load of the undamaged angle was 427.5 kN, whereas that of steel angles with a 2 mm deep local damage was reduced by 32.3% to 289.6 kN. Nonetheless, the reduction of ultimate load with increasing local damage depth becomes less significant when the slenderness of steel angles was increased from 50 to 100. Fig. 15(b) shows the effect of local damage depth on the ultimate load of steel angles when the local damage is located at the end. In general, the ultimate load of steel angles decreases gradually with the increase of the depth of local damage at the end when the slenderness of steel angles is 50. The ultimate load of steel angles with 2 mm deep local damage is 331.1 kN, 23.5% lower than that of the undamaged member. Nevertheless, when the slenderness of steel angles is 75 or 100, the effect of local damage depth on the ultimate load becomes less significant, in particular when the damage depth at the end is increased from 1 mm to 2 mm. Therefore, it can be concluded that local damages at the end of steel angles mainly affect the ultimate load of steel angles with smaller slendernesses.

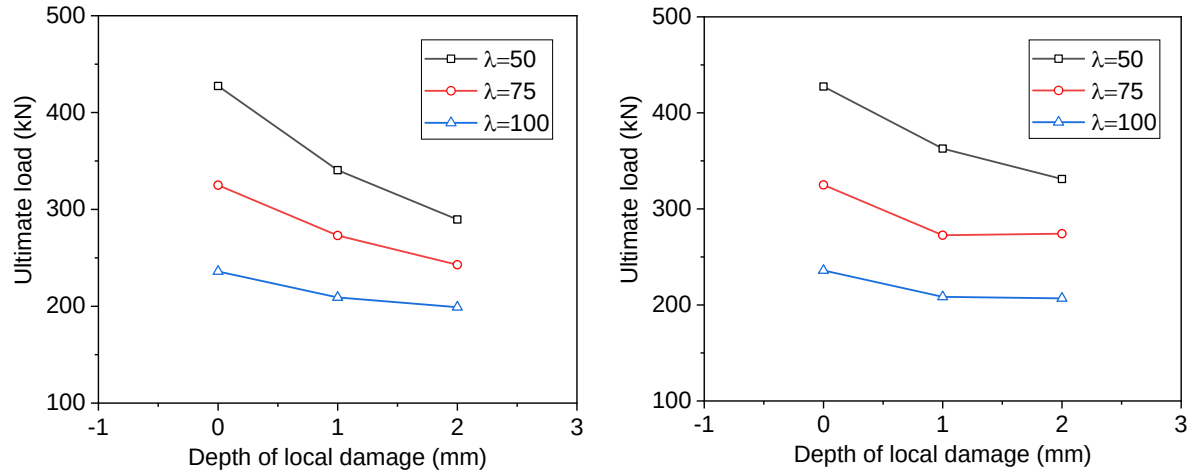


(a) Steel angles with local damage at mid-height (b) Steel angles with local damage at the end

**Fig. 15** Effect of damage depth on load capacity of steel angles

## 6. Design equations for steel angles

Existing design methods [29] can calculate the ultimate load or the buckling coefficient of steel angles under axial compression, but the effect of local damage at different locations cannot be considered in the design method. In this section, a set of design equations is proposed to take account of the effect of local damage on the global buckling resistance of steel angles. In the equation, the ultimate load of steel angles with local damage can be computed from

$$F = (1 - R\eta_s)F_c \tag{1}$$

in which $F_c$ is the ultimate load of steel angles without local damage, $\eta_s$ is the local damage ratio, $R$ is a reduction factor for the slenderness of steel angles, and $F$ is the load capacity of locally damaged steel angles.

For steel angles with different depths of local damage, the local damage ratio is expressed in Eq. (2).

$$\eta_s = \frac{x_z}{t} \tag{2}$$

$$x_z = \frac{(1-DOV)\times(2Bt-t^2)+t^2-2Bt}{2t-4B} \tag{3}$$

$$DOV = \frac{V_{dam}}{V_{total}} \tag{4}$$

where $x_z$ is the equivalent thickness of steel angles after considering the effect of local damage, $t$ is the original thickness of steel angles, $B$ is the original width of steel angles, $DOV$ is the volumetric ratio of the local damage to the whole steel angle, $V_{dam}$ is the volume of the local damage, and $V_{total}$ is the volume of the whole steel angle.

Additionally, the width-to-thickness ratio is a crucial parameter influencing the stability of structural components. Within the limit of the width-to-thickness ratio for equal-leg steel angle, a parametric study of the design equation suggests that $b/t$ may influence $x_z$ (the equivalent thickness of steel angles) and subsequently affect the load-carrying capacity after corrosion. Through the simplification of $x_z$, it is determined that $x_z$ is the product of DOV and t/2. Therefore, $x_z$ is independent of $b/t$, indicating that $b/t$ does not affect the proposed design equation.

Experimental and numerical results show that the effect of local damage on the load capacity is relevant to the slenderness of steel angles. The effect is more significant when the slenderness of steel angles is small. To determine the influence of slenderness, expressions are developed through linear regression for the reduction factor of slenderness, as expressed in Eqs. (5) and (6).

$$R = -0.03071\lambda + 4.65523 \quad (5)$$

$$R = -0.00916\lambda + 1.52063 \quad (6)$$

in which $\lambda$ is the slenderness of steel angles about the weakest axis.

Fig. 16 shows the comparison of the calculated buckling coefficient using the proposed equations with numerical results and the design curve. The buckling coefficient and normalised slenderness can be determined from Eqs. (7) and (8). It can be observed that the calculated result is in good agreement with the numerical result, but both the calculated and numerical buckling coefficients of steel angles with local damage at the mid-height are far below the design curve, as shown in Fig. 16(a), in particular when the normalised slenderness is small. The difference between the calculated result and the design curve is reduced with increasing normalised slenderness. Besides, the depth of local damage also has a significant influence on the calculated buckling coefficient. When the depth of local damage is 1 mm at the mid-height, the calculated result is around 35.0% lower than the design curve. When the depth of local damage is increased to 2 mm, the calculated buckling coefficient is further reduced by 41.5% as compared with the design curve.

$$\varphi = \frac{F}{Fc} \quad (7)$$

$$\lambda_n = \frac{\lambda}{\pi} \times \sqrt{\frac{f_y}{E}} \quad (8)$$

where $\varphi$ is the buckling coefficient, $\lambda_n$ is the normalised slenderness, $f_y$ is the yield strength of steel angles, and $E$ is the elastic modulus of steel angles.

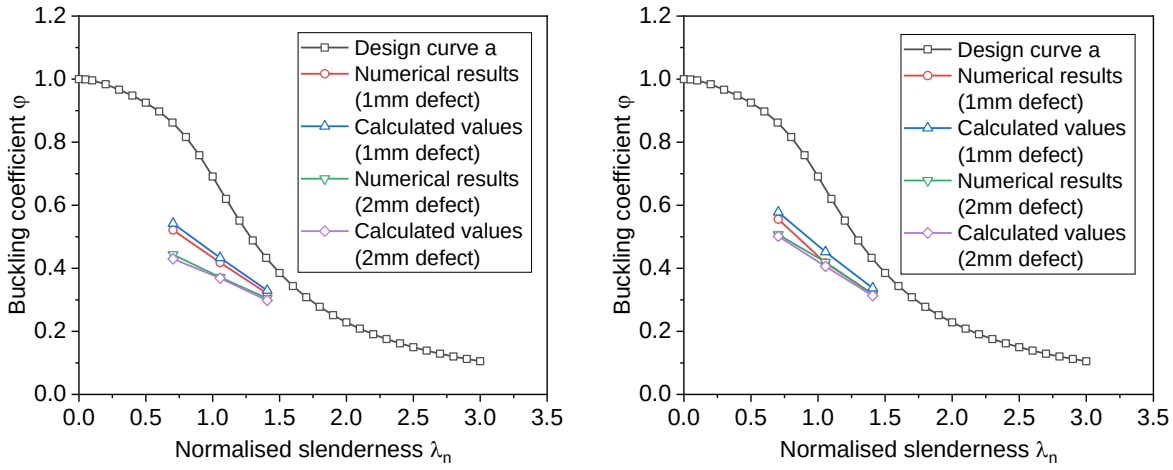


(a) Local damage at the mid-height (b) Local damage at the end

**Fig. 16** Comparisons between calculated buckling coefficient and design curve of steel angles with local damages

Fig. 16(b) shows the comparison of the calculated buckling coefficient using the proposed equation with the numerical result and design curve. It can be found that the calculated result agrees reasonably well with the numerical result, whereas both of them fall far below the design curve. When the local damage depth is 1 mm, the calculated buckling coefficient is roughly 33.8% lower than the design curve. If the local damage depth is increased to 2 mm, the calculated buckling coefficient becomes 35.8% smaller than the design curve. Furthermore, comparisons can also be made between the calculated buckling coefficient of steel angles with local damage at the mid-height and the end. In general, the local damage at the mid-height will have a more significant influence on the buckling coefficient than that at the end of steel angles. Therefore, in the design process, considerations should be taken to the impact of corrosion on the ultimate compressive load-bearing capacity of steel angles.

## 7. Conclusions

This paper presents experimental and numerical investigations on the compression behaviour of locally damaged steel angles with equal legs. Five groups of steel angles were tested under axial compression, in which local damages of different depths were prefabricated at different locations. The load resistance and failure pattern of steel angles were obtained through experimental tests. Besides, numerical models were also established for steel angles. Parametric studies were also conducted using the verified numerical model to investigate the influence of local damage depth and slenderness on the ultimate load of steel angles. Finally, design equations were developed to take account of the effect of local damages on ultimate resistance. The following conclusions could be drawn from experimental and numerical studies.

(1) When local damages were located at the mid-height of steel angles, the ultimate resistance of the angle decreased with increasing depth of local damages. The ultimate load of the undamaged steel angle DCN was 441.7 kN, whereas those of steel angles DC-M1 and DC-M2 with 1 mm and 2 mm deep local damages were 353.7 kN and 287.1 kN, respectively, reduced by 19.9% and 35.0% as compared with DCN.

(2) For steel angles with local damages at the end, the ultimate resistance also decreased when the depth of local damages increased from 0 to 2 mm. The ultimate loads of damaged steel angles DC-E1 and DC-E2 were 357.4 kN and 310.4 kN, respectively, roughly 19.1% and 29.7% lower than that of DCN.

(3) Numerical results showed that the influence of local damages on the ultimate load becomes increasingly insignificant when the slenderness of steel angles is increased from 50 to 75. For instance, when the slenderness of steel angles is 120, a 2.0 deep local damage at the mid-height will only reduce the ultimate load of the steel angle by 15.6% from 235.9 kN to 199.0 kN compared with the undamaged steel angle.

(4) A design method is proposed based on the experimental and numerical results of locally damaged steel angles. In the method, the effect of local damage is considered by converting it to equivalent overall reduction of the steel angle thickness, and a reduction factor is defined to reflect the influence of slenderness on the buckling coefficient of locally damaged steel angles.

## Acknowledgements

The authors gratefully acknowledge the support provided by China Power Engineering Consulting Group Co., LTD (Grant No.: GSKI2-T05-2020) and the Structural Laboratory of Chongqing University.

## References

[1] S.H. Xu, Z.X. Zhang, G.C. Qin, Study on the seismic performance of corroded H-shaped steel columns, Engineering Structures 191 (2019) 39-61.
[2] Y. Sharifi, S. Tohidi, J.K. Paik, Ultimate compressive strength of deteriorated steel web plate with pitting and uniform corrosion wastage, Sci. Iran. 23(2) (2016) 486-499.
[3] A. Cinitha, P.K. Umesha, N.R. Iyer, An overview of corrosion and experimental studies on corroded mild steel compression members, KSCE Journal of Civil Engineering 18(6) (2014) 1735-1744.
[4] T. Kaita, J. Appuhamy, K. Itogawa, M. Ohga, K. Fujii, Experimental Study on Remaining Strength Estimation of Corroded Wide Steel Plates under Tensile Force, 12th East Asia-Pacific Conference on Structural Engineering and Construction (EASEC), Hong Kong, PEOPLES R CHINA, 2011.
[5] V. Sarveswaran, J.W. Smith, D.I. Blockley, Reliability of corrosion-damaged steel structures using interval probability theory, Structural Safety 20(3) (1998) 237-255.
[6] H. Tang, J.X. Peng, C.S. Cai, D.D.K. Lee, Test, 3D Scanning and FE Study on Flexural Behavior of Q550E HPS Beams Subjected to Local Corrosion at Mid-Span Region, International Journal of Steel Structures 22(5) (2022) 1452-1473.
[7] Y.D. Wang, S.H. Xu, A.B. Li, Flexural performance evaluation of corroded steel beams based on 3D corrosion morphology, Structure and Infrastructure Engineering 16(11) (2020) 1562-1577.
[8] J. Peng, L. Xiao, J. Zhang, C.S. Cai, L. Wang, Flexural behavior of corroded HPS beams, Engineering Structures 195 (2019) 274-287.
[9] Z.X. Zhang, S.H. Xu, H. Wang, B.A. Nie, C. Su, Flexural buckling behavior of corroded hot-rolled H-section steel beams, Engineering Structures 229 (2021).
[10] Y. Chai, J.X. Peng, L.F. Xiao, X.H. Liu, J.R. Zhang, Fatigue Behavior of High-Performance Steel Beams Subjected to Different Corrosion Conditions, International Journal of Steel Structures 23(4) (2023) 1105-1118.
[11] X.H. Liu, J.R. Zhang, Experimental Study on Effect of Corrosion on Flexural Load-carrying Capacity of Q550E High-performance Steel Girder, Zhongguo Gonglu Xuebao/China Journal of Highway and Transport 32(11) (2019) 184-191and201.

[12] Z.W. Zhao, S.J. Mo, Q.Q. Xiong, H.Q. Liu, B. Liang, Moment capacity of H-section steel beam with randomly located pitting corrosion, Probabilistic Engineering Mechanics 66 (2021).
[13] Z.W. Zhao, L.M. Tang, N. Zhang, Q. Cai, S.J. Mo, B. Liang, Shear capacity of H-shaped steel beam with randomly located pitting corrosion, Applied Ocean Research 115 (2021).
[14] J. Sheng, J.W. Xia, H.F. Chang, Bending Behavior of Corroded H-Shaped Steel Beam in Underground Environment, Appl. Sci.-Basel 11(3) (2021).
[15] S. Xu, B. Nie, H. Zhang, Time-dependent Reliability Analysis of Corroded Steel Beam Based on Probability Density Evolution Theory, Hunan Daxue Xuebao/Journal of Hunan University Natural Sciences 47(7) (2020) 75-83.
[16] B. Wang, W.Z. Huang, S.S. Zheng, Study on Restoring Force Performance of Corrosion Damage Steel Frame Beams under Acid Atmosphere, Applied Sciences-Basel 9(1) (2019).
[17] K.K. Toledo, H.S. Kim, Y.S. Jeong, I.T. Kim, Residual Compressive Strength of Short Tubular Steel Columns with Artificially Fabricated Local Corrosion Damage, Materials 13(4) (2020).
[18] Y.D. Wang, T. Shi, B. Nie, H. Wang, S.H. Xu, Seismic performance of steel columns corroded in general atmosphere, Steel and Composite Structures 40(2) (2021) 217-241.
[19] A. Hussain, Y.-P. Liu, S.-L. Chan, Finite Element Modeling and Design of Single Angle Member Under Bi-axial Bending, Structures 16 (2018) 373-389.
[20] Q. Zhang, J.N. Wen, Q. Han, Z.F. Wang, J.B. Sun, Seismic performance evaluation of steel circular hollow section bridge piers with corroded ends, Bulletin of Earthquake Engineering (2023).
[21] Z.X. Zhang, S.H. Xu, B. Nie, R. Li, Z. Xing, Experimental and numerical investigation of corroded steel columns subjected to in-plane compression and bending, Thin-Walled Structures 151 (2020).
[22] S.S. Zheng, X.H. Zhang, X.R. Zhao, Experimental investigation on seismic performance of corroded steel columns in offshore atmospheric environment, Structural Design of Tall and Special Buildings 28(4) (2019).
[23] B. Nie, S.H. Xu, H.J. Zhang, Z.X. Zhang, Experimental and numerical studies on the behaviour of corroded cold-formed steel columns, Steel and Composite Structures 35(5) (2020) 611-625.
[24] Z.-L.D. A.H.A. Abdelrahman, Yao-Peng Liu, S.-L.C. ∗ Stability design of single angle member using effective stress-strain method, Structures 20 298-308.
[25] K. Oszvald, P. Tomka, L. Dunai, The remaining load-bearing capacity of corroded steel angle compression members, Journal of Constructional Steel Research 120 (2016) 188-198.
[26] Y. Huang, Z.G. Su, B.R. Zhu, Y.X. Chen, T. Wan, Z.X. Tuo, The influence of corrosion on the bearing capacity characteristics of overhead transmission line tower, Nonferrous Metals Science and Engineering(2023) 1-11.
[27] ABAQUS, Analysis user's manual version 6.13, ABAQUS Inc2013.
[28] Standard for design of steel structures (GB50017-2017), Standards Press of China, Beijing, 2017(in Chinese).
[29] M. Chen, W. Fang, H. Huang, Static behavior of corroded concrete-filled steel tubular members by simulating acid rain solution, Engineering Mechanics 37(2) (2020) 34-43.

**Advanced Steel Construction** – Vol. 20 No. 3 (2024) 292–299
**DOI:**10.18057/IJASC.2024.20.3.8


# BENDING ANALYSIS OF RECYCLED CONCRETE BEAMS REINFORCED WITH GFRP BARS UNDER HIGH TEMPERATURE

Qi Guo [1, 2] and Hao Chen [3, *]

[1] *School of Civil Engineering, Xi'an University of Architecture and Technology, Xi'an 710055, Shanxi, China.*
[2] *Key Lab of Structural Engineering and Earthquake Resistance, Ministry of Education (XAUAT), Xi'an 710055, Shanxi, China.*
[3] *XAUAT UniSA An De College, Xi'an University of Architecture and Technology, Xi'an 710311, Shanxi, China*
** (Corresponding author: E-mail: 1054686243@qq.com)*

**ABSTRACT**

GFRP (Fiber Reinforced Polymer) reinforcement material is characterized by high strength and excellent corrosion resistance, which exhibits promising application prospects in engineering. The GFRP reinforcement for steel-concrete beams can increase the structural load-bearing capacity and durability. In this study, a refined finite element model of high-temperature GFRP-reinforced recycled steel-concrete beams was established by using ABAQUS software. The temperature distribution and residual load-carrying capacity of GFRP-reinforced recycled steel-concrete beams were analyzed, and the reliability of the model was validated based on the results of full-scale experiments on 16 groups of recycled steel-concrete beams. By using the validated model, the influence of heating temperature, reinforcement strength, steel strength, strengthening method, and concrete strength on the residual load-carrying capacity of the structure was analyzed. The stress patterns and failure mechanisms of GFRP-reinforced recycled steel-concrete beams were also analyzed. As can be seen from the results, the Type II strengthening method significantly increased the load-carrying capacity of recycled steel-concrete beams. It was also found that the load-carrying capacity of the tested beams was greatly affected by temperature. Under the temperature of 200℃ and 600℃, the load-carrying capacity of the unreinforced specimens decreases by approximately 13% and around 25%, respectively. Under the same heating temperature, compared to the unreinforced specimens, the load-carrying capacity was increased by approximately 10% by using the Type I strengthening method, but only around 4.7% by the Type II strengthening method. Finally, based on the results of this study and existing relevant experimental and numerical simulation results, and considering its feasibility and effectiveness, the Type I strengthening method for reinforced recycled steel-concrete beams was proposed. In general, the research findings of this paper can provide theoretical support for the design of reinforced recycled steel-concrete beams.

**ARTICLE HISTORY**

Received: 13 November 2023
Revised: 28 May 2024
Accepted: 11 June 2024

**KEYWORDS**

GFRP reinforcement;
High temperature;
Steel-reinforced recycled aggregate concrete beams;
Residual load-carrying capacity;
Bending performance



## 1. Introduction

Green and energy conservation are increasingly prevailing in the development of the construction industry. The application of new materials and new structures can better protect the environment [1-2], and Glass Fiber Reinforced Plastic Fiber (GFRP) is such a new type of green high-performance material with prominent advantages of lightweight, high strength, great corrosion resistance, and easy machinability, which has been widely used in practical engineering structures [3-5]. Research shows that the compressive strength and elastic modulus of recycled aggregate concrete (RCAC) are lower than that of ordinary concrete, while its strength and durability can be improved by changing the addition method of admixtures. [6-10] Compared to ordinary reinforced concrete beams, steel-reinforced recycled aggregate concrete (SRRAC) [11-14] is advantageous in load-carrying capacity and stiffness, which is mainly due to the mutual restraint and effective force collaboration between steel and concrete. Moreover, as an environmentally friendly material, recycled concrete can address the pollution caused by construction waste. The GFRP reinforcement for recycled steel-concrete beams enhances, on the other hand, the load-carrying capacity and durability of the structure. However, the high-temperature caused by fires can deteriorate the GFRP reinforcement, consequently impacting the overall durability, load-carrying capacity, and even threatening the structural safety.

Currently, scholars from China and abroad have conducted systematic studies on the mechanical properties of recycled concrete beams reinforced with steel at both room temperature and above, including experimental research, numerical simulations, and theoretical analysis. [15-20] Chen et al. proposed a new structure of steel-reinforced recycled aggregate concrete (SRRAC), thereby using the confinement effect of section steel sections to compensate for the deficiencies of RA [21]. Danying Gao, et al. conducted a four-point bending test on 13 beams, and found that the shear bearing capacity of recycled aggregate and steel fiber concrete beams decreased with the increase of the replacement rate of recycled coarse aggregate. In the meantime, the volume of steel fiber gradually increases as the score increases. Emmanuel E. Anike et al. [22] found that the bearing capacity of hybrid beams prepared by conventional methods, containing 100% recycled aggregate (RA) and 1% steel fiber (SF) is comparable to that of similar mixtures without SF and the reference. Compared with the mixture, it has increased by 13% and 8%, respectively. Arash Karimi Pour et al. [23] studied the influence of simultaneous effects of GFRP and PP fibers on improving the shear properties of high-strength (HS) recycled coarse aggregate (RCA) concrete beams. The test was conducted on 36 RC beams fabricated, showing that as the RCA content increased, PP fibers were more effective in enhancing the shear properties of GFRP steel-reinforced high-strength concrete (HSC) beams. Faraz Tariq et al. [24] studied the mechanical properties and bonding properties of fire-exposed recycled coarse and fine aggregate concrete (RAC), and provided the load and residual slip as well as bond temperature relationships and subsequent deterioration based on the test result. A model of interrelationships was proposed to help in the prediction of the performance of structural elements made of RAC after exposure to fire or high temperature. Zongping Chen et al. [25] studied the eccentric compression behavior of recycled aggregate concrete (RRAC) columns at high temperature by means of experiments and numerical simulations. They found that temperature is the main factor affecting the eccentric compression behavior, followed by eccentricity, and the replacement percentage of RCA. They also proposed an equivalent model for the residual bearing capacity of RRAC columns. Xue Jianyang et al. [26] conducted comparative experimental research on ordinary steel-reinforced concrete beams and steel-reinforced recycled concrete beams, with concrete strength, shear-span ratio, and replacement of recycled aggregate as experimental parameters. As can be seen from the study, the two types of beams exhibited similar load-carrying mechanisms, and the strength reduction of the steel-reinforced recycled concrete beams was not significant compared to ordinary steel-reinforced concrete beams. Wu Ping Chuan et al. [27] conducted static load tests on four groups of steel recycled concrete beams, and observed the failure modes of the test beams. In the study, the aggregate replacement rate was found to have little impact on the bearing capacity of the test beams. Chen Zongping et al. [28] conducted comparative experimental research on steel-reinforced concrete specimens, focusing on the replacement rate of recycled coarse aggregate, bonding location between steel and recycled concrete, and the thickness of the steel protection layer. In the study, they proposed a calculation and prediction formula for the bonding strength between steel and concrete. Han Fei et al. [29] carried out flexural performance tests on basalt fiber-reinforced polymer (BFRP) reinforced recycled concrete beams and ordinary reinforced recycled concrete beams. It was revealed that BFRP-reinforced recycled concrete beams exhibited superior ductility and load-carrying capacity compared to ordinary reinforced recycled concrete beams. In the experimental research on steel-reinforced recycled concrete beams after exposure to high temperatures, Chen Zongping et al. considered the heating temperature and replacement rate of recycled aggregate as experimental parameters, and revealed the bending failure and damage mechanism of steel-reinforced recycled concrete

beams after high-temperature exposure. Additionally, they proposed a calculation formula for predicting the residual load-carrying capacity of steel-reinforced recycled concrete beams after high-temperature exposure. Furthermore, scholars from China and abroad conducted experimental studies and analysis on the mechanical performance degradation of FRP reinforcement after exposure to high temperatures with substantial research achievements in this field. For instance, Lu Chunhua et al. [31] conducted experimental research on the tensile properties of two types of FRP reinforcements (BFRP and GFRP), and observed the microstructure of the two types of reinforcements after high-temperature damage using scanning electron microscopy. Based on the experimental results, they proposed a tensile strength degradation model for both types of reinforcements in the temperature range of 20-220°C. Gao Yong Hong et al. [32] analyzed the tensile strength characteristics of GFRP reinforcement with different steel bar diameters (16mm, 22mm and 25mm) after exposure to high temperatures, using the steel bar diameter as an experimental parameter. Based on the relationships established between the ultimate tensile strength, ultimate elongation, elastic modulus, and temperature, extensive research has been conducted on the mechanical properties of steel-reinforced recycled concrete beams under ambient and high-temperature conditions, as well as on the degradation of FRP reinforcement after high-temperature exposure. However, the research on high-temperature GFRP-reinforced recycled concrete beams is limited. To explore the influence of GFRP reinforcement strength and strengthening methods on the load-carrying capacity of steel-reinforced recycled concrete beams, a refined finite element model of high-temperature GFRP-reinforced steel-recycled concrete beams was established by using ABAQUS software. The accuracy and reliability of the model were validated by the full-scale experimental results of high-temperature steel-reinforced recycled concrete beams from both domestic and international sources. Furthermore, parameter analysis was performed to find out the factors influencing the high-temperature steel-reinforced recycled concrete beams. The accuracy of the composite beam design method as specified in GB 50017-2017 [33] “Code for Design of Steel Structures" was evaluated based on the finite element analysis results and using the variability analysis approach. Consequently, a design method considering GFRP reinforcement for steel-reinforced recycled concrete beams was proposed.

## 2. Establishment of finite element model

### *2.1. Overview of the model*

Finite element model of GFRP-reinforced recycled concrete beams for vertical shear performance was established by using ABAQUS software. The model mainly includes I-shaped steel beams, GFRP reinforcement bars, steel bars, and concrete beams, etc. The 3D structure of the recycled concrete beams with I-shaped steel is shown in Fig. 1(a), and the established finite element model is shown in Fig. 1(b).

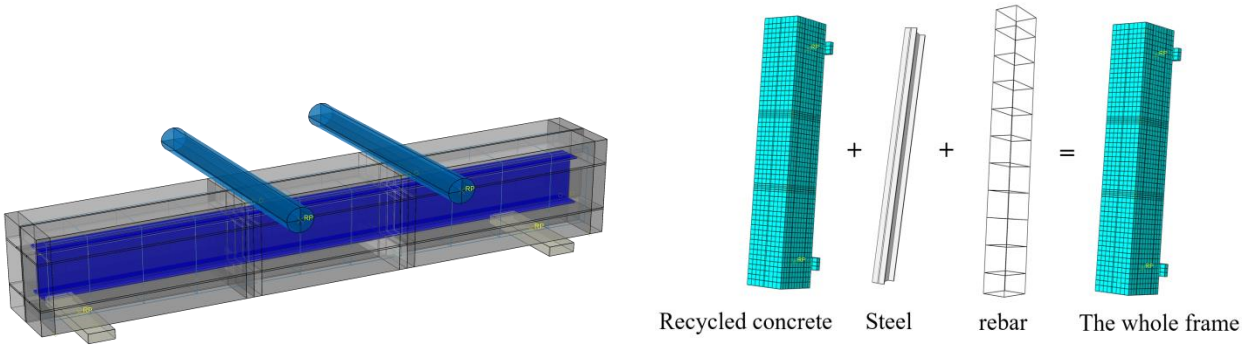


(a) 3D structure diagram (b) Finite element analysis model of component

**Fig. 1** Schematic diagram of steel reinforced recycled concrete beam

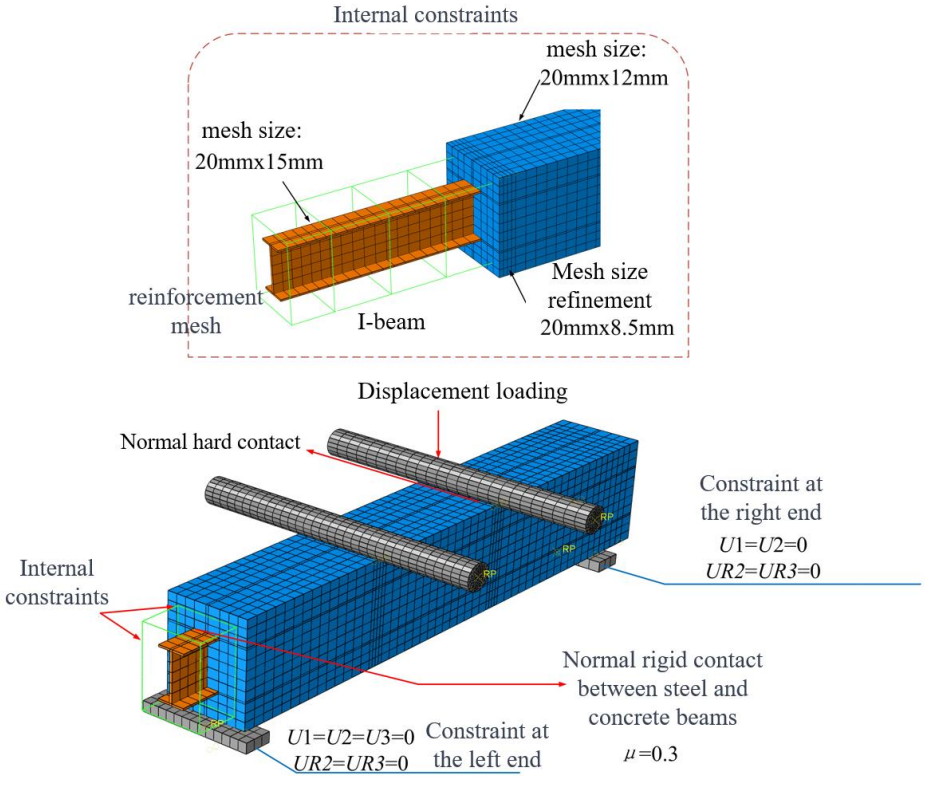


**Fig. 2** Interaction and Boundary Condition Setting of GFRP Reinforcement Reinforced Steel Recycled Concrete Beams

### 2.2. Element selection and mesh division

The model of GFRP-reinforced recycled concrete beams was established based on three types of elements, namely, I-shaped steel beams, bearing pads, and concrete beams, using hexahedral eight-node solid elements (C3D8R). On the other hand, the longitudinal bars and stirrups were simulated using truss elements (T3D2). To improve the computational accuracy, during mesh division, the mesh element size of the concrete beams is set to be up to 15mm, ensuring a minimum of 4 elements in the thickness direction to satisfy the requirements of integral calculations, and avoid numerical singularities. The element size of the steel beams is controlled within 20mm, and that of the steel bars does not exceed 20mm. A "void" operation is performed in the concrete beams to accommodate the placement of I-shaped steel beams, which enables the interaction of bond-slip between the steel beams and the concrete beams.

To ensure the smooth introduction of the temperature field ODB file, the mesh partitioning of the temperature field model and the mechanical model of GFRP-reinforced recycled concrete beams must be identical.

### 2.3. Interaction and boundary condition settings

The interaction settings for the components of the GFRP-reinforced recycled concrete beam model are as follows.

(1) The coupling of degrees of freedom between the steel reinforcement cage and the concrete beam is achieved through the built-in area command, which enables them to work together.

(2) Interactions are set at the interface between the steel beam and the concrete beam to define the bond-slip behavior between them.

(3) Thermal convection and thermal radiation are applied to the surface of the concrete to simulate heat conduction. The thermal convection coefficient is set to 25 W/($m^2$·K), and the thermal radiation coefficient is set to 0.5. The I-shaped steel beam and the concrete are tied together during the temperature field analysis to enable heat transfer.

(4) The steel bars are bonded to the surface region of the concrete beam, and loading is achieved through the coupling of degrees of freedom.

(5) Binding constraints are applied between the steel beam and the loading pad.

The boundary conditions of the GFRP-reinforced recycled concrete beam test specimen are consistent with that of the experiment, with one end fixed and the other end hinged. Displacement-controlled loading is applied during the modeling, and the specific boundary and interaction settings are shown in Fig. 2.

### 2.4. Material constitutive models

The constitutive models of concrete and steel materials have to be determined in the finite element model. The specific constitutive models are as follows.

(1) Constitutive model of concrete: the concrete is modeled by using the concrete plastic damage (CDP) model, with a Poisson's ratio of 0.2[34]. The elastic modulus of ordinary concrete is calculated by using the equation specified in the European Concrete Design Code EC2-2004[33] as follows.

$$E_c = 22 \cdot (f_{cr}/10)^{0.3} \quad (1)$$

where $f_{cr}$ represents the axial compressive strength of the concrete.

The $E_{C,RAC}$ model is adopted for recycled concrete, which considers the replacement ratio (k) and the residual mortar content $Y_{RM}$ of recycled coarse aggregates, as described in Reference [35].

$$E_{C,RAC}=\left(1-{}^{2}/_{3}\cdot kY_{Rm}\right)E_C \quad (2)$$

where $Y_{Rm}$ represents the residual mortar content, which is typically between 30% and 50% [36]. In the case of unknown residual mortar content, an average value of 40% can be used. k refers to the replacement ratio of recycled coarse aggregates.

The compressive stress-strain behavior of recycled concrete and ordinary concrete is simulated by using the concrete stress-strain model proposed by Xiao et al. [37], which accounts for the influence of the replacement ratio of recycled coarse aggregates, as illustrated in Fig. 4.The equation of the model is as follows：

$$\sigma_x=\begin{cases} m\varepsilon_x+(3-2m){\varepsilon_x}^2+(m-2){\varepsilon_x}^2 & (0\le\varepsilon_x<1) \\ \dfrac{\varepsilon_x}{n(\varepsilon_x-1)^2+\varepsilon_x} & (\varepsilon_x\ge 1) \end{cases} \quad (3)$$

where $\varepsilon_x$ represents the relative compressive strain of concrete, $\varepsilon_x=\varepsilon_c/\varepsilon_u$ , $\varepsilon_c$ refers to the compressive strain of concrete, $\varepsilon_u$ stands for the peak compressive strain of concrete; $\sigma_x$ denotes the relative compressive strength of concrete, $\sigma_x=\sigma_c/f_{cr}$， $\sigma_c$ is the compressive stress of concrete, $f_{cr}$represents the axial compressive strength of concrete; and m and n are the influence factors of the replacement ratio of recycled coarse aggregates, which can be calculated by using the following equation.

$$m=2.2(0.478k^2-1.231k+0.975)$$

$$n=0.8(7.664k+1.142) \quad (4)$$

The tensile stress-strain relationship of recycled concrete is similar to that of ordinary concrete [38], and the concrete tensile stress-strain model proposed by Xiao et al. [37] is adopted, which is expressed as follows:

$$\sigma_{t,x}=p\varepsilon_{t,x}-(p-1)\varepsilon_{t,x}^6 \quad (5)$$

where $\varepsilon_{t,x}$represents the relative tensile strain of concrete, $\varepsilon_{t,x}=\varepsilon_t-\varepsilon_{tu}$ , $\varepsilon_t$ refers to the tensile strain of concrete, $\varepsilon_{tu}$ denotes the peak tensile strain of concrete; $\varepsilon_{t,x}$ stands for the relative tensile strength of concrete, $\sigma_{t,x}=\sigma_t/f_{tu}$, $\sigma_t$ is the tensile strength of concrete; and p refers to the ratio of tangent modulus to secant modulus at the reference point, which can be calculated by using the following equation:

$$P=0.007k+1.190 \quad (6)$$

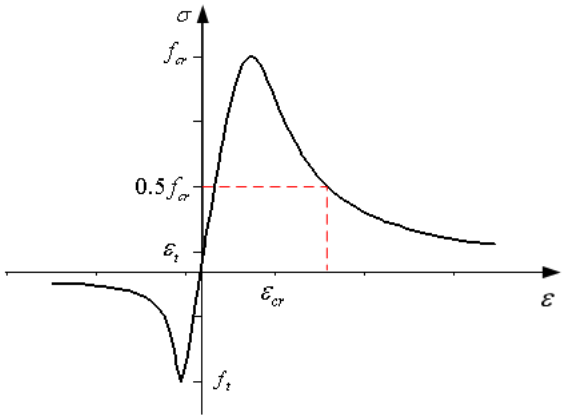


**Fig. 3** Stress-strain curve of concrete

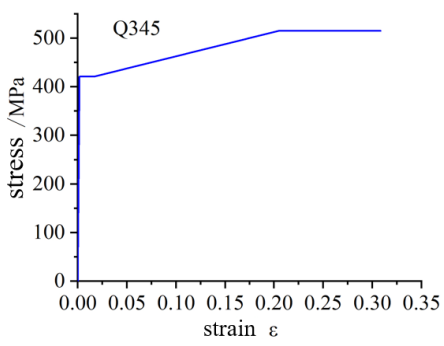


(a) Constitutive Model of Q345 and Bolts

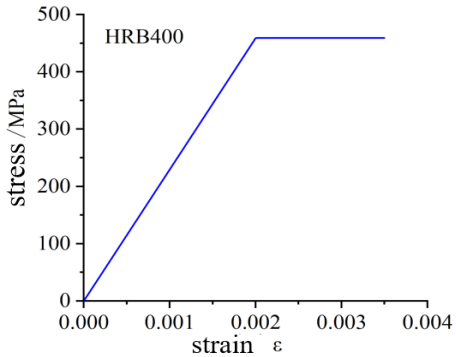


(b) Constitutive Model of HRB400 Reinforcing Steel

**Fig. 4** Steel constitutive

### 2.5. Material constitutive model

The constitutive relationships for steel beams and bolts are shown in Fig. 4(a). The constitutive model for steel beams considers strain hardening at both room temperature and high temperature, while the steel reinforcement is calculated by using an ideal elastic-plastic model with the strength values determined based on the experimental results. The constitutive relationships are illustrated in Fig. 4(b).

$$\sigma = \begin{cases} E_s\varepsilon & \varepsilon \le \varepsilon_y \\ f_y & \varepsilon_y \le \varepsilon \end{cases} \tag{8}$$

where $f_y$ represents the yield strength of the steel material; $E_s$ refers to the elastic modulus of the steel material; and $\varepsilon_y$ stands for the yield strain of the steel material.

### 2.6. Model verification

Finite element analysis was conducted on high-temperature recycled steel-reinforced concrete beams, as shown in [39], and the accuracy and feasibility of the model were verified by comparing the finite element simulation data with the experimental data obtained from previous studies.

#### 2.6.1. Existing experimental parameters and results

Existing test results of steel-reinforced concrete composite beams using recycled materials were collected to validate the accuracy and feasibility of the finite element analysis. The parameters of the steel-reinforced concrete composite beam specimens employed in this study were as follows: length of 1100mm, width of 150mm, height of 200mm, protective layer thickness of 25mm, recycled concrete strength grade of C40, Steel type 10, Q345 for internal steel, longitudinal reinforcement of 14mm-diameter HRB335, stirrups of 6.5mm-diameter HPB300, temperatures of room temperature, 200°C, 400°C, and 600°C. Besides, the replacement rates were 0%, 30%, 70%, and 100%. The detailed cross-section of the test beam is shown in Fig. 5, and Table 1 summarizes the test parameters and results for all specimens.

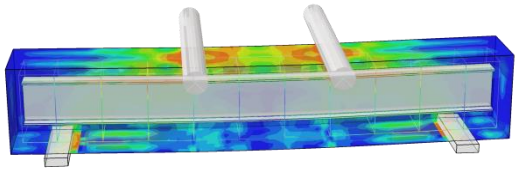

(a) Three-dimensional view of composite beam

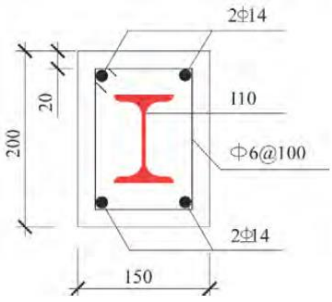


(b) Cross-section view at mid-span

**Fig. 5** Detailed drawings of the test piece

#### 2.6.2. Finite element model verification

Experimental research was conducted on steel-concrete beams using recycled concrete under room-temperature and high-temperature conditions, as shown in the reference [39]. Fig. 6 shows the comparison between the experimental and finite element results of the load-deflection curves of selected test beams. The error of simulated ultimate load values of the model created in ABAQUS ranges from 0.15% to 3.82% compared to the experimental values. It can be seen from the diagram that the overall distribution of the two curves is similar, and can be divided into three stages. The load-deflection curve of the steel-concrete beams using recycled concrete, obtained based on the thermal-structural coupling analysis method, is generally like the experimental curve with some differences. Overall, the difference between the two curves is within 10%, indicating a good agreement between the experimental results and the simulated values. The above results indicate that the finite element model can well predict the flexural performance of steel-concrete beams using recycled concrete. On this basis, further mechanical performance analysis can be conducted for GFRP-reinforced steel-concrete beams using recycled concrete.

**Table 1**
Major experimental parameters and results of steel-reinforced recycled composite beams

| Test specimen number | $K_0$/kN·$mm^{-1}$ | $P_u$/kN | θ | $f_u$/mm | Strength grade/MPa | $T$/°C | λ/% |
|---|---|---|---|---|---|---|---|
| SA-T25-0-1 | 153.8 | 249.5 | 2.0 | 4.06 | C30 | Room temperature | 0 |
| SA-T25-30-2 | 166.7 | 257.2 | 2.0 | 5.75 | C30 | | 30 |
| SA-T25-70-3 | 200.0 | 255.3 | 2.0 | 7.11 | C30 | | 70 |
| SA-T25-100-4 | 160.0 | 256.7 | 2.0 | 2.99 | C30 | | 100 |
| SA-T200-0-1 | 103.4 | 255.4 | 2.0 | 3.39 | C30 | 200 | 0 |
| SA-T200-30-2 | 146.3 | 230.0 | 2.0 | 4.76 | C30 | | 30 |
| SA-T200-70-3 | 171.4 | 237.9 | 2.0 | 5.15 | C30 | | 70 |
| SA-T200-100-4 | 181.8 | 263.0 | 2.0 | 4.80 | C30 | | 100 |
| SA-T400-0-1 | 136.4 | 234.0 | 2.0 | 4.37 | C30 | 400 | 0 |
| SA-T400-30-2 | 157.9 | 227.6 | 2.0 | 3.50 | C30 | | 30 |
| SA-T400-70-3 | 126.6 | 242.7 | 2.0 | 5.64 | C30 | | 70 |
| SA-T400-100-4 | 133.3 | 248.0 | 2.0 | 4.90 | C30 | | 100 |
| SA-T600-0-1 | 92.0 | 188.4 | 2.0 | 4.67 | C30 | 600 | 0 |
| SA-T600-30-2 | 87.0 | 194.5 | 2.0 | 5.85 | C30 | | 30 |
| SA-T600-70-3 | 81.3 | 202.8 | 2.0 | 6.95 | C30 | | 70 |
| SA-T600-100-4 | 88.9 | 170.0 | 2.0 | 4.71 | C30 | | 100 |

Note: The letter group "SA" in the specimen code represents steel-concrete beams, and the letter "T" indicates the heating temperature. $K_0$ refers to the initial stiffness value of the specimen, and the secant stiffness at P=0.4$P_u$ is taken as the initial stiffness of the specimen. θ represents the shear span ratio, where θ=a/h0, a stands for the length of the shear span, and $h_0$ is the effective height of the cross-section. $f_u$ denotes the peak load, and λ represents the replacement rate of recycled aggregates.

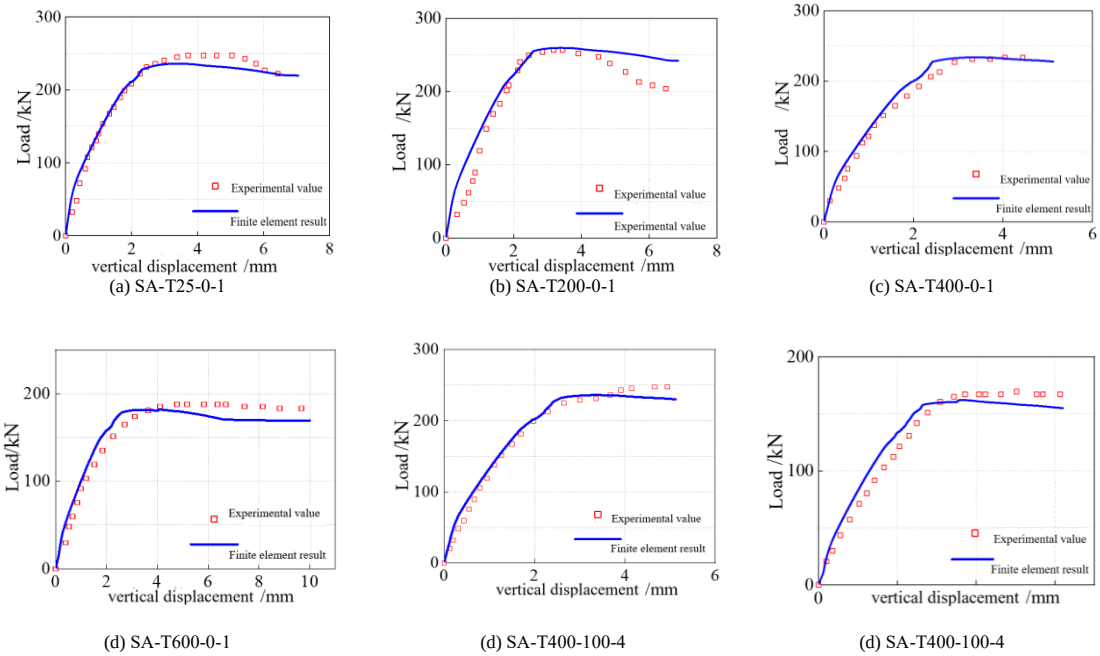


(a) SA-T25-0-1 (b) SA-T200-0-1 (c) SA-T400-0-1

(d) SA-T600-0-1 (d) SA-T400-100-4 (d) SA-T400-100-4

**Fig. 6** Comparison of section steel recycled concrete beam test and finite element results


(a) Temperature distribution at mid-span at 400° C (b) Temperature distribution at mid-span at 600° C

**Fig. 7** Temperature field distribution of section steel recycled concrete beams

The temperature distribution of the heated specimen is shown in Fig. 7, as can be seen, the surface temperature of the steel-concrete beam is higher when being heated. Due to the low thermal conductivity of concrete, outside-in heat transfer is relatively slow, exhibiting a significant thermal inertia. Conversely, steel experiences faster heat transfer.

The simulated results of the specimens are shown in Fig. 8. It can be observed from Fig. 7(a) to Fig. 7(b) that the steel-reinforced recycled concrete beams undergo deformation within the plane only without out-of-plane torsional deformation. The analysis based on Fig. 8(c) indicates that the failure mode of the steel-ECC composite beam simulated by using finite element method is flexural failure. Fig. 8(b) shows that the tensile damage simulated by using the finite element method reproduces the cracking pattern of the steel-reinforced recycled concrete beams. Fig. 8(d) illustrates the stress and deformation of the steel beams and steel reinforcement cages in the finite element model. It can be concluded that the finite element model can be used to accurately analyze the failure mode of steel-reinforced recycled concrete beams.

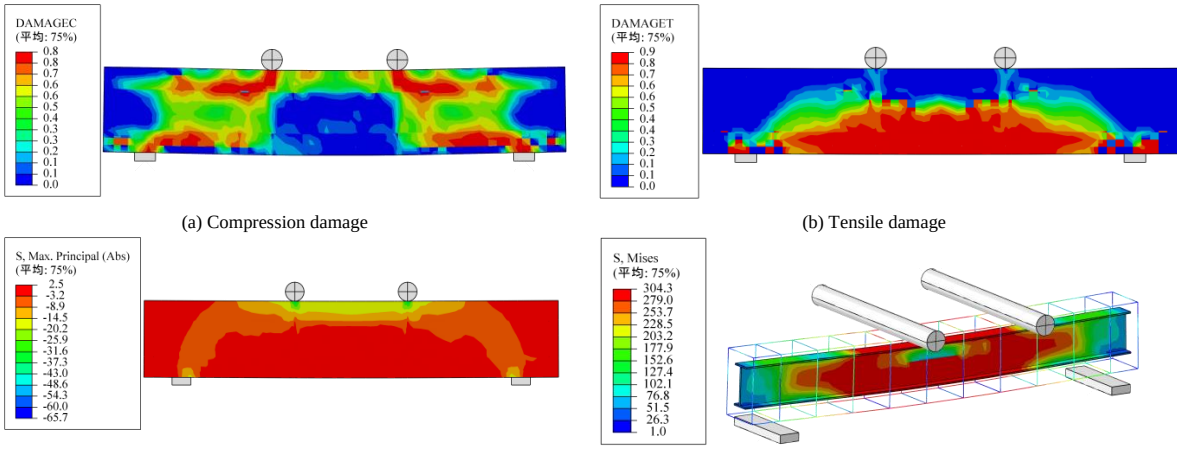


(a) Compression damage (b) Tensile damage

(c) Principal tensile stress (d) Stress and deformation of steel beam and steel reinforcement cage

**Fig. 8** Simulation results of section steel recycled concrete beam

## 3. Parameter analysis

### *3.1. GFRP reinforcement for tension members*

The type I strengthening method involves using GFRP tendons to reinforce the steel-reinforced recycled concrete beams, with the reinforcement configuration shown in Fig. 9. The strength of GFRP tendons under normal temperature and high temperature is shown in Table 2 [40]. Fig. 10(a) shows the analysis of the load-displacement curves of steel-reinforced recycled concrete beams with different diameters (4mm, 6mm and 8mm) under a fire temperature of 600°C, and a replacement ratio of 100%. As can be seen from the diagram, the curves based on different GFRP tendon diameters are similar at the elastic

stage. The ultimate load-carrying capacity of the members increases with the increase of GFRP tendon diameter. Compared to the unreinforced specimens, the ultimate load-carrying capacity of the 4mm, 6mm and 8mm GFRP tendon-steel-reinforced recycled concrete beam was increased by 6.38%, 13.03% and 22.35%, respectively. Fig. 10(b) illustrates the analysis of the load-displacement curves of steel-reinforced recycled concrete beams with different spacing (50mm, 75mm and 100mm) of GFRP tendons under a fire temperature of 600°C and a replacement ratio of 100%. By changing the spacing of the tendons, as can be seen, compared to the unreinforced specimens, the ultimate load-carrying capacity of the GFRP tendon-steel-reinforced recycled concrete beams was increased by 4.79% at a spacing of 100mm, 12.80% at a spacing of 75mm, and 16.74% at a spacing of 50mm, respectively.

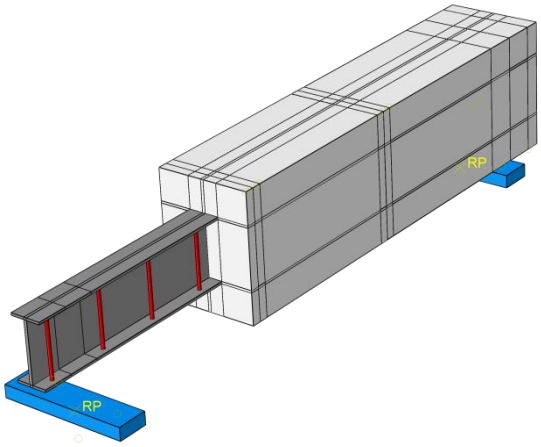


**Fig. 9** Type I reinforcement method

**Table 2**
Mechanical properties of GFRP ribs at room temperature and high temperature

| Heating temperature/°C | Elastic modulus/GPa | Tensile strength/MPa |
|---|---|---|
| 20 | 32.8 | 884.6 |
| 50 | 28.7 | 774.0 |
| 100 | 24.6 | 663.5 |
| 150 | 20.5 | 552.9 |
| 200 | 16.4 | 442.3 |
| 250 | 12.3 | 331.7 |
| 300 | 8.2 | 221.2 |
| 350 | 4.1 | 110.6 |

### *3.2. Longitudinal reinforcement with GFRP bars*

Type II strengthening method involves the use of GFRP longitudinal bars to reinforce the steel-reinforced recycled concrete beams. Fig. 11 shows the analysis of the load-displacement curves of steel-reinforced concrete beams in different diameters (12mm, 15mm and 18mm) of GFRP bars under a fire temperature of 600°C and a substitution rate of 100%. As can be seen, in the elastic stage, the curves based on different diameters of GFRP bars are essentially the same. For the ultimate load of each component, the increase of the diameter of GFRP longitudinal bars can increase the ultimate bearing capacity of the component. Compared to the ordinary specimens, the ultimate bearing capacity of the steel-reinforced concrete beams was increased by 2.14% with 12mm GFRP bars, 3.89% with 15mm GFRP bars, and 4.67% with 18mm GFRP bars.

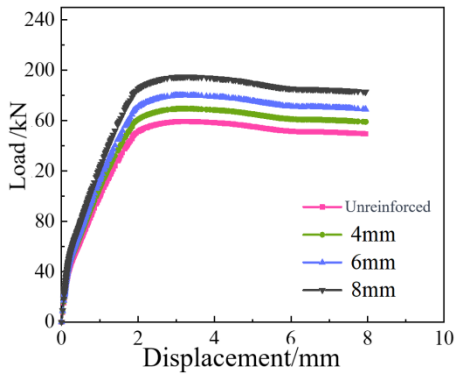


(a) Diameter of GFRP reinforcement bar

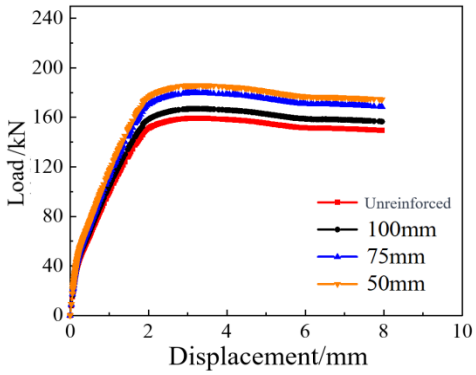


(b) Spacing between GFRP reinforcement bars

**Fig. 10** Parametric analysis of Type I reinforcement method

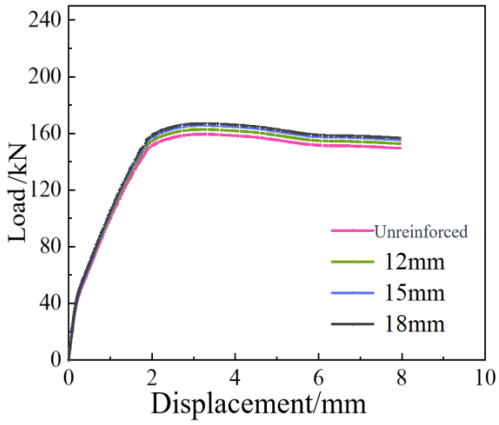


**Fig. 11** Parametric analysis of Type II reinforcement method-longitudinal rib diameter

### *3.3. GFRP strength*

Parameter analysis of the ultimate bearing capacity of steel-concrete beams with different reinforcement material strengths is conducted for Type I and Type II strengthening methods. The tensile strength of the reinforcement material is set as the original strength including 1000MPa, 1100MPa and 1200MPa. Fig. 12(a) presents the load-displacement curves of steel-concrete beams with different strengths of GFRP reinforcement (diameter of 4mm) using Type I strengthening method under a fire temperature of 600°C and a replacement ratio of 100%. In the elastic stage, the curves are generally consistent for different GFRP reinforcement strengths, and with the increase of GFRP reinforcement strength, the ultimate bearing capacity of the components increases. Compared to the specimens with original strength, the ultimate bearing capacity of GFRP-reinforced steel-concrete beams is increased by 1.97% with 1000MPa, 3.86% with 1100MPa, and 5.97% with 1200MPa. Fig. 12(b) shows the load-displacement curves of steel-concrete beams with different strengths of GFRP reinforcement (with the diameter of 4mm) using the Type II strengthening method at a fire temperature of 600°C and a replacement ratio of 100%. At the elastic phase, the curves based on different GFRP reinforcement strengths are generally consistent, and with the increase of GFRP reinforcement strength, the ultimate bearing capacity of the components increases. Compared to the specimens with original strength, the ultimate bearing capacity of GFRP-reinforced steel-concrete beams was increased by 1.15% with 1000MPa, 2.04% with 1100MPa, and 3.37% with 1200MPa.

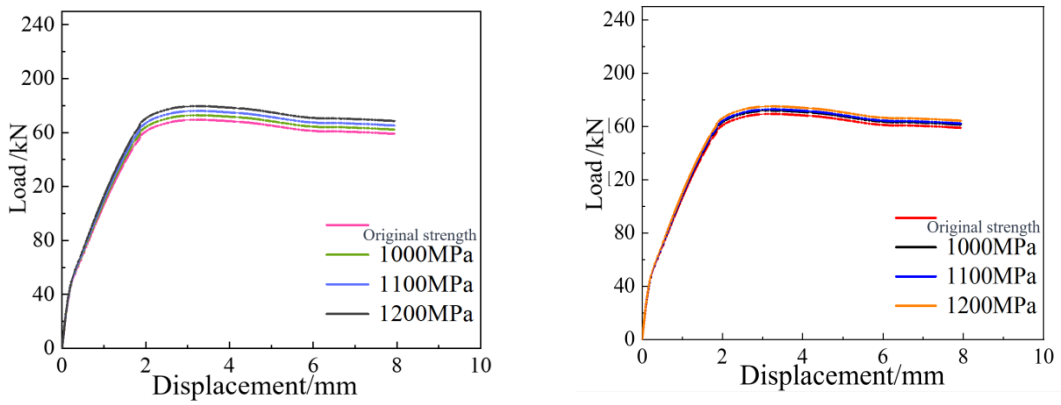


(a) Reinforcement method Type I (b) Reinforcement method Type II

**Fig. 12** Analysis of reinforcement strength parameters

## 4. Conclusion

In this study, the influence of reinforcement methods and reinforcement material strength on the ultimate load-carrying capacity of GFRP-steel reinforced concrete beams was explored, and the load-carrying mode and failure mechanism of GFRP-steel reinforced concrete beams were analyzed. The following conclusions are drawn as follows:

(1) In a high-temperature fire environment, there is a noticeable temperature lag between the interior steel and GFRP reinforcement surfaces compared to the surface of the steel-concrete composite beams.

(2) A refined GFRP-SARC beam model was established by incorporating nonlinear material mechanics and bond-slip models for steel-reinforced concrete beams. The finite element model constructed by using ABAQUS software can predict the flexural performance of GFRP-steel-reinforced concrete beams accurately and effectively. Full-scale tests on six composite beam specimens revealed that the bending load-carrying capacity predicted by the finite element analysis deviated by an average of approximately 2% from the experimental results, while the flexural stiffness deviated by an average of approximately 3%.

(3) The Type I strengthening method significantly improves the load-carrying capacity of steel-reinforced recycled concrete beams. The load-carrying capacity of the tested beams is greatly affected by temperature, which is decreased by approximately 13% after exposure to a temperature of 200°C, and around 25% after exposure to a temperature of 600°C without strengthening. After being treated at the temperature of 600°C, the Type I strengthening method exhibited an average increase in load-carrying capacity of 10% compared to the unreinforced specimens, while the Type II strengthening method showed an average increase of approximately 4.7%.

(4) The Type I strengthening method is a key influencing parameter for the flexural behavior of steel-reinforced recycled concrete beams. The proposed Type I strengthening method can significantly enhance the load-carrying capacity of SARC beams, while providing higher safety reserves.

## Acknowledgment

The authors thank Dr. Qi Guo, a professor at Xi'an University of Science and Technology in Xi'an, Shaanxi Province, China, for helping explain the significance of the findings of this study.

## References

[1] Ghalehnovi M, Roshan N, Hakak E, et al. Effect of red mud (bauxite residue) as cement replacement on the properties of self-compacting concrete incorporating various fillers[J]. Journal of Cleaner Production, 2019, 240: 118213.
[2] Meghdadian M, Gharaei-Moghaddam N, Arab Shahi A, et al. Proposition of an equivalent reduced thickness for composite steel plate shear walls containing an opening[J]. Journal of Constructional Steel Research, 2020, 168: 105985.
[3] Huang Jingyi, Zhu Dayong, Gao Peng, Zhou An, Dai Liangjun. Research on seismic performance of BFRP reinforced high axial compression ratio and low strength concrete columns [J]. Journal of Building Materials, 2020,23 (06): 1366-1373
[4] Huang Jingyi. Research on Seismic Performance of Low Strength Concrete Reinforced Columns Strengthened with Basalt Fiber Composite Materials [D]. Hefei University of Technology, 2020.
[5] Lian Yu, Xiao Ru-cheng, Sun Bin, Cheng Jin, Jia Lijun, Zhuang Dong-li. Static characteristics of GFRP composite bridge decks reinforced with rivets and self-tapping screws [J]. China Journal of Highway and Transport, 2016,29 (10): 54-65,94.
[6] Etxeberria M, Vázquez E, Marí A, et al. Influence of amount of recycled coarse aggregates and production process on properties of recycled aggregate concrete[J]. Cement and concrete research, 2007, 37(5): 735-742.
[7] Yehia S, Helal K, Abusharkh A, et al. Strength and durability evaluation of recycled aggregate concrete[J]. International journal of concrete structures and materials, 2015, 9(2): 219-239.
[8] McNeil K, Kang H K. Recycled Concrete Aggregates: A Review, International Journal of Concrete Structures and Materials[J]. 2013.
[9] Xie T, Gholampour A, Ozbakkaloglu T. Toward the development of sustainable concretes with recycled concrete aggregates: comprehensive review of studies on mechanical properties[J]. Journal of Materials in Civil Engineering, 2018, 30(9): 04018211.
[10] Ozbakkaloglu T, Gholampour A, Xie T. Mechanical and durability properties of recycled aggregate concrete: effect of recycled aggregate properties and content[J]. Journal of Materials in Civil Engineering, 2018, 30(2): 04017275.
[11] Liu Yibin, Cao Wanlin, Xing Feng, et al. Full-scale test of flexural performance of steel reinforced recycled concrete beams [J]. Building Structure, 2023,53 (09): 108-114.
[12] Wang Bing, You Hong Xu, Liu Xiao. Research on the bending behavior of recycled steel reinforced concrete beams after high temperature [J]. Engineering Mechanics, 2018, 35 (S1): 161-165,180.
[13] Li Yuanyuan. Experimental and Numerical Simulation Study on the Bending Performance of Steel Reinforced Recycled Concrete Beams [D]. Hebei University of Engineering, 2015.
[14] Ke X, Tang Z, Yang C. Shear bearing capacity of steel-reinforced recycled aggregate concrete short beams based on modified compression field theory[C]//Structures. Elsevier, 2022, 45: 645-658.
[15] Chen Z P, Chen Y L, Zhong M. Shear performance test and bearing capacity calculation of steel reinforced recycled coarse aggregate concrete beam[J]. Journal of Experimental Mechanics, 2014, 29(1): 97-104.
[16] Jian yang X, Xiu Zhen W, Hui M. Experimental study on shear performance of steel reinforced recycled aggregate concrete beams[J]. Building Structure, 2013, 43(7): 69-72.
[17] Al Mahmoud F, Boissiere R, Mercier C, et al. Shear behavior of reinforced concrete beams made from recycled coarse and fine aggregates[C]//Structures. Elsevier, 2020, 25: 660-669.
[18] Arezoum andi M, Steele A R, Volz J S. Evaluation of the bond strengths between concrete and reinforcement as a function of recycled concrete aggregate replacement level[C]//Structures. Elsevier, 2018, 16: 73-81.
[19] Thomas J, Thaickavil N N, Wilson P M. Strength and durability of concrete containing recycled concrete aggregates[J]. Journal of Building Engineering, 2018, 19: 349-365.
[20] Pliya P, Hajiloo H, Romagnosi S, et al. The compressive behavior of natural and recycled aggregate concrete during and after exposure to elevated temperatures[J]. Journal of Building Engineering, 2021, 38: 102214.
[21] Gao D, Zhu W, Fang D, et al. Shear behavior analysis and capacity prediction for the steel fiber reinforced concrete beam with recycled fine aggregate and recycled coarse aggregate[C]//Structures. Elsevier, 2022, 37: 44-55.
[22] Anike E E, Saidani M, Olubanwo A O, et al. Flexural performance of reinforced concrete beams with recycled aggregates and steel fibres[C]//Structures. Elsevier, 2022, 39: 1264-1278.
[23] Pour A K, Shirkhani A, Zeng J J, et al. Experimental investigation of GFRP-RC beams with Polypropylene fibers and waste granite recycled aggregate[C]//Structures. Elsevier, 2023, 50: 1021-1034.
[24] Tariq F, Ahmad S. Mechanical and bond properties of completely recycled aggregate in concrete exposed to elevated temperatures[C]//Structures. Elsevier, 2023, 56: 104979.
[25] Chen Z, Liao H, Zhou J, et al. Eccentric compression behavior of reinforced recycled aggregate concrete columns after exposure to elevated temperatures: Experimental and numerical study[C]//Structures. Elsevier, 2022, 43: 959-976.
[26] Xue Jian yang, Wang Xiuzhen, Ma Hui, Lin Jianpeng, Chen Zongping. Experimental study on shear performance of steel reinforced recycled concrete beams [J]. Building Structure, 2013,43 (07): 69-72
[27] Wu Ping Chuan, Xie Lulu, Li Yuanyuan, Zhao Shuli. Experimental study on the flexural performance of steel reinforced recycled concrete beams [J]. Journal of Hebei Engineering University (Natural Science Edition), 2016,33 (01): 31-34
[28] Chen Zongping, Zheng Huahai, Xue Jian yang, Su Yi sheng. Bond slip test and bond strength analysis of steel reinforced recycled concrete [J]. Journal of Building Structures, 2013,34 (05): 130-138. DOI: 10.14006/j.jzjgxb.2013.05.05.015
[29] Han Fei, Kong Xiangqing, Bao Chengcheng, Liu Huaxin, Zhang Wenjiao. Experimental study on the flexural performance of recycled concrete beams with BFRP reinforcement [J]. Fiberglass reinforced plastic/composite materials, 2017 (12): 45-50
[30] Chen Zhongping, Zheng Wei, Xue Jian yang, et al. Bending test and bearing capacity calculation of steel reinforced recycled concrete beams after high temperature [J]. Industrial Architecture, 2014,44 (11): 45-50.
[31] Lu Chunhua, Ping An, Yan Yong Dong, Zhang Julian. Experimental study on tensile properties and Strength reduction calculation of GFRP/BFRP bars after high temperature action [J/OL]. Journal of Harbin Engineering University: 1-8.
[32] Gao Yong Hong, Tian Yun, Jin Qingping. Study on the effect of temperature on the tensile mechanical properties of GFRP reinforcement [J]. Plastic Industry, 2016,44 (09): 95-99。
[33] GB50017-2017. Code for Design of Steel Structures [S]. China Planning Press

[34] WANG Q H, YANG J S, LIANG Y Z, et al. Prediction of time-dependent behavior of steel-recycled aggregate concrete(RAC)composite slabs via thermo-mechanical finite element modeling[J]. Journal of Building Engineering, 2020, 29: 101191.
[35] CEN. Eurocode 2: design of concrete structure-part 1-1: general rules and rules for buildings: ENV 1992-1-2 [S]. Brussels: Europe Committee for Standardization(CEN), 2004.
[36] DE JUAN M S, GUTIÉRREZ P A. Study on the influence of attached mortar content on the properties of recycled concrete aggregate[J]. Construction and Buildings Materials, 2009, 23(2):872-877.
[37] XIAO J Z, LI W G, FAN Y H, et al. An overview of study on recycled aggregate concrete in China(1996-2011)[J]. Construction and Building Materials, 2012,(31): 364-383.
[38] LIU Q, XIAO J Z, SUN Z H. Experimental study on the failure mechanism of recycled concrete[J]. Cement and Concrete Research, 2011, 41(10): 1050-1057.
[39] Chen Z P, et al. Mechanical behavior and bearing capacity calculation of steel reinforced recycled concrete beam after experiencing high temperature [J]. China Civil Engineering Journal.2016, 49(2): 49—58.
[40] Chunhua LU, Zhong Hao QI, Hao GE, et al. Experimental and theoretical investigation on shear performance degradation of GFRP bars in concrete after fire and high temperature[J]. Acta Materiae Compositae Sinica.

**Advanced Steel Construction** – Vol. 20 No. 3 (2024) 300–309
**DOI:**10.18057/IJASC.2024.20.3.9


# BUCKLING MODES OF SCREWED CONNECTIONS IN COLD-FORMED STEEL BUILT-UP PLATES

Yan-Chun Li [1], Tian-Hua Zhou [2], Ai-Hong Han [1], Yan Lu [3, *] and Ji-Hao Chen [1]

[1] *School of Civil Engineering and Communication, North China University of Water Resources and Electric Power, Zhengzhou 450045, China*
[2] *School of Civil Engineering, Chang'an University, Xi'an 710061, China*
[3] *School of Civil Engineering, Inner Mongolia University of Technology, Hohhot 010051, China*
** (Corresponding author: E-mail: luyanchd@163.com)*

**ABSTRACT**

Discrete screws can introduce discontinuities at the interface of built-up plates, leading to various buckling modes in cold-formed steel (CFS) built-up plates, namely coordinated buckling and delamination buckling. The impact of these buckling deformation modes on the stability mechanism of CFS screw-connected built-up plates is significant and cannot be overlooked. Consequently, this paper establishes theoretical models for both buckling modes. Analytical solutions for the critical buckling stress (CBS) of the screw-connected built-up plate under these two modes are derived. The validity of the buckling modes and the analytical solutions is confirmed through experimental verification. The results indicate that: (1) delamination buckling is invariably a higher-order mode in comparison to coordinated buckling, and as such, only coordinated buckling is required for calculating the CBS; (2) the CBS calculation method proposed in this paper aligns more closely with the actual mechanical behavior of screw connections in CFS built-up plates.

**ARTICLE HISTORY**

Received: 20 January 2024
Revised: 27 February 2024
Accepted: 10 March 2024

**KEYWORDS**

Cold-formed steel;
Screwed connection of built-up plates;
Shear slip;
Coordinated buckling;
Delamination buckling;
Critical buckling stress



## 1. Introduction

Cold-formed steel (CFS) members are widely used domestically and internationally due to their flexible forming, simple production process, and high post-buckling strength. The built-up members assembled using self-drilling screws are commonly used in engineering circles. The stability of a single plate has been studied by Timoshenko [1] and the relatively perfect elastic stability theories have been established [2,3]. The CFS built-up members are being used to meet the increasing demand for practical projects in recent years. Self-drilling screws have gradually become one of the primary methods for connecting composite plates due to their simple construction, excellent connection stiffness, and high bearing capacity [4-6].

Therefore, scholars have studied the mechanical characteristics of CFS composite plates [7-9]. The results indicate that the shear capacity of self-drilling screw groups exhibits a "group reduction effect". Recently, the influences of screws on the high-strength (G550) CFS members were experimentally and numerically investigated [10]. Different behaviors that occur simultaneously in the screw connection test were successfully simulated: steel plate tearing and pulling out, end plate failure, screw tilting, and fracture. The shear behavior of the CFS plate connected by self-drilling screws was studied using experimental, numerical, and analytical models. Three typical failure modes were identified [11]. A model was proposed and calibrated to predict the shear deformation of the screw built-up plate. A revised reduction factor for the bearing capacity is presented based on the Australian Standard. The shear behavior of self-drilling screw connections in CFS plates was studied through experiments and numerical analysis. Three typical failure modes were identified through research, and it was found that these three failure modes are closely linked to the ratio of screw diameter to plate thickness [12]. Liu [13] conducted an experimental and numerical investigation of screwed connections of CFS plates, studying the shear strength and failure modes of the specimens. A calculation method for determining the bearing capacity was proposed. Screw connections have been extensively used in CFS constructions due to their convenient installation and high load-bearing capacity. A sophisticated finite element model was developed to analyze the pull-out performance of screw connections. It is indicated that the failure types of the specimen include screw hole compression failure and screw shear failure [14].

CFS is often assembled using screw fasteners because they can be easily drilled through thin sheets of steel [15-21]. However, individual screws can cause discontinuities in the interface of the built-up plate. Therefore, the impact of screws on CFS built-up members cannot be ignored. Ting et al. [22-24] conducted experimental and numerical simulation studies on the influence of screw arrangements and screw diameters on the bearing capacity of various types of CFS built-up members. Owing to the shear action of the screw [25], the buckling mode and failure type of the built-up part of the member will change compared to the member without the influence of the screw. Therefore, screws are an important factor that affects the capacity of the CFS built-up members. Additionally, the failure mode of the screw will also impact the ultimate capacity of the built-up member [26,27]. Previous studies have focused on the mechanical behavior of CFS built-up members. However, the research on the buckling mechanism and critical buckling stress (CBS) of composite members in CFS built-up structures is still incomplete.

The most significant feature of the SBP is the discontinuity of the connection interface. However, due to this structural property, the application of the small deflection theory in the SBP raises the following two problems that need to be considered:

(1) There may be either coordinated buckling with the same deformation direction or delamination buckling with the opposite deformation direction between each single plate due to the discontinuity of the connection interface between the SBP. It remains to be studied whether the delamination buckling is considered when studying the CBS of the SBP.

(2) The discontinuity in the screwed connection may cause the shear deformation of the SBP during buckling. However, the shear deformation can also be constrained extent by discrete screw fasteners. While the effects of shear deformation of the built-up plate and screw constraint are not reflected in the current design method for the CBS.

Therefore, this paper investigates the instability mechanism of the SBP by using a four-sided simply supported plate as an example. The SBP in this paper is extracted from the built-up webs in the CFS back-to-back built-up column, as presented in Fig. 1(a). The constraint of the flanges on the webs is assumed to be a simply supported edge. The connection between the column ends and the end plates through spot welding is also considered a simply supported boundary condition. Therefore, a screw built-up plate with simply supported on four sides is established, as shown in Fig. 1(b).

The possible instability deformation modes are analyzed, and the calculation models of different deformation modes are established by comparing the various buckling modes between the built-up plate and the single plate. The analytical expression of the CBS for the built-up plate was derived considering the effects of different deformation modes on the structural behavior of the plate. The influence of various deformation modes on the SBP is then examined to identify the specific instability mode of the built-up plate. Finally, the discussion explores the influences of boundary conditions on the instability modes of the SBP.

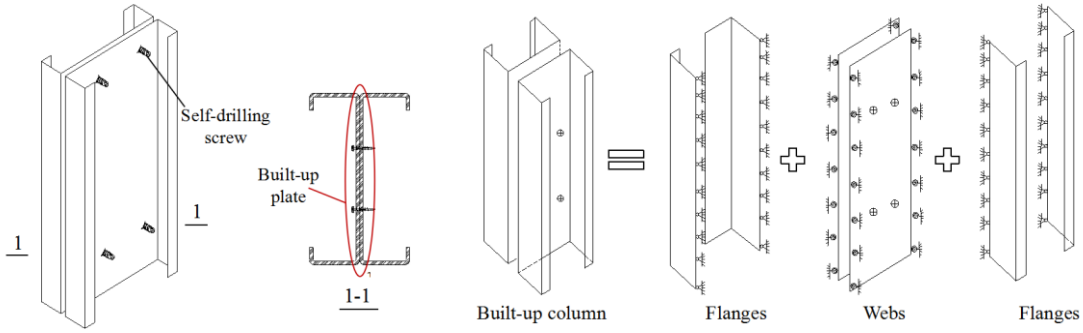


(a) Screw built-up plates (b) Boundary conditions

**Fig. 1** The source of the SBP and the determination of the boundary conditions

## 2. Buckling deformation modes

To study the deformation modes of the simply supported on four sides SBP, this paper analyzes the following three cases: (1) SBP may experience coordinated buckling and delamination buckling, without considering the coordination action of the plate, as shown in Fig. 2(a). The opposite deformation occurs at the deformation area within the partial panels for the delamination buckling mode. (2) When considering the coordinated deformation between two single plates, the plates at the opposite deformation location of the delamination buckling will compress each other. This compression causes the bending deformations to cancel each other out, forming a straight section, as illustrated in Fig. 2 (b). (3) In practice, the plates at the screw area also have the same deflection direction and dimension out of plane due to the constraint of screws, as presented in Fig. 2(c). Therefore, it can be concluded that two main modes of instability deformation occur, namely coordinated buckling and delamination buckling for the SBP simply supported on four sides.

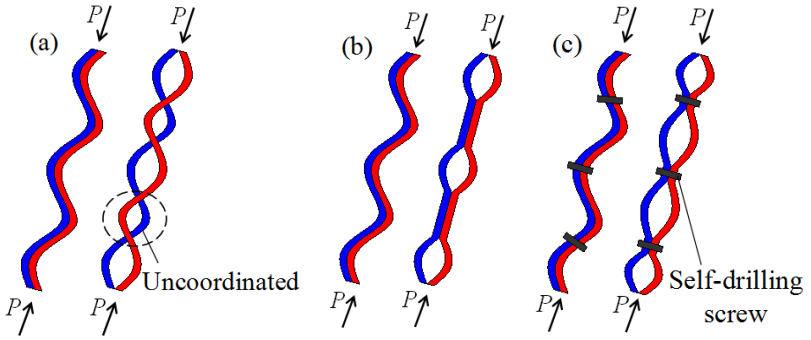


**Fig. 2** Deformation modes of the SBP with four edges simply supported. ((a) Without considering the effect of plates; (b) Considering the effect of plates; (c) Considering the effect of plates and screws)

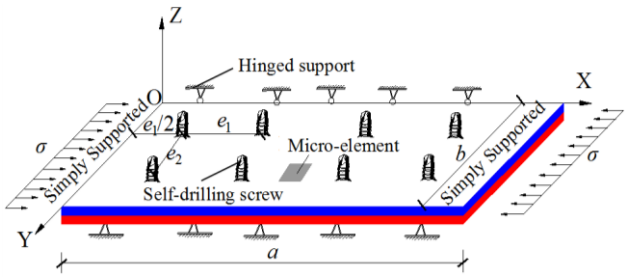


(a) The simplified model of the SBP

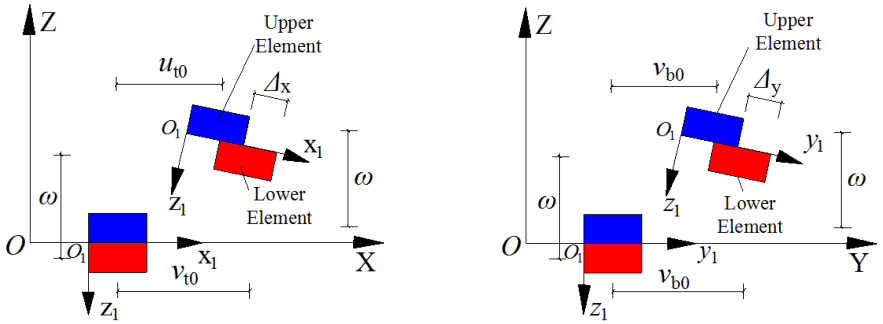


(b) Shear slip in the XOZ plane (c) Shear slip in the YOZ plane

**Fig. 3** Calculation models of the SBP with four edges simply supported

## 3. Buckling modes

### 3.1. Coordinate buckling mode

#### 3.1.1. Calculation model

A computational model of the CBS for the coordinated buckling deformation mode is presented in Fig. 3. The model consists of two identical plates connected by self-drilling screws, as shown in Fig. 3(a). A micro-element is extracted from the SBP to analyze the buckling deformation relationship between the upper and lower plates, as presented in Figs. 3(a)-3(c). Additionally, the overall coordinate system and local coordinate systems are established in Figs. 3(b)-3(c) to analyze the mechanical behavior between two individual plates in detail. Figs. 3(b) and 3(c) demonstrate the mechanical behaviors of the SBP during buckling in the XOZ plane and YOZ plane, respectively. At the connection interface for the built-up plate, coordinate systems $x_1o_1z_1$ and $y_1o_1z_1$ are established for follow-up purposes, as shown in Fig. 3(b)-3(c). The theoretical derivation can then be developed based on the energy method. Therefore, the following two basic assumptions are made for the convenience of the mathematical modeling.

(1) The influence of the size of the screw hole on the stability of the built-up plate is disregarded because the diameter of self-drilling screws being much smaller than the plate width.

(2) The constraint of self-drilling screws on the shear deformation of SBP can be simplified as shown in Fig. 4. The imaginary shear body is only subjected to shear deformation.

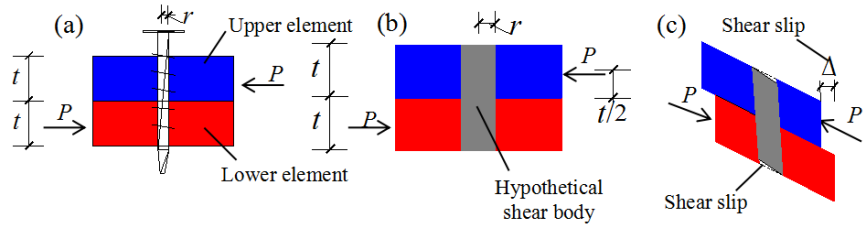


Note：$P$ is the pressure acting on the middle surface of each veneer

**Fig. 4** Mechanism behaviors of the ((a) Micro-element of the SBP; (b) Hypothetical shear body of screws; (c) Shear slip deformation)

#### 3.1.2. The mechanism behaviors of the micro-element

According to Fig. 3 and the assumption (1), the displacement of any point on the upper element is:

$$u_t = u_{t0} - (z_1 + t/2)\frac{\partial \omega}{\partial x} \tag{1a}$$

$$v_t = v_{t0} - (z_1 + t/2)\frac{\partial \omega}{\partial y} \tag{1b}$$

where, $u_t$ and $v_t$ represent the displacement of the upper element along the X-axis and the Y-axis directions of the global coordinate system, respectively. $\omega$ represents the deflection along the Z-axis direction of the global coordinate system. $z_1$ represents the displacement in the $z_1$ direction of the follow-up coordinate system.

Similarly, the displacement of any point of the lower elements is:

$$u_b = u_{b0} - (z_1 - t/2)\frac{\partial \omega}{\partial x} \tag{1c}$$

$$v_b = v_{b0} - (z_1 - t/2)\frac{\partial \omega}{\partial y} \tag{1d}$$

where $u_b$ and $v_b$ represent the displacement of the lower element along the X-axis and the Y-axis directions of the global coordinate system, respectively.

The strain of each element is then derived from the formulas (1a) to (1d):

$$\varepsilon_{xt} = \frac{\partial u_{t0}}{\partial x} - (z_1 + t/2)\frac{\partial^2 \omega}{\partial x^2} \tag{2a}$$

$$\varepsilon_{yt} = \frac{\partial v_{t0}}{\partial y} - (z_1 + t/2)\frac{\partial^2 \omega}{\partial y^2} \tag{2b}$$

$$\varepsilon_{xb} = \frac{\partial u_{b0}}{\partial x} - (z_1 - t/2)\frac{\partial^2 \omega}{\partial x^2} \tag{2c}$$

$$\varepsilon_{vb} = \frac{\partial v_{b0}}{\partial y} - (z_1 - t/2)\frac{\partial^2 \omega}{\partial y^2} \tag{2d}$$

where, $\varepsilon_{xt}$、 $\varepsilon_{xt}$ and $\varepsilon_{xb}$、 $\varepsilon_{xb}$ are the strains of any point of the upper element and lower element along the X-axis and the Y-axis directions of the global coordinate system, respectively.

Therefore, the normal stress of the upper and lower elements is obtained according to Hooke's law [1]:

$$\sigma_{xt} = \frac{E}{1-\nu^2}(\varepsilon_{xt} + \nu\varepsilon_{yt}) \tag{3a}$$

$$\sigma_{yt} = \frac{E}{1-\nu^2}(\varepsilon_{yt} + \nu\varepsilon_{xt}) \tag{3b}$$

$$\sigma_{xb} = \frac{E}{1-\nu^2}(\varepsilon_{xb} + \nu\varepsilon_{yb}) \tag{3c}$$

$$\sigma_{yb} = \frac{E}{1-\nu^2}(\varepsilon_{yb} + \nu\varepsilon_{xb}) \tag{3d}$$

where $\sigma_{xt}$、 $\sigma_{yt}$ and $\sigma_{xb}$、 $\sigma_{yb}$ are the normal stresses of the upper and lower body elements along the directions of the X-axis and the Y-axis of the global coordinate system, respectively. $E$ is the elastic modulus. $\upsilon$ is poisson's ratio.

#### 3.1.3. Shear strain of the micro-element

The shear strain will be generated under the influence of in-plane shear stresses based on the mechanical characteristics of the SBP. The deformation diagram is shown in Fig 5. According to the displacement of each point in Fig 5, the formulas for the shear strain at any point of the upper and lower elements can be respectively obtained:

$$\gamma_{xyt} = \frac{\partial u_t}{\partial y} + \frac{\partial v_t}{\partial x} = \frac{\partial u_{t0}}{\partial y} + \frac{\partial v_{t0}}{\partial x} - 2(z_1 + t/2)\frac{\partial^2 \omega}{\partial x \partial y} \tag{4a}$$

$$\gamma_{\mathrm{xyb}}=\frac{\partial u_{\mathrm{b}}}{\partial y}+\frac{\partial v_{\mathrm{b}}}{\partial x}=\frac{\partial u_{\mathrm{b0}}}{\partial y}+\frac{\partial v_{\mathrm{b0}}}{\partial x}-2(z_1+t/2)\frac{\partial^2\omega}{\partial x\partial y} \tag{4b}$$

According to Hooke's law [1], the shear stresses of the upper and lower elements are follows:

$$\tau_{\mathrm{xyt}}=G\gamma_{\mathrm{xyt}} \tag{5a}$$

$$\tau_{\mathrm{xyb}}=G\gamma_{\mathrm{xyb}} \tag{5b}$$

where the shear modulus of the material is $G=E/2(1+\nu)$.

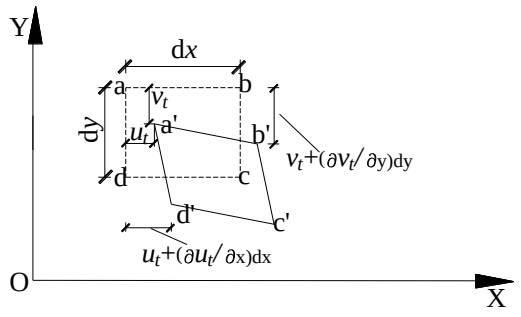


**Fig. 5** Mechanism model of the shear strain

*3.1.4. Shear slip of the connecting interface*

In addition to self-deformation, the upper and lower elements also undergo shear slip deformation at their connection interfaces based on the geometric relationship shown in Fig. 3. The shear slip deformations can be decomposed into the shear slip deformation $\Delta x$ and $\Delta y$ along the X-axis and Y-axis directions, respectively.

$$\Delta_x=u_{\mathrm{b}}\big|_{z_1=0}-u_{\mathrm{t}}\big|_{z_1=0}=(u_{\mathrm{b0}}-u_{\mathrm{t0}})+t\frac{\partial\omega}{\partial x} \tag{6a}$$

$$\Delta_{\mathrm{y}}=v_{\mathrm{b}}\big|_{z_1=0}-v_{\mathrm{t}}\big|_{z_1=0}=(v_{\mathrm{b0}}-v_{\mathrm{t0}})+t\frac{\partial\omega}{\partial y} \tag{6b}$$

where $\Delta_x$ and $\Delta_y$ represent the shear slip deformation of the upper and lower elements along the X-axis and Y-axis of the global coordinate system, respectively.

*3.1.5. Potential energy expression*

According to the principle of energy conservation, the following equilibrium equation can be established:

$$\int_v\sigma_{ij}\varepsilon_{ij}\mathrm{d}V=U_1+U_2-W \tag{7}$$

where

$$U_1=\int_{V_1}[(\sigma_{\mathrm{xt}}\varepsilon_{\mathrm{xt}}+\sigma_{\mathrm{yt}}\varepsilon_{\mathrm{yt}}+\tau_{\mathrm{xyt}}\gamma_{\mathrm{xyt}})dV_1+\int_{V_2}[(\sigma_{\mathrm{xb}}\varepsilon_{\mathrm{xb}}+\sigma_{\mathrm{yb}}\varepsilon_{\mathrm{yb}}+\tau_{\mathrm{xyb}}\gamma_{\mathrm{xyb}})dV_2 \tag{8a}$$

$$U_2=\frac{K_{\mathrm{L}}}{2}\sum_{i=1}^{n}\int_{A_{si}}(\Delta_x^2+\Delta_y^2)dA_{si} \tag{8b}$$

$$W=\frac{\sigma}{2}\int_{V_1}[\frac{\partial u_{\mathrm{t}}}{\partial x}+(\frac{\partial\omega}{\partial x})^2]dV_1+\frac{\sigma}{2}\int_{V_2}[\frac{\partial u_{\mathrm{b}}}{\partial x}+(\frac{\partial\omega}{\partial x})^2]dV_2 \tag{8c}$$

where $U_1$ represents the sum of the bending potential energy of the two individual plates in the SBP; $U_2$ represents the total the potential energy of each shear element; $W$ denotes the sum of external potential energy; $V_1$ and $V_2$ stand for the volumes of the upper plate and the lower plate; $A_{si}$ represents the cross-sectional area of the $i^{\mathrm{th}}$ self-drilling screw; $\sigma$ represents the compressive stress; and $n$ represents the number of self-drilling screws.

The total potential energy expression of the SBP is derived according to equations (2)~(8).

$$\begin{aligned}\Pi&=U_1+U_2-W\\&=\frac{Et}{1-\nu^2}\int_0^a\int_0^b\frac{1}{2}\{[(\frac{\partial u_{\mathrm{t0}}}{\partial x}+\frac{\partial u_{\mathrm{b0}}}{x})+(\frac{\partial v_{\mathrm{t0}}}{\partial y}+\frac{\partial v_{\mathrm{b0}}}{\partial y})]^2+[(\frac{\partial u_{\mathrm{t0}}}{\partial x}-\frac{\partial u_{\mathrm{b0}}}{\partial x})+(\frac{\partial v_{\mathrm{t0}}}{\partial y}-\frac{\partial v_{\mathrm{b0}}}{\partial y})]^2\}dxdy+\\&\frac{Et^3}{12(1-\nu^2)}\int_0^a\int_0^b\{(\frac{\partial^2\omega}{\partial x^2}+\frac{\partial^2\omega}{\partial y^2})^2-2(1-\nu)[\frac{\partial^2\omega}{\partial x^2}\frac{\partial^2\omega}{\partial x^2}-(\frac{\partial^2\omega}{\partial x\partial y})^2]\}dxdy-\frac{Et^2}{1-\nu^2}\cdot\\&\int_0^a\int_0^b\frac{(1-\nu)}{2}\{[4\frac{\partial u_{\mathrm{t0}}}{\partial x}\frac{\partial v_{\mathrm{t0}}}{\partial y}-(\frac{\partial u_{\mathrm{t0}}}{\partial y}+\frac{\partial v_{\mathrm{t0}}}{\partial x})^2]+[4\frac{\partial u_{\mathrm{b0}}}{\partial x}\frac{\partial v_{\mathrm{b0}}}{\partial y}-(\frac{\partial u_{\mathrm{b0}}}{\partial y}+\frac{\partial v_{\mathrm{b0}}}{\partial x})^2]\}dxdy+\\&\frac{K_{\mathrm{L}}}{2}\sum_{i=1}^{n}\int_{A_{si}}\{[(u_{\mathrm{b0}}-u_{\mathrm{t0}})+t\frac{\partial\omega}{\partial x}]^2+[(v_{\mathrm{b0}}-v_{\mathrm{t0}})+t\frac{\partial\omega}{\partial y}]^2\}dA_{si}-\sigma t\int_0^a\int_0^b[\frac{1}{2}(\frac{\partial u_{\mathrm{t0}}}{\partial x}+\frac{\partial u_{\mathrm{b0}}}{\partial x})+(\frac{\partial\omega}{\partial x})^2]dxdy\end{aligned} \tag{9}$$

The shear slip influence parameters ($u_{\mathrm{b0}}$, $v_{\mathrm{b0}}$, $u_{\mathrm{t0}}$, $v_{\mathrm{t0}}$) between the two single plates and the constraint of self-drilling screws (the generalized stiffness $K_{\mathrm{L}}$) are introduced in the total potential energy equation (9) in this paper. This can accurately reflect the mechanical characteristics of the SBP.

*3.1.6. The critical stress of the coordinated buckling*

The boundary conditions of the built-up plate with the four edges simply supported are as follows [1]:

$$\omega\big|_{x=0,x=a,y=0,y=b}=0 \tag{10a}$$

$$-D\frac{\partial^2\omega}{\partial y^2}\big|_{x=0,x=a,y=0,y=b}=0 \tag{10b}$$

where $D$ represents the bending rigidity of the plate.

The deflection function [1] that satisfies equations (10a) - (10b) could be taken as:

$$\omega=A_1\sin(\frac{m\pi x}{a})\sin(\frac{\pi y}{b}) \tag{11a}$$

The displacement function satisfying the mid-plane boundary condition of

each single plate is:

$$u_{t0} = A_2 \frac{\partial \omega}{\partial x} \tag{11b}$$

$$u_{b0} = A_3 \frac{\partial \omega}{\partial x} \tag{11c}$$

$$v_{t0} = A_4 \frac{\partial \omega}{\partial y} \tag{11d}$$

$$v_{b0} = A_5 \frac{\partial \omega}{\partial y} \tag{11e}$$

where $m$ is the number of the buckling half-wave; $A_1$、$A_2$、$A_3$、$A_4$ and $A_5$ are undetermined constants.

Substituting equations (10a)~(11e) into equation (9), and then perform the integration. A linear system of equations about $\partial\Pi/\partial A_1 = 0$, $\partial\Pi/\partial A_2 = 0$, $\partial\Pi/\partial A_3 = 0$, $\partial\Pi/\partial A_4 = 0$, $\partial\Pi/\partial A_5 = 0$ is established based on the principle of stationary potential energy. The condition for the system to have non-zero solutions is that the determinant of the coefficient matrix of this equation system is zero. The critical stress for the coordinated buckling of the SBP is then determined.

$$\sigma_{cr1} = k \frac{\pi^2 E}{12(1-\nu^2)} (\frac{\eta t}{b})^2 \tag{12}$$

where $k$ is the stability coefficient of the SBP with four edges simply supported; $\eta$ is the thickness reduction coefficient of the built-up plate reflecting the shear slip deformation and the influence of the self-drilling screw constraint. The formulas for these two parameters are:

$$k = (\frac{mb}{a} + \frac{a}{mb})^2 \tag{13a}$$

$$\eta = \sqrt{\frac{\pi^2 Et\sqrt{k} + 16aK_L(1-\nu^2)/me_1}{\pi^2 Et\sqrt{k} + 4aK_L(1-\nu^2)/me_1}} \tag{13b}$$

where $a$ refers to the length of the plate. $b$ refers to the width of the plate. $m$ represents the half-wavelength of buckling. $K_L$ represents the generalized stiffness parameter that reflects the constraint effect of self-drilling screws. $e_1$ refers to the screw spacing along the length of the plate.

### 3.2. Delamination buckling mode

The boundary conditions and the plate constraints inside the built-up plate have a significant influence on the mechanical characteristics of the SBP, as illustrated in Figs. 6(a)-6(b).

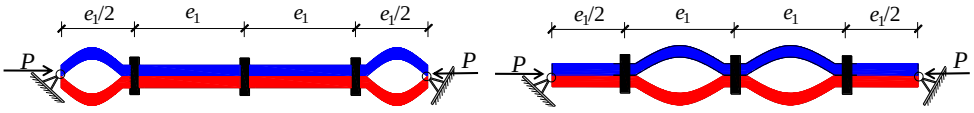


(a) End buckling (b) Inside buckling

**Fig. 6** Buckling modes of the delamination buckling

#### 3.2.1. calculation model

The calculation model is presented to analyze the mechanics characteristics of the delamination buckling of the SBP, as presented in Fig. 7.

The compression of each single plate is considered in both models. The angle and out-of-plane deflection are assumed to be close to "0", allowing for the further simplification of the complex deformation coordination and self-drilling screw constraint as the impact of the "boundary constraint condition" on the stability of the single plate.

Additionally, a critical half-wavelength is selected as the length of the SBP in the calculation model since the buckling behaviors are closely related to the buckling wavelength of members [17]. Meanwhile, this section also needs to meet the assumptions (1) and (2) outlined in Section 3.1.1 for further analysis.

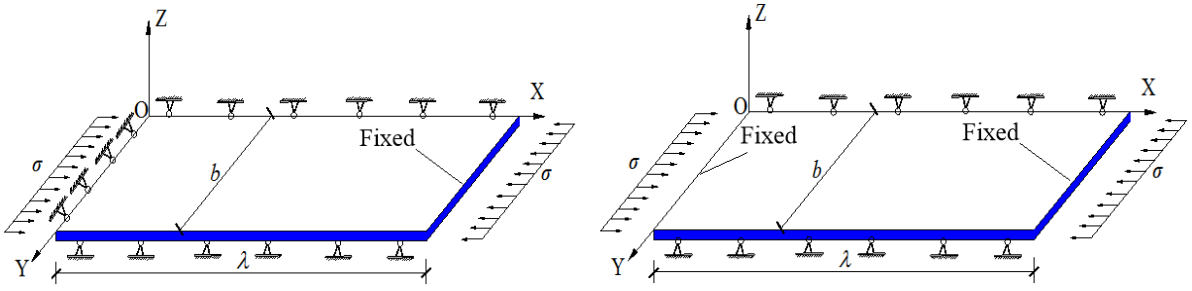


(a) End buckling (b) Inside buckling

**Fig. 7** Calculation models of the delamination buckling

#### 3.2.2. Potential energy expression

The total potential energy of the delamination buckling of the SBP consists of two parts: the bending strain energy and the external force potential energy:

$$\Pi = \frac{D}{2}\int_0^{\lambda}\int_0^{b}\{(\frac{\partial^2\omega}{\partial x^2}+\frac{\partial^2\omega}{\partial y^2})^2 + 2(1-\nu)[(\frac{\partial^2\omega}{\partial x\partial y})^2 - \frac{\partial^2\omega}{\partial x^2}\frac{\partial^2\omega}{\partial y^2}]\}dxdy - \frac{1}{2}\int_0^{\lambda}\int_0^{b}\sigma t(\frac{\partial\omega}{\partial x})^2 dxdy \tag{14}$$

where the flexural rigidity of the plate $D=Et^3/12(1-\nu^2)$; $\sigma$ is the compressive stress; $\omega$ is the deflection along the Z-axis.

#### 3.2.3. The critical stress of the delamination buckling

(1) End buckling

The boundary conditions [1] of the model in Fig. 7(a) are as follows:

$$\omega\big|_{x=0,x=\lambda,y=0,y=b} = 0 \tag{15a}$$

$$-D\frac{\partial^2\omega}{\partial y^2}\Big|_{x=0,y=0,y=b}=0 \tag{15b}$$

$$\frac{\partial\omega}{\partial x}\Big|_{x=\lambda}=0 \tag{15c}$$

The deflection function [27] that satisfies equations (17a)-(17c) can be expressed as:

$$\omega=A_1[\sin(\frac{2\pi x}{\lambda})+2\sin(\frac{\pi x}{\lambda})]\sin(\frac{\pi y}{b}) \tag{16}$$

By substituting the equations (15) and (16) into equation (14), the final buckling stress can be determined through simplification as follows:

$$\sigma_{f1}=k_{21}\frac{E\pi^2}{12(1-v^2)}(\frac{t}{b})^2 \tag{17a}$$

where the stability coefficient $k_{21}$ is:

$$k_{21}=\frac{(20b^4+16b^2\lambda^2+5\lambda^4)}{8b^2\lambda^2} \tag{17b}$$

From this $\partial k_2/\partial\lambda=0$, it can get the critical half-wavelength as follows:

$$\lambda_{cr}=\sqrt{2}b\approx1.41b \tag{17c}$$

According to the influence of the screw spacing, the stability coefficient $k_{21}$ is:

$$k_{21}=\begin{cases}4.5 & e_1>2.82b\\ \dfrac{(320b^4+64b^2{e_1}^2+5{e_1}^4)}{32b^2{e_1}^2} & e_1<2.82b\end{cases} \tag{17d}$$

(2) Inside buckling

The boundary conditions [1] of the model in Fig 7(b) are as follows:

$$\omega\Big|_{x=0,x=\lambda,y=0,y=b}=0 \tag{18a}$$

$$-D\frac{\partial^2\omega}{\partial y^2}\Big|_{y=0,y=b}=0 \tag{18b}$$

$$\frac{\partial\omega}{\partial x}\Big|_{x=0,x=\lambda}=0 \tag{18c}$$

The deflection function [26] that satisfies the equations (18a)-(18c) can be expressed as:

$$\omega=A_1\sin(\frac{\pi x}{\lambda})\sin(\frac{\pi x}{\lambda})\sin(\frac{\pi y}{b}) \tag{19}$$

Submitting the equations (18)-(19) into the equation (14), the inside buckling stress can be obtained through simplification as follows:

$$\sigma_{f2}=k_{22}\frac{E\pi^2}{12(1-v^2)}(\frac{t}{b})^2 \tag{20a}$$

where the stability coefficient $k_{22}$ is:

$$k_{22}=\frac{(16b^4+8b^2\lambda^2+3\lambda^4)}{4b^2\lambda^2} \tag{20b}$$

From this $\partial k_{22}/\partial\lambda=0$, it can get the critical half-wavelength as follows:

$$\lambda_{cr}=\sqrt[4]{16/3}b\approx1.52b \tag{20c}$$

According to the influence of the screw spacing, stability coefficient $k_{22}$ is:

$$k_{22}=\begin{cases}5.464 & e_1>1.52b\\ \dfrac{(16b^4+8b^2{e_1}^2+3{e_1}^4)}{4b^2{e_1}^2} & e_1<1.52b\end{cases} \tag{20d}$$

Therefore, from equations (17)-(20), the critical stress of the delamination buckling of the SBP is:

$$\sigma_{cr2}=k_2\frac{E\pi^2}{12(1-v^2)}(\frac{t}{b})^2 \tag{21a}$$

where the stability coefficient $k_2$ is the smaller of $k_{21}$ and $k_{22}$, that is:

$$k_2=\min[k_{21},k_{22}] \tag{21b}$$

*3.3. Comparison of coordinated buckling and delamination buckling*

It can be observed from the instability mechanism that the members always progress towards the most unfavorable failure mode. Therefore, the CBS of the SBP should be smaller than the coordinated buckling and the delamination buckling, that is:

$$\sigma_{cr}=\min[\sigma_{cr1},\sigma_{cr2}] \tag{22}$$

where $\sigma_{cr}$ represents the CBS of the SBP with the four edges simply supported; $\sigma_{cr1}$ denotes the coordinated buckling stress, and $\sigma_{cr2}$ indicates the delamination buckling stress.

It can be seen that the buckling deformation mode of the built-up plate must be determined before calculating the critical stress based on the above theoretical analysis. It is convenient for calculating the CBS.

Therefore, the thickness reduction coefficient ($\eta$) of the SBP in formula 13(b) should be combined with the stability coefficient ($k$) of the single plate. The stability coefficient of the SBP with four edges can be determined.

$$k_s=(\frac{mb}{a}+\frac{a}{mb})^2\frac{\pi^2Et(a/mb+mb/a)+16aK_L(1-v^2)/me_1}{\pi^2Et(a/mb+mb/a)+4aK_L(1-v^2)/me_1} \tag{23}$$

That is $\sigma_{cr1}=k_3\frac{E\pi^2}{12(1-v^2)}(\frac{t}{b})^2$. Therefore, only $k_2$ and $k_3$ need to be compared for the comparison of the CBSes of the coordinated buckling and the delamination buckling. Variables in $k_2$ are $b$ and $e_1$. Variables in $k_3$ are $b$, $e_1$, and $a$. Hence, the relationship among the variables $b$, $e_1$, $a$, and $k$ *is* discussed. The three-dimensional relationship of the $b$/a, $e_1/a$, and $k$ in equations (21b) and (23) is illustrated in Fig. 8 to explore the determination of the buckling modes that occur in the SBP. It can be seen from Figs 8(a)-8(b) that the three-dimensional surface calculated by equation (21b) is always above the three-dimensional surface calculated by equation (23). In the case of the self-drilling screw arrangement shown in Fig. 3, the delamination buckling represents a higher order buckling mode of the coordinated buckling. Therefore, only the coordinated buckling is considered in the calculation of the CBS of the SBP. Thus, the CBS of the SBP with four edges simply supported is as follows:

$$\sigma = k\frac{E\pi^2}{12(1-v^2)}(\frac{\eta t}{b})^2 \quad (24)$$

where $k$ is the stability coefficient of the single plate [1], and $\eta$ is the thickness reduction coefficient of the SBP [5].

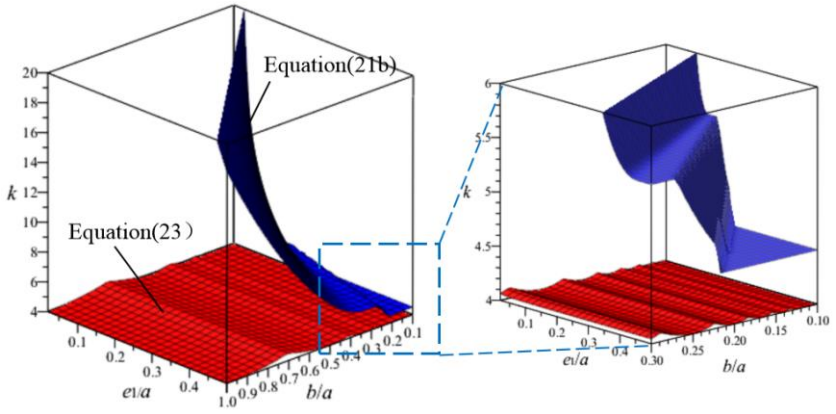


(a) Three-dimensional relationships for $b/a$, $e_1/a$ and $k$ at $K$= 100N/mm

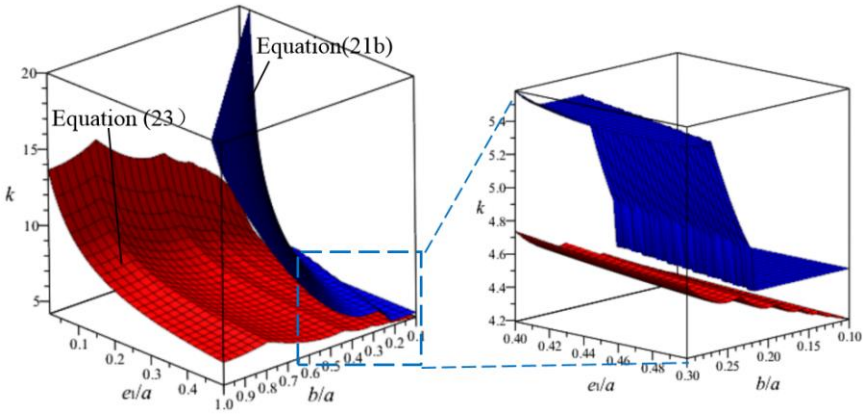


(b) Three-dimensional relationships for $b/a$, $e_1/a$ and $k$ at $K$= 90000N/mm

**Fig. 8** Comparisons of the formula (21b) and the formula (23)

## 4. Reliability study

The SBP in this paper is extracted from the built-up web in the CFS back-to-back built-up column, as presented in Fig. 1. The constraint of the flanges on the webs is assumed to be a simply supported edge. The connection between the column ends and the end plates through spot welding is also considered as a simply supported boundary condition. Therefore, a screw built-up plate with simply supported on four sides is set up. This paper not only investigates the shear slip and screw constraint during the buckling of the SBP but also lays the foundation for subsequent works on CFS built-up columns.

The CFS built-up columns designed in this paper are divided into two series based on the different web heights: the 120 series and the 140 series. There are three different screw spacings for each different length of the CFS built-up columns. The screw spacing for the 120 series columns is 45mm, 90mm, and 150mm, respectively. The screw spacing for the 140 series columns is 50mm, 100mm, and 150mm, respectively. A total of 18 specimens were tested. The measured dimensions of the specimens are listed in Table 1. The representative positions of cross-sectional geometric dimensions are shown in Fig. 9, while naming rules for the members are illustrated in Fig. 10.

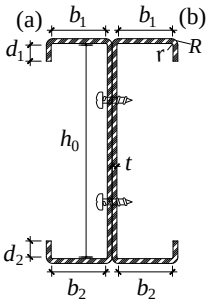


**Fig. 9** Section diagram of specimens

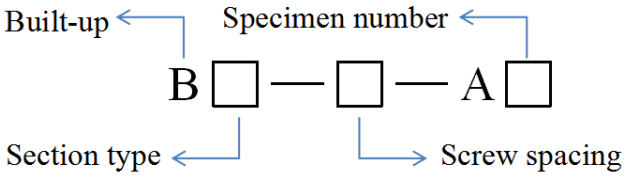


**Fig. 10** Labeling rule of specimens

**Table 1**
The measured dimensions of the tested specimens

| Specimens | Part | Measure length/mm | Geometric dimensions/mm | | | | | | Outside diameter/mm | Inside diameter/mm |
|---|---|---|---|---|---|---|---|---|---|---|
| | | $L_s$ | $h_0$ | $b_1$ | $b_2$ | $d_1$ | $d_2$ | $t$ | $R$ | $r$ |
| B120-45-A1 | a | 367 | 114 | 55 | 54 | 23 | 15 | 1.22 | 4.0 | 2.8 |
| | b | 366 | 115.5 | 54.5 | 53.5 | 22.8 | 14.8 | 1.18 | 3.8 | 2.6 |
| B120-45-A2 | a | 376 | 115 | 53 | 52 | 22 | 14 | 1.21 | 3.0 | 1.8 |
| | b | 376.5 | 115 | 55 | 54 | 23 | 15 | 1.18 | 4.0 | 2.8 |
| B120-45-A3 | a | 369 | 115 | 54 | 53 | 22.5 | 14.5 | 1.21 | 3.5 | 2.3 |
| | b | 367 | 116 | 53 | 52 | 22 | 14 | 1.19 | 3.0 | 1.8 |
| B120-90-A1 | a | 362 | 115 | 53 | 52 | 22 | 14 | 1.22 | 3.0 | 1.8 |
| | b | 366 | 115 | 54 | 53 | 22.5 | 14.5 | 1.22 | 3.5 | 2.3 |
| B120-90-A2 | a | 380 | 116.5 | 53.5 | 52.5 | 22.3 | 14.3 | 1.17 | 3.3 | 2.1 |
| | b | 376 | 116 | 55 | 54 | 23 | 15 | 1.17 | 4.0 | 2.8 |
| B120-90-A3 | a | 372.5 | 115.5 | 53.5 | 52.5 | 22.3 | 14.3 | 1.18 | 3.3 | 2.1 |
| | b | 370 | 115.5 | 53.5 | 52.5 | 22.3 | 14.3 | 1.17 | 3.3 | 2.1 |
| B120-150-A1 | a | 367 | 116 | 52 | 51 | 21.5 | 13.5 | 1.22 | 2.5 | 1.3 |
| | b | 371.5 | 115 | 54 | 53 | 22.5 | 14.5 | 1.18 | 3.5 | 2.3 |
| B120-150-A2 | a | 375 | 115 | 54 | 53 | 22.5 | 14.5 | 1.15 | 3.5 | 2.4 |
| | b | 374 | 115 | 56 | 55 | 23.5 | 15.5 | 1.17 | 4.5 | 3.3 |
| B120-150-A3 | a | 364 | 114 | 54 | 53 | 22.5 | 14.5 | 1.22 | 3.5 | 2.3 |
| | b | 362 | 115 | 54 | 53 | 22.5 | 14.5 | 1.17 | 3.5 | 2.3 |
| B140-50-A1 | a | 420.5 | 135 | 51.5 | 52.5 | 23.3 | 19.4 | 1.18 | 3.3 | 2.1 |
| | b | 420 | 135 | 51 | 52 | 23 | 19.1 | 1.19 | 3.0 | 1.8 |
| B140-50-A2 | a | 420 | 136 | 51.5 | 52.5 | 23.3 | 19.4 | 1.18 | 3.3 | 2.1 |
| | b | 419.5 | 135.5 | 51.5 | 52.5 | 23.3 | 19.4 | 1.20 | 3.3 | 2.1 |
| B140-50-A3 | a | 420 | 136 | 51 | 52 | 23 | 19.1 | 1.18 | 3.0 | 1.8 |
| | b | 420 | 134.5 | 52 | 53 | 23.5 | 19.6 | 1.20 | 3.5 | 2.3 |
| B140-100-A1 | a | 419 | 135 | 52.5 | 53.5 | 23.8 | 19.9 | 1.15 | 3.8 | 2.6 |
| | b | 420 | 135 | 52 | 53 | 23.5 | 19.6 | 1.15 | 3.5 | 2.4 |
| B140-100-A2 | a | 420 | 135.5 | 51.5 | 52.5 | 23.3 | 19.4 | 1.16 | 3.3 | 2.3 |
| | b | 415 | 135 | 52 | 53 | 23.5 | 19.6 | 1.16 | 3.5 | 2.3 |
| B140-100-A3 | a | 420 | 136 | 51 | 52 | 23 | 19.1 | 1.22 | 3.0 | 1.8 |
| | b | 419.5 | 135 | 53 | 54 | 24 | 20.1 | 1.20 | 4.0 | 2.8 |
| B140-150-A1 | a | 420 | 135 | 52.5 | 53.5 | 23.8 | 19.9 | 1.17 | 3.8 | 2.6 |
| | b | 420 | 135.5 | 51.5 | 52.5 | 23.3 | 19.4 | 1.16 | 3.3 | 2.1 |
| B140-150-A2 | a | 418 | 138 | 50 | 51 | 22.5 | 18.6 | 1.17 | 2.5 | 1.3 |
| | b | 419 | 136 | 52 | 53 | 23.5 | 19.6 | 1.22 | 3.5 | 2.3 |
| B140-150-A3 | a | 418.5 | 138 | 49 | 50 | 22 | 18.1 | 1.20 | 2.0 | 0.8 |
| | b | 421 | 136 | 50 | 51 | 22.5 | 18.6 | 1.17 | 2.5 | 1.3 |

The buckling characteristics of the test specimens are presented in Fig. 11. The buckling half-wave gradually appears on the specimen webs as the load increases. One of the built-up web plates undergoes convex deformation, while the other undergoes concave deformation. The coordination buckling phenomenon is becoming increasingly prominent under loading. The SBP undergoes coordinated buckling.

Additionally, this formula (24) is verified using data from the experiment, as listed in Table 2. The mean and standard deviation (SD) are 1.04 and 0.02, respectively. It can be seen that the calculated results are in good agreement with the experimental results. Therefore, it indicates that the study in this paper is accurate and reliable. In Table 2, $\sigma_{crt}$ represents the experimental results. $\sigma_{crc}$ represents the calculation results. The critical stress ($\sigma_{crt}$) is obtained based on the reverse point of strain, as detailed in the reference [4].

**Table 2**
Comparison of theoretical and experimental results

| Specimens | $\sigma_{crt}$(N/mm$^2$) | $\sigma_{crc}$/(N/mm$^2$) | $\sigma_{crc}/\sigma_{crt}$ |
|---|---|---|---|
| B120-45-A1 | 105.74 | 109.56 | 1.04 |
| B120-45-A2 | 105.63 | 110.41 | 1.05 |
| B120-45-A3 | 108.08 | 111.57 | 1.03 |

| | | | |
|---|---|---|---|
| B120-90-A1 | 101.86 | 104.46 | 1.03 |
| B120-90-A2 | 91.27 | 92.92 | 1.02 |
| B120-90-A3 | 93.06 | 95.57 | 1.03 |
| B120-150-A1 | 92.27 | 97.37 | 1.06 |
| B120-150-A2 | 85.34 | 87.55 | 1.03 |
| B120-150-A3 | 92.57 | 95.21 | 1.03 |
| B140-50-A1 | 82.67 | 85.12 | 1.03 |
| B140-50-A2 | 80.96 | 84.53 | 1.04 |
| B140-50-A3 | 82.23 | 85.34 | 1.04 |
| B140-100-A1 | 66.46 | 70.21 | 1.06 |
| B140-100-A2 | 67.90 | 71.94 | 1.06 |
| B140-100-A3 | 74.21 | 77.97 | 1.05 |
| B140-150-A1 | 65.70 | 69.46 | 1.06 |
| B140-150-A2 | 67.10 | 73.33 | 1.09 |
| B140-150-A3 | 72.79 | 73.91 | 1.02 |
| | Mean | | 1.04 |
| | SD | | 0.02 |

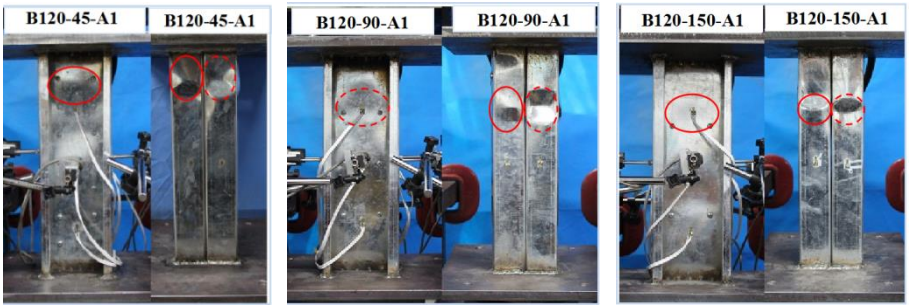


(a) 120 series built-up columns


(b) 140 series built-up columns

**Fig. 11** Buckling characteristics of test specimens

## 5. The CBS of the SBP with other boundary conditions

Research has shown that the CBS of the SBP is closely related to the boundary conditions. These boundary conditions include the fixed at four sides, the two loading edges with simple support and two non-loading edges with fixed support, the two loading edges with fixed support, as well as two non-loading edges with simple support. The influence of the boundary constraint condition on the CBS of the SBP is discussed in this paper. The calculation model for the CBSes of the three boundary conditions of the SBP still refers to Fig. 1. Depending on the distinct boundary conditions, the displacement function [26] of the SBP can be approximated as follows:

(1) Fixed at four sides

$$\omega = \mathrm{A}\sin(\frac{m\pi x}{a})\sin(\frac{\pi x}{a})\sin(\frac{\pi y}{b})^2 \tag{25a}$$

(2) Two loading edges with simple support and two non-loading edges with fixed support

$$\omega = \mathrm{A}\sin(\frac{m\pi x}{a})\sin(\frac{\pi y}{b})^2 \tag{25b}$$

(3) Two loading edges with fixed support and two non-loading edges with simple support

$$\omega = \mathrm{A}\sin(\frac{m\pi x}{a})\sin(\frac{\pi x}{a})\sin(\frac{\pi y}{b}) \tag{25c}$$

The CBS of the coordinated buckling of the SBP can be obtained by referring to the above theoretical ideas.

$$\sigma = k\frac{E\pi^2}{12(1-\nu^2)}\left(\frac{\eta t}{b}\right)^2 \tag{26}$$

(1) Fixed at four sides

$$k=\frac{\pi^2(3b^4m^4+8a^2b^2m^2+18b^4m^2+16a^4+8a^2b^2+3b^4)}{3(m^2+1)a^2b^2} \tag{27a}$$

(2) Two loading edges with simple support and two non-loading edges with fixed support

$$k=\frac{16a^4+8a^2b^2m^2+16b^4m^4}{3m^2a^2b^4} \tag{27b}$$

(3) Two loading edges with fixed support and two non-loading edges with simple support

$$k=[\frac{b^2(m^4+6m^2+1)}{a^2(m^2+1)}+2+\frac{a^2}{b^2(m^2+1)}] \tag{27c}$$

It can be seen that the boundary conditions significantly affect the CBSes for the SBP. It can be proven that delamination buckling is still a higher order buckling mode of coordinated buckling under these boundary conditions. Therefore, only the coordinated buckling is considered when calculating the CBS of the SBP under the specified boundary conditions.

## 6. Conclusions and discussions

The influences of the coordinated buckling and delamination buckling on the CBS of the SBP are studied in this paper. The calculation models of the CBS are established. A calculation method for calculating the CBS of SBP is proposed. Therefore, the main conclusions can be drawn as follows:

(1) Delamination buckling always represents the higher-order mode of coordinated buckling when the SBP buckles. Based on the instability mechanism of the plate, it can be observed that the CBS of the SBP always consistently shifts towards the most unfavorable mode of development. Therefore, only the coordinated buckling should be considered when calculating the CBS of the screw built-up plate.

(2) The shear slip effect and the constraint effect of self-drilling screws are considered when deducing the CBS of the SBP. It indicates that the CBS is more accurate and closer to the actual situation of the SBP.

(3) The equation of the CBS for the SBP with four edges simply supported is derived and validated. However, the accuracy of the equations under different boundary conditions needs further verification.

(4) In this paper, it is proposed that the generalized stiffness $K_L$ (shear stiffness) in the equation of the CBS of the SBP represents as the ability to prevent the sliding deformation of the plates along the connection interface. However, the theoretical analysis of shear stiffness needs to be further studied through experiments and theoretical study.

**Authorship Statement** derived and validated

Yanchun Li: Writing -original draft, Validation, Data curation; Tianhua Zhou: Supervision, Resources; Aihong Han: Writing - review & editing; Yan Lu: Writing -original draft; Jihao Chen: Software.

## Acknowledgments

The authors are grateful to the financial support provided by the National Natural Science Foundation of China (No. 51878055), Key R&D and promotion projects in Henan Province (No. 242102321151) and (No. 242102321152), Key Scientific Research Projects of Universities (No. 23A560011) and (No. 22A560013).

## References

[1] S.P. Timoshenko, J.M. Gere, Theory of Elastic Stability, 2nd ed. Mcgraw-Hill, New York, 1961.

[2] Lu Y, Zhou TH, Li WC, et al. On the plate assembly effects of compressed thin-walled C-section members at post-buckling stage. Journal of Huazhong University of Science and Technology (Natural Science Edition), 2017, 45(07):30-35 (In Chinese).

[3] Lu Y, Zhou TH, Li WC, et al. The critical local buckling load and ultimate strength of cold formed thin-walled C-sections under axial compression. Journal of Harbin Institute of Technology, 2017,49(06):72-76(In Chinese).

[4] Zhou TH, Li YC, Ren LJ, et al. Research on the elastic buckling of composite webs in cold-formed steel back-to-back built-up columns-Part I: Experimental and numerical investigation. Structures, 2021, 30:115-133.

[5] Li YC, Zhou TH, Ren LJ, et al. Elastic buckling of composite webs in back-to-back cold-formed steel built-up columns-Part II: Design formula. Structures, 2021, 33:3515-3525.

[6] Lu LF, Zhang YP, Fang WY, et al. Experimental investigation on shear-bearing capacity for self-drilling screw connections of cold-formed thin-walled steel. Journal of Central South University (Natural Science Edition), 2013, 44(07):2997-3005 (In Chinese).

[7] Shi Y, Wang SW, Liu YJ. Research on Shear Behavior of Single Tapping Screw Connection in Cold formed Thin-wall Steel Structures. Journal of Architecture and Civil Engineering, 2014, 31(02):57-64 (In Chinese).

[8] Roy K, Lau HH, Ting TCH. Experiments and finite element modelling of screw pattern of self-drilling screw connections for high strength cold-formed steel. Thin-Walled Structures, 2019, 145:106393.

[9] Li YC, Li RB, Zhou TH, et al. Novel design method of screwed connections of cold-formed steel built-up plates. Structures, 2023, 55:2433-2444.

[10] Huynh MT, Pham CH, Hancock GJ. Experimental behaviour and modelling of screwed connections of high strength sheet steels in shear. Thin-Walled Structures, 2020, 146:106357.

[11] Cai KY, Yuan HX. Testing, numerical and analytical modelling of self-drilling screw connections between thin steel sheets in shear. Thin-Walled Structures, 2023, 182:110292.

[12] Liu S, Feng RQ, Zhong YT. Experimental and numerical studies of screwed connections with hot-rolled steel plate and cold-formed steel sheet. Structures, 2023, 51:311-319.

[13] Liu WH, Deng L, Zhong WJ. Parametric study on the pull-out performance of screw connections in cold-formed thin-walled steel structures. Engineering Structures, 2023, 274:115007.

[14] Chen BS, Roy K. Uzzaman A. Axial strength of back-to-back cold-formed steel channels with edge-stiffened holes, un-stiffened holes and plain webs. J Constr Steel Res, 2020, 174:106313.

[15] Roy K, Ting TCH, Lau HH. Nonlinear behaviour of back-to-back gapped built-up cold-formed steel channel sections under compression. J Constr Steel Res, 2018, 147:257-76.

[16] Zhang JH, Young B. Experimental investigation of cold-formed steel built-up closed section columns with web stiffeners. J. Constr. Steel Res, 2018, 147:380-392.

[17] Roy K. Mohammadjani C, Lim JBP. Experimental and numerical investigation into the behaviour of face-to-face built-up cold-formed steel channel sections under compression. Thin-Walled Structures, 2019, 134:291-309.

[18] Dar MA, Subramanian N, Dar DA, et al. Flexural Strength of cold-formed steel built-up composite beams with rectangular compression flanges. Steel & Composite Structures, 2020, 34(2):171-188.

[19] Li YC, Zhou TH, Z L, et al. Distortional buckling behavior of cold-formed steel built-up closed section columns. Thin-walled Structures, 2021, 166:108069.

[20] Selvaraj S, Madhavan M. Experimental investigation and design considerations on cold-formed steel built-up I-section columns subjected to interactive buckling modes. Thin-Walled structures, 2022, 6:175.

[21] Ting TCH, Roy K, Lau HH. Effect of screw spacing on behavior of axially loaded back-to-back cold-formed steel built-up channel sections. Advances in Structural Engineering, 2018, 21(3):474-487.

[22] Wang LP, Young B. Behaviour and design of cold-formed steel built-up section beams with different screw arrangements. Thin-Walled Structures, 2018, 131:16-32.

[23] Chen BS, Roy K, Uzzaman A. Axial strength of back-to-back cold-formed steel channels with edge-stiffened holes, un-stiffened holes and plain webs. Journal of Constructional Steel Research, 2020, 174:106313.

[24] Fratamico DC, Torabian S, Zhao X. Experimental study on the composite action in sheathed and bare built-up cold-formed steel columns. Thin-Walled Structures, 2018, 127:290-305.

[25] Roy K, Lau HH, Ting TCH. Experiments and finite element modelling of screw pattern of self-drilling screw connections for high strength cold-formed steel. Thin-Walled Structures, 2019, 145:106393.

[26] Kechidi S, Fratamico DC, Schafer BW, et al. Simulation of screw connected built-up cold-formed steel back-to-back lipped channels under axial compression. Engineering Structures, 2020, 206:110109.

[27] Schafer, B. W. Cold-formed steel behavior and design: analytical and numerical modeling of elements and members with longitudinal stiffeners. New York: Cornell University. 1997.

**Advanced Steel Construction** – Vol. 20 No. 3 (2024) 310–318
**DOI:**10.18057/IJASC.2024.20.3.10


# A MODEL FOR PREDICTING THE MOMENT-CURVATURE BEHAVIOR OF STEEL TUBE CONFINED REINFORCED SELF-STRESSING STEEL SLAG CONCRETE COLUMNS UNDER CYCLIC LOADING

Feng Yu [1, 2], Wei Liu [1], Shuang-Shuang Bu [1, *], Guang-Fei Kuang [1] and Yuan Fang [1]

[1] *Department of Civil Engineering and Architecture, Anhui University of Technology, Maanshan, 243032, China*
[2] *Wuhu Technology and Innovation Research Institute, Anhui University of Technology, Wuhu, 241002, China*
** (Corresponding author: E-mail: biluo12345@163.com)*

**ABSTRACT**

This paper evaluates the moment-curvature response of steel tube confined reinforced self-stressing steel slag concrete (STCRSSSC) columns by conducting cyclic loading tests on ten STCRSSSC columns and four steel tube confined reinforced steel slag concrete (STCRSSC) columns. Four parameters are considered: axial compression ratio, shear-span ratio, diameter-thickness ratio, and expansion rate of steel slag concrete (SSC). The results show that the specimens exhibit a bending failure mode. As the expansion rate of SSC or shear-span ratio increase, the area of the moment-curvature $M-\phi$ hysteretic loops expands, but the slope of the skeleton curve remains basically unchanged. The slope of the skeleton curve rises as the diameter-thickness ratio or axial compression ratio increase. With the reduction of the axial compression ratio or diameter-thickness ratio, the area of the $M-\phi$ hysteretic loops increases. Based on the experimental results, the characteristic points of the $M-\phi$ response are identified, and a simplified model is proposed to predict the skeleton curves. Lastly, a hysteresis rule of the specimens is suggested based on the Clough trilinear degeneration model, and a predicting model of the $M-\phi$ response of the specimens is established.

**ARTICLE HISTORY**

Received: 13 October 2023
Revised: 8 April 2024
Accepted: 21 April 2024

**KEYWORDS**

Concrete-filled steel tube;
Steel tube confined concrete;
Steel slag;
Self-stressing concrete;
Hysteresis behavior;
Restoring force model



## 1. Introduction

Steel tube confined concrete (STCC) columns are widely used in engineering owing to their significant advantages such as excellent ductility, high bearing capacity, and convenient construction [1-5]. However, shrinkage of the concrete core leads to a reduction in the bonding performance between the steel tube and concrete core, which can significantly weaken the bearing capacity and safety of the structures [6-7].

To solve the shrinkage problem of the core concrete, self-stressing concrete is used as an effective solution to balance the shrinkage of the core concrete and promote collaboration between the steel tube and core concrete [8-9]. Traditional self-stressing concrete is produced by adding expansion agents, and it has been proven that the bond behavior of self-stressing concrete-filled steel tubes (SCFST) can be improved by increasing the content of the expansive agent [10-12]. Subsequently, some scholars carried out a series of further studies and revealed that SCFST columns exhibit excellent axial compressive behaviors, flexural capacity, and seismic properties [13-17]. However, the extensive use of expansion agents in practical engineering applications has resulted in problems such as high construction costs and preparation complexity.

Steel slag concrete (SSC) is prepared using steel slag as an aggregate, and appropriate proportions can guarantee the mechanical properties and durability of SSC [18-22]. It has been proven to have potential for engineering applications [23-24]. In addition, the volumetric expansion of SCC after hydration is caused by the presence of free CaO/MgO in the steel slag. This characteristic makes it possible to satisfy the expansion performance requirements of self-stressing concrete [25]. Self-stressing steel slag concrete can not only solve the problems of high cost and complex preparation of traditional self-stressing concrete but also improve the mass utilization of steel slag.

Combining the advantages of SCFST and the expansion performance of SSC, Yu et al. investigated the feasibility of preparing self-stressing SSC-filled steel tubular (SSSCFST) columns. It appears that increasing the expansion rate of the SSSC may lead to an improvement in both the compression performance and bond-slip behaviors of the specimens [26-28]. However, current studies on the behavior of steel tube confined reinforced self-stressing SSC (STCRSSSC) under different loading conditions are limited.

Seismic performance is crucial for structural applications and designs. In this study, four steel tube confined reinforced steel slag concrete (STCRSSC) columns and ten STCRSSSC columns were used. Furthermore, this study analyzed and discussed the effects of the diameter-thickness ratio, axial compression ratio, expansion rate of SSC, and shear-span ratio on the seismic behaviors of the specimens. Finally, an analysis model for evaluating the $M-\phi$ behavior of STCRSSSC columns is established, which is expected to complete the elastoplastic seismic response analysis of such composite structures.

## 2. Experimental program

### *2.1. Specimens design*

Ten STCRSSSC columns and four STCRSSC columns are presented in this paper. As shown in Fig. 1, the entire specimen was designed to have an inverted T-shape. The specimen consisted of a column head, column body, and foundation. The total height of the specimen was 1600 mm. The height of the column head was 400 mm. The heights of the column bodies were 400, 600, and 800 mm. The shear-span ratio, axial compression ratio, diameter-thickness ratio, and expansion rate of SSC are listed in Table 1.

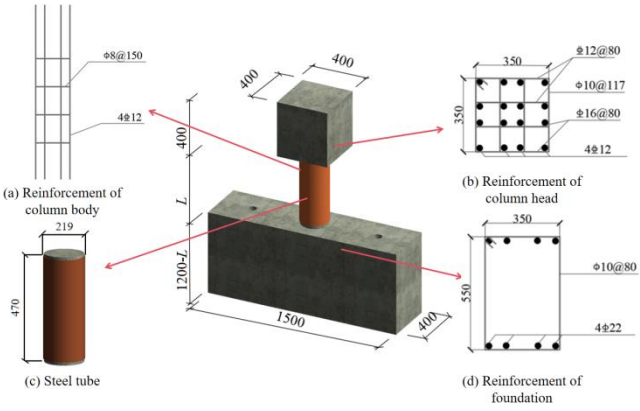


**Fig. 1** Details of the specimens

As shown in Fig. 1(c), the outer diameter and height of the steel tube were 219 and 470 mm, respectively. To ensure the restraining effect of the steel tube on the concrete core, the ends of the steel tube were spaced 15 mm apart from the foundation and column head. The thicknesses of the steel tubes were 2.85, 3.73, and 4.88 mm, respectively. Longitudinal steel bars of the column body were 4C12 with a longitudinal bar ratio of 1.210%, whereas the stirrups were A8@150 with a stirrup ratio of 0.022%. Table 1 lists the specific design parameters.

*2.2. Material properties*

*2.2.1. SSC*

According to references [29-32], the axial and cube compressive strength of the SSSC are 26.33 MPa and 39.30 MPa, respectively, while the axial and cube compressive strength of the SSC are 24.41 MPa and 36.44 MPa, respectively. To determine the expansion rate of the SSC $P_{ct}$, three test blocks were constructed and tested, as shown in Fig. 2, and the value of $P_{ct}$ was obtained using Eq. (1).

$$P_{ct} = \frac{L_t - L_e}{L_0} \tag{1}$$

where $L_t$ is the distance between the two copper heads measured over 90 days, $L_0$ is the initial distance between the two copper heads, and $L_e = 250$ mm is the reference distance.

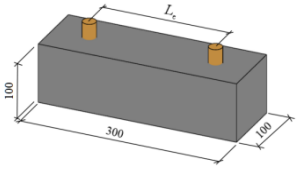


**Fig. 2** Test specimen used to determine the expansion rate of SSC

*2.2.2. Steel tube*

Longitudinal and circumferential strains were measured using strain gauges according to the Chinese code [32]. The material properties are listed in Table 2.

**Table 1**
Specimen design parameters

| Specimen label | $L$ (mm) | D (mm) | t (mm) | $n_0$ | $D/t$ | $\lambda$ | $P_{ct}$ ($\times 10^{-4}$) |
|---|---|---|---|---|---|---|---|
| A1 | 800 | 219 | 2.85 | 0.2 | 76.8 | 1.83 | 11.1 |
| A2 | 800 | 219 | 3.73 | 0.2 | 58.7 | 1.83 | 11.1 |
| A3 | 800 | 219 | 4.88 | 0.2 | 44.8 | 1.83 | 11.1 |
| A4 | 600 | 219 | 2.85 | 0.2 | 76.8 | 1.37 | 11.1 |
| A5 | 400 | 219 | 2.85 | 0.2 | 76.8 | 0.91 | 11.1 |
| A6 | 800 | 219 | 2.85 | 0.4 | 76.8 | 1.83 | 11.1 |
| A7 | 800 | 219 | 3.73 | 0.4 | 58.7 | 1.83 | 11.1 |
| A8 | 800 | 219 | 4.88 | 0.4 | 44.8 | 1.83 | 11.1 |
| A9 | 600 | 219 | 2.85 | 0.4 | 76.8 | 1.37 | 11.1 |
| A10 | 400 | 219 | 2.85 | 0.4 | 76.8 | 0.91 | 11.1 |
| B1 | 800 | 219 | 2.85 | 0.2 | 76.8 | 1.83 | -3.5 |
| B2 | 600 | 219 | 2.85 | 0.2 | 76.8 | 1.37 | -3.5 |
| B3 | 400 | 219 | 2.85 | 0.2 | 76.8 | 0.91 | -3.5 |
| B4 | 800 | 219 | 2.85 | 0.4 | 76.8 | 1.83 | -3.5 |

**Note:** $L$ is the length of the column, $t$ is the thickness of the steel tube, $D$ is the outer diameter of the steel tube, $D/t$ is the diameter-thickness ratio, $n_0$ is the axial compression ratio, $n_0 = N_a / f_c A_c$, $N_a$ is the designed axial compression strength of the specimen, $A_c$ is the cross-sectional area of the column, $f_c$ is the compressive strength of the SSC, and $\lambda$ is the shear-span ratio, $\lambda = L/2D$.

**Table 2**
Mechanical properties of the steel tube

| Thickness (mm) | Yield tensile strength (MPa) | Ultimate tensile strength (MPa) | Young's modulus ($\times 10^5$ MPa) | Poisson's ratio | Longitudinal strain ($\times 10^{-6}$ mm) | Circumferential strain ($\times 10^{-6}$ mm) | Initial self-stress (MPa) |
|---|---|---|---|---|---|---|---|
| 2.85 | 308 | 479 | 2.00 | 0.313 | 3.92 | 1.93 | 2.68 |
| 3.73 | 364 | 495 | 2.11 | 0.271 | 3.33 | 1.65 | 3.03 |
| 4.88 | 335 | 480 | 2.06 | 0.261 | 2.79 | 1.41 | 3.26 |

*2.2.3. Steel bars*

The tensile samples of the steel bars were tested according to the Chinese code [33] and were listed in Table 3.

**Table 3**
Mechanical properties of the steel bars

| Steel bars | Diameter (mm) | Yield strength (MPa) | Tensile strength (MPa) | Young's modulus ($\times 10^5$ MPa) |
|---|---|---|---|---|
| HPB300 | 8 | 308 | 426 | 2.01 |
| HPB300 | 10 | 313 | 432 | 1.97 |
| HRB400 | 12 | 439 | 644 | 1.98 |
| HRB400 | 16 | 451 | 620 | 1.95 |
| HRB400 | 22 | 438 | 618 | 1.94 |

*2.3. Loading protocol and test setup*

Fig. 3 shows a diagram of the loading device. A constant axial load and cyclic lateral loading were applied using a vertical jack and an MTS hydraulic

actuator, respectively. In this experiment, a displacement-loading control method was adopted. First, ensure that the test equipment works properly and that the axial load is applied slowly to the design value. Before the specimen yielded, a single-cycle displacement with increments of 1 mm was used for horizontal loading. After the specimen yielded, the loading mode was switched to a triple-cycle displacement with increments in integral multiples of the yield displacement. A specimen was considered damaged when its strength decreased to 85% of its peak load.

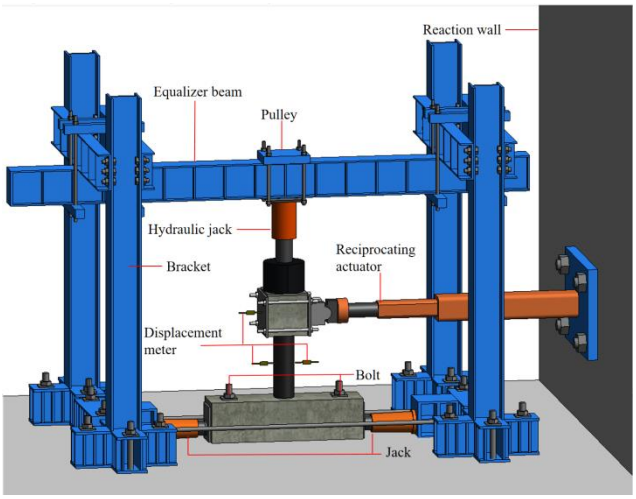


**Fig. 3** Test setup: (a) reaction wall, (b) pulley, (c) hydraulic jack, (d) reciprocating actuator, (e) counter-force truss, (f) specimen, (g) jack, (h) bracket, (i) equalizer beam, (j) portal frame, (k) loading plate, (l) displacement meter, (m) bolt

## 3. Experimental results

### *3.1. Failure mode*

Bending failure was observed as the typical failure mode of the STCRSSSC and STCRSSC columns, represented by the crushing of the SSC, yielding of the steel tubes and stirrups and circumferential tensile cracks in the inner core SSC. As illustrated in Fig. 4(a), the core SSC was crushed to a height of 0-15 mm, and circumferential tensile cracks appeared within a height of 15--60 mm from the bottom of the column. No damage was observed at other positions on the STCRSSSC columns. However, for the STCRSSC columns, as shown in Fig. 4(b), the degree of SSC crushing was more severe, and the range of heights in which circumferential tension cracks. Compared to the literature [34], the failure modes of the specimens were almost identical.

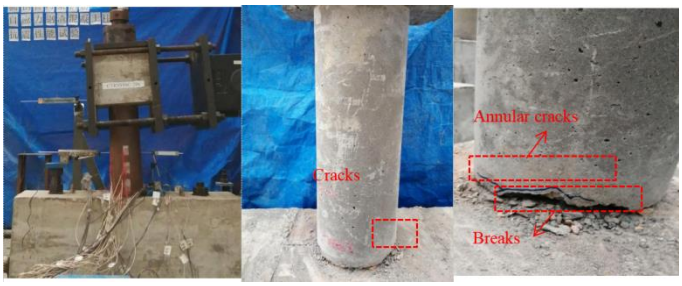


(a) A9 of the STCRSSSC column


(b) B4 of the STCRSSC column

**Fig. 4** Typical failure mode of the specimens

### *3.2. Hysteresis curve*

As shown in Fig. 5, the hysteresis loops of the specimens are saturated and slightly pinched. The $M-\phi$ hysteresis curves usually have three stages: elastic response, yielding and failure. The $M-\phi$ hysteresis curves appear to develop linearly in the elastic stage, with stiffness degradation remaining basically unchanged, and the hysteretic loops being very small. The hysteresis curves gradually deviate from the initial linear development as the load gradually increases. As the specimen enters the yield stage, the hysteresis loop area increases compared with the elastic stage. In the failure stage, the bow-shaped hysteretic loop with a slight pinching phenomenon indicates that the specimen exhibited high seismic performance and energy dissipation.

As shown in Figs. 5(a) and (f), an increase in the axial compression ratio decreases the plumpness of the $M-\phi$ hysteresis curves and the area of the hysteretic loops. For example, compared to specimen A1 ( $n_0=0.2$ ), the ultimate moment of specimen A6 ( $n_0=0.4$ ) increased by 17.30%. The reason for this might be that, with the increase in $n_0$ , the axial force at the end of the column increases. The tensile stress generated by the axial force resisting the bending moment was enhanced, leading the specimen to resist a higher bending moment. The ultimate curvature of the $M-\phi$ hysteresis curves decreases when $n_0$ increases, because higher axial forces lead to an increase in additional bending moments, accelerating specimen damage. The same effect of $n_0$ on the $M-\phi$ hysteresis curves of reinforced SCC-filled circular steel-tube columns was found by Gong et al. [35].

As shown in Figs. 5(a) and (d), the growth rate of the bending moment remains essentially unchanged as $\lambda$ increases, whereas that of the $M-\phi$ hysteresis curves decreases and the area of the hysteresis loops increases. This is because as the shear-span ratio increases, the specimen's cross-sectional deformability increases, resulting in an increase in the specimen's cross-sectional curvature. This conclusion was also verified by Yu et al. [36], who demonstrated that the ductility capacity increased with an increase in $\lambda$ .

In general, as illustrated in Figs. 5(a) and (b), an increase in $D/t$ accelerates the growth rate of the bending moment, reduces the area of the hysteretic loops, and intensifies the pinching phenomenon. Furthermore, the bending moment of the specimen section decreased, the curvature increased and the cycle number of the $M-\phi$ hysteresis curves decreased before the specimens failed. The cross-sectional moment of inertia of the core SSSC increased as $D/t$ increased, whereas that of the steel tube decreased. Consequently, the overall bending stiffness of the specimens improved, but the ductility decreased. The increase in $D/t$ produces the same effect on the CFST [37].

As shown in Figs. 5(d) and (l), the increment in $P_{ct}$ results in an improvement in the bending moment growth rate, an increase in the hysteretic loop area, and a reduction in the pinching degree. This may be because increasing $P_{ct}$ improves the expansion strain of the SSC under the constraint of the steel tube, leading to a dense specimen structure and reduced porosity. Therefore, the deformation resistance and bearing capacity of the specimens were enhanced. A similar conclusion was drawn by Dai et al. [38]. Meanwhile, the bond-slip between the steel tube and core SSSC decreased, and the pinching phenomenon of the $M-\phi$ hysteresis curves was significantly reduced. It is difficult to control the $P_{ct}$ and performance of STCRSSSC in practical engineering designs and applications, which requires further research.

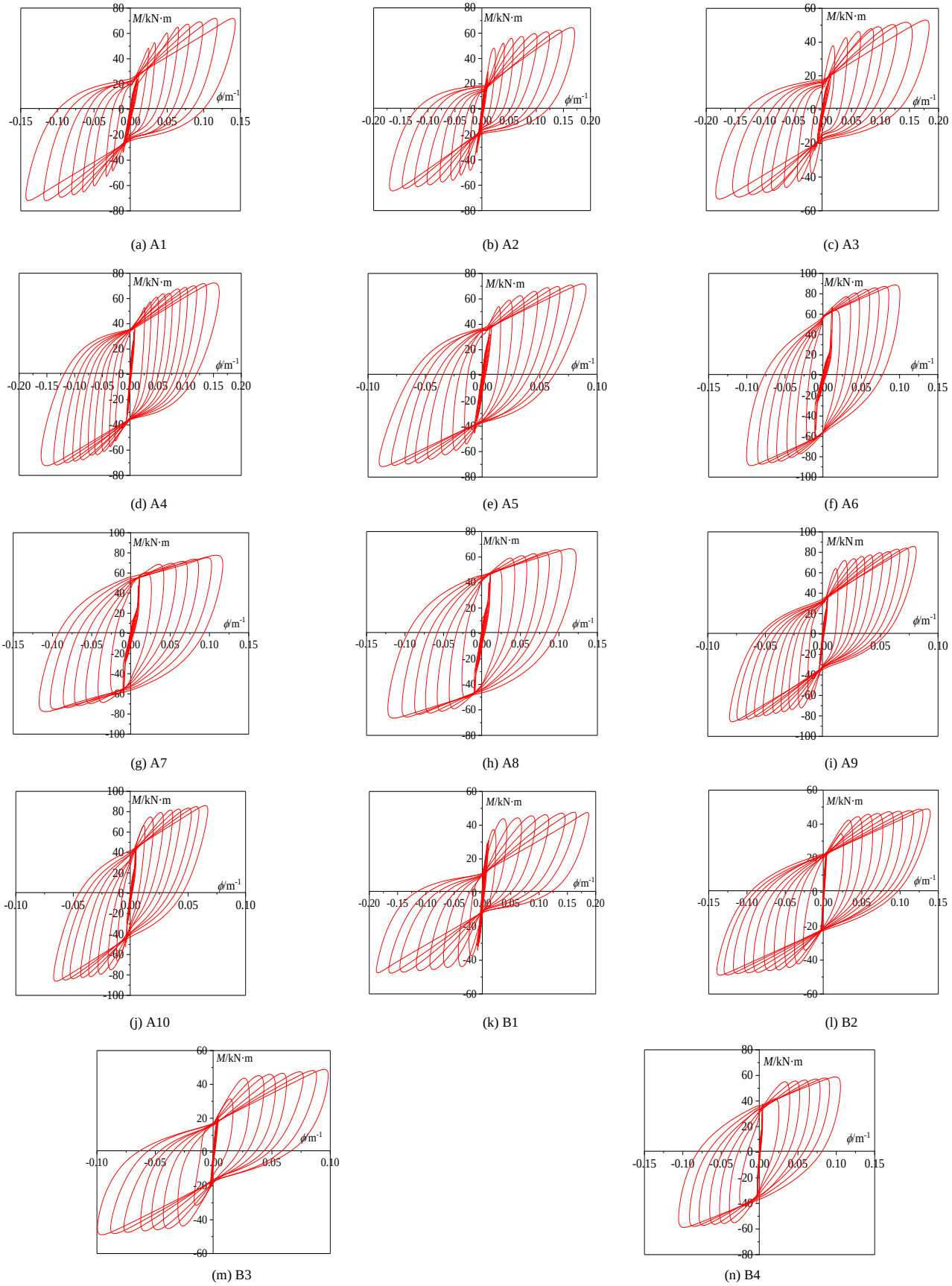


(a) A1 (b) A2 (c) A3

(d) A4 (e) A5 (f) A6

(g) A7 (h) A8 (i) A9

(j) A10 (k) B1 (l) B2

(m) B3 (n) B4

**Fig. 5** Moment-curvature hysteresis curves

### 3.3. Skeleton curve

The $M-\phi$ skeleton curve can be approximately divided into three stages, similar to the hysteresis curve shown in Fig. 6. The $M-\phi$ skeleton curves appeared linear in the elastic phase. Subsequently, with an increase in the horizontal displacement, the $M-\phi$ skeleton curves gradually exhibited nonlinear development, and an inflection point appeared. The slopes of the $M-\phi$ skeleton curves decreased, and the cross-sectional bending stiffness gradually degraded in the yield phase, intensifying during the failure stage.

As shown in Fig. 6(a), as $n_0$ increased, the peak moment, initial stiffness, and slope of the $M-\phi$ skeleton curves increased, whereas the ultimate curvature decreased. In contrast to specimen A5 ( $n_0=0.2$ ), the ultimate moment of specimen A10 ( $n_0=0.4$ ) increases by 20.25%. Additionally, as the axial compression ratio decreased, the ultimate curvature increased. This could be because the core SSSC of the specimen was destroyed when the peak load was reached, reducing the bending stiffness of the specimens. The degradation of bending stiffness is significantly accelerated if severe damage is caused to the SSSC core. The seismic behavior of STCRSSSC columns is more significantly affected by $n_0$ , so further research should be carried out to propose a more appropriate design value for $n_0$ to ensure the safety of structures in practical engineering applications.

Fig. 6(b) illustrates that the $M-\phi$ skeleton curve was not significantly affected by $\lambda$ . As $\lambda$ increased, the slopes of the $M-\phi$ skeleton curves and the ultimate bending moment hardly changed. It can be argued that the cross-sectional bending stiffness is primarily influenced by the cross-sectional moment of inertia and the Young's modulus of the specimen. The influence of the $\lambda$ on the bending stiffness was not significant when the height of the specimens was adjusted.

As $D/t$ increases, the slopes of the $M-\phi$ skeleton curves, peak moment, and initial stiffness increase, whereas the peak curvature decreases, as shown in Fig. 6(c). The ultimate moment of the specimens increased, and the ultimate curvature decreased with increasing $D/t$ . Considering specimens A1 and A3 as examples, when $D/t$ was reduced by 41.67%, the ultimate curvature of A3 was 1.29 times that of A1. This was because the bending stiffness of the specimens increased, leading to an increase in the load when the specimen was damaged. The SSSC was significantly damaged, resulting in a decrease in the bearing capacity of the specimens. The limited value of $D/t$ of STCRSSSC columns must be further explored to ensure the adequate seismic performance and economy of the columns.

Fig. 6(d) shows that the slope of the $M-\phi$ skeleton curves increases slightly, the initial stiffness and yield bending capacity increase, and the ultimate moment and curvature increase with the increment in $P_{ct}$ . For example, the ultimate moment of A4 ( $P_{ct}=11.1\times10^{-4}$ ) is 1.50 times that of B2 ( $P_{ct}=-3.5\times10^{-4}$ ), and the ultimate curvature is 1.12 times. This may be because the increasing expansion rate of the SSC enhances the confining effect on the SSSC, decreases the damage degree of the SSSC, and improves the bending capacity and ductility of the specimens. The increased ductility of the specimen was mainly due to the expansion of SSC, even when the steel tube was replaced with an FRP tube [39].

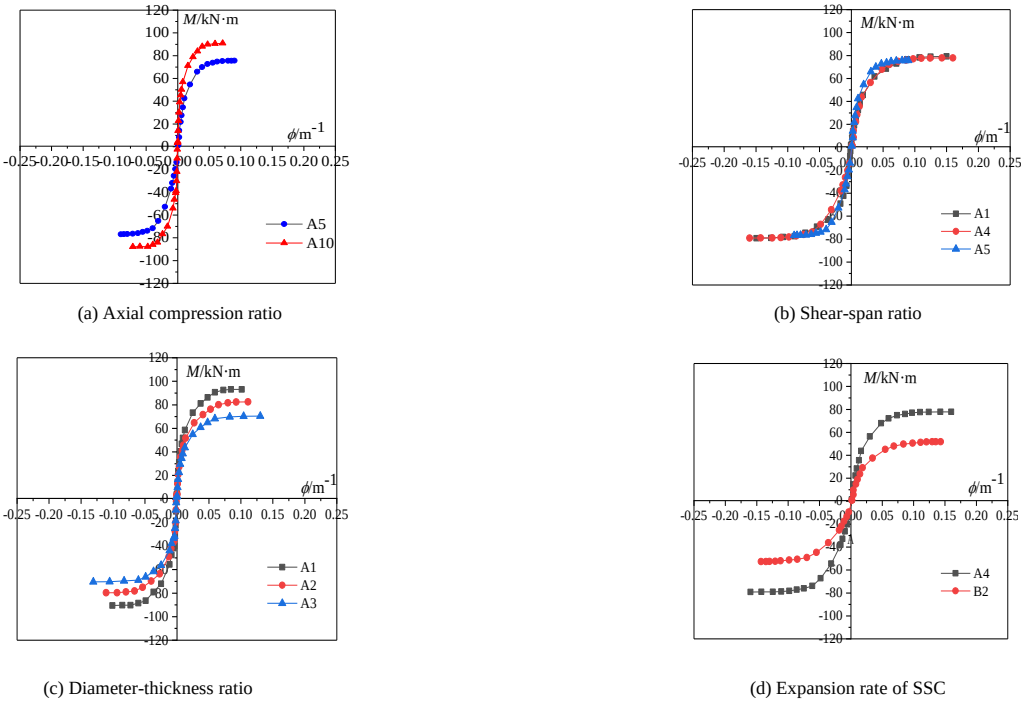


(a) Axial compression ratio

(b) Shear-span ratio

(c) Diameter-thickness ratio

(d) Expansion rate of SSC

**Fig. 6** Effects of the studied parameters on the skeleton curves of the specimens

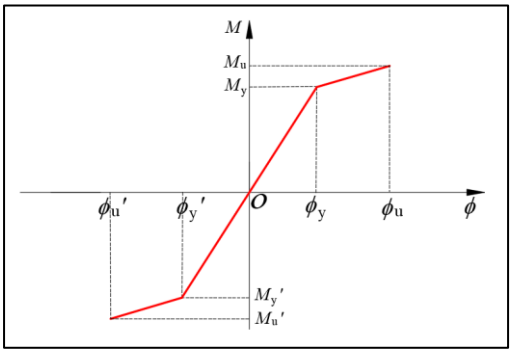


**Fig. 7** Simplified STCRSSSC columns moment-curvature skeleton curve

## 4. Model for predicting the moment-curvature performance of STCRSSSC columns

### 4.1. Prediction of the moment-curvature skeleton curves

Based on the limiting equilibrium principle, a simplified calculation model for predicting $M-\phi$ skeleton curves was proposed. Subsequently, four key parameters yield moment ( $M_y$ ), ultimate moment ( $M_u$ ), yield curvature ( $\phi_y$ ), and ultimate curvature ( $\phi_u$ ) of the $M-\phi$ skeleton curves were determined. The simplified $M-\phi$ skeleton curves were determined by connecting the four key parameters, as indicated in Fig. 7.

#### 4.1.1. Basic assumptions

To establish a prediction model for the moment-curvature performance of STCRSSSC columns, the following assumptions were made:

(1) The specimen's cross-section remained plane.

(2) There was no relative slip between the steel bars, SSC, and steel tube.

(3) The effect of core SSSC in the tension zone was not considered.

(4) The longitudinal stress in the steel tube owing to the tensile expansion of the SSSC was not considered.

(5) The axial force applied to the section was constant.

(6) The constitutive model described in [40] was assigned to the core SSSC.

*4.1.2. Yield moment and curvature*

According to reference [40], the yield moment $M_y$ can be obtained using Eqs. (2).

$$M_y = 1.59 f_{ccy}^e r_c^3 + 0.0037 N \sigma_z r_c - 19 r_c^3 + 0.57 f_{sy} \rho_s A_{sc} r_c \tag{2}$$

where $f_{ccy}^e$ denotes the stress of the core SSSC in the compression zone of the critical section, $r_c$ denotes the radius of the core SSSC section, $N$ denotes the axial compression of the SSSC core, $\sigma_z$ indicates the longitudinal self-stress caused by the initial self-stress, $\rho_s$ represents the steel ratio of the steel ring, $A_{sc}$ refers to the cross-sectional area of the column, and $f_{sy}$ represents the yield strength of the longitudinal reinforcement.

The yield curvature can be obtained from Eq. (3).

$$\phi_y = \frac{M_y}{K_{sc}} \tag{3}$$

where $\phi_y$ is the yield curvature of the specimen, $K_{sc}$ is the sectional bending stiffness of the STCRSSSC column, $K_{sc} = E_{sc} I_c$, $E_{sc}$ denotes the section deformation modulus of the STCRSSSC column, $E_{sc} = f_{ccy}^e / \varepsilon_{y1}$, $\varepsilon_{y1}$ designates the longitudinal strain of the specimen, and $I_c$ is the sectional inertia moment of the STCRSSSC column, $I_c = \pi (D - 2r_c)^4 / 64$.

*4.1.3. Ultimate moment and curvature*

According to [40], the ultimate moment $M_u$ considering the effects of the axial force, low-cycle reversed loading, and initial self-stress of the core SSSC on the bending capacity can be expressed as Eq. (4).

$$M_u = 1.59 f_{cc}^e r_c^3 - 19 r_c^3 + 0.037 N \sigma_z r_c + 0.95 f_{ss} \rho_s A_{sc} r_c \tag{4}$$

where $f_{cc}^e$ is the strength of the confined core SSSC and $f_{ss}$ denotes the actual strength of the longitudinal reinforcement.

The average strain along the height of the cross-section was linear based on the plane section assumption. Therefore, the ultimate curvature $\phi_u$ is calculated as follows:

$$\phi_u = \frac{\varepsilon_{cu}}{\zeta} = \frac{\varepsilon_{sy}(r_c \cos\gamma_0 + r_c - m) E_s + m f_{ss}}{m r_g E_s} \tag{5}$$

$$\varepsilon_{cu} = \frac{\varepsilon_{sy}(r_c \cos\gamma_0 + r_c - m)}{m} \tag{6}$$

$$\zeta = \frac{r_g \varepsilon_{cu}}{\varepsilon_{cu} + \varepsilon_{sy}} = \frac{r_g E_s \varepsilon_{cu}}{f_{sy} + E_s \varepsilon_{cu}} \tag{7}$$

$$m = \frac{(2r_c - a)\varepsilon_{sy}}{\varepsilon_{sy} + \varepsilon_{cu}} \tag{8}$$

$$\gamma_0 = \frac{\pi}{2} - \arccos\frac{2m - r_g}{r_g} \tag{9}$$

$$r_g = r_c - a \tag{10}$$

where $\varepsilon_{cu}$ is the ultimate strain of the confined core SSSC, $\varepsilon_{sy}$ is the yield compression strain of the steel ring, $E_S$ is the Young's modulus of the steel tube, $m$ stands for the distance from $\varepsilon_{sy}$ to strain 0, $\zeta$ designates the height of the core SSSC in the compression zone, $\gamma_0$ indicates the center angle of the core SSSC in the compression zone, $r_g$ is the radius of the equivalent steel ring of longitudinal reinforcement, and $a$ is the radius of the core SSSC section in the tensile zone.

*4.1.4. Assessment of the proposed skeleton curve prediction model*

Fig. 8 compares the proposed $M-\phi$ and experimental $M-\phi$ skeleton curves. The experimental results were in good agreement with the theoretical curves, demonstrating the high accuracy of the proposed model.

*4.2. Hysteresis rule*

Based on the numerical analysis of the $M-\phi$ skeleton curves for each factor, a Cough trilinear degeneration model was adopted to further analyze the $M-\phi$ hysteresis rules of the STCRSSSC columns. The parameters were determined using Eqs. (11)–(17), as shown in Fig. 9.

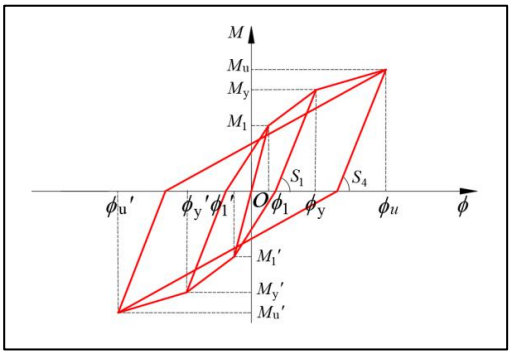


**Fig. 9** Loading and unloading rules for STCRSSSC columns under cyclic loading

$$S_1 = \frac{M_1}{\phi_1} \tag{11}$$

$$S_2 = \frac{M_y}{\phi_y} \tag{12}$$

$$M_1 = 0.6 M_y \tag{13}$$

$$S_3 = 0.112 n_0 + 2.864 \sigma_0 + 0.003 D/t - 1.443 \lambda + 0.883 \tag{14}$$

$$S_4 = S_1 \tag{15}$$

$$S_5 = S_1 \left(\frac{\phi_i}{\phi_y}\right)^{\beta} \tag{16}$$

$$\beta = 0.140 n_0 - 0.019 \lambda - 0.003 D/t + 0.133 \sigma_0 + 0.265 \tag{17}$$

where $S_1$ and $S_2$ denote the stiffnesses at the elastic and yield stages, respectively, $M_1$ and $\phi_1$ denote the bending moment and curvature, respectively, $S_3$ indicates the stiffness in the third stage, $M_u$ represents the ultimate moment, $S_4$ and $S_5$ are the unloading stiffnesses before and after yielding, respectively, $\phi_i$ is the curvature corresponding to the i-th unloading point of the $M-\phi$ curve starting from the yield point, and $\beta$ is an parameter related to $D/t$, $\lambda$, $n_0$, and the initial self-stress.

*4.3. Verification of the model for predicting the moment-curvature response of the specimens*

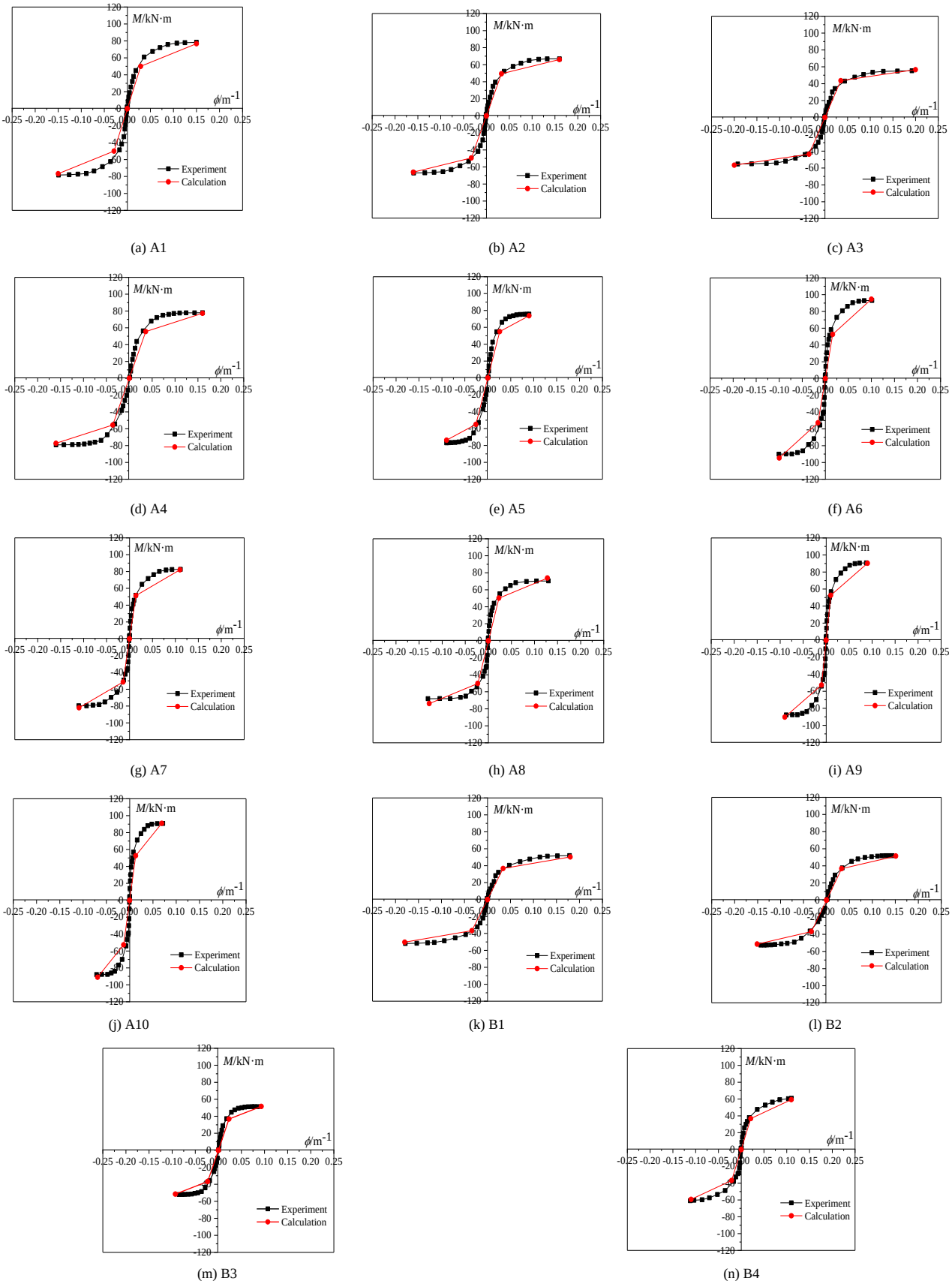


**Fig. 8** Verification of experimental and theoretical moment-curvature skeleton curves

The predicted hysteresis curves can be obtained by calculating the skeleton curves of the $M-\phi$ hysteresis relation and the loading-unloading stiffness of the specimens. As illustrated in Fig. 10, the theoretical curves of the specimens agreed well with the test results.

Owing to the limitations of the experimental conditions, the quantity and level of the studied parameters were limited, and the dimensions of the specimens were scaled down compared with the columns in the actual project. In future studies, refined models of full-scale STCRSSSC columns can be built using finite elements to analyze the performance of STCRSSSC columns under more key parameters and complex loads to adapt to actual engineering situations.

Based on the experimental study of specimens with specific stress states and geometric characteristics, a prediction model is generally proposed, which has certain limitations in its applicability. However, owing to the randomness and uncertainty of the seismic action, high discreteness of the crack development and bond-slip of concrete, and the fact that the errors of the prediction model are not very sensitive to the results of certain structures, the calculation of the hysteretic behavior of STCRSSSC columns based on the simplified model can still achieve satisfactory results.

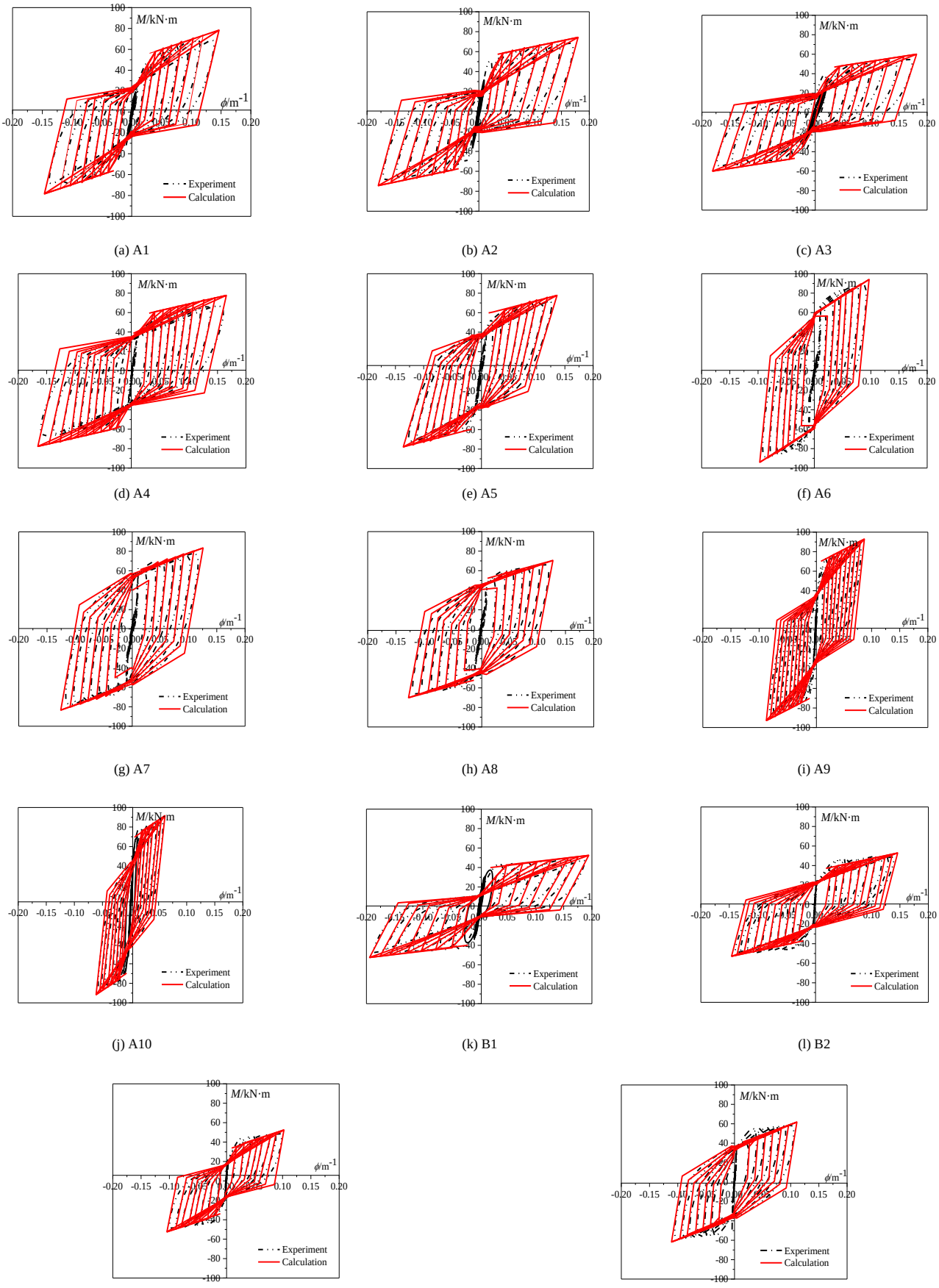


(a) A1 (b) A2 (c) A3

(d) A4 (e) A5 (f) A6

(g) A7 (h) A8 (i) A9

(j) A10 (k) B1 (l) B2

(m) B3 (n) B4

**Fig. 10** Comparisons between the theoretical and experimental moment-curvature hysteresis curves

## 5. Conclusions

This study presents the design and tests of ten STCRSSSC columns and four STCRSSC columns under cyclic loading, investigating the effects of various parameters on seismic performance, including $\lambda$, $P_{ct}$, $D/t$, and $n_0$. The conclusions are as follows:

(1) Bending failure occurred in all the specimens, characterized by longitudinal steel bar yield. Circumferential cracks were observed in the non-shear surface at the column bottom, and the core SSSC or SSC was broken at the column bottom. Plastic deformation of the specimens before damage to the STCRSSSC column was significant, with evident signs of failure.

(2) The specimens exhibited plump hysteresis loops with slight pinching. With an increase in $D/t$ or $n_0$, the plumpness of the hysteresis curves and the areas of the hysteretic loops decreased. However, an increase in $\lambda$ or $P_{ct}$ increased the area of the hysteretic loops of the hysteresis curves.

(3) The $M-\phi$ skeleton curves are roughly divided into three phases: elastic response, yielding, and failure. With increases in $D/t$, $n_0$, and $P_{ct}$, the slopes of the $M-\phi$ skeleton curves increased. The $M-\phi$ skeleton curves are not significantly affected by $\lambda$.

(4) Based on the principle of limiting equilibrium, theoretical calculations of the corresponding yield and ultimate points of the STCRSSSC column were performed based on the experimental studies, and the key characteristic points were connected to a simplified skeleton curve. A comparison of the experimental skeleton curves with the theoretical curves indicated that the model was highly accurate.

(5) Based on the Clough trilinear degeneration model, the hysteresis rule of the $M-\phi$ relationship of STCRSSSC columns is proposed. Furthermore, a prediction model for the performance of the STCRSSSC columns was established and validated.

(6) The proposed prediction model was applied to the STCRSSSC columns. Owing to the limitations of the experimental device, the designed specimen was a third of the actual specimen. Finite element analysis software was used to further analyze the influence of key factors on the behaviors of full-scale specimens in a subsequent study.

## Acknowledgments

This study was sponsored by National Natural Science Foundation of China (No. 52078001), Outstanding Youth Fund of Anhui Province (No. 2008085J29), Key Research and Development Project of Anhui Province (No. 2022i01020005), Major Science and Technology Project of Anhui Province (No. 202203a07020005), The University Synergy Innovation Program of Anhui Province (No. GXXT-2023-061, GXXT-2022-074), Wuhu Technology and Innovation Research Institute, Anhui University of Technology (No. 2022jc04), The University Outstanding Research and Innovation Team Program of Anhui Province (No. 2023AH010017).

## References

[1] Chin CL, Ma CK, Tan JY, Ong CB, Awang AZ, Omar W. Review on development of external steel-confined concrete. Construction and Building Materials 2019; 211: 919-931. http://doi.org/10.1016/j.conbuildmat.2019.03.295.

[2] Guo L, Liu Y, Fu F, Huang H. Behavior of axially loaded circular stainless steel tube confined concrete stub columns. Thin-Walled Structures 2019; 139: 66–76. https://doi.org/10.1016/j.tws.2019.02.014.

[3] Li WT, Zha XX, Wang HY. A unified formulation for axial compression of steel tube-confined concrete and concrete-filled steel tube stub columns. Structures 2023; 58: 105319. https://doi.org/10.1016/j.istruc.2023.105319.

[4] Zhang J, Ma L, Zhou C, Lee D, Filippou FC. Experimental study of axial compression behavior of circular concrete-filled steel tubes after being loaded at an early age. Construction and Building Materials 2021; 300: 124030. https://doi.org/10.1016/j.conbuildmat.2021.124020.

[5] Zhou XH, Gan D, Liu JP, Chen YF. Composite effect of stub sdquare steel tubed columns under axial compression. Advanced Steel Construction 2018; 14 (2): 274-290. https://doi.org/10.18057/IJASC.2018.14.2.8.

[6] Wang FC, Xie WQ, Li B, Han LH. Experimental study and design of bond behavior in concrete-filled steel tubes (CFST). Engineering Structures 2022; 268: 114750. https://doi.org/10.1016/j.engstruct.2022.114750.

[7] Fu ZQ, Ge HB, Ji BH, Chen JJ. Interface bond behaviour between circular steel tube and lightweight aggregate concrete. Advanced Steel Construction 2018; 14 (3): 424-437. https://doi.org/10.18057/IJASC.2018.14.3.7.

[8] Wang BX, Man T, Jin HN. Prediction of expansion behavior of self-stressing concrete by artificial neural networks and fuzzy inference systems. Construction and Building Materials 2015; 84: 184-191. https://dx.doi.org/10.1016/j.conbuildmat.2015.03.059.

[9] Carballosa P, Calvo JL, Revuelta D., Sánchez JJ, Gutiérrez JP. Influence of cement and expansive additive types in the performance of self-stressing and self-compacting concretes for structural elements. Construction and Building Materials 2015; 93: 223-229. https://dx.doi.org/10.1016/j.conbuildmat.2015.05.113.

[10] Li H, Wang Y, Wang YJ, Liu JP, Tian Q. Effect of CaO and MgO based expansive agent on deformation and mechanical properties of concrete-filled steel tubes. Construction and Building Materials 2020; 250: 118723. https://doi.org/10.1016/j.conbuildmat.2020.118723.

[11] Chang X, Lin HX, Huang CK. Experimental study on shear resistance of self-stressing concrete filled circular steel tubes. Journal of Constructional Steel Research 2009; 65 (4): 801-807. https://doi.org/10.1016/j.jcsr.2008.12.004.

[12] Natalli JF, Andrade HD, Carvalho JMF, Defóveri K, Mendes JC, Sarmanho AMC, et al. Performance of lightweight concrete with expansive and air-entraining admixtures in CFST columns. Journal of Materials in Civil Engineering 2020; 32 (6): 04020121. https://doi.org/10.1061/(ASCE)MT.1943-5533.0003143.

[13] Li X, Pan JL, Xiao Y. Mechanical performance of self-stressing CFST columns under uniaxial compression. Journal of Building Engineering 2021; 44: 103366. https://doi.org/10.1016/j.jobe.2021.103366.

[14] Guo YL, Geng Y, Qu LY. Time-dependent behaviour of circular steel tube confined reinforced concrete (STCRC) stub columns subjected to low axial load. Engineering Structures 2021; 243: 112663. https://doi.org/10.1016/j.engstruct.2021.112663.

[15] Liu ZZ, Huang DM, Li N, Lu YY. Mechanical behavior of steel-fiber-reinforced self-stressing concrete filled steel tube columns subjected to eccentric loading. Structures 2022; 45: 932-950. https://doi.org/10.1016/j.istruc.2022.08.118.

[16] Lu Y, Liu Z, Li S, Li W. Behavior of steel fibers reinforced self-stressing and self-compacting concrete-filled steel tube subjected to bending. Construction and Building Materials 2017; 156: 639-651. https://doi.org/10.1016/j.conbuildmat.2017.09.019.

[17] Yu F, Qin Y, Yao C. Experimental investigation on the seismic behavior of self-stressing steel slag CFST column. Structural Concrete 2022; 23: 1492-1507. https://doi.org/10.1002/suco.202100523.

[18] Lai MH, Zou JJ, Yao BY, Ho JCM, Zhuang X, Wang Q. Improving mechanical behavior and microstructure of concrete by using BOF steel slag aggregate. Construction and Building Materials 2021; 277: 122269. https://doi.org/10.1016/j.conbuildmat.2021.122269.

[19] Nemade PA, Pasla D, Chandrappa AK. Durability assessment of concrete with natural and Linz Donawitz slag as coarse aggregates. Construction and Building Materials 2023; 400: 132617. https://doi.org/10.1016/j.conbuildmat.2023.132617.

[20] Saxena S, Tembhurkar AR. Impact of use of steel slag as coarse aggregate and wastewater on fresh and hardened properties of concrete. Construction and Building Materials 2018; 165: 126-137. https://doi.org/10.1016/j.conbuildmat.2018.01.030.

[21] Ho JCM, Liang Y, Wang YH, Lai MH, Huang ZC, Yang D, Zhang QL. Residual properties of steel slag coarse aggregate concrete after exposure to elevated temperatures. Construction and Building Materials 2022; 316: 125751. https://doi.org/10.1016/j.conbuildmat.2021.125751.

[22] Lai MH, Chen ZH, Wang YH, Ho JCM. Effect of fillers on the mechanical properties and durability of steel slag concrete. Construction and Building Materials 2022; 335: 127495. https://doi.org/10.1016/j.conbuildmat.2022.127495.

[23] Guo YC, Xie JH, Zheng WY, Li JL. Effects of steel slag as fine aggregate on static and impact behaviours of concrete. Construction and Building Materials 2018; 192: 194-201. https://doi.org/10.1016/j.conbuildmat.2018.10.129.

[24] Huang ZC, Ho JCM, Cui J, Ren FM, Cheng X, Lai MH. Improving the post-fire behaviour of steel slag coarse aggregate concrete by adding GGBFS. Journal of Building Engineering 2023; 76: 107283. https://doi.org/10.1016/j.jobe.2023.107283.

[25] Yu F, Fang Y, Niu K, Zhang Y, Chen TY. Experimental study on bond-slip constitutive relation of SSSCFST columns. Structural Concrete 2021; 22(4): 1905-2497. https://doi.org/10.1002/suco.201900546.

[26] Yu F, Cao Y, Fang Y, Zhang Y, Niu K. Mechanical behavior of self-stressing steel slag aggregate concrete filled steel tubular short columns with different loading modes. Structures 2020; 26: 947-957. https://doi.org/10.1016/j.istruc.2020.05.015.

[27] Yu F, Yao C, Hu Y, Fang Y, Niu K, Xiang GS. Axial compressive behavior of self-stressing steel slag aggregate concrete filled steel tubular columns with bond-slip damage. Advanced Steel Construction 2020; 16(1): 13-19. https://doi.org/10.18057/IJASC.2020.16.1.2.

[28] Yu F, Chen T, Niu K, Wang S, Fang Y. Study on bond-slip behaviors of self-stressing steel slag concrete-filled steel tube. KSCE Journal of Civil Engineering 2020; 24: 3309-3319. https://doi.org/10.1007/S12205-020-1596-7.

[29] Wang XL. Study on basic properties of steel slag concrete based on controllable expansion rate. Anhui University of Technology, China. (in Chinese).

[30] GB/T 50081-2002, Standard for test method of mechanical properties on ordinary concrete, Beijing, 2003, China. (in Chinese).

[31] GB/T 50082-2009, Standard for test methods of long-term performance and durability of ordinary concrete, Beijing, 2009, China. (in Chinese).

[32] GB/T 228.1-2010, Metallic materials-Tensile testing-Part 1:Method of test at room temperature, Beijing, 2010, China. (in Chinese).

[33] GB/T 228-2002, Metallic materials-Tensile testing at ambient temperature, Beijing, 2002, China. (in Chinese).

[34] Shang ZQ, Huang CK, Chang X, Xu ST. Experrimental research on shear-resistance properties of self-stressing concrete filled steel tube. Journal of Earthquake Engineering and Engineering Vibration. 2008; 28 (3): 77-81. (in Chinese). https://doi.org/10.13197/j.eeev.2008.03.026.

[35] Gong TN, Xu DF. Seismic performance of reinforced self-compacting concrete-filled circular steel-tube columns. Journal of Constructional Steel Research 2014; 212: 108300. https://doi.org/10.1016/j.jcsr.2023.108300.

[36] Yu F, Xu GS, Niu DT, Cheng AC, Wu P, Kong ZY. Experimental study on PVC-CFRP confined concrete columns under low cyclic loading. Construction and Building Materials 2018; 177: 287-302. https://doi.org/10.1016/j.conbuildmat.2018.05.111.

[37] Chen HY, Liao FY, Yang YX, Ren Y. Behavior of ultra-high-performance concrete (UHPC) encased concrete-filled steel tubular (CFST) stub columns under axial compression. Journal of Constructional Steel Research 2023; 202: 107795. https://doi.org/10.1016/j.jcsr.2023.107795.

[38] Dai S, Zhu HJ, Zhang DR, Liu ZQ, Cheng SY, Zhao JX. Insights to compressive strength, impermeability and microstructure of micro-expansion steel slag cement under constraint conditions. Construction and Building Materials 2022; 326: 126540. https://doi.org/10.1016/j.conbuildmat.2022.126540.

[39] Feng P, Li ZY, Zhang SB, Yang JQ. Steel slag aggregate concrete filled-in FRP tubes: Volume expansion effect and axial compressive behaviour. Construction and Building Materials 2022; 318: 125961. https://doi.org/10.1016/j.conbuildmat.2021.125961.

[40] Chen TY. Experimental study and theoretical analysis on seismic behavior of circular tube confined reinforced self-stressing of steel slag concrete columns, Anhui University of Technology, China. (in Chinese).